Conference Proceedings of the Society for Experimental Mechanics Series

Chad Walber
Matthew Stefanski
Julie Harvie *Editors*

Sensors and Instrumentation, Aircraft/ Aerospace and Dynamic Environments Testing, Volume 7

Proceedings of the 40th IMAC, A Conference and Exposition on Structural Dynamics 2022

Springer

Conference Proceedings of the Society for Experimental Mechanics Series

Series Editor

Kristin B. Zimmerman, Ph.D.
Society for Experimental Mechanics, Inc.,
Bethel, CT, USA

The Conference Proceedings of the Society for Experimental Mechanics Series presents early findings and case studies from a wide range of fundamental and applied work across the broad range of fields that comprise Experimental Mechanics. Series volumes follow the principle tracks or focus topics featured in each of the Society's two annual conferences: IMAC, A Conference and Exposition on Structural Dynamics, and the Society's Annual Conference & Exposition and will address critical areas of interest to researchers and design engineers working in all areas of Structural Dynamics, Solid Mechanics and Materials Research.

Chad Walber • Matthew Stefanski • Julie Harvie
Editors

Sensors and Instrumentation, Aircraft/Aerospace and Dynamic Environments Testing, Volume 7

Proceedings of the 40th IMAC, A Conference and Exposition on Structural Dynamics 2022

Springer

Editors
Chad Walber
PCB Piezotronics, Inc.
Depew, NY, USA

Julie Harvie
Albuquerque, NM, USA

Matthew Stefanski
Air Force Research Laboratory
Dayton, OH, USA

ISSN 2191-5644 ISSN 2191-5652 (electronic)
Conference Proceedings of the Society for Experimental Mechanics Series
ISBN 978-3-031-05414-3 ISBN 978-3-031-05415-0 (eBook)
https://doi.org/10.1007/978-3-031-05415-0

This Springer imprint is published by the registered company Springer Nature Switzerland AG
The registered company address is: Gewerbestrasse 11, 6330 Cham, Switzerland

Preface

Sensors and Instrumentation, Aircraft/Aerospace and Dynamic Environments Testing represents one of nine volumes of technical papers presented at the 40th IMAC, a conference and exposition on structural dynamics, organized by the Society for Experimental Mechanics, and held February 7–10, 2022. The full proceedings also include volumes on nonlinear structures and systems; dynamic substructures; model validation and uncertainty quantification; dynamic substructures; special topics in structural dynamics and experimental techniques; rotating machinery, optical methods, and scanning LDV methods; topics in modal analysis and parameter identification; and data science in engineering.

Each collection presents early findings from experimental and computational investigations on an important area within sensors and instrumentation and other structural dynamics areas. Topics represent papers on calibration, smart sensors, shock calibration and shock environment synthesis, and applications for aircraft/aerospace structures.

The organizers would like to thank the authors, presenters, session organizers, and session chairs for their participation in this track.

PCB Piezotronics, Inc., NY, USA — Chad Walber
US Air Force Research Laboratory, Dayton, OH, USA — Matthew Stefanski
Cummins Power Systems, Columbus, MN, USA — Steve Seidlitz
Vibes Technology, Delft, Netherlands — Julie Harvie

Contents

Chapter 1
Test Data Measurement Uncertainty Analysis

David T. Buck

Abstract The Structural Validation Branch (AFRL/RQVV) provides test services for internal and external customers covering a wide range of research and development programs. Calculating and documenting test data uncertainty is a necessary capability for a test organization. Test data uncertainty analysis provides error limit values based on the combined effects of random and systematic error sources. Error source examination can also be used to determine if corrective actions are necessary and/or possible to eliminate or reduce the measurement errors. This project was initiated to review uncertainty calculation methods and develop the internal processes and procedures that will be used to calculate, document, and report measurement uncertainty values.

Keywords Test · Data · Measurement · Uncertainty · Analysis

1.1 Introduction

AFRL/RQVV is the Air Force Research Structures Validation lab that provides research and design testing capabilities in the static, dynamic, acoustic, thermal, and vibration testing of aerospace structures. All RQVV tests use instrumentation and equipment that meets US Air Force Metrology Laboratory calibration requirements. However, AFRL/RQVV did not have a program in place to provide measurement uncertainty values that included not only the instrument accuracy but also uncertainties related to the data collection system, cables and connectors, and position errors.

AFRL/RQVV implemented a program that has led to the completion of uncertainty calculations for a list of "critical instrumentation," established a database of typical uncertainty estimates, and developed "user-friendly" processes and procedures for calculating uncertainty estimates.

1.2 Background

Test data uncertainty analysis provides measurement error limit estimates based on the combined effects of random and systematic error sources. The following sections will briefly describe the two error sources and define the method for combining their effects into a final measurement uncertainty value.

1.3 Random Uncertainty

Random uncertainty, also known as precision error, is an error source that is calculated from test data with statistical methods. Random errors add scatter to the test data and also increase the scatter in the final uncertainty calculation. Random errors usually follow the data scatter of a Gaussian (normal) distribution shown in Fig. 1.1. For large data sets (≥30 points), 68%

D. T. Buck (✉)
Air Force Research Laboratory, Aerospace Vehicles Division, Structural Validation Branch (AFRL/RQVV), Wright-Patterson AFB, OH, USA
e-mail: david.buck.5@us.af.mil

C. Walber et al. (eds.), *Sensors and Instrumentation, Aircraft/Aerospace and Dynamic Environments Testing, Volume 7*,
Conference Proceedings of the Society for Experimental Mechanics Series, https://doi.org/10.1007/978-3-031-05415-0_1

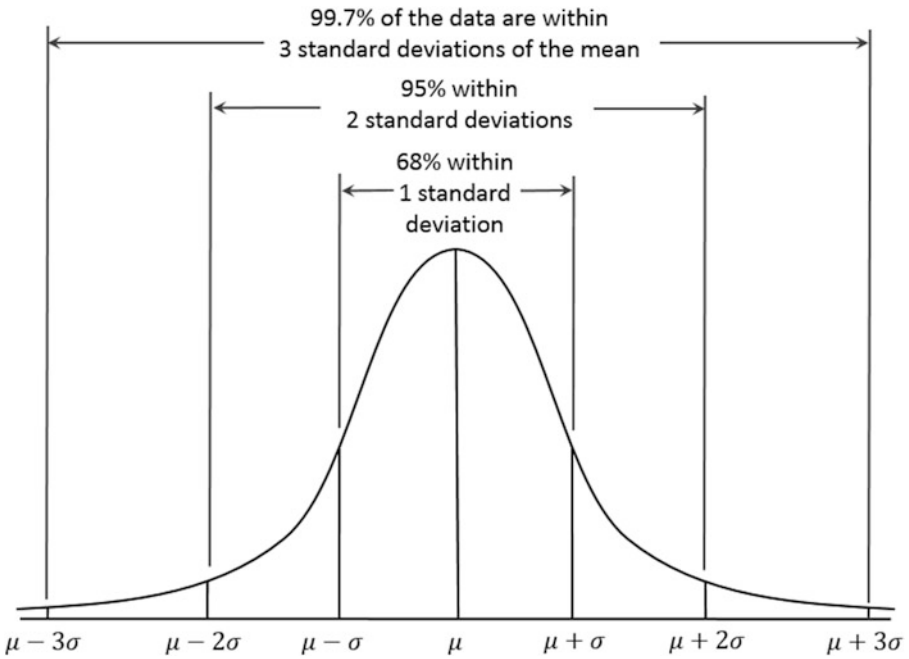

Fig. 1.1 Gaussian (normal) distribution

of the measurements will fall within ± one standard deviation; 95% of the measurements will fall within ± two standard deviations.

Distribution Statement A: Approved for public release; distribution unlimited. Approval given by AFRL/PA, October 2021.

The data scatter is defined by the sample standard deviation (Eq. 1.1).

$$\text{Sample standard deviation} \quad S_x = \left[\frac{\sum_{i=1}^{N} (x_i - \overline{x})^2}{N-1} \right]^{1/2} \tag{1.1}$$

The final uncertainty calculation requires a term that defines the scatter of the averages. This term is known as the random standard uncertainty (Eq. 1.2).

$$\text{Random standard uncertainty} \quad S_{\overline{x},R} = \frac{S_{x,i}}{\sqrt{N_i}} \tag{1.2}$$

1.4 Systematic Uncertainty

Systematic uncertainty, also known as bias or offset error, is an error source that does not add scatter to the test data. They are constant for the duration of the test. Typical systematic error sources include instrument accuracy (calibration), data collection system accuracy, connectors and cabling/wiring, and position error (strain gauges/accelerometers, thermocouples). Manufacturers usually supply uncertainty data at a 95% confidence level (± two standard deviations).

Systematic uncertainty examples are listed below.

- LeBow 500 lbf load cell (model 3143) accuracy (calibration): ± 0.1% full scale.
- Thermocouple (K-type) accuracy: ±2.2 °C or ±0.75% of range whichever is greater.
- HBM data collection system – published error: ±0.0025% in instrument full scale.
- Strain gauge alignment error: A five-degree alignment error can result in a strain measurement 1% lower than the actual strain (on steel – Poisson's ratio of 0.3).

Table 1.1 Student's t values

DOF	t_{95}	DOF	t_{95}	DOF	t_{95}
1	12.706	11	2.201	21	2.080
2	4.303	12	2.179	22	2.074
3	3.182	13	2.160	23	2.069
4	2.776	14	2.145	24	2.064
5	2.571	15	2.131	25	2.060
6	2.447	16	2.120	26	2.056
7	2.365	17	2.110	27	2.052
8	2.306	18	2.101	28	2.048
9	2.262	19	2.093	29	2.045
10	2.228	20	2.086	30+	2.000

1.5 Final Uncertainty Calculation

The final uncertainty calculation is performed using Eq. 1.3. This is known as the U_{95} uncertainty model.

$$\text{U}_{95}\text{ uncertainty model } \quad U_{95} = \pm t_{95}\left[(b_R)^2 + \left(S_{\overline{x},R}\right)^2\right]^{1/2} \tag{1.3}$$

The calculated U_{95} value represents the measurement uncertainty at a 95% confidence level. The term b_R is the combined systematic standard uncertainty. The term $S_{x,R}$ is the combined random standard uncertainty.

All uncertainty calculations are performed using terms at a 68% (one sigma) confidence level. The term t_{95} is known as Student's t and defines the data scatter multiplication factor that must be used to reach a 95% (two sigma) confidence level (the reported uncertainty). For example, when a sample size is ≥30, the value of Student's t is 2.000. Therefore, 68% confidence level × 2.000 = 95% confidence level. Student's t values are shown in Table 1.1.

The t_{95} value in Eq. 1.3 is dependent on the combined degrees of freedom for the entire system (all random and systematic error sources). The Welch-Satterthwaite equation shown below (Eq. 1.4) is used to combine the degrees of freedom. The terms in the numerator and denominator represent the individual random and systematic error sources.

$$\text{Welsh} - \text{Satterthwaite equation } \quad \nu = \frac{\left[\sum_{i=1}^{N}\left(S_{\overline{x},R}\right)^2 + \sum_{j=1}^{M}\left(b_j\right)^2\right]^2}{\left[\sum_{i=1}^{N}\frac{\left(S_{\overline{x},R}\right)^4}{\nu_p} + \sum_{j=1}^{M}\frac{\left(b_j\right)^4}{\nu_j}\right]} \tag{1.4}$$

1.6 Consultant

AFRL/RQVV hired Mr. Ron Dieck (Ron Dieck Associates, Inc.) to provide guidance and assistance in the development and implementation of this uncertainty program. Mr. Dieck is a nationally known subject matter expert in measurement uncertainty.

- Aerospace experience (35 years with Pratt & Whitney)
- Current vice-chairman of the ASME Test Uncertainty Committee (after 25 years as chairman)

Mr. Dieck is the author of the following book (used as a reference form the RQVV uncertainty project):

Dieck, Ronald H., Measurement Uncertainty, Methods and Applications, Research Triangle Park, NC, ISA, 5th Edition, 2017

Mr. Dieck developed a software tool as an aid for uncertainty calculations. Values for random and systematic uncertainty error sources are input at the 68% confidence level along with the associated degrees of freedom. The spreadsheet combines the terms (errors and degrees of freedom) and provides the final uncertainty value at the 95% confidence level.

1.7 ASME and ISO Compliance

The measurement uncertainty calculation methods developed by AFRL/RQVV (and Mr. Dieck) comply with the following standards:

- American Society of Mechanical Engineers, US National Standard on Uncertainty, ASME PTC19.1-2013, Test Uncertainty, ASME, New York, NY, 2013
- International Organization for Standardization (ISO), Guide to the Expression of Uncertainty in Measurement (1993)

These two standards define the nationally and internationally accepted uncertainty calculation process. They are very similar with the primary difference being how the error sources and uncertainties are categorized, or grouped, for analysis.

1.8 Example

The following is an example of the work that has been performed.

Load Cell

Manufacturer: LeBow
Model Number: 3143
Range: 500 lbf

Systematic Error Sources

- Calibration accuracy: ± 0.1% full scale (±0.5 lbf at 95% confidence level/±0.25 lbf at 68% confidence level)
- HBM data collection system – published error: ±0.0025% of instrument full scale (±0.0125 lbf at 95% confidence level/±0.00625 lbf at 68% confidence level)

Random Error Source

- The random uncertainty was calculated using data from a test program completed in 2013. This value was ±0.13 lbf (68% confidence level).

The final uncertainty value (95% confidence level) for this load cell was ±1.18 lbf.

1.9 Conclusion

All test measurements have error. The measurement uncertainty calculations provide a means to characterize the measurement methods and understand what the test data really represents. This allows engineers to make informed decisions based on the quality of the test data.

Chapter 2
Forced Vibrations of Damped Non-homogeneous Timoshenko Beams

Arnaldo J. Mazzei

Abstract This work is the next of a series on vibrations of non-homogeneous structures. It addresses the lateral harmonic forcing, with spatial dependencies, of a two-segment damped Timoshenko beam. In the series, frequency response functions (FRFs) were determined for segmented structures, such as rods and beams, using analytic and numerical approaches. These structures are composed of stacked cells, which are made of different materials and may have different geometric properties. The goal is the determination of frequency response functions (FRFs). Two approaches are employed. The first approach uses displacement differential equations for each segment, where boundary and interface continuity conditions are used to determine the constants involved in the solutions. Then the response, as a function of forcing frequency, can be obtained. This procedure is unwieldy, and determining particular integrals can become difficult for arbitrary spatial variations. The second approach uses logistic functions to model segment discontinuities. The result is a system of partial differential equations with variable coefficients. Numerical solutions are developed with the aid of MAPLE® software. For free/fixed boundary conditions, spatially constant force, and viscous damping, excellent agreement is found between the methods. The numerical approach is then used to obtain FRFs for cases including spatially varying load.

Keywords Layered structures · Logistic functions · Non-homogenous structures FRFs · Timoshenko damped beam

Nomenclature

A	Cross-section area (A_i, cross-section area for i-th material)
C_{Ti}, C_{Ri}	Viscous damping coefficients per unit length
C_i	Non-dimensional damping coefficients
D_{ij}	Proportional damping matrix coefficients
E	Young's modulus (E_i, Young's modulus for i-th material)
f_i	Non-dimensional logistic functions
G_i	Beam segment material shear modulus
I	Area moment of inertia of the beam cross-section (I_i, moment of inertia of i-cell)
k	Shear coefficient (k_i, shear coefficient of i-cell)
K	Non-dimensional logistic function parameter
K_{ij}	Stiffness matrix coefficients
L	Length of beam (L_i, length of i-th cell)
M	Bending moment
M_{ij}	Mass matrix coefficients
P_i	Generalized external forces
p_i	Force acting on the i-segment
Q	Non-dimensional forcing function
q	External force per unit length acting on the beam
q_1	Spatial forcing function for harmonic solution
r_1, s_1	Shape function constants
t	Time
$\hat{U}_i$, $\hat{V}_i$	Generalized coordinates
V	Shear force
x	Longitudinal coordinate

A. J. Mazzei (✉)
Department of Mechanical Engineering, C. S. Mott Engineering and Science Center, Kettering University, Flint, MI, USA
e-mail: amazzei@kettering.edu

C. Walber et al. (eds.), *Sensors and Instrumentation, Aircraft/Aerospace and Dynamic Environments Testing, Volume 7*,
Conference Proceedings of the Society for Experimental Mechanics Series, https://doi.org/10.1007/978-3-031-05415-0_2

w	Transverse displacement of the beam
Y	Non-dimensional transverse displacement of the beam, $Y = w/L$
Z, ϕ	Spatial functions for harmonic solution
α, β	Constants of mass and stiffness proportionality
α_1, γ_1	Non-dimensional parameters
γ	Shear strain
δ_j	Cell properties
ζ_i	Modal damping ratio
θ	Rotational angle of the beam cross-section
$\hat{\lambda}$	Complex frequency, $\hat{\lambda} = (a + bI)$
λ_i, η_i	Shape functions
ν	Non-dimensional frequency, $\nu = \Omega/\Omega_0$
ξ	Non-dimensional spatial coordinate, $\xi = x/L$
ρ	Mass density (ρ_i, density value for i-th material)
τ	Non-dimensional time, $\tau = \Omega_0 t$
υ_i	Beam segment material Poisson's ratio
Ω_0	Reference frequency

2.1 Introduction

This work adds to a series (see Refs. [1–3]) on transverse vibrations of layered beams. The main interest is the vibration analysis, both theoretical and numerical, of segmented damped beams. The media are structures with different materials and varying cross-sections, which are layered in cells and may be uniform or not.

The objective is the determination of frequency response functions (FRFs). Timoshenko beam theory is used for a two-segment configuration under harmonic forcing.

Two approaches are used to address the problem. In the first, analytic solutions are derived for the differential equations for each segment. The constants involved are determined using boundary and interface continuity conditions. The response, at a given location, can then be obtained as a function of forcing frequency (FRF). Note that the procedure can become unwieldy for arbitrary spatial variations. In the second, the discrete cell properties are modeled by continuously varying functions, specifically logistic functions. This provides for a system of differential equations with variable coefficients. The system is then solved numerically utilizing MAPLE®[1] software.

Similar analytical and numerical approaches were applied in Refs. [1–3] (Euler-Bernoulli and Timoshenko models). Overall results showed that the numerical method worked very well when compared to the analytical solutions.

A brief literature review is given next.

For vibrations of layered beams, one may refer to the list given in Refs. [1–3]. Solids composed by discrete layers are studied in Refs. [4–7]. Reference [8] provides a review of articles on this subject.

Reference [9] treats damping effects on Timoshenko beams. The numerical analyses allowed for outlining the relevant influences on the dynamic response associated with any singular damping mechanism and the evaluation of the modal critical damping values. In Ref. [10] a generalized Fourier analysis is applied to damped Timoshenko beam equation to evaluate displacements and bending stresses from random loading. Some of the models were found to be adequate for that purpose. In Ref. [11] the equations of motion for a non-uniform damped Timoshenko beam with distributed axial force are used to extract principal modes of vibration, by numerical means and for specific boundary and orthogonality conditions. Reference [12] deals with Timoshenko beam equations with external damping and internal damping terms plus forcing terms. Different boundary conditions such as pinned ends, hinged-sliding ends, and sliding ends are considered. Unboundedness of solutions of boundary value problems is studied, and it is shown that the magnitude of the displacement of the beam grows up to ∞ as $t \to \infty$ under some assumptions on the forcing term. In Ref. [13], the dynamic behavior of nonlocal viscoelastic damped nanobeams is studied. A Kelvin–Voigt viscoelastic model, velocity-dependent external damping, and Timoshenko beam theory are employed to establish the governing equations and boundary conditions for the vibration of nanotubes. Using transfer function methods (TFMs), the natural frequencies and frequency response functions (FRF) are calculated for different boundary conditions. Reference [14] investigates the effects of axial compressive load and internal viscous damping on the free vibration characteristics of Timoshenko beams using the dynamic stiffness formulation and the differential transformation method. A dynamic stiffness method (DSM) is used where the dynamic stiffness matrix of an axially loaded Timoshenko beam with internal viscous damping is constructed to calculate natural frequencies. The numerical

[1] www.maplesoft.com

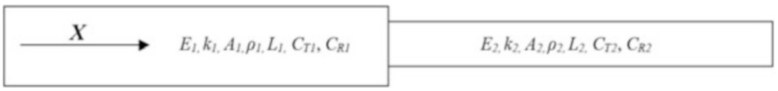

Fig. 2.1 Layered beam

approach compares well to the analytical solutions. Parametric studies on vibrations of twisted Timoshenko damped beams are given in Ref. [15]. Using Timoshenko beam theory and Hamilton's principle, bending–bending vibrations of axially loaded twisted beams with locally distributed Kelvin–Voigt damping are analyzed. A finite element method is used to reduce the equations of motion into linear second-order ordinary differential equations with constant coefficients. It was asserted that the approach led to a better understanding of the variables affecting the beam vibration characteristics.

2.2 Basic Structure

The segmented beam is shown in Fig. 2.1. It is composed of two cells of different materials. E, ρ, and A may vary in a discontinuous manner. The segments are under transverse loads q_1 and q_2 (force per unit length) and viscous damping forces due to translation and rotation of the cross-section during deflection (per unit length, damping coefficients C_{T1}, C_{R1}, and C_{T2}, C_{R2}).

The equations of motion for a transversely loaded, viscously damped Timoshenko beam are given below. (Details for deriving the equations are discussed in Ref. [2]; see also Refs. [11, 16]). A displacement-velocity and rotation-velocity–dependent viscous damping model is used [13]:

$$\begin{aligned}
&\rho(x)\ A(x)\ \frac{\partial^2 w(x,t)}{\partial t^2} + C_{\mathrm{T}}(x)\frac{\partial w(x,t)}{\partial t} - \frac{\partial V}{\partial x} = q\ (x,t)\\
&\rho(x)\ I(x)\frac{\partial^2 \theta(x,t)}{\partial t^2} + C_{\mathrm{R}}(x)\frac{\partial \theta(x,t)}{\partial t} + \frac{\partial M}{\partial x} - V = 0
\end{aligned} \tag{2.1}$$

Using a linearized curvature model, Eq. (2.1) can be re-written as:

$$\begin{aligned}
&\rho(x)A(x)\ \frac{\partial^2 w(x,t)}{\partial t^2} + C_{\mathrm{T}}(x)\frac{\partial w(x,t)}{\partial t} = q\ (x,t) + \frac{\partial}{\partial x}\left[kA(x)G(x)\left(\frac{\partial w(x,t)}{\partial t} - \theta\ (x,t)\right)\right]\\
&\rho(x)I(x)\frac{\partial^2 \theta(x,t)}{\partial t^2} + C_{\mathrm{R}}(x)\frac{\partial \theta(x,t)}{\partial t} = \frac{\partial}{\partial x}\left[E(x)I(x)\frac{\partial \theta(x,t)}{\partial x}\right] + kA(x)G(x)\left(\frac{\partial w(x,t)}{\partial t} - \theta\ (x,t)\right)
\end{aligned} \tag{2.2}$$

In Eq. (2.2) the shear force is given by $V = kA(x)G(x)\gamma$, where k is the "shear coefficient" (see Ref. [17]), which relates the maximum shear stress to the average value in the cross-section of the beam. Also, $\frac{\partial w}{\partial x} = \theta + \gamma$ and $M = -\mathrm{EI}\frac{\partial \theta}{\partial x}$.

Approaches for obtaining the steady-state response, due to harmonic forcing, are sought next.

2.3 Solution Approaches

Non-dimensional versions of Eq. (2.2) can be obtained by taking $\tau = \Omega_0 t$, $\nu = \frac{\Omega}{\Omega_0}$, $\xi = \frac{x}{L}$, $Y = \frac{w}{L}$, $E(x) = E_1 f_1(\xi)$, $I(x) = I_1 f_2(\xi)$, $\rho(x) = \rho_1 f_3(\xi)$, $A(x) = A_1 f_4(\xi)$, and $kG(x) = k_1 G_1 f_5(\xi)$. This leads to:

$$\begin{aligned}
&f_3\ (\xi)\, f_4\ (\xi)\ \frac{\partial^2 Y(\xi,\tau)}{\partial \tau^2} + C_1(x)\frac{\partial Y(\xi,\tau)}{\partial \tau} = Q\ (\xi,\tau) + \alpha_1 \frac{\partial}{\partial \xi}\left(f_4\ (\xi) f_5\ (\xi)\left(\frac{\partial Y(\xi,\tau)}{\partial \xi} - \theta\ (\xi,\tau)\right)\right)\\
&f_3\ (\xi)\, f_2\ (\xi)\ \frac{\partial^2 \theta(\xi,\tau)}{\partial \tau^2} + C_2(x)\frac{\partial \theta(\xi,\tau)}{\partial \tau} = \gamma_1 \frac{\partial}{\partial \xi}\left(f_1\ (\xi)\ f_2\ (\xi)\ \frac{\partial \theta(\xi,\tau)}{\partial \xi}\right) + (\alpha_1 \gamma_1 f_4\ (\xi) f_5\ (\xi))\left(\frac{\partial Y(\xi,\tau)}{\partial \xi} - \theta\ (\xi,\tau)\right)
\end{aligned} \tag{2.3}$$

where $\Omega_0 = \sqrt{\frac{E_1 I_1}{\rho_1 A_1 L^4}}$ (reference frequency), $C_1 = C_T\sqrt{\frac{L^4}{\rho_1 A_1 E_1 I_1}}$, $C_2 = C_R\sqrt{\frac{A_1 L^4}{\rho_1 E_1 {I_1}^3}}$, $Q\ (\xi,\tau) = q\ (x,t)\ \frac{L^3}{E_1 I_1}$, $\alpha_1 = \frac{k_1 G_1 A_1 L^2}{E_1 I_1}$, and $\gamma_1 = \frac{A_1 L^2}{I_1}$. f_i are functions representing the transitions from one cell to another. (For the continuous variation approach, logistic functions will be utilized; details are given below.)

Assuming harmonic forcing with frequency $\hat{\lambda}$, $Q(\xi,\tau) = q_1(\xi)\exp\left(\hat{\lambda}\tau\right)$, one can take $Y(\xi,\tau) = Z(\xi)\exp\left(\hat{\lambda}\tau\right)$ and $\theta(\xi,\tau) = \phi(\xi)\exp\left(\hat{\lambda}\tau\right)$. This leads to:

$$\begin{array}{l} f_3(\xi) f_4(\xi)\ \hat{\lambda}^2 Z(\xi) + C_1\hat{\lambda} Z(\xi) - \alpha_1 \frac{d}{d\xi}\left(f_4(\xi) f_5(\xi)\left(\frac{dZ(\xi)}{d\xi} - \phi(\xi)\right)\right) - q_1(\xi) = 0 \\ f_3(\xi) f_2(\xi)\ \hat{\lambda}^2\phi(\xi) + C_2\hat{\lambda}\phi(\xi) - \gamma_1 \frac{d}{d\xi}\left(f_1(\xi) f_2(\xi)\frac{d\phi(\xi)}{d\xi}\right) - (\alpha_1\gamma_1 f_4(\xi) f_5(\xi))\left(\frac{dZ(\xi)}{d\xi} - \phi(\xi)\right) = 0 \end{array} \tag{2.4}$$

Taking $\hat{\lambda} = (a + bI)$ and separating real and imaginary parts, after some manipulation, gives:

$$\begin{array}{l} \left(f_3(\xi) f_4(\xi) b^2 + \frac{{C_1}^2}{4 f_3(\xi) f_4(\xi)}\right) Z(\xi) + \alpha_1 \frac{d}{d\xi}\left(f_4(\xi) f_5(\xi)\left(\frac{dZ(\xi)}{d\xi} - \phi(\xi)\right)\right) + q_1(\xi) = 0 \\ \left(f_3(\xi) f_2(\xi) b^2 + \frac{{C_2}^2}{4 f_3(\xi) f_2(\xi)}\right)\phi(\xi) + \gamma_1 \frac{d}{d\xi}\left(f_1(\xi) f_2(\xi)\frac{d\phi(\xi)}{d\xi}\right) + (\alpha_1\gamma_1 f_4(\xi) f_5(\xi))\left(\frac{dZ(\xi)}{d\xi} - \phi(\xi)\right) = 0 \end{array} \tag{2.5}$$

The result, Eq. (2.5), is a set of non-homogeneous ordinary differential equations with variable coefficients. Analytic and numerical solutions are discussed next.

2.3.1 Analytical Approach

For constant properties in each segment, Eq. (2.5) can be written as:

$$\begin{array}{l} \left(f_3 f_4 b^2 + \frac{{C_1}^2}{4 f_3 f_4}\right) Z(\xi) + \alpha_1 f_4 f_5 \frac{d}{d\xi}\left(\left(\frac{dZ(\xi)}{d\xi} - \phi(\xi)\right)\right) + q_1(\xi) = 0 \\ \left(f_3 f_2 b^2 + \frac{{C_2}^2}{4 f_3 f_2}\right)\phi(\xi) + \gamma_1 f_1 f_2 \frac{d^2\phi(\xi)}{d\xi^2} + (\alpha_1\gamma_1 f_4 f_5)\left(\frac{dZ(\xi)}{d\xi} - \phi(\xi)\right) = 0 \end{array} \tag{2.6}$$

Note that, for the beam segments, the functions f_i are constants and can be calculated from:

$$\begin{array}{l} f_{k,i} = 1,\ k = 1\cdots 5,\quad i = 1 \\ f_{1,i} = \frac{E_i}{E_{i-1}},\ f_{2,i} = \frac{I_i}{I_{i-1}},\ f_{3,i} = \frac{\rho_i}{\rho_{i-1}},\ f_{4,i} = \frac{A_i}{A_{i-1}},\ f_{5,i} = \frac{K_i G_i}{K_{i-1} G_{i-1}},\ i = 2\cdots n \end{array} \tag{2.7}$$

Equations (2.6) and (2.7) are valid for cases with multiple segments (n).

Solutions to the system of ODEs (2.6), with constant coefficients, involve solutions to the homogeneous equations and particular integrals. Depending on the forcing function $q_1(\xi)$, tracking particular solutions may pose a problem. In this section attention is directed to obtaining solutions for the case of constant spatial forcing. (Non-constant spatial forcing is treated later numerically.)

Here this is done using MAPLE®. The solutions consist of exponential functions containing unknown coefficients, which must be determined based on the set of boundary conditions for the problem. In addition, solutions must match at the interface between the elements. Interface continuity requires matching of displacement, slope, moment, and shear force.

These conditions provide a set of algebraic equations for the unknown coefficients. The FRFs can then be obtained by monitoring solutions, for different values of the forcing frequency b, at a specific point of the beam (here this is taken at the center).

Solutions require that the boundary conditions be defined. Two sets are discussed below.

2.3.2 Numerical Approach

For the numerical approach, a continuous variation model is used. With this model, transitions from one cell to another are modeled via logistic functions. Here these functions, f_i, in non-dimensional form are taken to be:

$$f_i(\xi) = 1 + \left(\frac{\delta_2 - \delta_1}{\delta_1}\right)\left(\frac{1}{2} + \frac{1}{2}\tanh\left(K\left(\xi - \frac{1}{2}\right)\right)\right), i = 1, 2, 3, 4, 5 \tag{2.8}$$

δ_j represents a material property, geometric property, or damping (E, I, ρ, kG, A, or C). K controls the sharpness of the transition from one cell to another in the function. A larger value corresponds to a sharper transition at $\xi = \frac{1}{2}$.

Substituting Eqs. (2.8) into (2.5) leads to a system of differential equations, with variable coefficients, which may not have analytic solutions. Given the material layout and cross-section variation, i.e., the corresponding logistic functions, a MAPLE® routine can be used to obtain numerical approximations to the FRF of the system. This is done by monitoring the response for different values of the frequency b. Resonances can also be obtained via a forced-motion approach (see Ref. [18]). It consists of using MAPLE®'s two-point boundary value solver to solve a forced-motion problem. A constant value for the forcing function G is assumed and the frequency b is varied. By observing the mid-span deflection of the beam, resonant frequencies can be found on noting where changes in sign occur.

The approaches are illustrated in the following numerical examples.

2.4 Numerical Examples

Consider the beam shown in Fig. 2.1. Here the segment cross-sections are assumed to have the same geometry and to be joined at the center of the beam. The cross-section is taken to be a *S 24 X 121* (ASTM A6 – American Standard Beam),[2] and the following materials are used: aluminum ($E_1 = 71$ GPa, $\rho_1 = 2710$ Kg/m^3, $\upsilon_1 = 0.33$, $G_1 = 26.69$ GPa, $k_1 = 0.89$) and silicon carbide ($E_2 = 210$ GPa, $\rho_2 = 3100$ Kg/m^3, $\upsilon_2 = 0.16$, $G_2 = 90.52$ GPa, $k_2 = 0.87$). These values are taken from Refs. [17, 19].

2.4.1 Free/Fixed Boundary Conditions

Consider a free/fixed set. The boundary conditions are as follows (i subscript refers to the segment number).

The moment and shear free end at $\xi = 0$ gives $\frac{d\phi_1(\xi)}{d\xi}\Big|_{x=0} = 0$ and $\frac{dZ_1(\xi)}{d\xi}\Big|_{\xi=0} = \phi_1(\xi)$. The conditions at the fixed end give: $Z_2(\xi) = 0$ and $\phi_2(\xi) = 0$. Interface continuity conditions are $Z_1(\xi) = Z_2(\xi)$, $\xi = 0.5$ (displacement continuity), $\phi_1(\xi) = \phi_2(\xi)$, $\xi = 0.5$ (slope continuity), $\frac{d\phi_1(\xi)}{d\xi} = f_1 f_2 \frac{d\phi_2(\xi)}{d\xi}$, $\xi = 0.5$ (moment continuity), and $\left(\frac{dZ_1(\xi)}{d\xi} - \phi_1(\xi)\right) = f_4 f_5 \left(\frac{dZ_2(\xi)}{d\xi} - \phi_2(\xi)\right)$, $\xi = 0.5$ (shear continuity). $q_1(\xi)$ is set to 1.

Utilizing the analytical approach described above allows for the calculation of the FRF for the system. Setting $\xi = 0.50$ (beam mid-span), amplitudes can be calculated for different values of the non-dimensional frequency b.

The frequency response function, spanning the first two natural frequencies, for the mid-point of the beam is shown in Fig. 2.2. (The following parameters apply: $f_1 = 2.9577, f_2 = 1.0000, f_3 = 1.1439, f_4 = 1.0000, f_5 = 3.3368$, $C_1 = 10.0000$, and $C_2 = 10.0000$.)

A comparison between this damped and an undamped version of the same beam is given in Fig. 2.3. Note the shift on the frequencies and changes of amplitude.

For the continuous variation model and using the numerical values given above, the continuously varying functions are shown in Fig. 2.4 (note: $K = 500$).

Assuming a value of 1 for the external forcing $q_1(\xi)$ and using the forced-motion approach [18], the resultant deflections are plotted bellow for two distinct values of the frequency b.

The resonance frequency is taken to occur at $b = 1.55$, as seen in Fig. 2.5.

Amplitudes for the response at the center of the beam can be monitored from Eq. (2.5). The approach leads to the numerical FRF shown in Fig. 2.6. The figure shows the results from the numerical simulation and an overlap of those with the analytical results. Excellent agreement is seen; the first two resonances and amplitude values correspond very well.

From the numerical FRF, the damping ratio of the system, corresponding to the assumed non-dimensional values of damping ($C_1 = 10.0000$, $C_2 = 10.0000$), can be estimated. The method used here is the half-power bandwidth [20], applied to the first mode, which, although only applicable to lightly damped single degree of freedom systems, is frequently applied to well-separated modes of multi-degree of freedom systems. It leads to a ratio of approximately 2%.

[2] www.efunda.com/math/areas/RolledSteelBeamsS.cfm

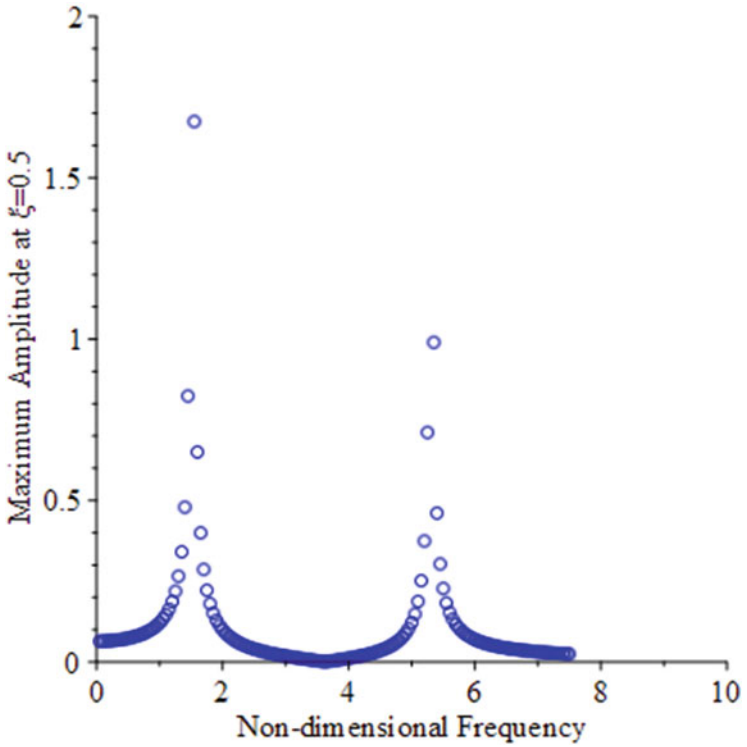

Fig. 2.2 FRF for non-homogeneous Timoshenko beam at mid-point: free/fixed

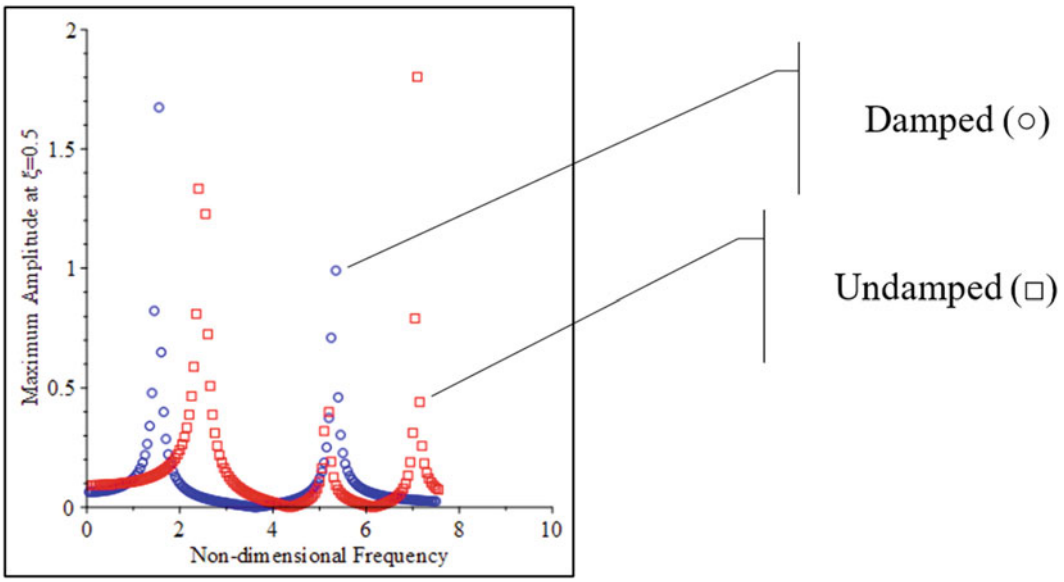

Fig. 2.3 FRFs for damped and undamped non-homogeneous Timoshenko beam: free/fixed

2.4.2 Fixed/Fixed Boundary Conditions

For fixed/fixed conditions, the left-side ($\xi = 0$) constraints change to $Z_1(\xi) = 0$ and $\phi_1(\xi) = 0$, whereas all the other remain the same. The FRF for this case is shown in Fig. 2.7.

A comparison between the damped and undamped results for this beam is given in Fig. 2.8. Note the shift on the frequencies and changes of amplitude.

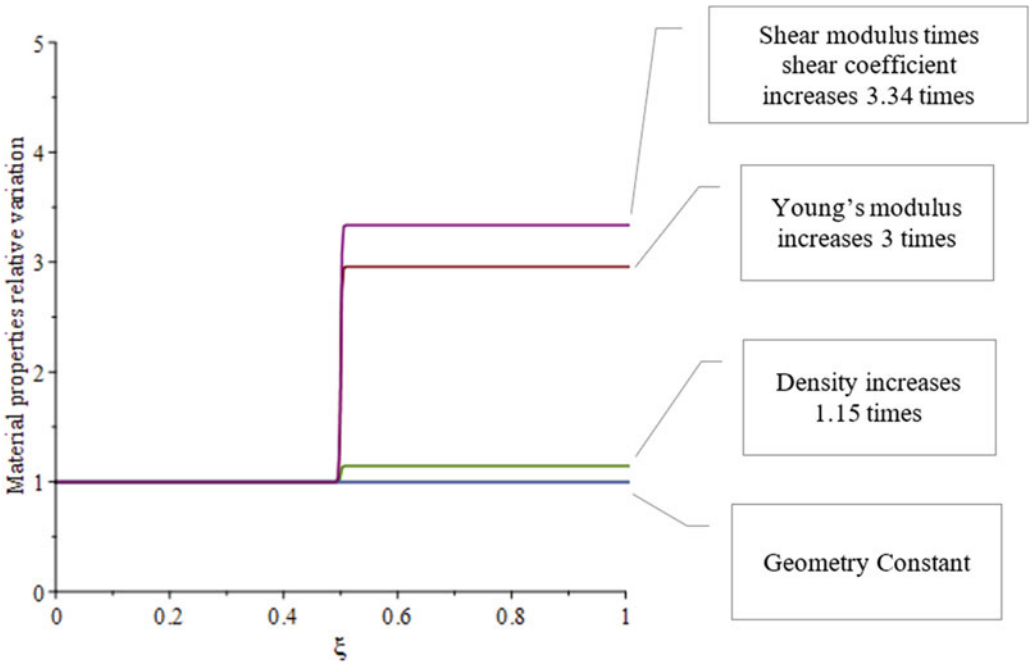

Fig. 2.4 Relative property variation for two-cell Timoshenko beam

Assuming the same external forcing $q_1(\xi)$ as above and using the forced-motion approach, the resultant deflections are shown in Fig. 2.9, for two distinct values of the frequency b.

The resonance frequency is taken to occur at $b = 1.55$.

Monitoring amplitudes at the center of the beam leads to the numerical FRF shown in Fig. 2.10. Results show the numerical simulation and an overlap of these with the analytical results. As in the previous case, excellent agreement is observed.

Consider next a case in which the spatial force is non-constant. For example, a variable force given by the exponential function: $G(\xi) = e^{-\xi^2}$ is assumed. The results can be found using the continuous variation model. The FRFs for this case are seen in Fig. 2.11.

2.5 Assumed Modes Method

In this section, an approach similar to the one described in Ref. [2] is pursued. The solution to Eq. (2.1) is assumed to have the form of a Rayleigh-Ritz expansion:

$$w(x,t) = \sum_{i=1}^{n} \hat{U}_i(t)\eta_i(x), \quad \theta(x,t) = \sum_{i=1}^{n} \hat{V}_i(t)\lambda_i(x) \tag{2.9}$$

where the generalized coordinates $\hat{U}_i$ and $\hat{V}_i$, in the linear combination of shape functions η_i and λ_i, are functions of time.

The shape functions must form a linearly independent set, possessing derivatives up to the order appearing in the strain energy expression for the problem. They also must satisfy the prescribed boundary conditions.

For the undamped case, one can use the expressions for the kinetic energy, strain energy, and the external work done by the transverse loads, for each segment [2], in Lagrange's equations. This leads to a set of n differential equations for the generalized coordinates [21, 22].

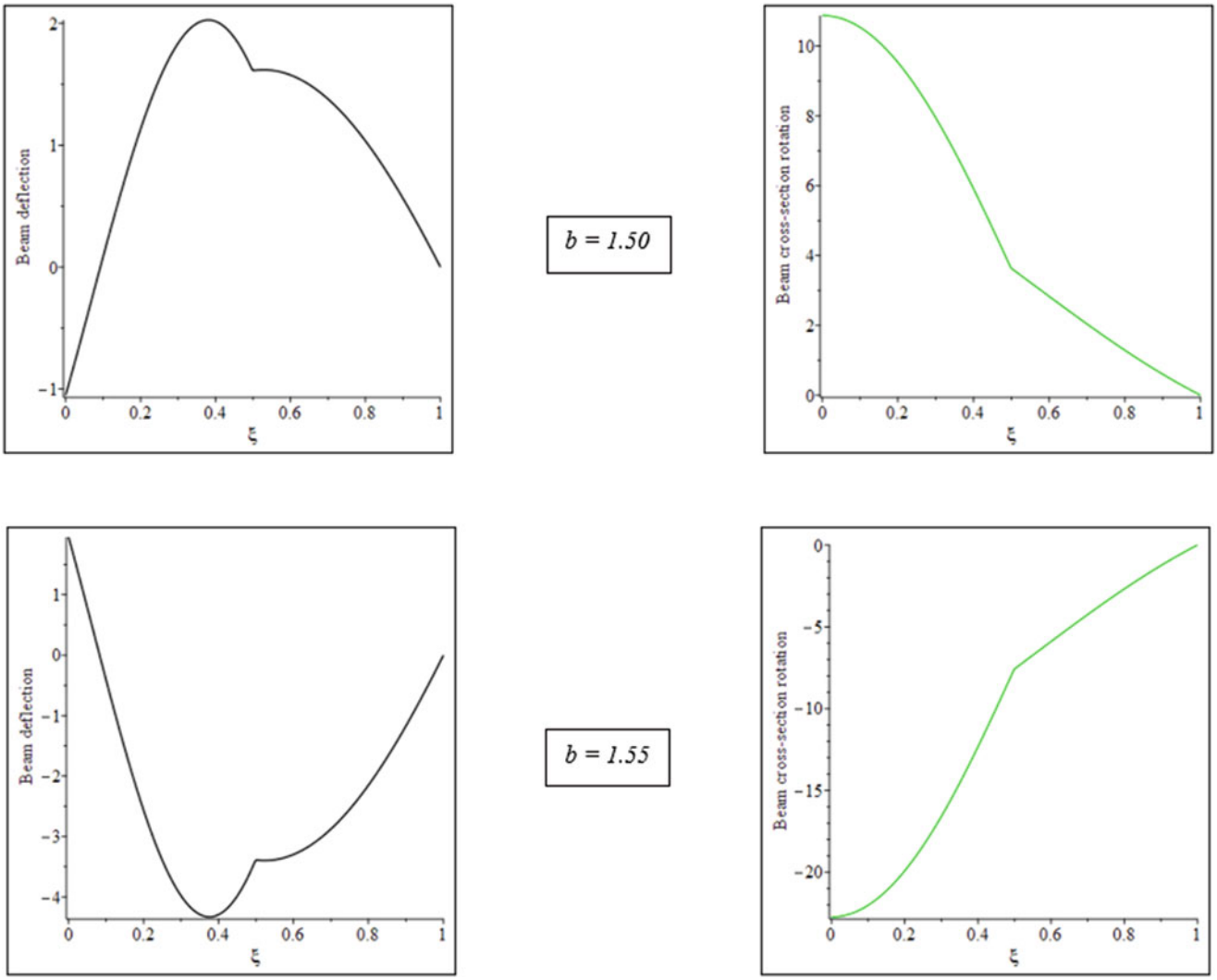

Fig. 2.5 Beam deflections for distinct values of b: free/fixed – first resonance

Then the discrete non-dimensional mass and stiffness matrices [23] can be obtained from:

$$
\begin{aligned}
&M^{\mathrm{I}}{}_{i,j} = \int_0^{\frac{1}{2}} \eta_i \eta_j \, dx + A_r \rho_r \int_{\frac{1}{2}}^{1} \eta_i \eta_j \, dx, \quad M^{\mathrm{II}}{}_{i,j} = \int_0^{\frac{1}{2}} \lambda_i \lambda_j \, dx + I_r \rho_r \int_{\frac{1}{2}}^{1} \lambda_i \lambda_j \, dx, \\
&K^{\mathrm{I}}{}_{i,j} = \int_0^{\frac{1}{2}} \eta_i' \eta_j' \, dx + k_r G_r A_r \int_{\frac{1}{2}}^{1} \eta_i' \eta_j' \, dx, \quad K^{\mathrm{II}}{}_{i,j} = -\int_0^{\frac{1}{2}} \eta_i' \lambda_j \, dx - k_r G_r A_r \int_{\frac{1}{2}}^{1} \eta_i' \lambda_j \, dx, \\
&K^{\mathrm{III}}{}_{i,j} = \int_0^{\frac{1}{2}} \lambda_i' \lambda_j' \, dx + E_r I_r \int_{\frac{1}{2}}^{1} \lambda_i' \lambda_j' \, dx + \int_0^{\frac{1}{2}} \lambda_i \lambda_j \, dx + k_r G_r A_r \int_{\frac{1}{2}}^{1} \lambda_i \lambda_j \, dx, \quad K^{\mathrm{IV}}{}_{i,j} = -\int_0^{\frac{1}{2}} \eta_j' \lambda_i \, dx - k_r G_r A_r \int_{\frac{1}{2}}^{1} \eta_j' \lambda_i \, dx
\end{aligned}
\tag{2.10}
$$

Taking the external transverse loads to be sinusoidal with frequency ν, the generalized external forces can be calculated from:

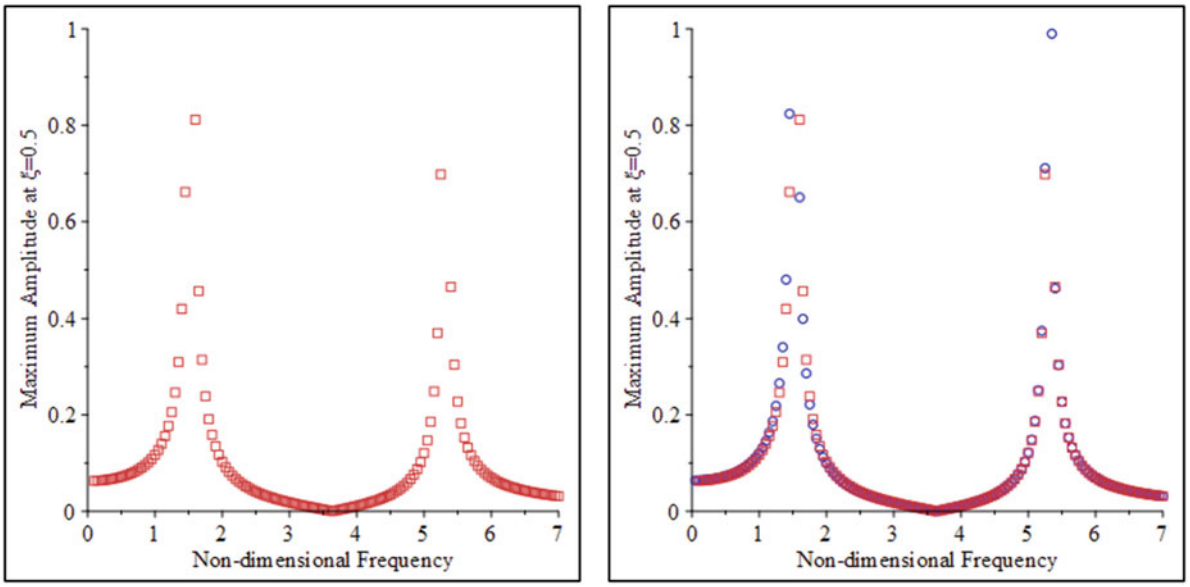

Fig. 2.6 Results comparison: numerical and analytical approaches – free/fixed

$$P_i^{\mathrm{I}} = \left[\int_0^{\frac{1}{2}} p_1 \eta_i dx + \int_{\frac{1}{2}}^{1} p_2 \eta_i \, dx \right] \sin(\nu\tau) \,, \; P_i^{\mathrm{II}} = \left[\int_0^{\frac{1}{2}} p_1 \lambda_i dx + \int_{\frac{1}{2}}^{1} p_2 \lambda_i \, dx \right] \sin(\nu\tau) \tag{2.11}$$

where p_i is the amplitude of the force acting on the i-segment.

Damping is introduced by assuming proportional damping:

$$\begin{bmatrix} [D^{\mathrm{I}}] & [D^{\mathrm{II}}] \\ [D^{\mathrm{IV}}] & [D^{\mathrm{III}}] \end{bmatrix} = \alpha \begin{bmatrix} [M^{\mathrm{I}}] & [0] \\ [0] & [M^{\mathrm{II}}] \end{bmatrix} + \beta \begin{bmatrix} [K^{\mathrm{I}}] & [K^{\mathrm{II}}] \\ [K^{\mathrm{IV}}] & [K^{\mathrm{III}}] \end{bmatrix} \tag{2.12}$$

where α and β are constants of mass and stiffness proportionality, respectively.

The resulting system of equations can be written as:

$$\begin{bmatrix} [M^{\mathrm{I}}] & [0] \\ [0] & [M^{\mathrm{II}}] \end{bmatrix} \begin{Bmatrix} \{\ddot{U}_i\} \\ \{\ddot{V}_i\} \end{Bmatrix} + \begin{bmatrix} [D^{\mathrm{I}}] & [D^{\mathrm{II}}] \\ [D^{\mathrm{IV}}] & [D^{\mathrm{III}}] \end{bmatrix} \begin{Bmatrix} \{\dot{U}_i\} \\ \{\dot{V}_i\} \end{Bmatrix} + \begin{bmatrix} [K^{\mathrm{I}}] & [K^{\mathrm{II}}] \\ [K^{\mathrm{IV}}] & [K^{\mathrm{III}}] \end{bmatrix} \begin{Bmatrix} \{U_i\} \\ \{V_i\} \end{Bmatrix} = \begin{Bmatrix} \{P^{\mathrm{I}}{}_i\} \\ \{P^{\mathrm{II}}{}_i\} \end{Bmatrix} \tag{2.13}$$

The undamped natural frequencies can be evaluated via an eigenvalue problem for the undamped case. The overall system response to external forcing can be estimated through modal analysis.

In order to generate the damping matrix, the constants of mass and stiffness proportionality must be determined. If the modal damping ratios are known, then the constants can be evaluated from:

$$\zeta_i = \frac{\alpha m_{ii} + \beta k_{ii}}{2\sqrt{k_{ii} m_{ii}}} \tag{2.14}$$

where m_{ii} and k_{ii} are coefficients from the modal mass and stiffness matrices, respectively. (See also the approach described in reference [24] for the same purpose, which, for the example considered here, led to similar numerical values.)

Here the modal ratios are not known, but they can be estimated from the previous analytical results. Two modes are needed to calculate α and β. For the free/fixed case, shown in Fig. 2.2, two modes are well defined; then the ratios can be evaluated. The approach used is the half-power bandwidth. For the fixed/fixed case, Fig. 2.7, parameters for the second mode are difficult to evaluate, so, for the numerical example, only the former will be considered.

The procedure requires a choice of shape functions, which are taken to be beam characteristic orthogonal polynomials. They are generated by the Gram-Schmidt process [25] as demonstrated by Bhat [26].

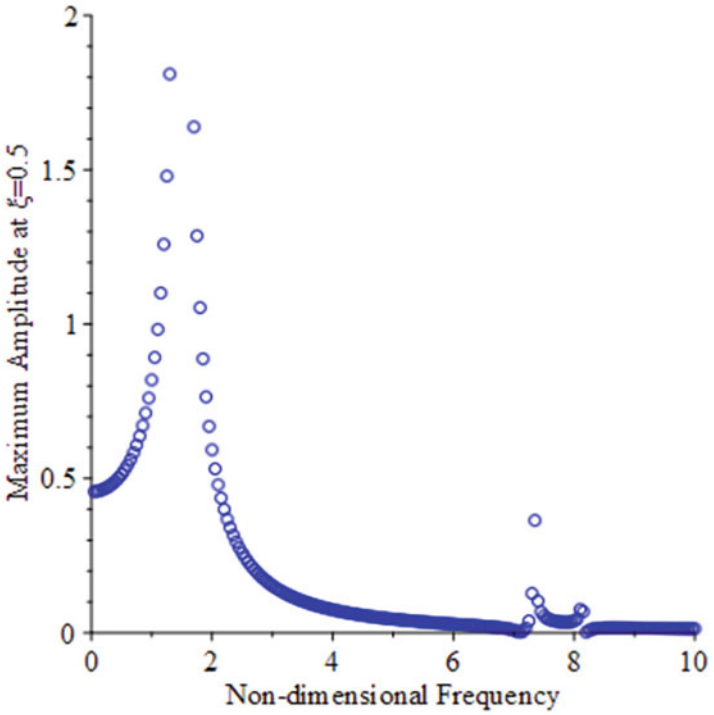

Fig. 2.7 FRF for non-homogeneous Timoshenko beam at mid-point: fixed/fixed

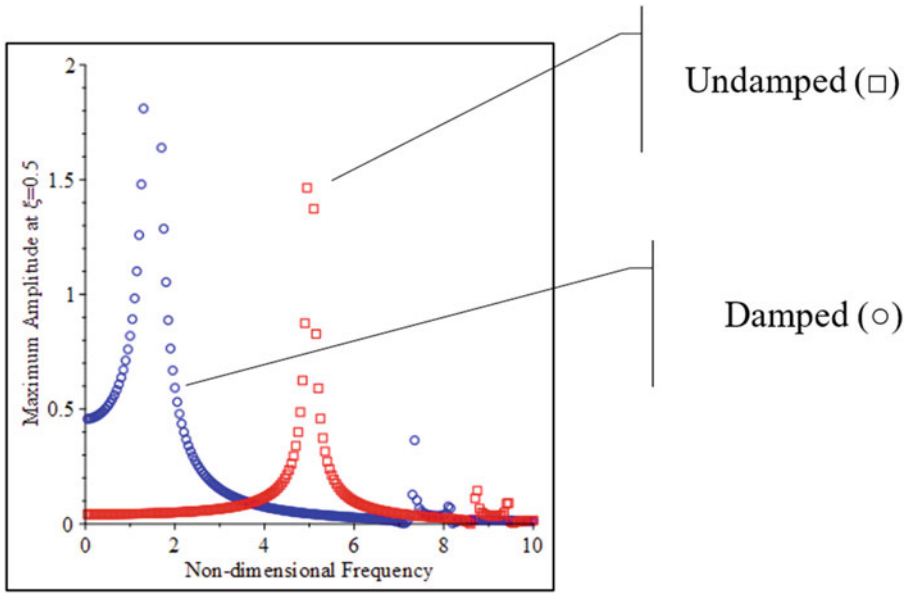

Fig. 2.8 FRFs for damped and undamped non-homogeneous Timoshenko beam: fixed/fixed

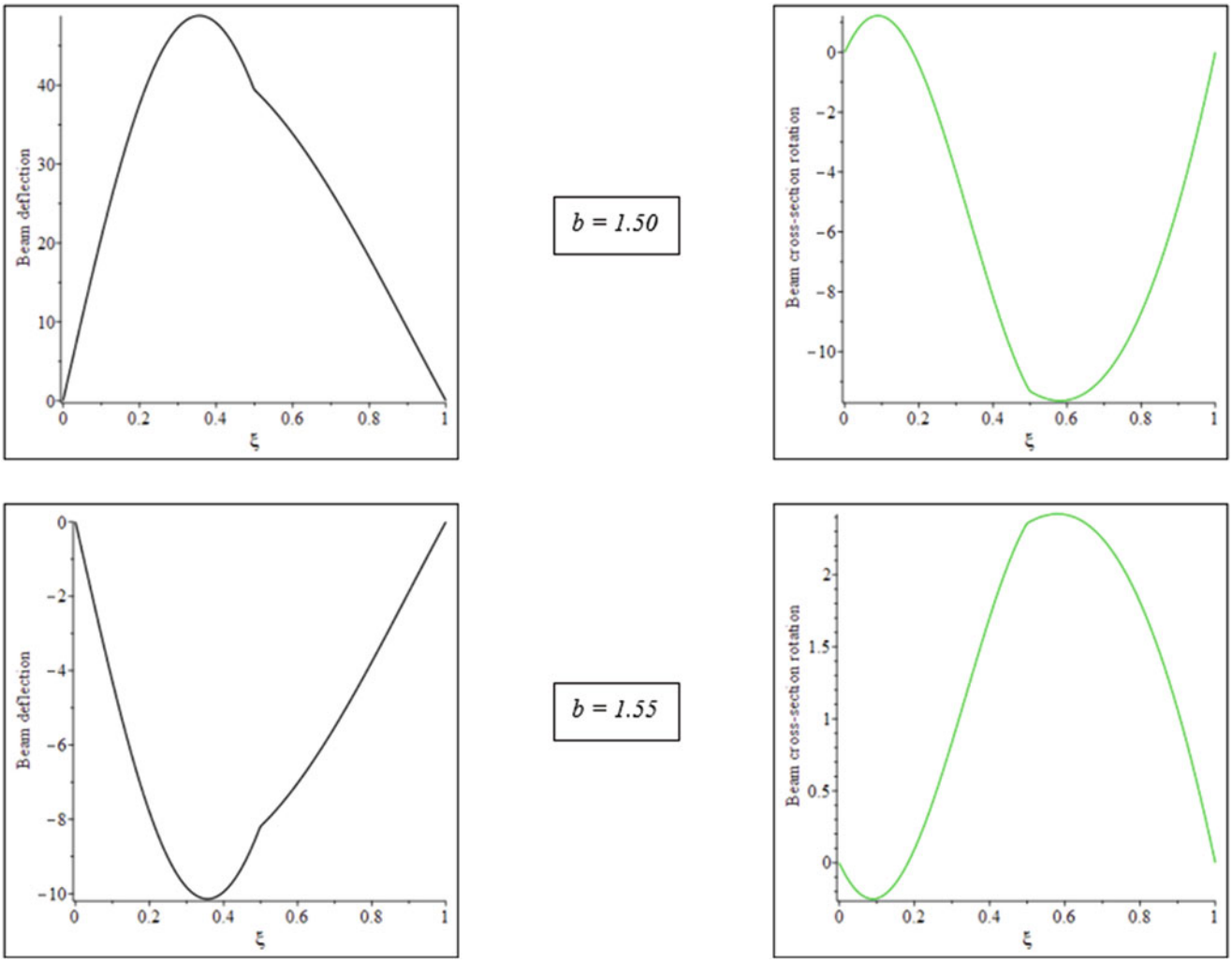

Fig. 2.9 Beam deflections for distinct values of b: fixed/fixed – first resonance

For the free/fixed case, the procedure is described in reference [2]. The first polynomial follows the static deflection of a homogeneous beam, under constant distributed load and with these boundary conditions. In non-dimensional form:

$$\eta_1(x) = s_1\left[\frac{qL}{2kGA}\left(1-\xi^2\right)+\frac{qL^3}{6\mathrm{EI}}\left(\frac{1}{4}\xi^4-\xi+\frac{3}{4}\right)\right], \lambda_1(x) = r_1\left[\frac{qL^3}{6\mathrm{EI}}\left(\xi^3-1\right)\right] \tag{2.15}$$

The constants s_1 and r_1 are chosen such that:

$$\int_0^1 (\eta_k)^2 dx = 1, \int_0^1 (\lambda_k)^2 dx = 1 \tag{2.16}$$

The remainder polynomials are generated by the Gram-Schmidt approach. In addition, the set is also normalized. They are divided by normalization parameters that are taken to be the inverse of the magnitude of their maximum values in the interval $\xi = 0...1$.

Assuming non-dimensional values of damping $C_1 = 0.1$ and $C_2 = 0.1$ ($\zeta_1 \approx 0.0153$, $\zeta_2 \approx 0.0122$), the procedure is tackled using MAPLE®. For 18 polynomials and a non-dimensional time $\tau = 100$, monitoring the amplitudes at $\xi = 0.5$ leads to the results shown in Fig. 2.12. The figure shows a comparison (overlap) between the analytical results and the

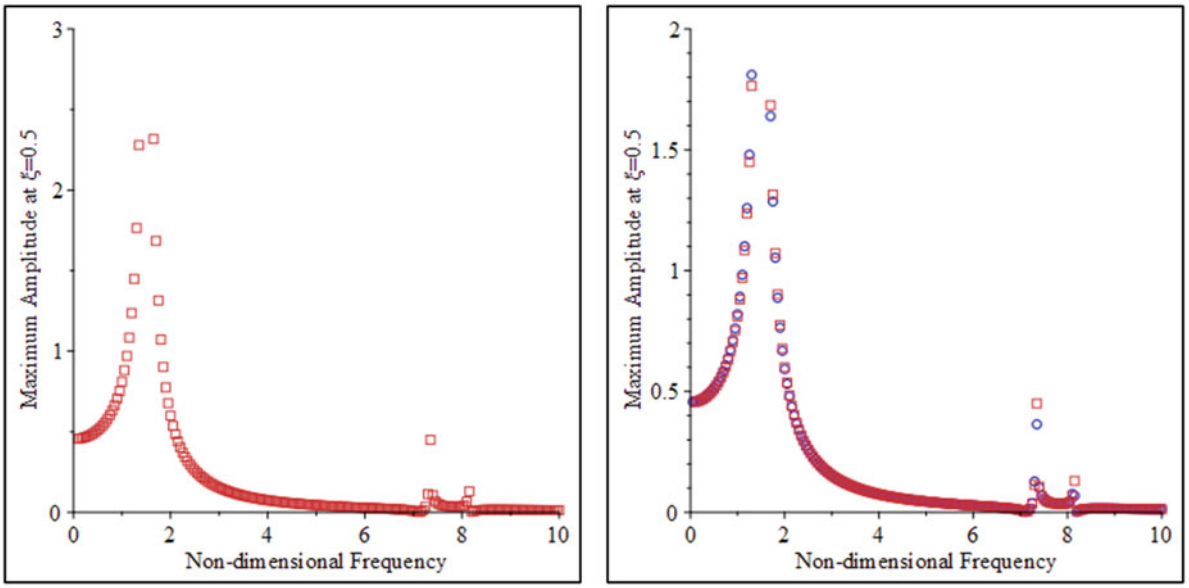

Fig. 2.10 Results comparison: numerical and analytical approaches – fixed/fixed

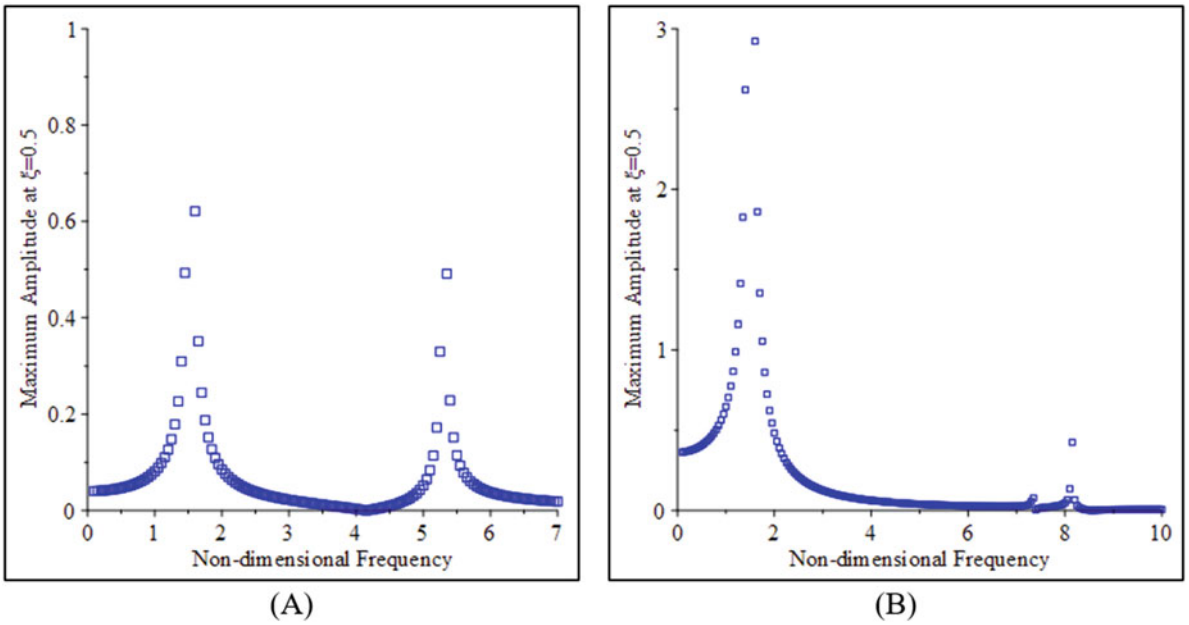

Fig. 2.11 FRFs for exponential force: free/fixed (**a**), fixed/fixed (**b**)

assumed modes approach. The eigensolution gives the following first two frequencies: $\nu_1 = 2.75$ and $\nu_2 = 5.45$, whereas the analytical results are $\nu_1 = 2.50$ and $\nu_2 = 5.20$. The results differ by 10% and 5%, respectively.

2.6 Conclusion

Modeling discrete property variations via continuously varying functions, in conjunction with numerical solutions, has been shown to lead to good results for resonant frequencies and FRFs of viscously damped Timoshenko layered beams subject to harmonic excitation.

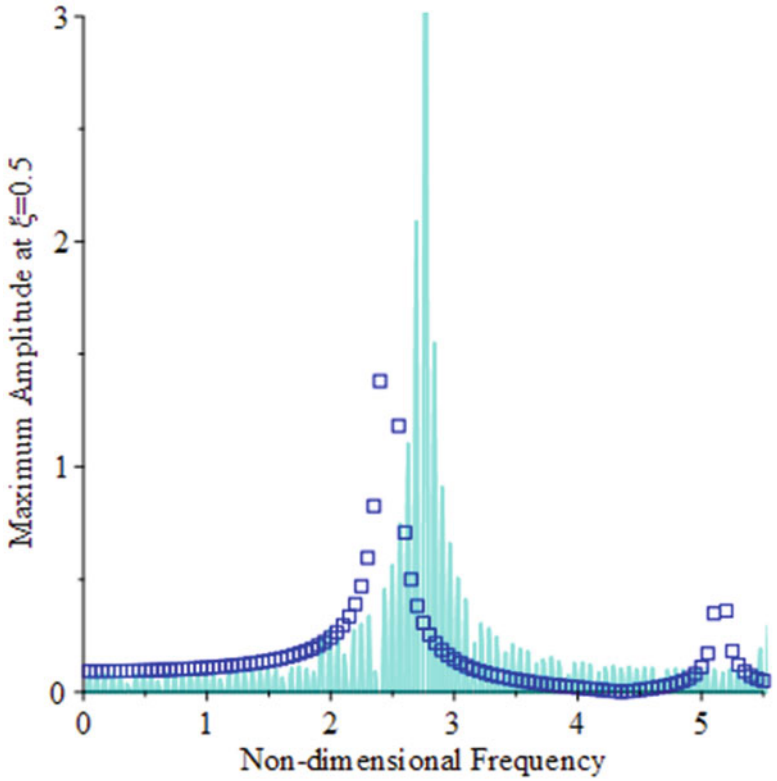

Fig. 2.12 Comparison of FRFs: assumed modes and analytical results – free/fixed

A numerical approach was conducted using MAPLE® software, which shows to lead to accurate solutions based on a comparison to analytical results for specific cases.

Two sets of boundary conditions were studied, namely, free/fixed and fixed/fixed for a uniform two-cell beam made of aluminum and silicon carbide.

Very good agreement was observed for both cases.

The continuous variation approach was used to produce solutions for a case with external spatially varying force, which could be intractable analytically.

Finally, an assumed modes approach was used to estimate the FRF for one of the cases. Good agreement was found with maximum error, when compared to the analytical solution, of 10%.

References

1. Mazzei, A.J., Scott, R.A.: Harmonic forcing of a two-segment Euler-Bernoulli beam. In: Dervilis, N. (ed.) Special Topics in Structural Dynamics, Volume 6: Proceedings of the 35th IMAC, A Conference and Exposition on Structural Dynamics 2017, pp. 1–15. Springer International Publishing, Cham (2017). https://doi.org/10.1007/978-3-319-53841-9_1
2. Mazzei, A.J., Scott, R.A.: Harmonic forcing of a two-segment Timoshenko beam. In: Dervilis, N. (ed.) Special Topics in Structural Dynamics, vol. 5, pp. 1–15. Springer International Publishing (2019). https://doi.org/10.1007/978-3-030-12676-6_3
3. Mazzei, A.J., Scott, R.A.: Harmonic forcing of damped non-homogeneous Euler-Bernoulli beams. In: Epp, D.S. (ed.) Special Topics in Structural Dynamics & Experimental Techniques, vol. 5, pp. 11–23. Springer International Publishing, Cham (2021). https://doi.org/10.1007/978-3-030-47709-7_2
4. Lee, E.H., Yang, W.H.: On waves in composite materials with periodic structure. SIAM J. Appl. Math. **25**, 492–499 (1973). https://doi.org/10.1137/0125049
5. Hussein, M.I., Hulbert, G.M., Scott, R.A.: Dispersive elastodynamics of 1D banded materials and structures: analysis. J. Sound Vib. **289**, 779–806 (2006). https://doi.org/10.1016/j.jsv.2005.02.030
6. Hussein, M.I., Hulbert, G.M., Scott, R.A.: Dispersive elastodynamics of 1D banded materials and structures: design. J. Sound Vib. **307**, 865–893 (2007). https://doi.org/10.1016/j.jsv.2007.07.021

7. Vasseur, J.O., Deymier, P., Sukhovich, A., Merheb, B., Hladky-Hennion, A.C., Hussein, M.I.: Phononic band structures and transmission coefficients: methods and approaches. In: Deymier, P.A. (ed.) Acoustic Metamaterials and Phononic Crystals, pp. 329–372. Springer, Berlin Heidelberg (2013). https://doi.org/10.1007/978-3-642-31232-8_10
8. Hussein, M.I., Leamy, M.J., Ruzzene, M.: Dynamics of phononic materials and structures: historical origins, recent progress, and future outlook. Appl. Mech. Rev. **66**, 040802-040802–38 (2014). https://doi.org/10.1115/1.4026911
9. Capsoni, A., Maria Viganò, G., Bani-Hani, K.: On damping effects in Timoshenko beams. Int. J. Mech. Sci. **73**, 27–39 (2013). https://doi.org/10.1016/j.ijmecsci.2013.04.001
10. Samuels, J.C., Eringen, A.C.: Response of a Simply Supported Timoshenko Beam to a Purely Random Gaussian Process. Purdue Univ Lafayette in Div of Engineering Sciences (1957). https://apps.dtic.mil/dtic/tr/fulltext/u2/134729.pdf
11. Bishop, R.E.D., Price, W.G.: The vibration characteristics of a beam with an axial force. J. Sound Vib. **59**, 237–244 (1978)
12. Kobayashi, K., Yoshida, N.: Unboundedness of Solutions of Timoshenko Beam Equations with Damping and Forcing Terms. https://doi.org/10.1155/2013/435456
13. Lei, Y., Adhikari, S., Friswell, M.I.: Vibration of nonlocal Kelvin–Voigt viscoelastic damped Timoshenko beams. Int. J. Eng. Sci. **66–67**, 1–13 (2013). https://doi.org/10.1016/j.ijengsci.2013.02.004
14. Bozyigit, B., Yesilce, Y., Catal, H.H.: Free flexural vibrations of axially loaded Timoshenko beams with internal viscous damping using dynamic stiffness formulation and differential transformation. In: Kasimzade, A.A., Şafak, E., Ventura, C.E., Naeim, F., Mukai, Y. (eds.) Seismic Isolation, Structural Health Monitoring, and Performance Based Seismic Design in Earthquake Engineering: Recent Developments, pp. 307–328. Springer International Publishing, Cham (2019). https://doi.org/10.1007/978-3-319-93157-9_15
15. Chen, W.-R.: Parametric studies on bending vibration of axially-loaded twisted Timoshenko beams with locally distributed Kelvin–Voigt damping. Int. J. Mech. Sci. **88**, 61–70 (2014). https://doi.org/10.1016/j.ijmecsci.2014.07.006
16. Esmailzadeh, E., Ohadi, A.R.: Vibration and stability analysis of non-uniform Timoshenko beams under axial and distributed tangential loads. J. Sound Vib. **236**, 443–456 (2000). https://doi.org/10.1006/jsvi.2000.2999
17. Cowper, G.R.: The shear coefficient in Timoshenko's beam theory. J. Appl. Mech. **33**, 335–340 (1966)
18. Mazzei, A.J., Scott, R.A.: On the effects of non-homogeneous materials on the vibrations and static stability of tapered shafts. J. Vib. Control. **19**, 771–786 (2013). https://doi.org/10.1177/1077546312438429
19. Chiu, T.C., Erdogan, F.: One-dimensional wave propagation in a functionally graded elastic medium. J. Sound Vib. **222**, 453–487 (1999). https://doi.org/10.1006/jsvi.1998.2065
20. Chopra, A.K.: Dynamics of Structures: Theory and Applications to Earthquake Engineering. Pearson, Hoboken (2017)
21. Craig, R.R., Kurdila, A., Craig, R.R.: Fundamentals of Structural Dynamics. John Wiley, Hoboken (2006)
22. Kelly, S.G.: Advanced Vibration Analysis. CRC/Taylor & Francis, Boca Raton (2007)
23. Eslami, M.R.: Finite Elements Methods in Mechanics. Springer, Cham (2014)
24. Schwarz, B., Richardson, M.: Proportional damping from experimental data. In: Allemang, R., De Clerck, J., Niezrecki, C., Wicks, A. (eds.) Topics in Modal Analysis, vol. 7, pp. 179–186. Springer New York, New York (2014)
25. Chihara, T.S.: Introduction to Orthogonal Polynomials. Gordon and Breach, London (1978). https://doi.org/10.1007/978-1-4614-6585-0_17
26. Bhat, R.B.: Transverse vibrations of a rotating uniform cantilever beam with tip mass as predicted by using beam characteristic orthogonal polynomials in the Rayleigh-Ritz method. J. Sound Vib. **105**, 199–210 (1986). https://doi.org/10.1016/0022-460X(86)90149-5

Chapter 3
Parametric Simulations of the BARC Model in SDOF and MIMO Configurations for Estimating Service Environment Severity

Sebastian Chirinos, Aneesh Pawar, Haley Tholen, Scott Ouellette, and Thomas Roberts

Abstract Multiple single-axis vibration tests are commonly linearly superposed as a multi-axis test. However, due to cross-axial responses in single-axis, the net response of multiple single-axis vibration tests results in an overestimation of the severity of the service environment. In practice, over-testing has been a result of the limitations associated with physical experimentation, which indicates a need to improve simulation methods and accuracy of current lifetime test strategies. In this chapter, single- and multi-axis experimental vibration tests of the Box Assembly with Removable Component (BARC) model are simulated with implicit and explicit methods using the commercial FEA tool ABAQUS, where the multiple observed outputs are vibrational responses in the three translational degrees of freedom. The model looks to validate physically obtained experimental data by replicating certain boundary conditions and service environments.

Keywords Vibration qualification · Multiple-input/multiple-output · BARC · Parametric simulation · Model validation

3.1 Introduction

Single-axis vibration testing, also referred to as single degree of freedom (SDOF) testing, is often used as a control approach to replicate the multidimensional vibration of real structures in the lab environment [1]. A major limitation of SDOF testing is the recurrent omission of cross-axial responses that result from excitation in a single direction [2]. These cross-axial responses can alter the dynamic behavior of the test specimen, thereby causing the overall equivalent multi-axis result to be more severe than the service environment. Using a multi-input multi-output (MIMO) control strategy is a more accurate alternative to the single-input single-output (SISO) approach [3, 4]; however, the availability of multi-axis test apparatuses is rare, costly, and mostly in active research; so the industry continues to rely heavily on single-axis vibration testing [1].

In the interest of making improvements to current shock and vibration testing methodologies, Sandia National Laboratories and Kansas City National Security Campus designed the Box Assembly with Removable Component (BARC) structure for the Boundary Condition Round Robin Challenge to provide researchers with a common model to use in experiments [5]. The BARC model consists of two C-channels connected by a beam as a component and is attached to the box assembly. The structure is designed to address the effects of boundary conditions on structural dynamic tests [6] and guarantee dynamic interaction between the component and box assembly [5]. As a result, the design of the BARC model facilitates vibration qualification in both simulated and physical experiments [6].

The BARC has been used for experiments [6] and simulated for modal analyses [7, 8] on multiple accounts. Comparatively, the simulation realm has been sparsely explored. To bridge the gap between experimentation and simulation, a simplified BARC assembly was simulated with varying boundary conditions and solvers to attempt to match previously collected single-axis vibration tests based off generated service environment data [2].

S. Chirinos
Department of Mechanical Engineering, Texas A&M University, College Station, TX, USA

A. Pawar
Department of Mechanical Engineering, Carnegie Mellon University, Pittsburgh, PA, USA

H. Tholen
Department of Mechanical Engineering, The Pennsylvania State University, University Park, PA, USA

S. Ouellette · T. Roberts (✉)
Los Alamos National Laboratory, Los Alamos, NM, USA
e-mail: tproberts@lanl.gov

C. Walber et al. (eds.), *Sensors and Instrumentation, Aircraft/Aerospace and Dynamic Environments Testing, Volume 7*,
Conference Proceedings of the Society for Experimental Mechanics Series, https://doi.org/10.1007/978-3-031-05415-0_3

3.2 Methods

3.2.1 Structure Modeling in ABAQUS

The structure that was used for this simulation was the BARC structure, seen in Fig. 3.1, which is composed of 6061 Aluminum T6 and consists of a beam and three C-channels oriented in each principal direction. Using the standard and explicit packages of the commercially available finite element software ABAQUS, the BARC was simulated with eight-node brick elements with reduced integration (C3D8R). The geometry of the BARC offers complexity sufficient to develop analytical methods applicable to fielded systems. In ABAQUS, the BARC model is constructed as a monolithic structure, which is a simplified representation in comparison to the physical model, which consists of several components assembled with fasteners. This simplification removes the inherent complexity of bolted connections but allows for boundary conditions to be more closely observed.

Justification for the engineering model simplification was accomplished by comparing two existing modal analyses of a roving hammer test [9, 10] to a simulated roving hammer test of the experimental BARC structure, which results can be seen in Table 3.1 and Fig. 3.2. The resulting natural frequencies were within 10% error of the existing modal analyses, with the first two modes of each analysis within 3% error, as seen in Table 3.1. These error values were within the acceptable limits for the purposes of this analysis. Visually, the mode shapes of the experimental analysis are like Modal Analysis 1, as seen in Fig. 3.2, with the orientation of some modes being opposite. This discrepancy is likely due to a differing location of impact during the roving hammer test. The article incorporating Modal Analysis 2 did not include figures for all 10 modes, so the visual comparison was only conducted for one study.

3.2.2 Usage of Existing Data

To get output data that was representative of service environment data, previously collected single-axis acceleration time history input data on the BARC, based on generated service data, was used as inputs for the simulations [2]. To achieve consistency across all datasets and account for equipment limitations from the experimental data collection, the data was

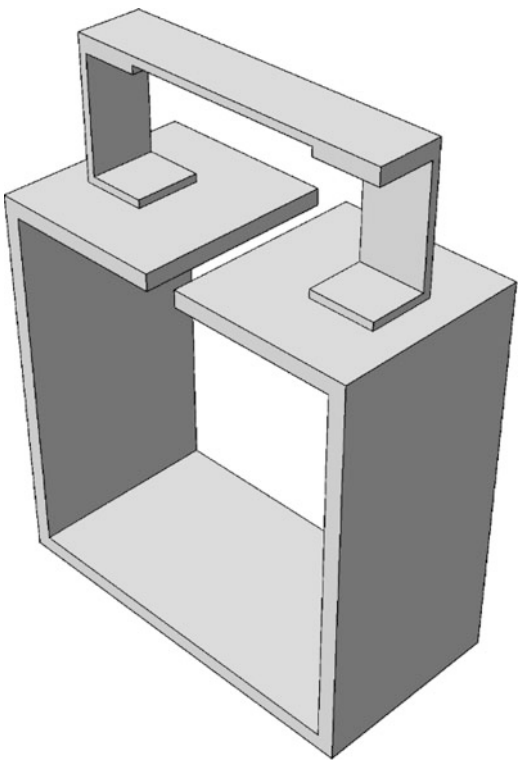

Fig. 3.1 ABAQUS model of the Box Assembly with Removable Component (BARC) fixture

Table 3.1 Comparison of first 10 modes with existing modal analyses

	Experimental modal analysis	Existing modal analysis 1 [9]		Existing modal analysis 2 [10]	
Mode	Frequency (Hz)	Frequency (Hz)	Percent error (%)	Frequency (Hz)	Percent error (%)
1	190	185	2.87%	188	1.39%
2	206	206	0.01%	209	1.66%
3	270	296	8.71%	271	0.28%
4	453	438	3.45%	451	0.41%
5	486	482	0.78%	489	0.47%
6	583	544	7.00%	574	1.41%
7	590	591	0.24%	581	1.48%
8	676	732	7.73%	665	1.50%
9	1140	1040	9.85%	1090	4.34%
10	1220	1140	7.43%	1140	7.29%

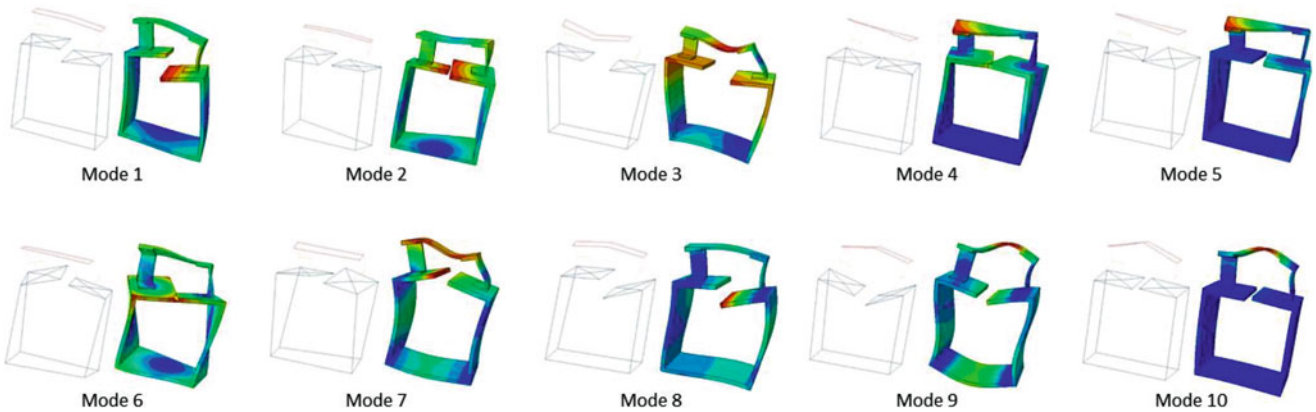

Fig. 3.2 Comparison of existing Modal Analysis 1 [9] (left images) and simplified BARC modal analysis (right images)

resampled to have a sampling frequency of 10,000 Hz. Sampling 0.75-second intervals from nine different sections of the acceleration time histories, various simulations were conducted in multiple configurations of interest.

3.2.3 Boundary Conditions and Parameterization

A key factor was determining the boundary conditions of how the BARC was fixed onto the shaker table. To attempt to explore the significance of the bolted connections along with the surface friction, two cases were considered: constrained displacement along the base in Fig. 3.3a and linear springs attached to the bolt holes modeled with one in Fig. 3.3b. In both boundary conditions, the respective directional motion from the time histories was applied along an orthogonal direction with the remaining translational boundary conditions being fixed and all rotational degrees of freedom being fixed at the selected areas. Additionally, the spring boundary condition in Fig. 3.3b included a rigid plate on the bottom to account the shaker table slip plate being underneath the BARC.

3.3 Analysis

3.3.1 History Outputs

To compare the outputs from the performed simulation with the experimental results from [2], acceleration time histories were recorded at nodes that were in similar locations to the triaxial accelerometers specified within the study. Additionally, the sampling frequency of the acceleration time inputs was matched in the collected outputs; as such, the outputs at the nodes can be properly compared to the experimental data collected. The triaxial accelerometer locations are shown in Fig. 3.4.

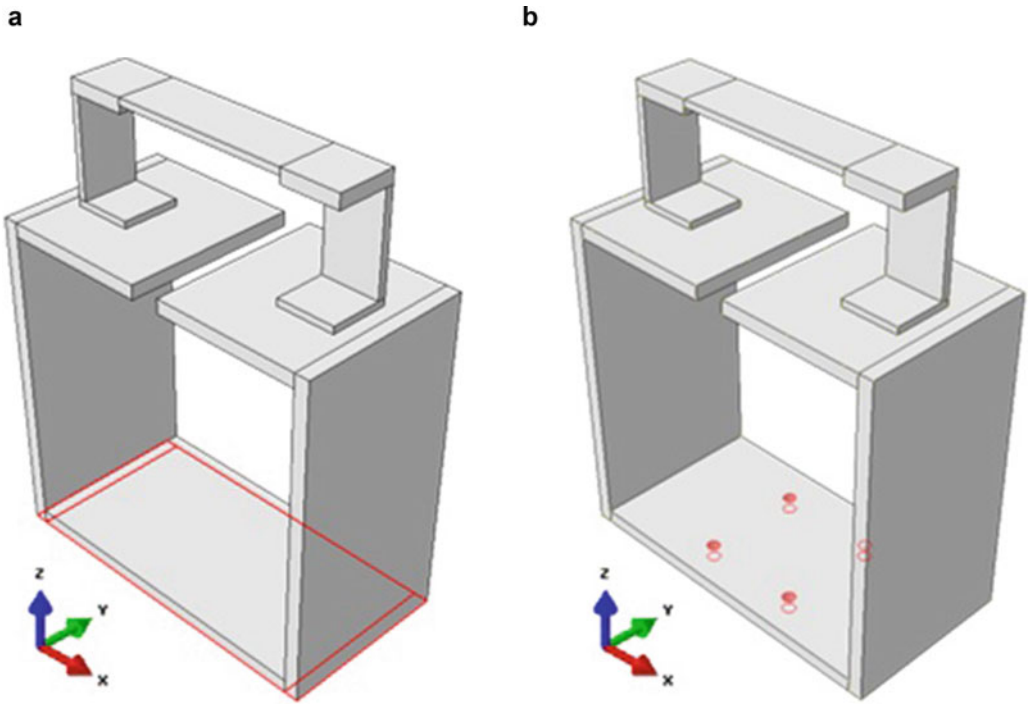

Fig. 3.3 Different boundary conditions of BARC model tested in simulations (**a**) fixed along the bottom face and (**b**) attached to ground by springs at representative bolt holes from experimental data collection

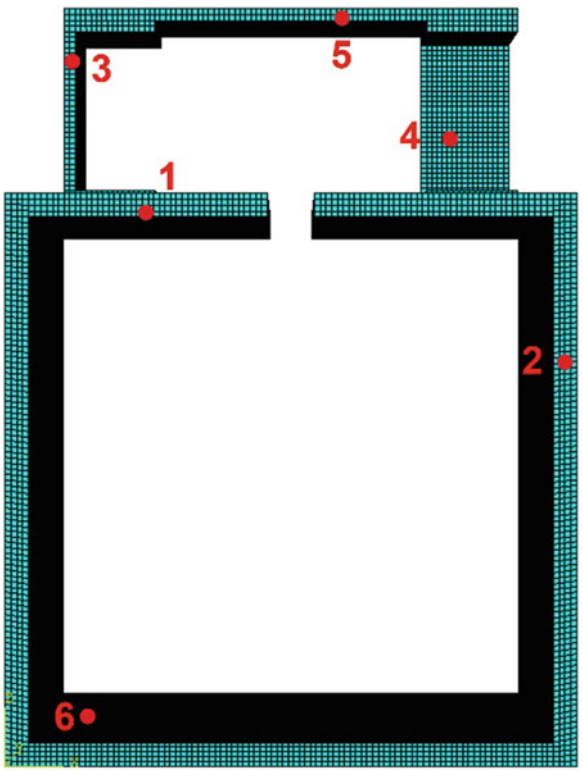

Fig. 3.4 Locations of accelerometers on BARC model from recorded acceleration time history data

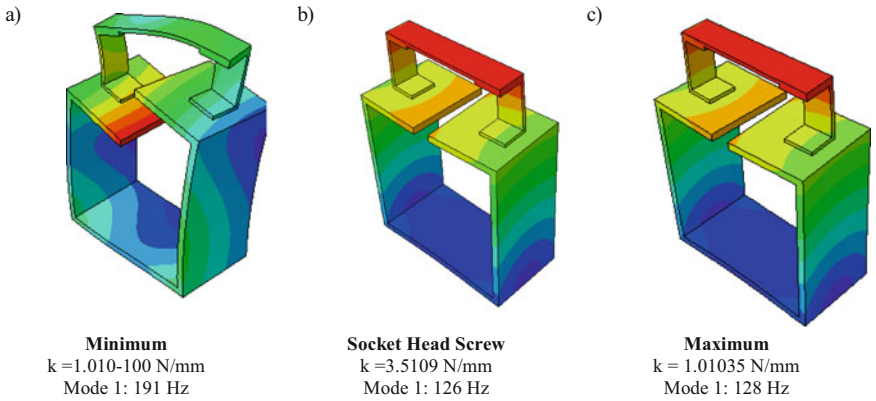

Fig. 3.5 First mode of BARC with varying spring stiffness values

3.3.2 Implicit Analysis

Boundary Conditions

One consistent limitation of single-axis vibration testing is the ability to recreate boundary conditions of the service environment. In ABAQUS, the types of boundary conditions available for use differ depending on which solver is used. To represent the rigidity of the shaker table more accurately, an analytically rigid plate was modeled as a 3D shell component to ensure the BARC could not deform past the boundaries of the simulated shaker table in experimentation. A constrained displacement boundary condition was also implemented to observe the difference in behavior of the BARC model. The base of the BARC was fixed except for the excitation direction.

To accurately represent the physical single-axis vibration tests completed in [2], springs were included in the implicit model to replicate the bolted connections between the BARC base plate and the shaker table. The springs were modeled to connect from the node located at the bolt centers to the ground. Each bolt location included three linear springs, one for each principal direction. The springs were justified for use by analyzing the effects of varying stiffness (k) with a simplified modal analysis. The first mode between 100 and 1000 Hz was determined for near-zero stiffness, the calculated stiffness based on the socket head screws used in the construction of the BARC [5], and the maximum allowable stiffness, as seen in Fig. 3.5. The stiffness value of the socket head screw was calculated based on Equation Set 1 [11].

In the case of Fig. 3.5a, c, the minimum stiffness case exhibits a stiffness value of $1 \cdot 10^{-100}$ N/mm applied to the four bolt hole locations, and a stiffness value of $1 \cdot 10^{35}$ N/mm was used for the maximum stiffness case. The minimum stiffness case replicates a free-free boundary condition, while the maximum stiffness case represents a fixed boundary condition. In practice, there will always be flaws in the system; thus completely fixed structures are unattainable. Figure 3.5b represents this case where the stiffness value of $3.5 \cdot 10^{9}$ N/mm was only applied in the excitation direction, while the other two directions were assigned the maximum stiffness value of $1 \cdot 10^{35}$ N/mm. The difference in stiffness values accounts for flaws in the bolted connections and grants flexibility in the excitation direction.

$$k_{\text{shank}} = \frac{A_{\text{nom}} E_{\text{bolt}}}{L_{\text{shank}}} \tag{3.1a}$$

$$k_{\text{thd}} = \frac{A_{\text{t}} E_{\text{bolt}}}{L_{\text{thd.g}}} \tag{3.1b}$$

$$k_{\text{bolt}} = \frac{k_{\text{shank}} k_{\text{thd}}}{k_{\text{shank}} + k_{\text{thd}}} \tag{3.1c}$$

where the variables are defined as the following:

A_{nom} is the nominal area of the bolt
E_{bolt} is the elastic modulus of the bolt material
L_{shank} is the length of the bolt shank
A_t is the tensile stress area
$L_{thd.\ g}$ is the length of the threaded portion within the grip of the bolt
k_{shank} is the stiffness of the shank
k_{thd} is the stiffness of the thread
k_{bolt} is the stiffness of the bolt

The method of solving implicitly requires definition of a primary base before acceleration can be applied to the model. In ABAQUS/Standard, the primary base is specified by the boundary conditions attached to the model in the Frequency step of the simulation, which is discussed in subsection "Boundary Conditions" in Sect. 3.3.2 of this study. The acceleration is defined as an acceleration base motion with a tabular input in the mode-based steady-state dynamics step of the simulation, which is discussed in subsection "Mode-Based Steady-State Dynamics" in Sect. 3.3.2.

Modal Analysis

Implicit analysis is solved in two steps, the first of which is a Frequency step to complete a modal analysis. The frequency range of interest was set to be 100–1000 Hz, based on the experimental results from [2].

Mode-Based Steady-State Dynamics

The second step in the implicit calculation is a mode-based steady-state dynamics analysis. This step is dependent on the modal analysis, as resonant frequency values and the corresponding mode shapes are required for completion of the calculation. A running average of damping values from five modal analyses detailed in [9] was used as inputs in the steady-state dynamics step to control the magnitudes of the response from the structure. Acceleration values were applied to the primary base as a tabular input from the data sets retrieved from the experiments conducted by [2]. After the analysis is complete, a Frequency Response Function (FRF) is output and can be compared to other results as outlined in Sect. 3.3.4.

3.3.3 Explicit Analysis

Boundary Conditions

To accurately capture the resulting dynamic motion, ABAQUS/Explicit was utilized for inputting the discontinuous acceleration time history recorded in the test results from [2]. Two different boundary conditions were applied to the explicit analyses. The first boundary condition applies motion on the bottom surface of the BARC while fixing the remaining translational degrees of freedom and all rotational degrees of freedom, as seen in Fig. 3.3a. The second boundary condition, like the implicit analysis, includes the use of linear springs to replicate the vibration effects of the bolted connections, seen in Fig. 3.3b; this was conducted by applying the motion on a rigid plate and connecting the plate to the BARC by springs in the same manner as the implicit model.

Computational Cost

While explicit analysis can account for discrete changes from the acceleration time history that is input, it comes at the cost of computational time. While the implicit solver has multiple steps to first complete a modal analysis and then use the said modal analysis for a steady-state dynamic response, both processes are at the order of a few minutes; conversely, depending on the length of the input acceleration time history, the explicit analyses ran could take a few hours to a few days to complete. To balance run time and output data with significant resolution in the frequency range, based on time ranges that showed similar frequency responses as more extensive time ranges with experimental data, time ranges slightly under 1 second were input for both explicit and implicit analyses, as mentioned in Sect. 3.2.2.

3.3.4 Frequency Response and Data Analysis

Frequency response analysis is performed using two methods. The first uses the acceleration time history data from both the experimental data and explicit analysis. Using the *modalfrf* function in the Signal Processing Toolbox from MATLAB, frequency responses are calculated. Explicit analysis data is preprocessed using a bandpass filter to have frequencies between 100 and 1000 Hz. Using a Hanning window with window length half the size of the sample size and a sampling frequency of 10,000 Hz, the frequency response is generated. The second method is generated in ABAQUS. The implicit modal analysis calculates the frequency response of the analysis and generates plots from it. The frequency response analysis is key for calculating the stiffness of the screws used in the analyses. Additionally, the peak responses are compared to test boundary condition parameter combinations.

Spectral Measurements

Power spectral density (PSD) was used to determine the acceleration magnitude present in the signal as a function of frequency. The PSD is used to test lifetime severity. Applied with Miner's rule, as seen in Eq. 3.2a, the severity ratio is calculated and used to compare accuracy of simulation procedures in contrast to experimental results. PSD of acceleration time histories is calculated using MATLAB's *pwelch* function which calculates the PSD using Welch's method.

Scalar Measurements

Scalar measurement, root mean squared (RMS), was applied to the test data set to find the RMS acceleration magnitude of experimental data. This was used to determine a baseline magnitude response. The RMS value was compared to the RMS values of both explicit acceleration time histories. The RMS value is calculated using the *rms* function in MATLAB but is based on Eq. 3.2b.

$$\frac{t_{\text{test}}}{t_{\text{service}}} = \left(\frac{S_{\text{service}}}{S_{\text{test}}}\right)^{m} \tag{3.2a}$$

$$x_{\text{RMS}} = \sqrt{\frac{1}{N}\sum_{n=1}^{N}|x_n|^2} \tag{3.2b}$$

where the variables are defined as the following:

t_{test} is the time of the experimental test
t_{service} is the time of the service environment test
S_{test} is the severity of the experimental test
S_{service} is the severity of the service environment test
m is the material damage measure
x_{RMS} is the root mean square value
N is the data set size

Correlation Measurements

The Pearson correlation coefficient is based on the range of $[-1, +1]$ where (-1) conveys a perfectly negative correlation, $(+1)$ conveys a perfectly positive correlation, and 0 conveys no correlation. Applying the Pearson correlation between a method and the experimental data further quantifies which response is an adequate representation.

3.4 Results and Discussion

The frequency responses of each calculation method provide insight into how the structure responds in the different simulation techniques. With reference to Fig. 3.4, the locations of Accelerometers 2, 4, and 6 are particularly important as they represent whether the simulation implementations accurately represent the experimental setup. Accelerometer 6, on the bottom of the base, provides insight into the accuracy of the input since it is the closest representation to the shaker table excitation. Accelerometer 2, further up the base, provides insight into how various boundary condition implementations change the response. Upon adding structural elements in series, the sensitivity of the modal response will increase additively as the distance increases from the source boundary condition. Accelerometer 4, at the very top, is the furthest accelerometer from the excitation input. Additionally, it is an additional structural element to the base. Studying Accelerometers 2 and 4 shows how well transmissibility is modeled.

The FRF response of the experimental data is a ratio of the input and the output. For Accelerometer 6, the input is the data collected at Accelerometer 6, which results in no response for the experimental data, as expected. However, the magnitude of the data provides context for how the input behavior exists in each method. Implicit analyses show responses that do not necessarily exist as a result of the nature of the integration scheme. Shifting focus to include other accelerometers, we notice the magnitudes of the responses of the implicit analyses to exist at different magnitudes compared to the experimental test data. The constrained displacement (CD) is always higher in magnitude and the springs are always lower.

The explicit analyses also resulted in response for Accelerometer 6 input and Accelerometer 6 output. The dynamics of the explicit analyses are like implicit analyses; however, the magnitudes are within a reasonable variance to the experimental data, as seen in Fig. 3.6.

The constrained displacement did not create a response in the *y*- and *z*-directions at Accelerometer 6 using the explicit method, as can be seen in Figs. 3.7 and 3.8, which is a result of the implementation of boundary conditions in the simulation. The response only exists within the *x*-direction, which does not accurately represent the input and ultimately the basic response of the system.

At Accelerometer 2, responses consistently occur in each method. The magnitude relationships between the methods and the experimental data remain. Encouraging features are visible in the 600–700 Hz range. A peak response exists in the experimental data in the *x*- and *z*-directions which is reciprocated by each method. This continues with responses between 100–200 Hz and 400–500 Hz. Comparing Accelerometer 4 provides similar responses; however, response locations are slightly different between the methods and the experimental data. Further evidence of these trends can be found in Appendix A.

In both cases, the transmissibility of the vibration excitation has not yet been accurately represented in the implicit methods, and tuning boundary conditions will achieve that. The explicit methods were closer in magnitude to the experimental data, and the response had encouraging features with general alignment of peak frequencies and divergences.

PSD provides insight into what frequency the average power is distributed. In the FRF responses, the important frequency ranges exist between 100–200 Hz, 400–500 Hz, and 600–700 Hz. The implicit methods (Figs. 3.9 and 3.10) reinforce the importance of the critical frequency ranges. It also detects critical frequencies at 300 Hz and in the implicit springs method (Fig. 3.10) critical frequencies at 800 Hz. In the FRF responses above, peaks do exist at these frequencies and are potential severity indicators.

For both PSD measurements of the explicit methods (Figs. 3.11 and 3.12), the responses tail off after 700 Hz. The PSD measurement for the explicit constrained displacement (Fig. 3.11) has no critical response between 100 and 200 Hz but has a critical response at 200 Hz and two between 300 and 500 Hz. The explicit springs data had noisier responses (Fig. 3.12). However, general trends indicate critical responses between 100–200 Hz and 400–500 Hz. In the *x*- and *y*-direction, there is a critical response at 200 Hz like the explicit constrained displacement method.

The baseline RMS value set by the experimental data was comparable in magnitude with both explicit methods (Table 3.2). This only occurred in the *x*-direction. The resulting magnitudes in the *y*- and *z*-directions in the experimental data were orders of magnitude lower. The explicit methods maintained the same magnitude as the *x*-direction.

The resulting values from the Pearson correlation coefficient analysis imply that there is close to no correlation between the experiment and the implicit methods (Table 3.3). Thus, the applied parameters here need to be further adjusted. The explicit springs method shows a more accurate correlation overall, which suggests that the boundary conditions, inputs, and other applied parameters are more representative of the experimental data.

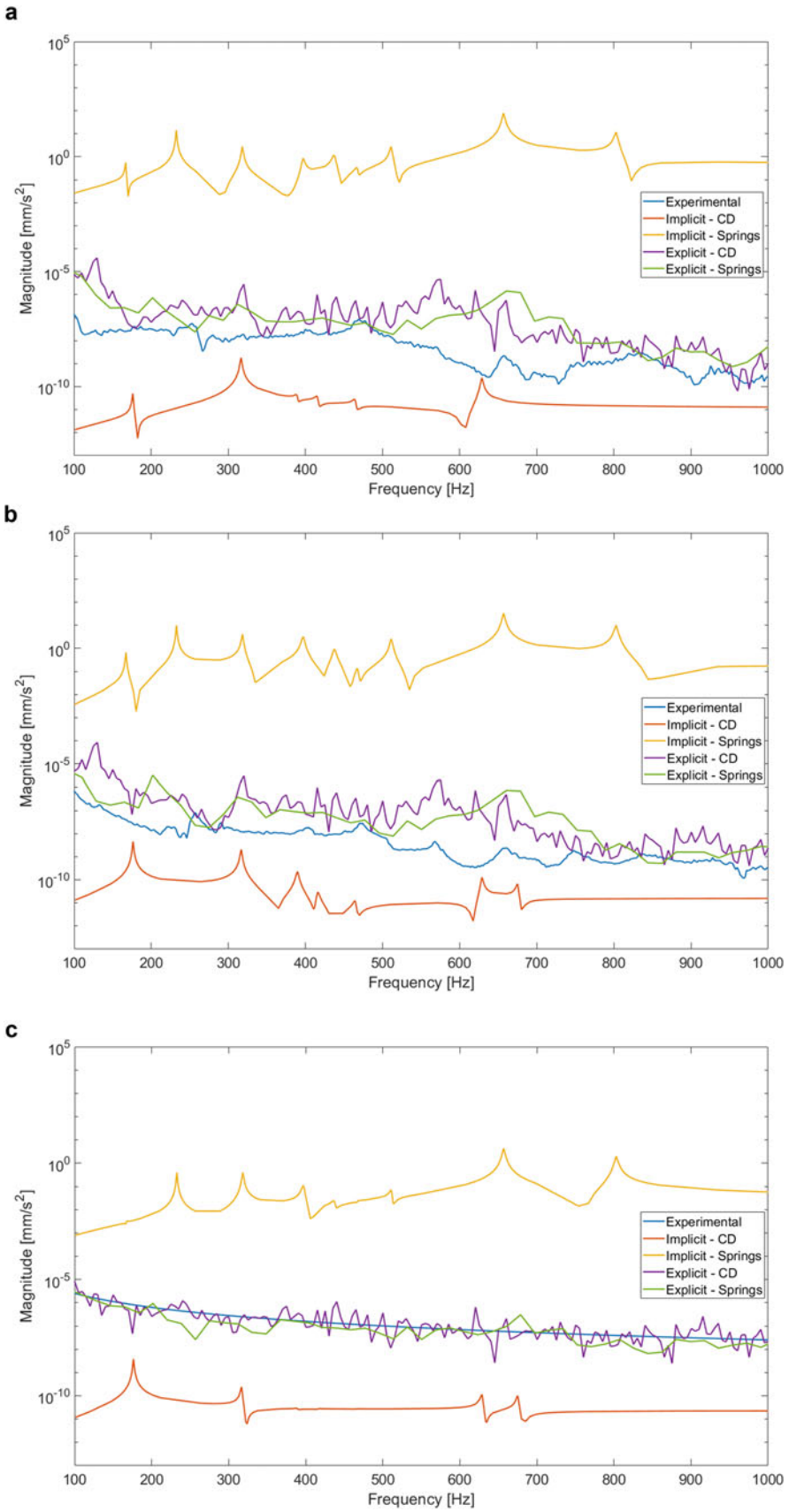

Fig. 3.6 Frequency responses of (**a**) Accelerometer 2, (**b**) Accelerometer 4, and (**c**) Accelerometer 6 in the *x*-direction

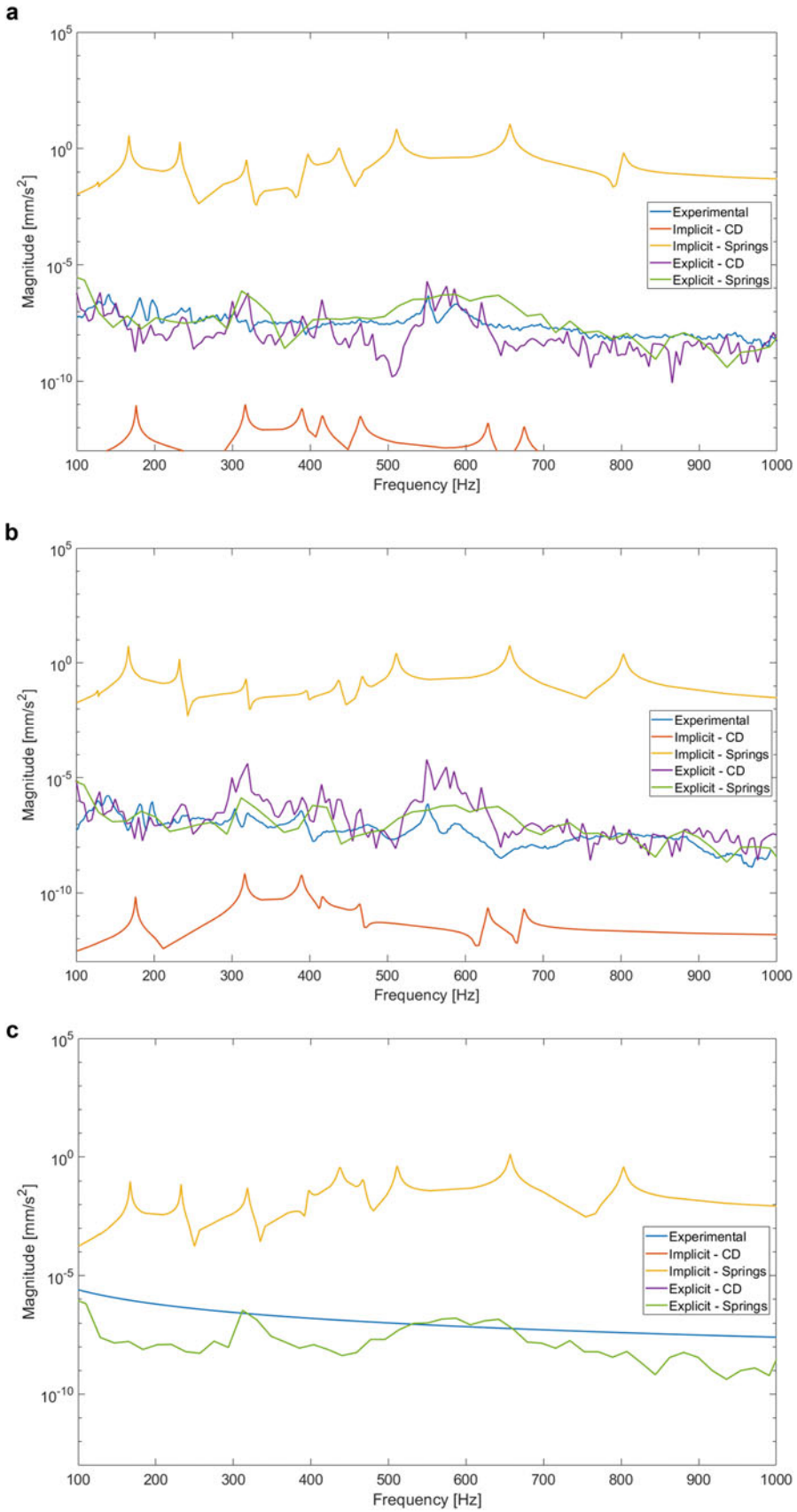

Fig. 3.7 Frequency responses of (**a**) Accelerometer 2, (**b**) Accelerometer 4, and (**c**) Accelerometer 6 in the *y*-direction

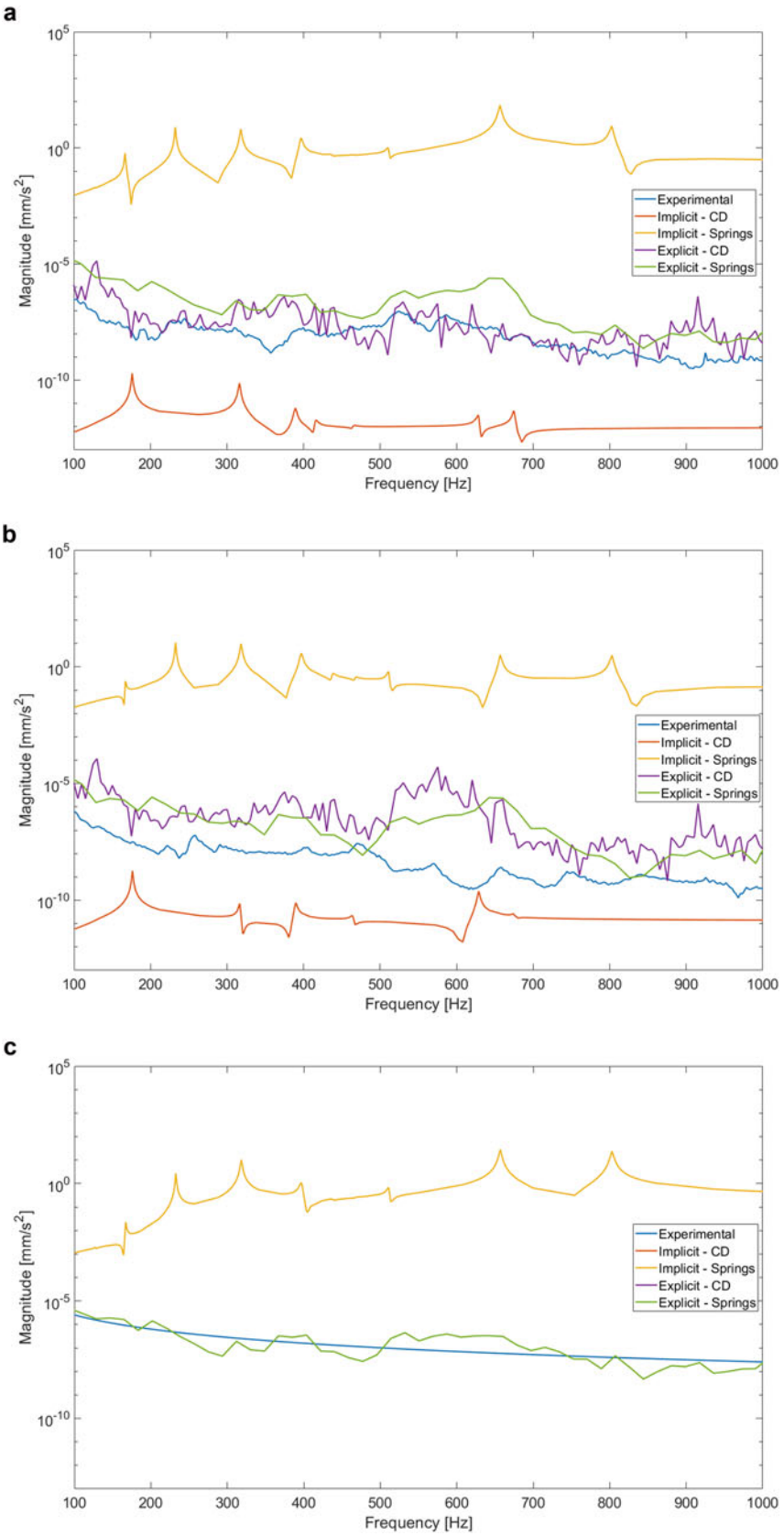

Fig. 3.8 Frequency responses of (**a**) Accelerometer 2, (**b**) Accelerometer 4, and (**c**) Accelerometer 6 in the z-direction

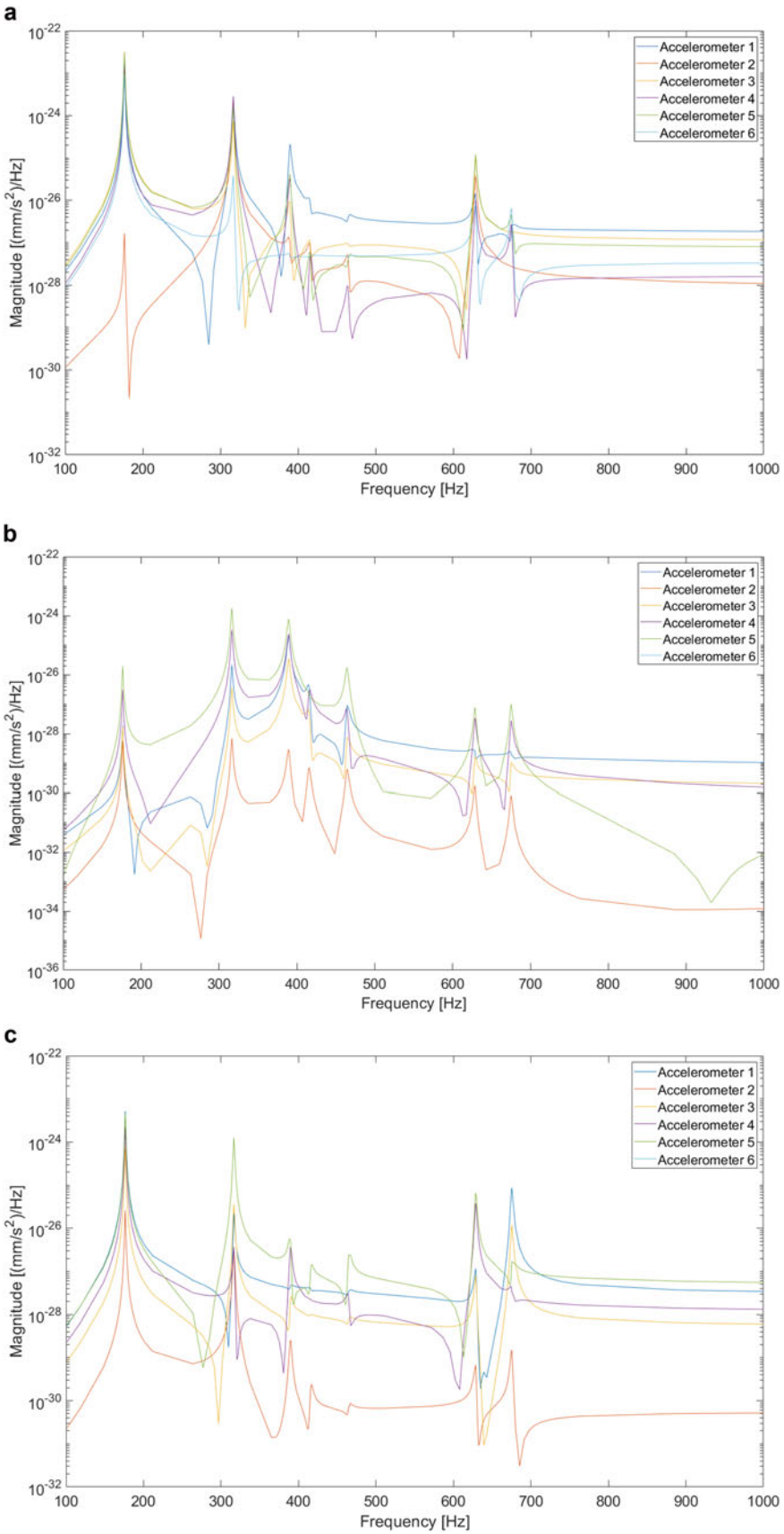

Fig. 3.9 Power spectral density measurement of each accelerometer for implicit constrained displacement data in (**a**) *x*-direction, (**b**) *y*-direction, and (**c**) *z*-direction

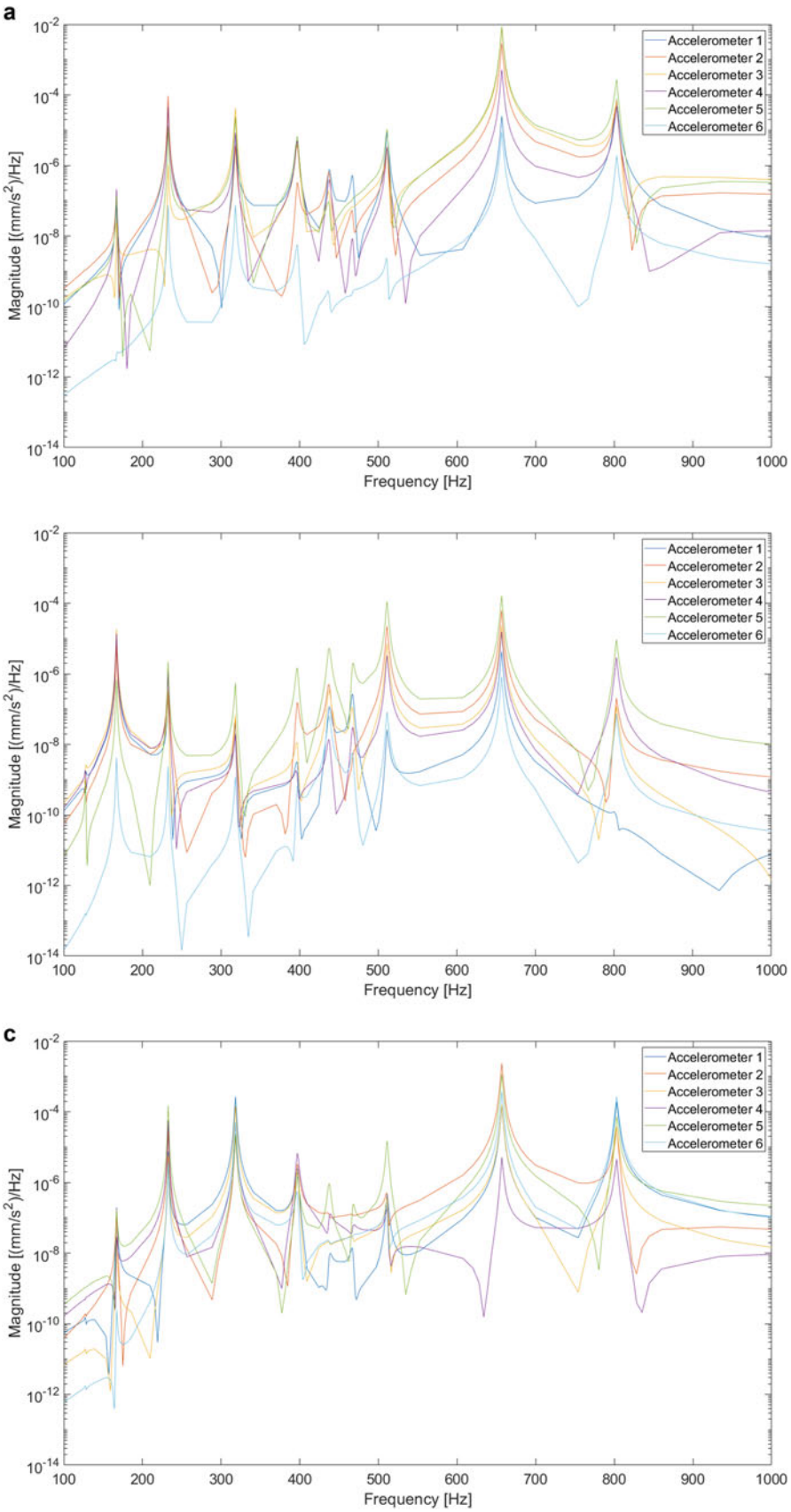

Fig. 3.10 Power spectral density measurement of each accelerometer for implicit springs data in (**a**) *x*-direction, (**b**) *y*-direction, and (**c**) *z*-direction

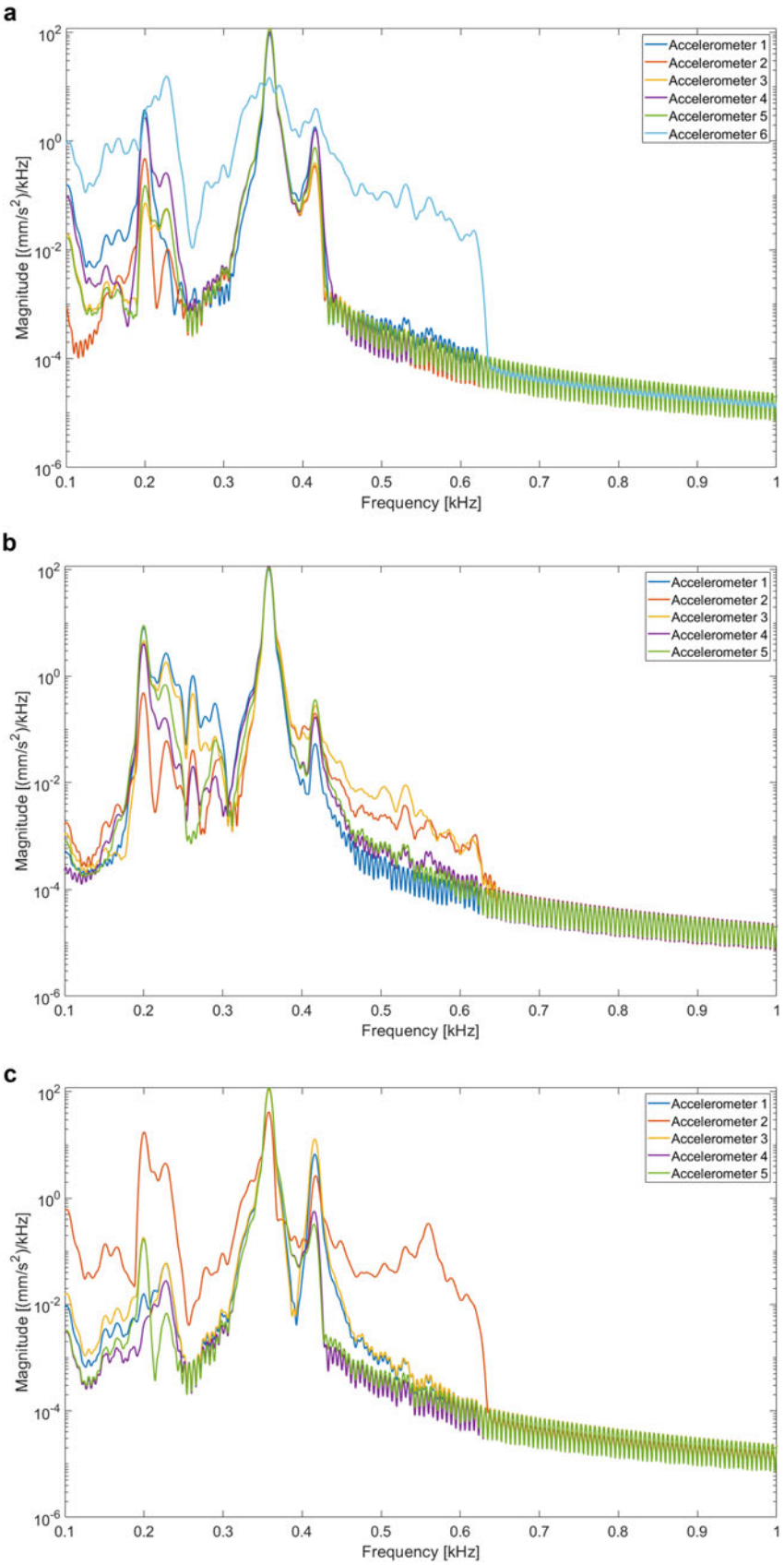

Fig. 3.11 Power spectral density measurement of each accelerometer for explicit constrained displacement data in (**a**) *x*-direction, (**b**) *y*-direction, and (**c**) *z*-direction

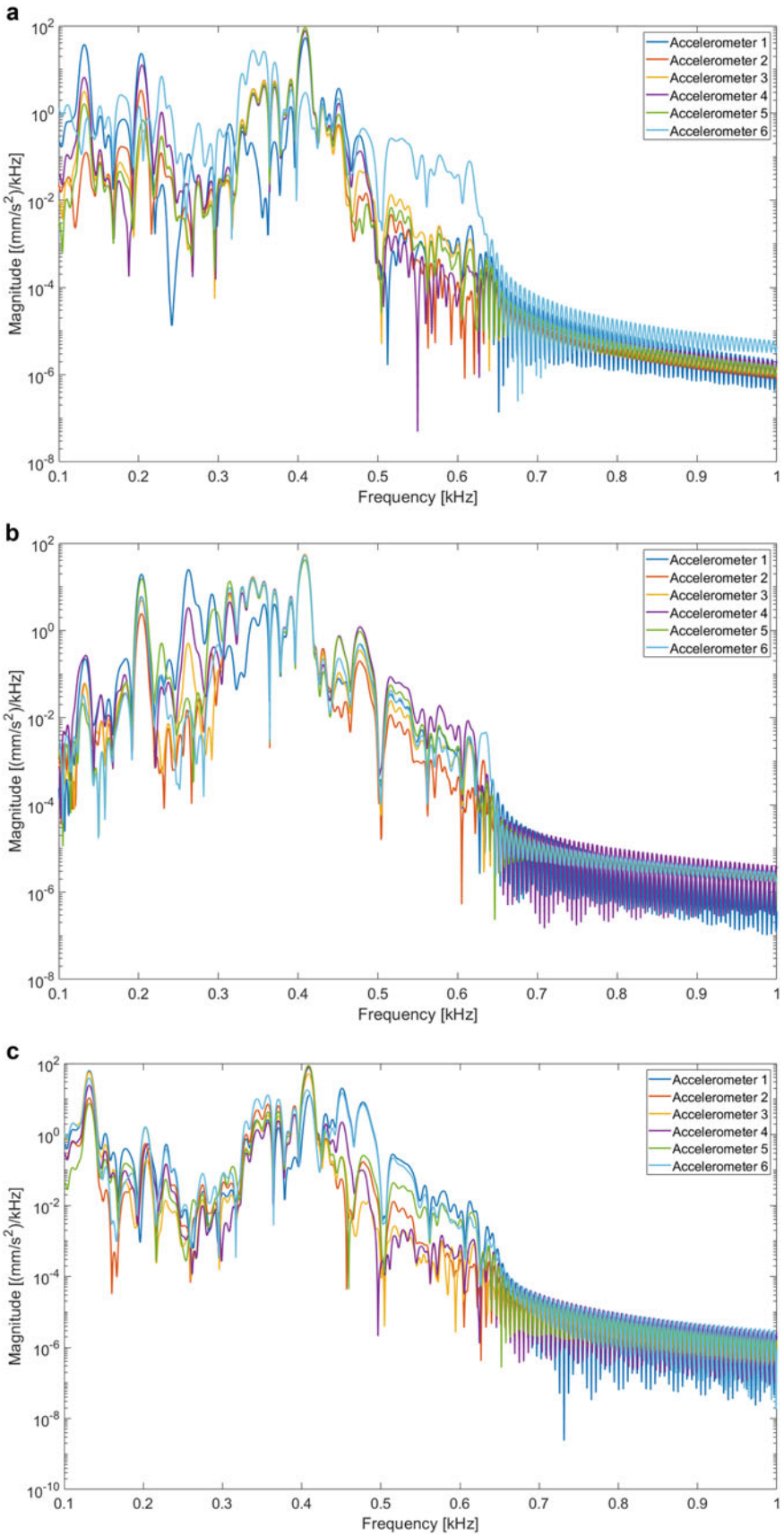

Fig. 3.12 Power spectral density measurement of each accelerometer for explicit springs data in (**a**) *x*-direction, (**b**) *y*-direction, (**c**) *z*-direction

Table 3.2 RMS of time history acceleration data of explicit data with corresponding boundary conditions

	Test	Explicit	
		Constrained displacement	Springs
Accelerometer	*x-Direction*		
1	5.14 E+11	2.42 E+12	5.14 E+11
2	1.13 E+12	5.96 E+12	1.13 E+12
3	1.78 E+12	9.10 E+12	1.78 E+12
4	6.10 E+11	2.80 E+12	6.10 E+11
5	1.96 E+12	9.36 E+12	1.96 E+12
6	4.11 E+11	4.93 E+11	4.11 E+11
	y-Direction		
1	3.49 E+06	1.46 E+12	5.85 E+10
2	4.97 E+06	3.30 E+10	9.11 E+10
3	8.01 E+06	7.89 E+10	1.47 E+11
4	6.99 E+06	7.99 E+11	1.10 E+11
5	1.24 E+07	1.25 E+12	2.56 E+11
6	1.60 E+07	–	2.73 E+10
	z-Direction		
1	1.27 E+07	4.65 E+12	4.40 E+11
2	5.78 E+06	4.15 E+10	5.82 E+11
3	5.69 E+06	1.30 E+12	3.37 E+11
4	1.73 E+07	5.34 E+12	5.69 E+11
5	2.43 E+08	7.34 E+12	9.89 E+11
6	4.01 E+07	–	2.46 E+11

Table 3.3 Pearson correlation coefficient of implicit and explicit data with corresponding boundary conditions

	Implicit		Explicit	
	Constrained displacement	Springs	Constrained displacement	Springs
Accelerometer	*x-Direction*			
1	−0.0501	−0.188	0.439	0.774
2	−0.0827	−0.212	0.463	0.738
3	0.0183	−0.126	0.507	0.713
4	0.0400	−0.146	0.723	0.983
5	−0.0243	−0.130	0.766	0.790
6	0.150	−0.195	0.334	0.740
	y-Direction			
1	−0.0147	−0.116	0.125	0.208
2	0.00680	−0.151	0.119	0.597
3	−0.0231	−0.153	0.0377	0.304
4	0.369	−0.192	0.0875	0.346
5	0.473	−0.252	0.617	0.859
6	–	−0.282	–	0.555
	z-Direction			
1	−0.103	−0.135	0.126	0.565
2	−0.0726	−0.107	0.0611	0.378
3	0.150	−0.139	0.0407	0.171
4	−0.0372	−0.158	0.375	0.998
5	−0.0683	−0.231	0.369	0.689
6	–	−0.223	–	0.274

3.5 Conclusion

For all simulations, frequency responses relatively align with respect to all methods and boundary condition implementations. Critical frequency ranges of 100–200 and 400–500 Hz consistently occur in each method. Unique responses occurring in each individual method also occur and are indicative of the boundary condition implementations and the resulting responses of the different dynamics. The implicit methods are orders of magnitudes different, but the explicit analyses are within similar magnitude ranges. Spectral severity analysis of PSD reinforces critical frequency responses with each method in comparison to the original. The RMS values of explicit analysis compared to the experimental baseline values are similar in magnitude in the *x*-direction but maintain the same magnitude even though the experimental data has values orders of magnitude lower. The Pearson correlation coefficients of each method in relation to the experimental data indicate the explicit method with spring boundary condition has the best positive correlation across each direction and accelerometer followed by the explicit analysis with constrained displacement. Both implicit analyses exhibit near-zero coefficient values, meaning they are uncorrelated.

Improving the results of each method would be a result of adjusting the nature of the boundary conditions. For true accurate representations, the constrained displacement boundary condition is restrictive and yields underwhelming or no measurable data outside of the unconstrained direction, not an accurate representation. The spring boundary conditions more accurately represent the dynamics of the system. The difference is how the analysis uses the boundary condition.

While implicit analysis offers computational efficiency, for single-axis simulations with steady-state dynamics, it seemingly comes at the expense of accuracy. Conversely, the explicit analyses indicate more promising results, which could be further improved with a more developed model. In the future, explicit models could be further explored with bolted connections implemented to attempt to get better resolution of results in areas furthest from the base. Additionally, convergence studies could be observed to study how much time history is needed to output results with significant resolution for both the explicit and implicit approach.

Appendix

Appendix A: Accelerometer Frequency Responses

The following plots compare the resulting frequency response functions of each simulation method to the experimental data. Accelerometer 6 was used as the input acceleration time history, and the corresponding response was recorded at Accelerometers 1, 3, and 5.

Frequency Responses of Each Accelerometer in the x-Direction

Accelerometer 1

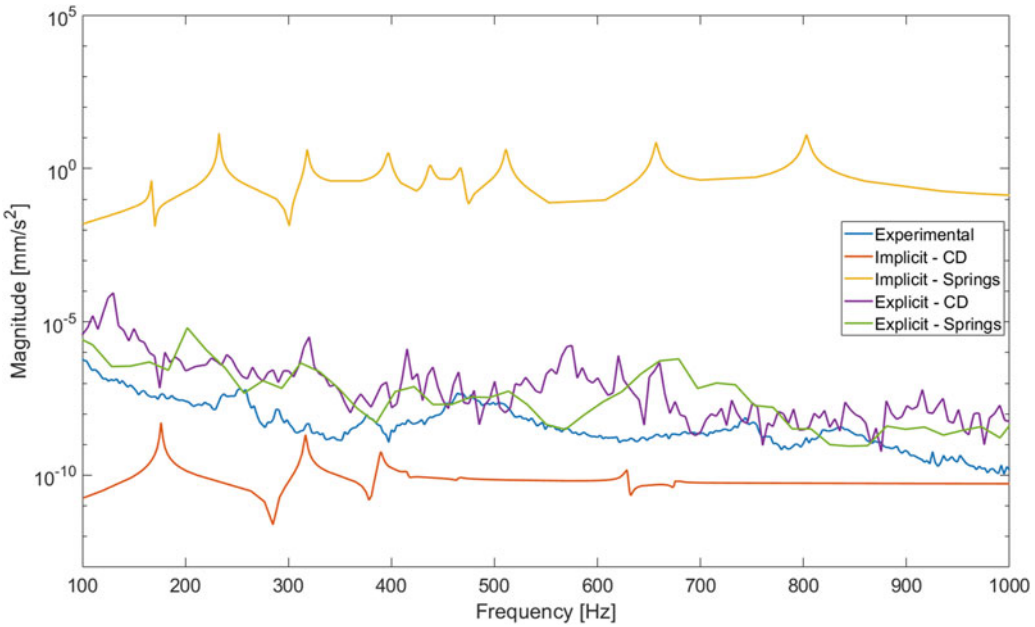

Accelerometer 3

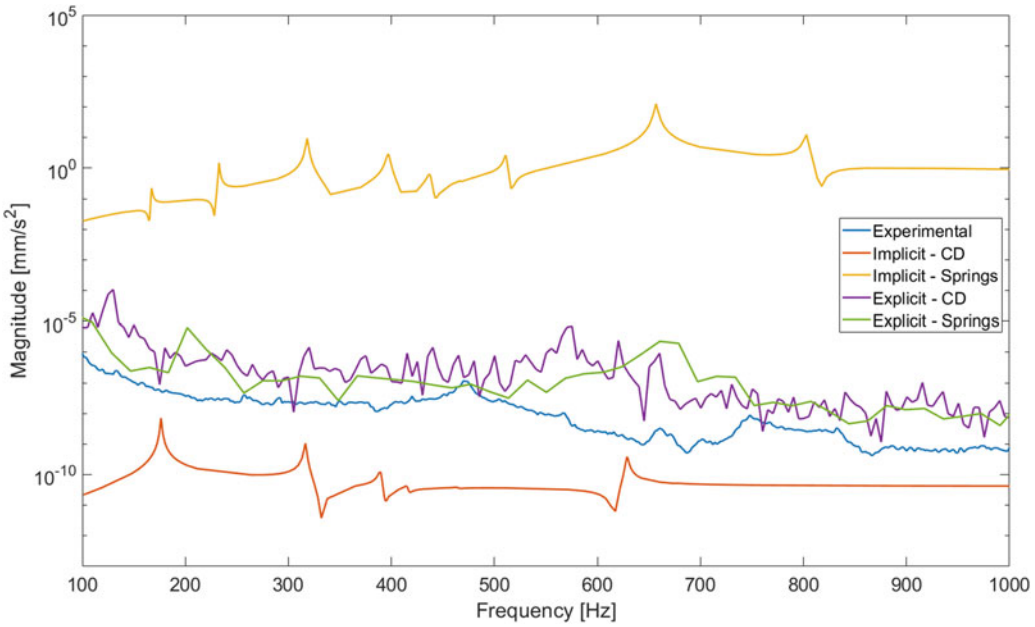

Accelerometer 5

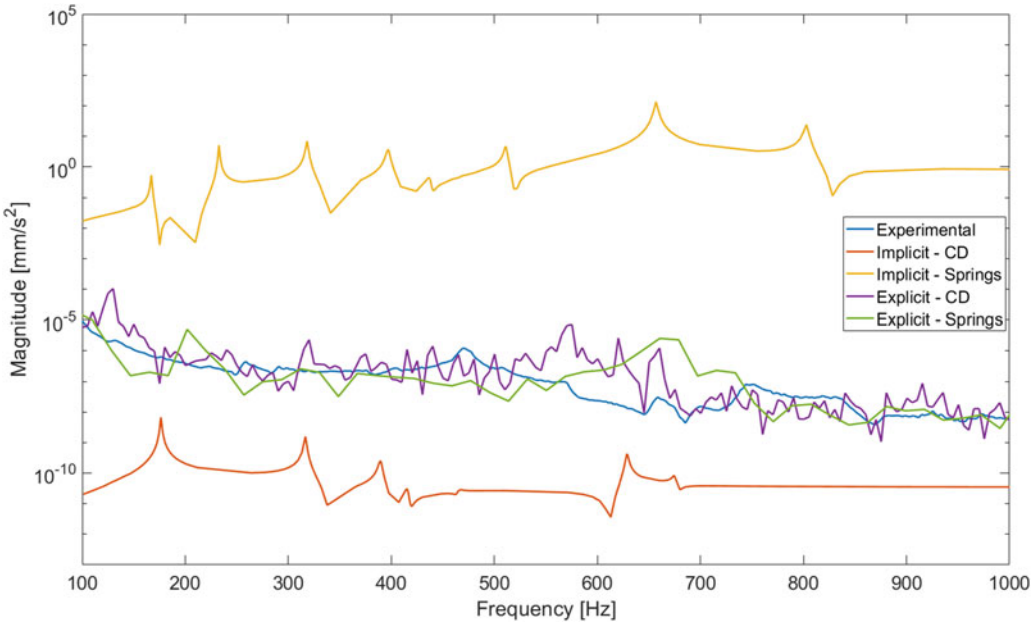

Frequency Responses of Each Accelerometer in the y-Direction

Accelerometer 1

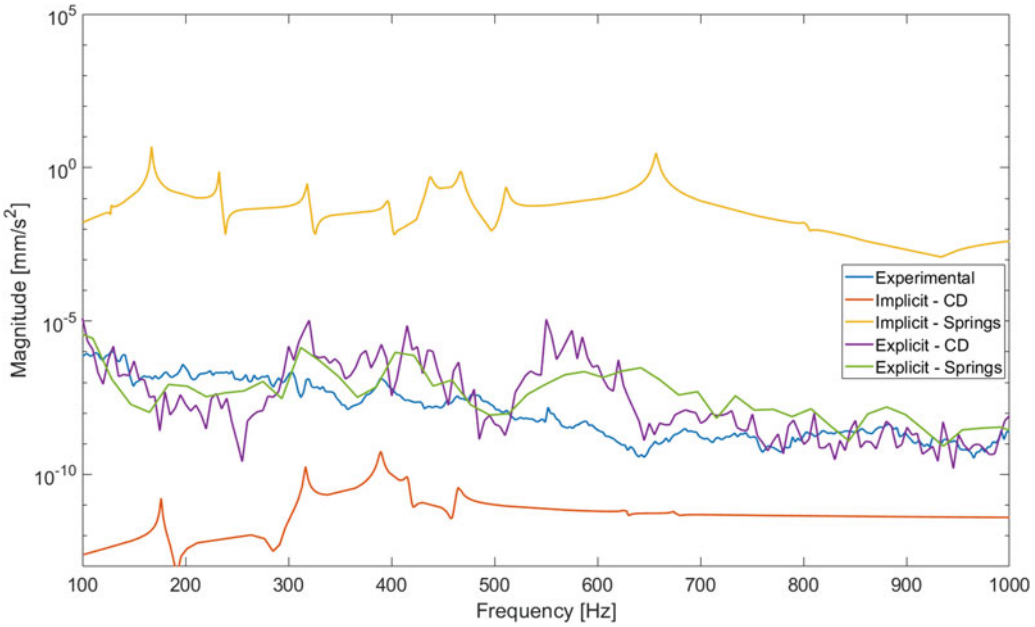

Accelerometer 3

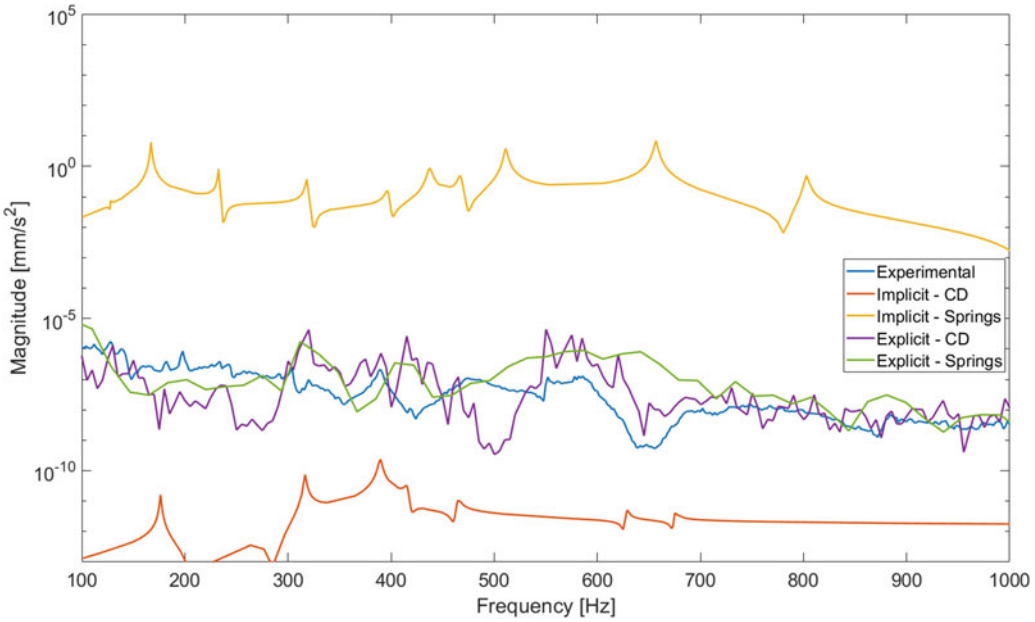

Accelerometer 5

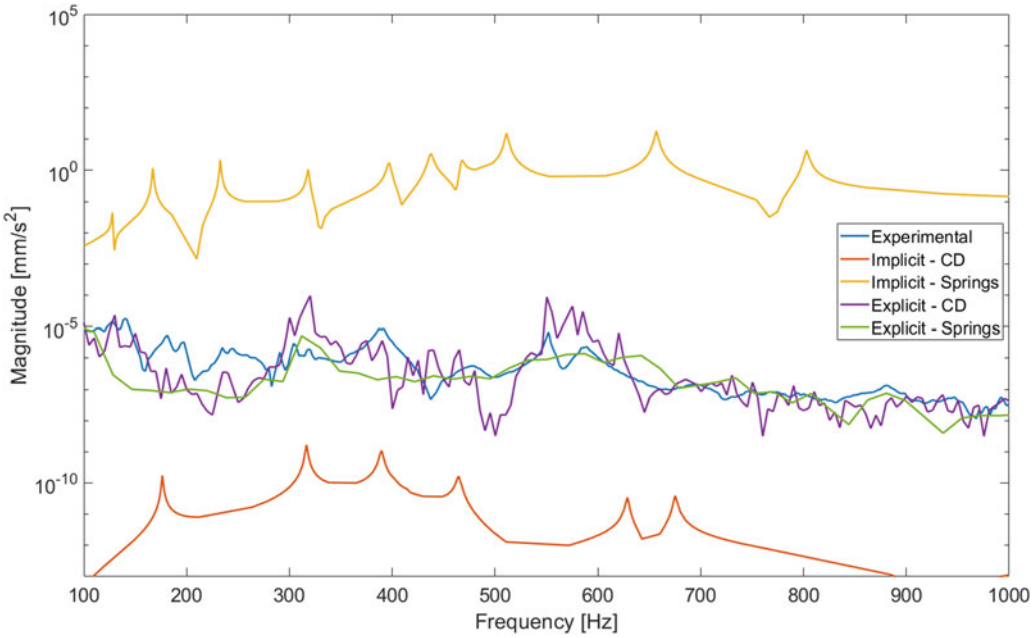

Frequency Responses of Each Accelerometer in the z-Direction

Accelerometer 1

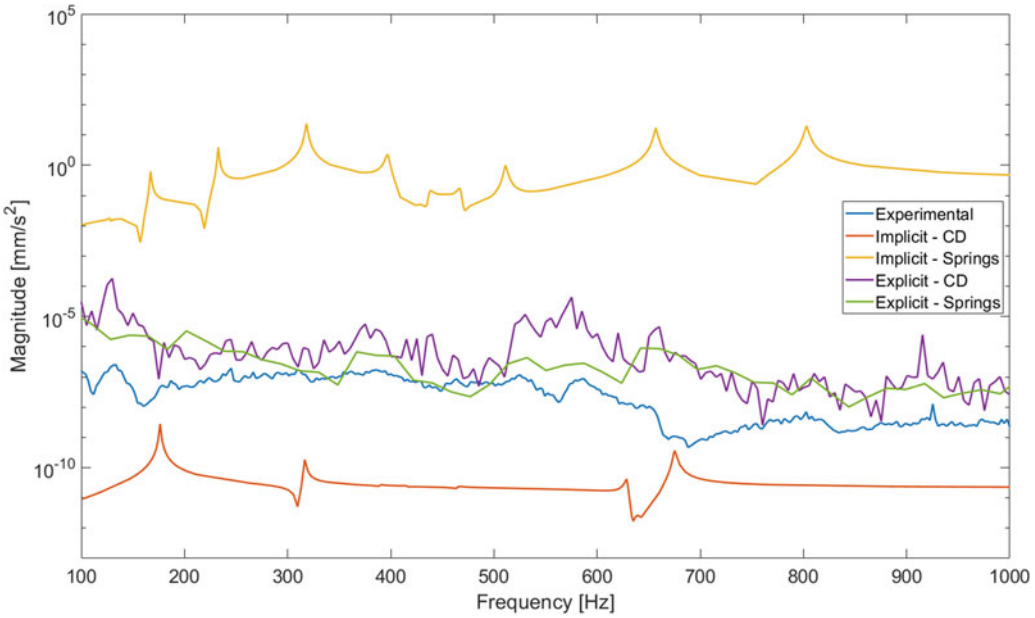

Accelerometer 3

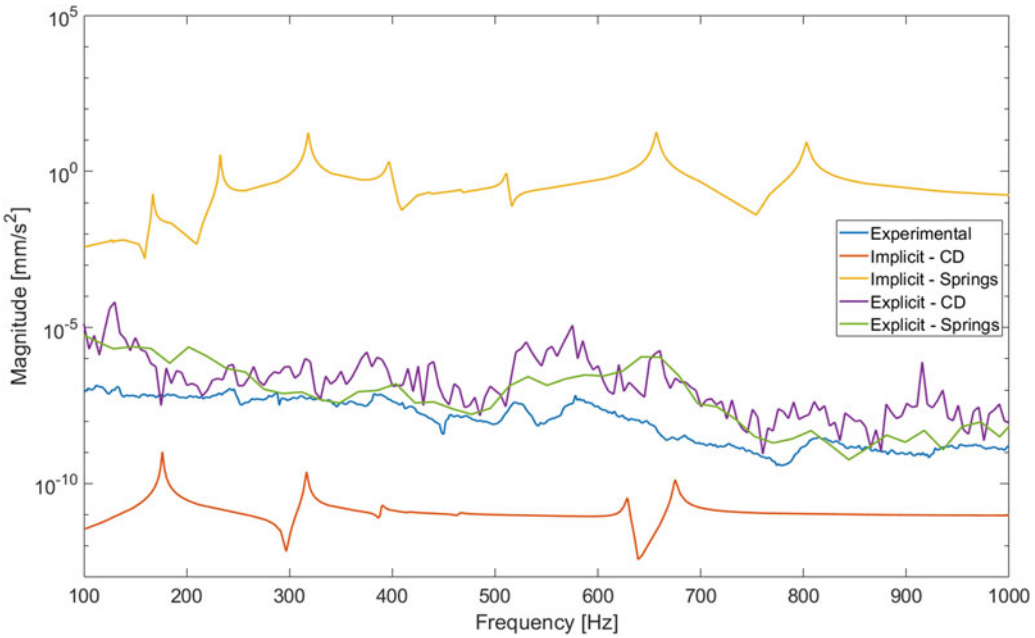

Accelerometer 5

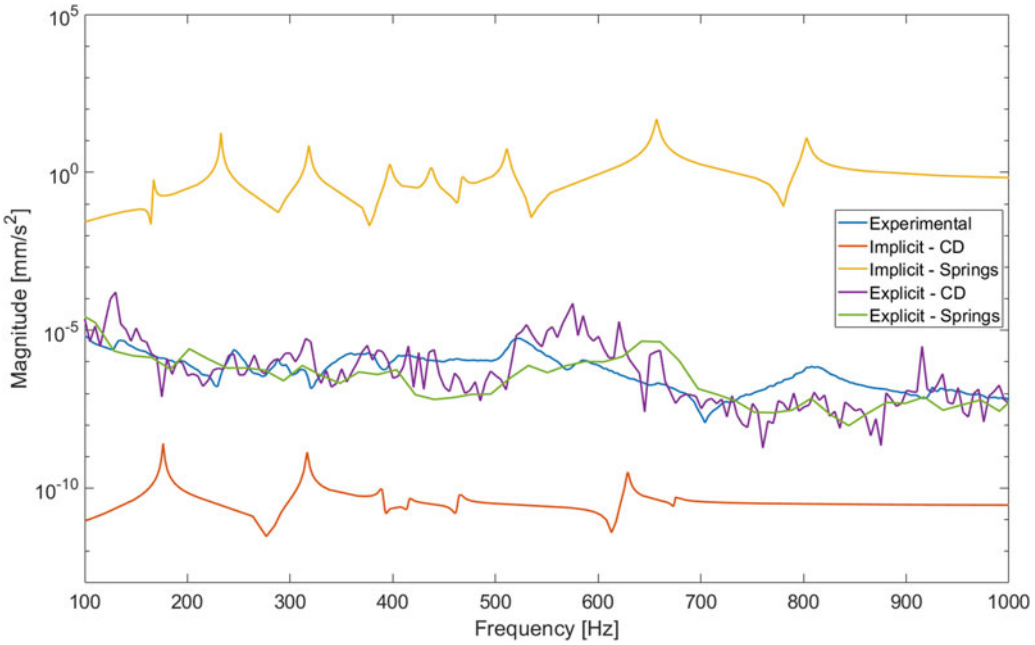

References

1. D'Elia, G., Mucchi, E.: Comparison of single-input single-output and multi-input multi-output control strategies for performing sequential single-axis random vibration control test. J. Vib. Control. **26**(21–22), 1988–2000 (2020). https://doi.org/10.1177/1077546320909975
2. Bouma, A., Campbell, A., Roberts, T., Taylor, S., Haynes, C., Harvey, D.: Accumulated lifetimes in single-axis vibration testing. In: Walber, C., Walter, P., Seidlitz, S. (eds.) Sensors and Instrumentation, Aircraft/Aerospace, Energy Harvesting & Dynamic Environments Testing. Conference Proceedings of the Society for Experimental Mechanics Series, vol. 7, pp. 131–146. Springer, Cham (2020)
3. Gregory, D., Fernando, B., Smallwood, D.O.: Comparison of the response of a simple structure to single axis and multiple axis random vibration inputs. In: Presented at the Shock and Vibration Symposium, Orlando, 2008
4. Ling, H., Shichao, F., Yaoqi, F.: Effect of multi-axis versus single-axis vibration test on the dynamic responses of typical spacecraft structure. ISMA Proceedings, 2012, pp. 2383–2392
5. Soine, D.E., Jones, R.J., Harvie, J.M., Skousen, T.J., Schoenherr, T.F.: Designing hardware for the boundary condition round robin challenge. In: Mains, M., Dilworth, B. (eds.) Topics in Modal Analysis & Testing. Conference Proceedings of the Society for Experimental Mechanics Series, vol. 9, pp. 119–126. Springer, Cham (2019)
6. Rohe, D., Schultz, R., Schoenherr, T., Skousen, T., Jones, R.: Comparison of multi-axis testing of the BARC structure with varying boundary conditions. In: Walber, C., Walter, P., Seidlitz, S. (eds.) Sensors and Instrumentation, Aircraft/Aerospace, Energy Harvesting & Dynamic Environments Testing. Proceedings of the 37th IMAC, A Conference and Exposition on Structural Dynamics 2019, vol. 7, pp. 179–193. Springer International Publishing, Cham (2020)
7. Musella, U., et al.: Combining test and simulation to tackle the challenges derived from boundary conditions mismatches in environmental testing. In: Walber, C., Walter, P., Seidlitz, S. (eds.) Sensors and Instrumentation, Aircraft/Aerospace, Energy Harvesting & Dynamic Environments Testing. Conference Proceedings of the Society for Experimental Mechanics Series, vol. 7, pp. 259–269. Springer, Cham (2020)
8. Smith, S.A., Brake, M.R.W.: Effects of multi-axial versus single-axial excitation of jointed systems. In: Walber, C., Walter, P., Seidlitz, S. (eds.) Sensors and Instrumentation, Aircraft/Aerospace, Energy Harvesting & Dynamic Environments Testing. Conference Proceedings of the Society for Experimental Mechanics Series, vol. 7, pp. 45–50. Springer, Cham (2020)
9. Rohe, D.P., et al.: Testing summary for the box assembly with removable component structure. In: Walber, C., Walter, P., Seidlitz, S. (eds.) Sensors and Instrumentation, Aircraft/Aerospace, Energy Harvesting & Dynamic Environments Testing. Proceedings of the 37th IMAC, A Conference and Exposition on Structural Dynamics 2019, vol. 7, pp. 167–177. Springer International Publishing, Cham (2020)
10. Manring, L.H., Mann, B.P., Schultze, J.F.: Modal analysis of the box assembly with removable component in two configurations. In: Epp, D.S. (ed.) Special Topics in Structural Dynamics & Experimental Techniques. Conference Proceedings of the Society for Experimental Mechanics Series, vol. 5, pp. 271–281. Springer, Cham (2021)
11. Budynas, R., Nisbett, J.K.: Shigley's Mechanical Engineering Design, 8th edn. McGraw-Hill Science/Engineering/Math, Singapore (2006)

Chapter 4
Experimental Modal Analysis of a Resonant Plate During a Mid-Field Pyroshock Replication Test

Tyler F. Schoenherr, David E. Soine, and Bryan L. Witt

Abstract Resonant plate and other resonant fixture shock techniques were developed in the 1980s at Sandia National Laboratories as flexible methods to simulate mid-field pyroshock for component qualification. Since that time, many high severity shocks have been specified that take considerable time and expertise to setup and validate. To aid in test setup and to verify the shock test is providing the intended shock loading, it is useful to visualize the resonant motion of the test hardware. Experimental modal analysis is a valuable tool for structural dynamics visualization and model validation. This chapter describes a method to perform experimental modal testing at pyroshock excitation levels, utilizing input forces calculated via the SWAT-TEEM (Sum of Weighted Accelerations Technique—Time Eliminated Elastic Motion) method and the measured acceleration responses. The calculated input force and the measured acceleration data are processed to estimate natural frequencies, damping, and scaled mode shapes of a resonant plate test system. The modal properties estimated from the pyroshock-level test environment are compared to a traditional low-level modal test. The differences between the two modal tests are examined to determine the nonlinearity of the resonant plate test system.

Keywords SWAT · Resonant plate · Modal analysis · Force reconstruction

4.1 Introduction

Testing components or subassemblies in the laboratory is a cheaper and faster alternative to testing an entire system in its field environments. In some instances, performing a field test of the environment is untenable. This is often true of high-level shock environments which a system may experience. One method the test laboratory imparts shock environments onto a system is via a resonant plate apparatus.

Sandia National Laboratories sometimes uses a resonant plate to create a two-sided shock response that is a more representative shock environment than a one-sided pulse. Photographs of a resonant plate test configuration are in Fig. 4.1. This test setup requires that the plate be flexible so its resonance can amplify the motion of the unit under test that is bolted to the plate at a frequency range present in the field environment. This flexibility at resonance allows for uncontrollable, off-axis motion during the test. This is an issue as the current environment specifications dictate that three orthogonal shock inputs are input separately to simulate one environment. Uncontrollable off-axis motion can cause damage in an off-axis direction that would inadvertently accumulate over the three hits.

One solution to produce a more realistic environment is to develop a test that meets shock environments in all directions simultaneously. Executing a single-shot test instead of three separate tests eliminates the desire to suppress off-axis motion and is more representative of the actual environment. Executing one test instead of three also reduces the time in the laboratory, which increases the lab capacity. However, executing a single-shot multi-axis test is difficult because there is little control over the test. The test fires a high-speed projectile to impact the resonant plate. There is little control over the projectile besides the projectile speed, the programmer that the projectile hits to shape the input force, and the size of the projectile.

T. F. Schoenherr (✉) · D. E. Soine · B. L. Witt
Sandia National Laboratories, Albuquerque, NM, USA
e-mail: tfschoe@sandia.gov; desoine@sandia.gov; blwitt@sandia.gov

C. Walber et al. (eds.), *Sensors and Instrumentation, Aircraft/Aerospace and Dynamic Environments Testing, Volume 7*,
Conference Proceedings of the Society for Experimental Mechanics Series, https://doi.org/10.1007/978-3-031-05415-0_4

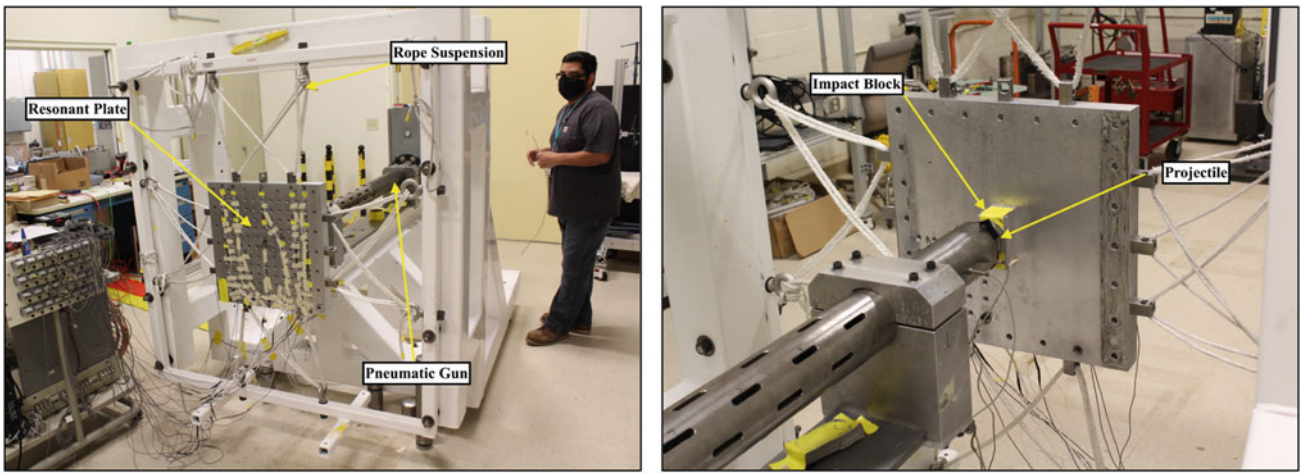

Fig. 4.1 Photographs of the resonant plate test configuration without a test unit attached or damping bars

Due to the limited control the test facility has in modifying the shock input, the success of the multi-axis test is contingent on the pre-test design using a finite-element model. Characterization and designs of multi-axis shock have been previously explored [6, 7, 9]. These efforts place high focus on the response of the base of the unit under test and the unit under test itself. These efforts also explore moving both the unit under test and the impact location as possible means for designing a multi-axis test. Through these past efforts, it is clear that the use of a finite-element model is critical in designing a test for a given multi-axis environment. Guessing on the test setup parameters in the lab is untenable due to the amount of time it takes to gather data on one test setup, assess the results, and formulate feedback to modify the resonant plate test setup.

Even with the use of a finite-element model, information about the input force to the resonant plate must be known in order to produce a meaningful model response. Direct measurements are infeasible at such high force levels and short durations due to hardware limitations of load sensors. In the absence of a direct measurement of the input force, inverse methods are used to calculate the force that causes the measured accelerations. This is also a challenge as traditional inverse methods are susceptible to slight nonlinearities in the structure. Nonlinearities are expected in the structure due to the bolting of the aluminum damping bars to the outer edge of the resonant plate. To further increase damping, a thin sheet of rubber is sandwiched between the damping bars and the resonant plate, all of which increases the nonlinearity of the system. These damping bars are added to make the test system damping closer to the fielded system. Another method to calculate the force is to use explicit models to determine these forces; however, modeling of the contact and programmer is difficult [4].

In order to determine the forces from the resonant plate tests, this body of work uses a spatial inverse method known as the Sum of Weighted Accelerations Technique—Time Eliminated Elastic Motions (SWAT-TEEM) [8]. This inverse method inverts spatial quantities (i.e., mode shapes) to calculate the causal force. Using mode shapes provides a buffer against most nonlinearities as mode shapes are not as sensitive to system nonlinearities as natural frequency and damping. Furthermore, the SWAT-TEEM technique uses shapes acquired from the test that reduces errors in the basis shapes.

This chapter details the force reconstruction process during the resonant plate environment. This chapter then uses the forcing function in conjunction with the acceleration measurements to calculate modal parameters of the test hardware at shock levels. These modal parameters calculated at shock input levels are compared to the experimental modal results obtained at low input levels to determine the linearity of the system and to show if modal superposition theory is acceptable for resonant plate shock tests.

4.2 Theory and Background

This chapter uses modal analysis theory and the force reconstruction algorithm known as the Sum of Weighted Acceleration Technique—Time Eliminated Elastic Motion (SWAT-TEEM) in order to compute the modal parameters of the resonant plate system. This section explains these topics in some detail to aid in digesting the analysis performed in this report, but the overview is not meant to be an exhaustive overview of the topics.

4.2.1 Modal Analysis

Modal analysis has been studied extensively, and entire books have been written to aid in its understanding and application [1, 3, 5]. This section covers modal analysis at a high level so that the reader can understand its importance and how the system's modal parameters are extracted from the data acquired.

Modal analysis theory is first examined by producing the equations of motion of a generic structure. A structure's motion can be estimated by the 2nd-order linear equations of motion

$$\mathbf{M}\ddot{\bar{x}} + \mathbf{C}\dot{\bar{x}} + \mathbf{K}\bar{x} = \bar{F}, \tag{4.1}$$

where $\mathbf{M}$ is the mass matrix, $\mathbf{C}$ is the damping matrix, and $\mathbf{K}$ is the stiffness matrix of the system. The displacement of the structure can be described in the frequency domain and reorganized as

$$\frac{\ddot{\bar{x}}(j\omega)}{\bar{F}(j\omega)} = -\omega^2[-\omega^2\mathbf{M} + j\omega\mathbf{C} + \mathbf{K}]^{-1}, \tag{4.2}$$

where j is the imaginary number. This form of the equations of motion is informative because it explicitly provides an input/output relationship between the displacement and the forcing function that caused the motion through a transfer function. This transfer function is specifically called a frequency response function (FRF). Although the mass, damping, stiffness matrices of the finite-element model can be calculated, these properties cannot be directly measured on a structure.

In order to be able to calculate and compare FRFs between the finite-element model and the physical structure, an eigen analysis is performed on the structure. The eigen analysis in the finite-element model calculates the eigenvalues and eigenvectors. The eigenvectors are calculated from the mass and stiffness matrices and are referred to in structural dynamics as the mode shapes. These shapes are related to the displacement of the structure through a linear combination shown as

$$x_i \approx \sum_{m=1}^{n} \boldsymbol{\phi}_{im} q_m, \tag{4.3}$$

where $\boldsymbol{\phi}_{im}$ is the mth mode shape of the structure at degree of freedom i and q_m is the modal coordinate corresponding to the participation of that mode shape in the displacement of the structure. The substitution shown in Eq. 4.3 is linear; however, it has been shown to be valid for systems with slight nonlinearities stemming from frictional contacts [2]. The modal substitution decouples the equations of motion shown in Eqs. 4.1 and 4.2. As a result, FRFs can be calculated for both the finite-element model and the experimental data. These FRFs in the modal domain are written as

$$\frac{\ddot{x}_i(j\omega)}{F_k(j\omega)} \approx \sum_{m=1}^{n_{\text{mode}}} \frac{-\omega^2 \boldsymbol{\phi}_{im}\boldsymbol{\phi}_{km}}{-\omega^2 + 2j\omega\omega_m\boldsymbol{\zeta}_m + \omega_m^2}, \tag{4.4}$$

where ω_m is the mth natural frequency of the structure and ζ_m is the modal damping corresponding to the mth mode. This expression of the FRF matrix is computed element by element of the ith response degree of freedom with respect to an input at the kth degree of freedom. With the physical structure, a directly measured force and directly measured accelerations are obtained in order to calculate parts of the FRF matrix over the frequency range for which there is adequate excitation. The modal parameters of the structure are fit to the experimental FRFs using any number of methods.

In summary, modal analysis or eigen analysis is a method of transforming the data into a domain that allows for the comparison of finite-element models and physical structures. Although the modal parameters are calculated from the finite-element model, the experimental modal parameters need to be fit to the experimental FRFs.

4.2.2 Formulation of SWAT-TEEM

The derivation of the SWAT-TEEM algorithm that is used to calculate the sum of the external forces begins with the 2nd-order linear equations of motion shown in Eq. 4.1. The modal approximation shown in Eq. 4.3 is substituted into Eq. 4.1 to get

$$\mathbf{M}\boldsymbol{\phi}\ddot{\bar{q}} + \mathbf{C}\boldsymbol{\phi}\dot{\bar{q}} + \mathbf{K}\boldsymbol{\phi}\bar{q} = \bar{F}. \tag{4.5}$$

At this point, Eq. 4.5 is premultiplied by the transpose of the rigid body modes, $\boldsymbol{\phi}_r^T$, to get

$$\boldsymbol{\phi}_r^T\mathbf{M}\boldsymbol{\phi}\ddot{\bar{q}} + \boldsymbol{\phi}_r^T\mathbf{C}\boldsymbol{\phi}\dot{\bar{q}} + \boldsymbol{\phi}_r^T\mathbf{K}\boldsymbol{\phi}\bar{q} = \boldsymbol{\phi}_r^T\bar{F}. \tag{4.6}$$

Because there is no internal damping or internal stiffness forces for the rigid body degrees of freedom, Eq. 4.6 simplifies to

$$\boldsymbol{\phi}_r^T\mathbf{M}\boldsymbol{\phi}\ddot{\bar{q}} = \boldsymbol{\phi}_r^T\bar{F} \tag{4.7}$$

due to

$$\boldsymbol{\phi}_r^T\mathbf{C} = 0 \;\&\; \boldsymbol{\phi}_r^T\mathbf{K} = 0. \tag{4.8}$$

The physical degrees of freedom are substituted for the modal degrees of freedom using the relationship in Eq. 4.3 into Eq. 4.7 to get

$$\boldsymbol{\phi}_r^T\mathbf{M}\ddot{\bar{x}} = \boldsymbol{\phi}_r^T\bar{F}. \tag{4.9}$$

At this point, a weighting matrix, $\boldsymbol{w}$, is defined as

$$\boldsymbol{w}^T = \boldsymbol{\phi}_r^T\mathbf{M} \tag{4.10}$$

and substituted into Eq. 4.9 to obtain

$$\boldsymbol{w}^T\ddot{\bar{x}} = \boldsymbol{\phi}_r^T\bar{F}. \tag{4.11}$$

To solve for the weighting vector, an assumption of the input force is made. In the case where the structure is impacted by an external force and then in a free state, there are no external forces after impact, and the accelerations of the system, $\ddot{\bar{x}}_{fd}$, are assumed to decay exponential and Eq. 4.11 after the impact simplifies to

$$\boldsymbol{w}^T\ddot{\bar{x}}_{fd} = 0. \tag{4.12}$$

To obtain a non-trivial solution, information about the rigid body modes needs to be included because they were not present in the free decayed response. The rigid body constraint is formed by post-multiplying Eq. 4.10 by the rigid body shapes to get

$$\boldsymbol{w}^T\boldsymbol{\phi}_r = \boldsymbol{\phi}_r^T\mathbf{M}\boldsymbol{\phi}_r, \tag{4.13}$$

which can be simplified to

$$\boldsymbol{w}^T\boldsymbol{\phi}_r = M_r, \tag{4.14}$$

where M_r is the modal mass of the rigid body modes. Equation 4.14 is added to Eq. 4.12 to get

$$\boldsymbol{w}^T\left[\boldsymbol{\phi}_r\ \ddot{\bar{x}}_{fd}\right] = \left[M_r\ 0\right]. \tag{4.15}$$

Equation 4.15 is solved for $\boldsymbol{w}^T$ and substituted back into Eq. 4.11 to solve for the sum of external forces acting on the center of gravity written as

$$\left[M_r\ 0\right]\left[\boldsymbol{\phi}_r\ \ddot{\bar{x}}_{fd}\right]^+ \ddot{\bar{x}} = \boldsymbol{\phi}_r^T \bar{F}. \tag{4.16}$$

Equation 4.15 is solved for the six weighting vectors, $\boldsymbol{w}^T$ in a constrained least squares problem with the rigid body shapes being the constraint. Because the pseudo-inverse includes the time-domain response of the system that is a linear combination of the mode shapes, the mode shapes of the system do not need to be separately calculated as it does with the SWAT algorithm.

4.3 Modal Analysis of the Resonant Plate Test

A series of resonant plate tests were executed on the resonant plate with damping bars. The tests consist of different configurations of the test environment varying the projectile size, pressure of the pneumatic gun used to fire the projectile, and the thickness of the felt programmer. Each test configuration was repeated at least 4 times with nominally the same parameters. Each configuration is referred to as a set of runs. Each set of runs tested can be seen in Table 4.1.

The forces for each test run are estimated using the SWAT-TEEM method. The reconstructed force from run 56 is in Fig. 4.2. From the environment, it is expected that the forcing function will look like a single-sided pulse that starts and ends at zero. The force from run 56 is exactly that, however, there are some transient "forces" after the main pulse. Knowing that the projectile disengages, it is known that the "force" after 0.3 ms is erroneous and an artifact of not filtering the acceleration through the SWAT-TEEM process.

Knowledge of the shape of the input force is a means in determining the fidelity of the force reconstruction. Another means to test the integrity of the force reconstruction uses the conservation of momentum shown as

$$mv_0 + \int_{t_1}^{t_2} F(t)dt = mv_f, \tag{4.17}$$

where m is the mass of the resonant plate system, v is the velocity of the resonant plate at the initial, o, and final, f, moments, and $F(t)$ is the imparted force calculated by SWAT-TEEM. Because the initial velocity of the plate is zero for each of the runs, the final velocity of the plate could be calculated by dividing the impulse of the force by the mass of the plate.

The conservation of momentum is calculated for run 32 with the force passed through a 6 kHz low-pass filter. The velocity is calculated by integrating the measured accelerations. Although there is a spread of velocities of the integrated

Table 4.1 Table of the run sets and associated test parameters

Run set name	Test runs	Pressure (psi)	Felt Thk (in)	Projectile length (in)	Average projectile speed (ft/s)
Set 14	[14:17]	10	1/8" Gray	6"	21.5
Set 21	[21:27]	14	1/8" Gray	6"	28.1
Set 28	[28:31]	10	1/8" Gray	6"	21.3
Set 32	[32:35]	10	1/2" Gray	6"	21.4
Set 36	[36:39]	20	1/2" Gray	6"	35.7
Set 41	[41:47]	20	1" Gray	6"	36.0
Set 48	[48:51]	40	1" Gray	6"	53.5
Set 54	[54:57]	50	1" Gray	6"	59.8
Set 58	[58:61]	20	1" Gray	12"	23.9
Set 62	[62:65]	40	1" Gray	12"	37.1
Set 66	[66:68]	60	1" Gray	12"	46.1
Set 69	[69:72]	15	1/2" Gray	12"	19.5
Set 73	[73:76]	25	1/2" Gray	12"	27.8
Set 78	[78:81]	35	1/2" Gray	12"	34.1
Set 82	[82:85]	15	1/8" Gray	12"	19.1
Set 86	[86:91]	25	1/8" Gray	12"	27.5

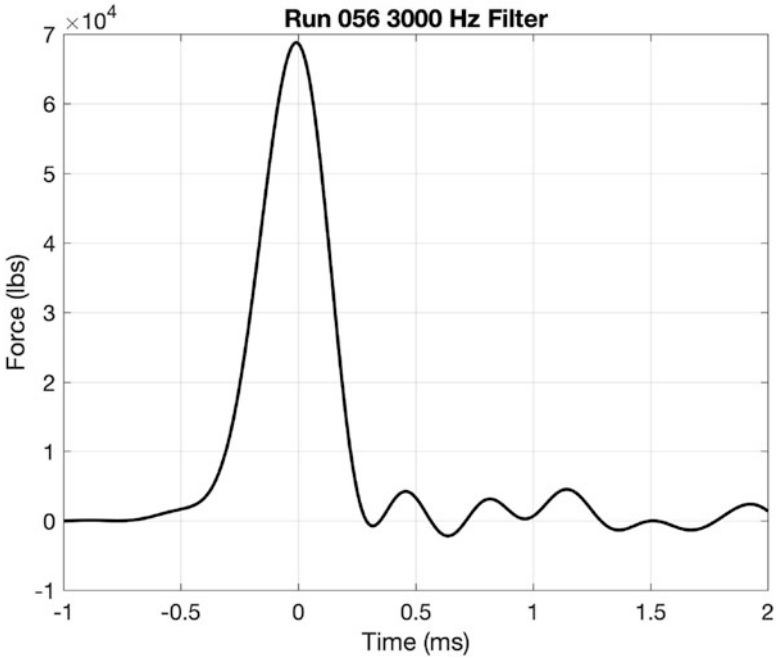

Fig. 4.2 The reconstructed force from run 56 using the SWAT-TEEM algorithm and a 3 kHz low-pass filter

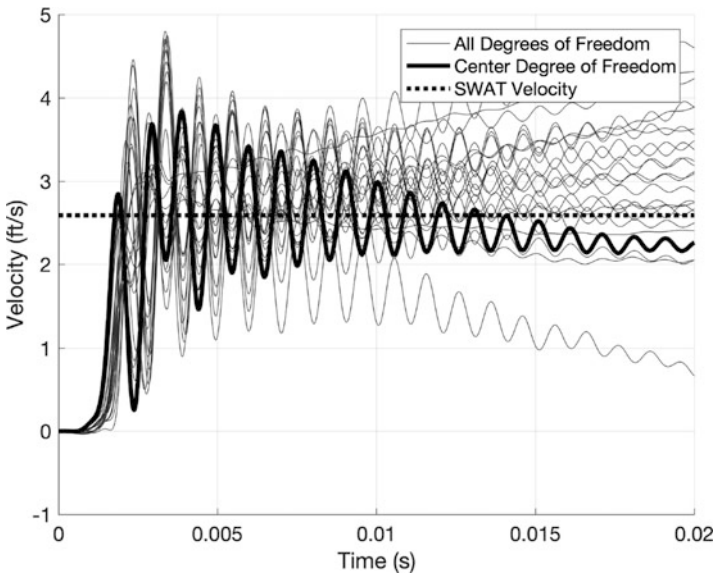

Fig. 4.3 Integrated velocities from acceleration responses in run 32 with the velocity at the center of the plate bolded

accelerometers due to rigid rotations and drift, the velocity calculated through the conservation of momentum is compared to the integrated measured accelerations. This integration of the measured accelerations is shown in Fig. 4.3. The velocity of the plate calculated through the conservation of momentum is approximately the average of the integrated accelerations.

All of the forces calculated for the runs in Table 4.1 are transformed into the frequency domain for examination. Examination in the frequency domain allows for direct comparison between the different test parameters and to determine at which frequency bandwidths contain the majority of the energy. This concatenation of forces in the frequency domain can be seen in Fig. 4.4.

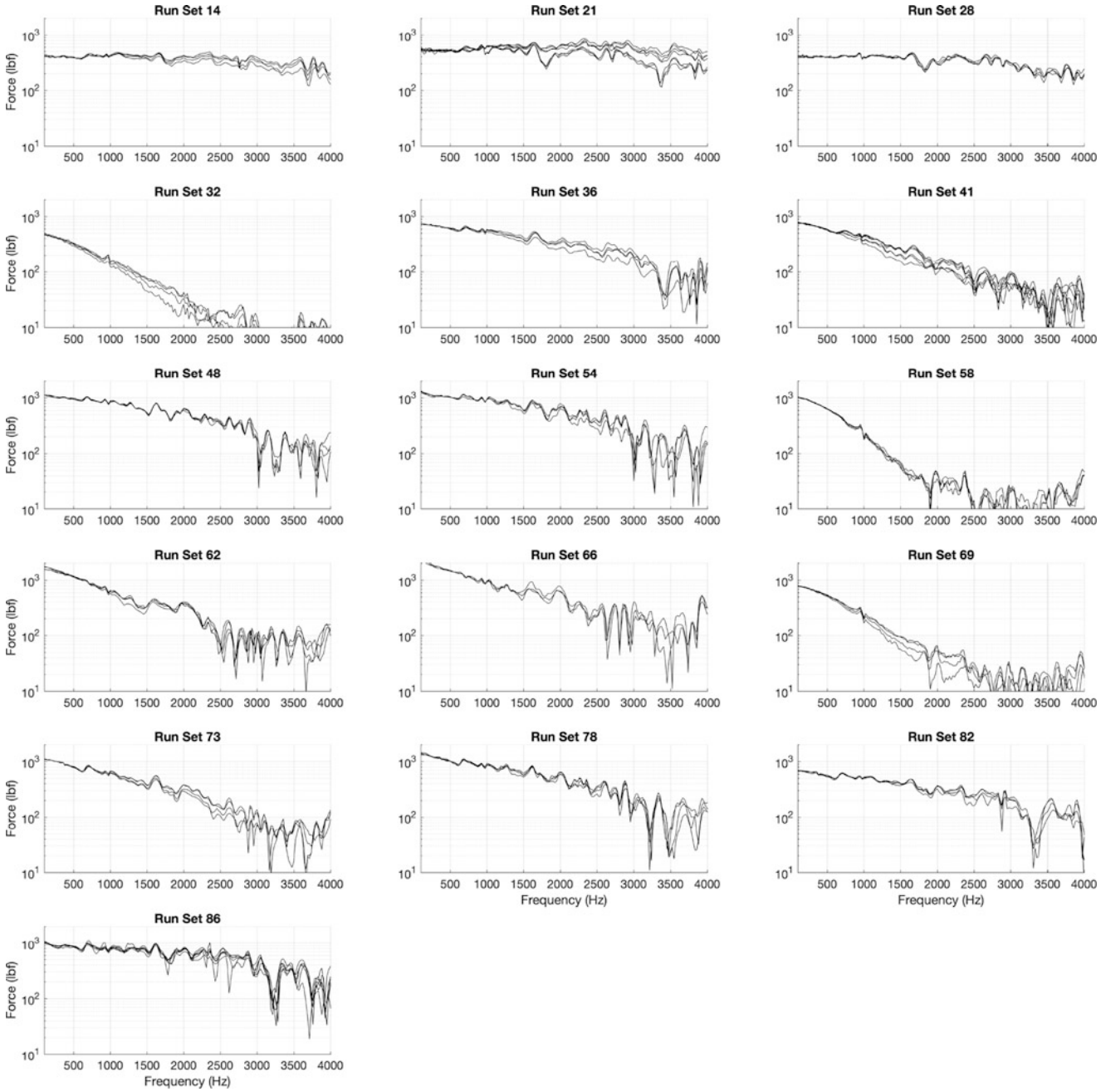

Fig. 4.4 Forces in the frequency domain of all the test runs on the bare resonant plate with damping bars

Conclusions from examining the forces calculated are that the forces are relatively consistent when using the same test parameters: gun pressure, projectile size, and felt thickness. Increasing the felt thickness does not significantly change the energy imparted by the projectile. When the felt thickness increases, the length of the pulse increases, which reduces the high frequency force and increases the force at low frequencies.

Increasing the gun pressure and consequentially the projectile speed increases the energy of the impact and also reduces the pulse width of the impact. This provides an increase in force over all frequencies. However, that increase in force is not uniform over the frequency domain.

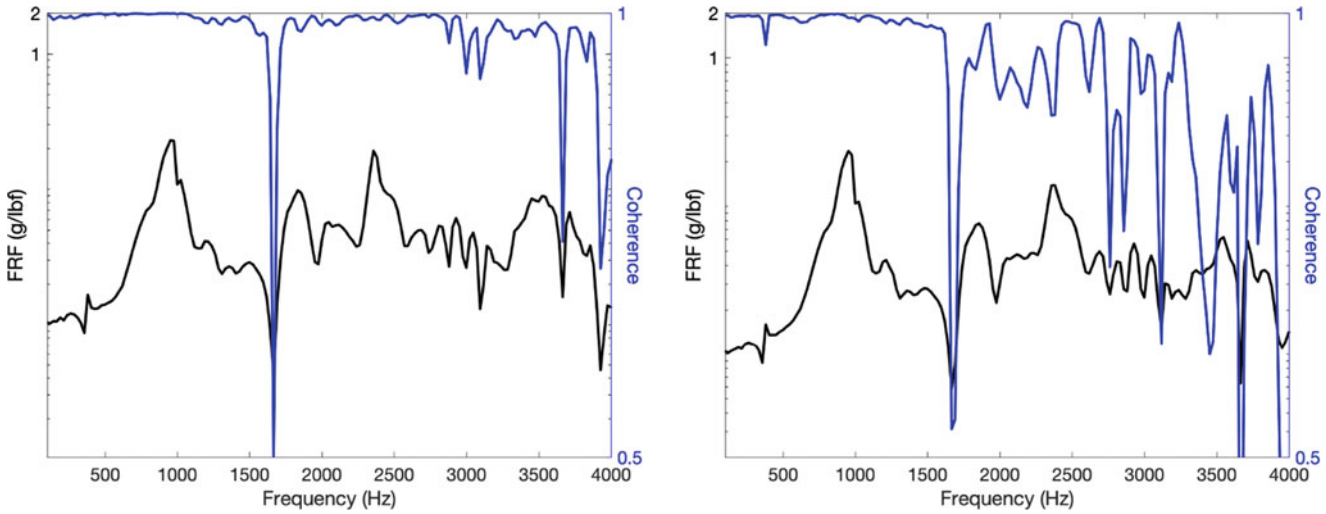

Fig. 4.5 FRFs and coherence from the same set of test parameters (left), and from a low- and high-level impact (right)

The last test parameter is the projectile size or weight. An increase in projectile weight provides a proportional increase in energy to the resonant plate. Another effect of increasing the weight of the projectile is a change in the pulse width of the force. This increases the forces for lower frequencies and reduces the force at higher frequencies.

With the force calculated at a known location, the acceleration data can be combined with the forcing function to calculate frequency response functions (FRFs). From the FRFs, coherence of the averaged runs and modal parameters are calculated. Coherence and the FRF with respect to one degree of freedom are shown in Fig. 4.5. The left plot in Fig. 4.5 shows the FRF and coherence from averaging four resonant plate test runs of the same test parameters. The figure shows high coherence, greater than 0.9, for frequencies less than 4000 Hz except at frequencies of anti-resonances.

The right plot of Fig. 4.5 averages four test runs of a low-level hit with four test runs of a high-level hit. The coherence is worse when compared to the coherence of data all at the same level, but it stays above 0.9 when less than 2500 Hz. This shows that although the system is not linear over different forcing levels, the nonlinearities are not significant enough to void modal superposition.

Modal parameters are fit to two discrete sets of data. One set is of low-level impact data, and the other is of high-level impact data. Six modes from the shock test are compared to the same modes acquired from traditional low-level experimental modal analysis testing. The forces from the low-level modal test are about two orders of magnitude lower in peak force from the shock test. The mode shapes of the test display are difficult to interpret visually. Finite-element mode shapes with high Modal Assurance Criteria (MAC) values to the test shapes are in Figs. 4.6 and 4.7. The frequency and damping comparisons of these modes are in Table 4.2. The table shows that there are some shifts in frequencies and damping of the different modes and that all modes are not affected the same with respect to the input load levels. This conclusion is expected, but predicting the shifts in frequency and damping is very difficult or impossible without data.

There are some difficulties in fitting the modal parameters from shock data. With the short-time histories of the test, the frequency spacing in the FRFs is very high, about 24 Hz. This leads to the modal parameters being sensitive to small changes in the FRFs. The resynthesized Complex Mode Indicator Functions (CMIFs) of the low force input and high force input are in Figs. 4.8 and 4.9, respectively. The resynthesis of the CMIF shows that the modes that are excited well are fit well to the test data. The resynthesized CMIFs also show that there are some modes indicated that are not fit well. Only modes fit with high confidence are included in the comparison shown in Table 4.2.

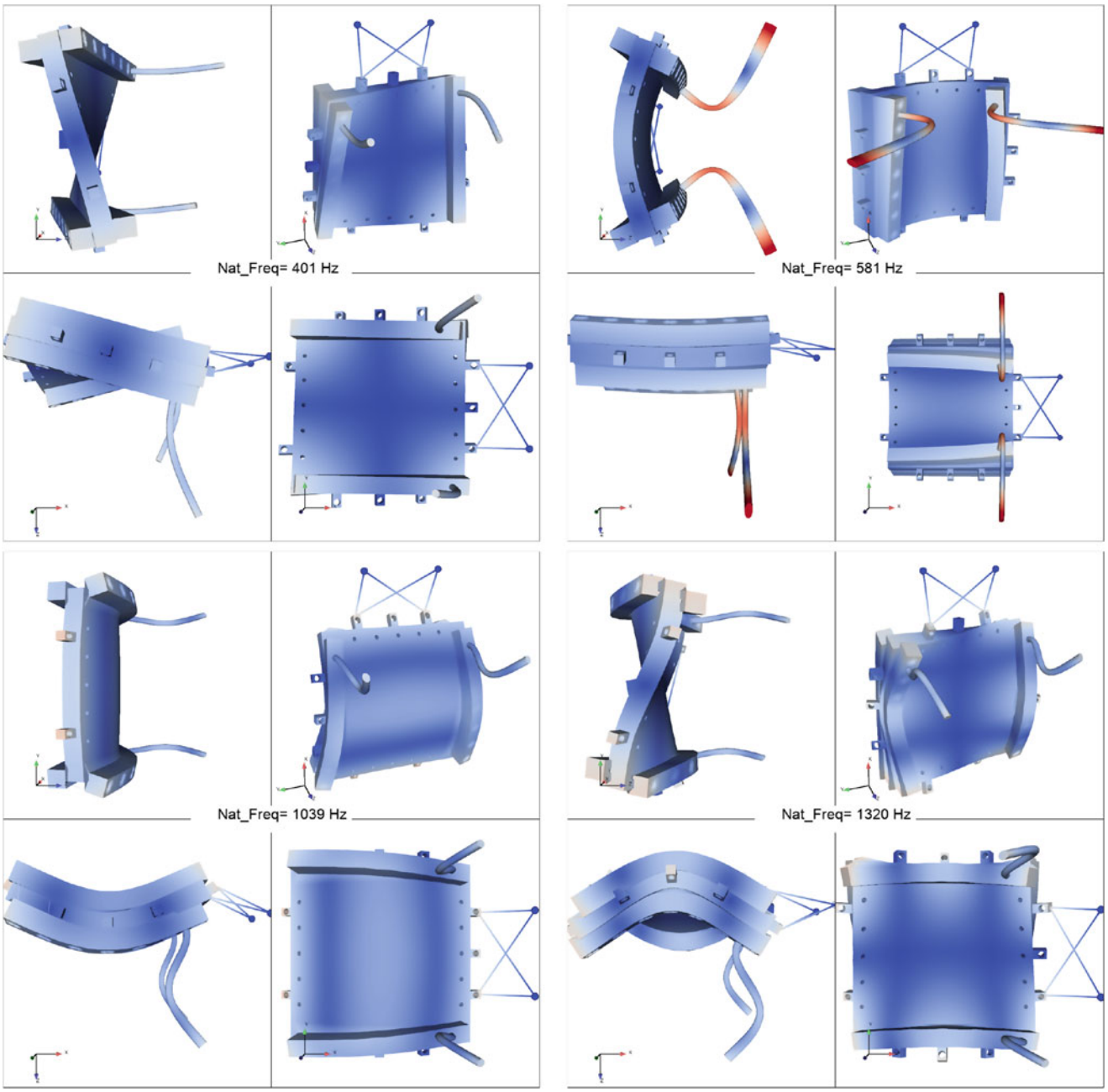

Fig. 4.6 Mode shapes generated from a finite-element model of test modes 1 (upper left), 2 (upper right), 3 (lower left), and 4 (lower right)

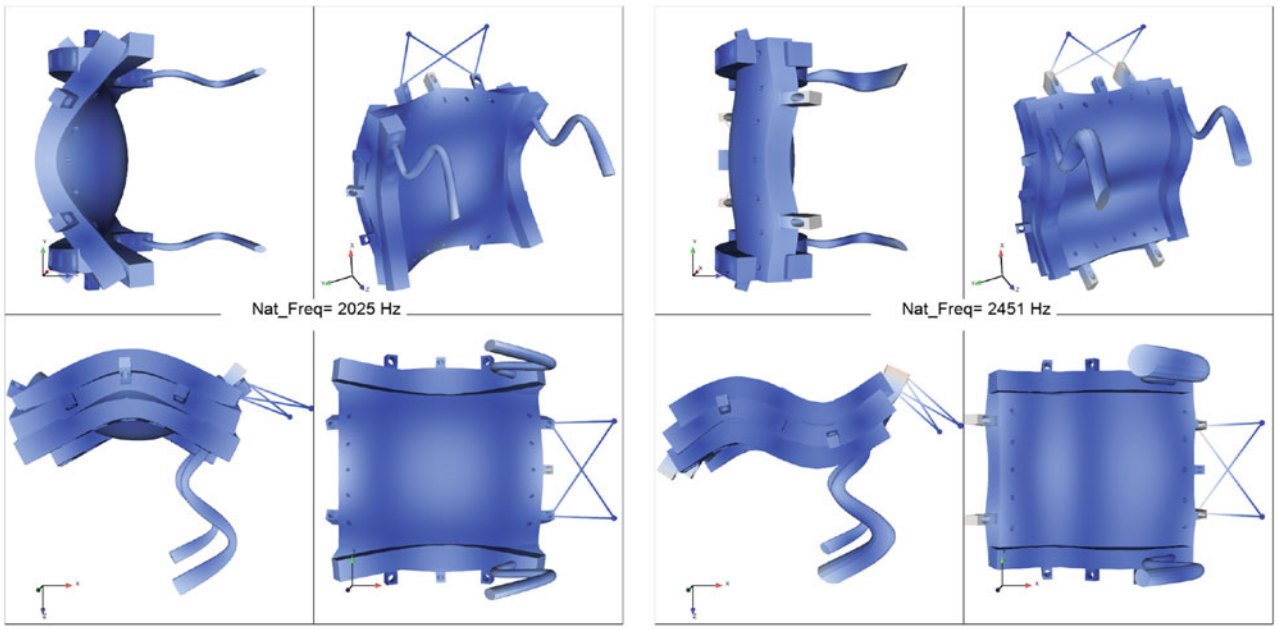

Fig. 4.7 Mode shapes generated from a finite-element model of test modes 5 (left) and 6 (right)

Table 4.2 Comparison of modal damping levels from experimental modal tests and resonant plate shock tests. NF = Mode Not Found

Mode number	Exp modal test nat freq (damping)	Low-level shock nat freq (damping)	High-level shock nat freq (damping)
Mode 1 frequency	391 Hz (0.35%)	379 Hz (0.41%)	383 Hz (0.40%)
Mode 2 frequency	582 Hz (1.4%)	697 Hz (9.6%)	656 Hz (6.9%)
Mode 3 frequency	1001 Hz (2.6%)	953 Hz (5.1%)	952 Hz (3.9%)
Mode 4 frequency	1288 Hz (2.5%)	1167 Hz (4.5%)	NF
Mode 5 frequency	2087 Hz (1.0%)	1822 Hz (4.0%)	NF
Mode 6 frequency	2397 Hz (0.93%)	2359 Hz (1.2%)	NF

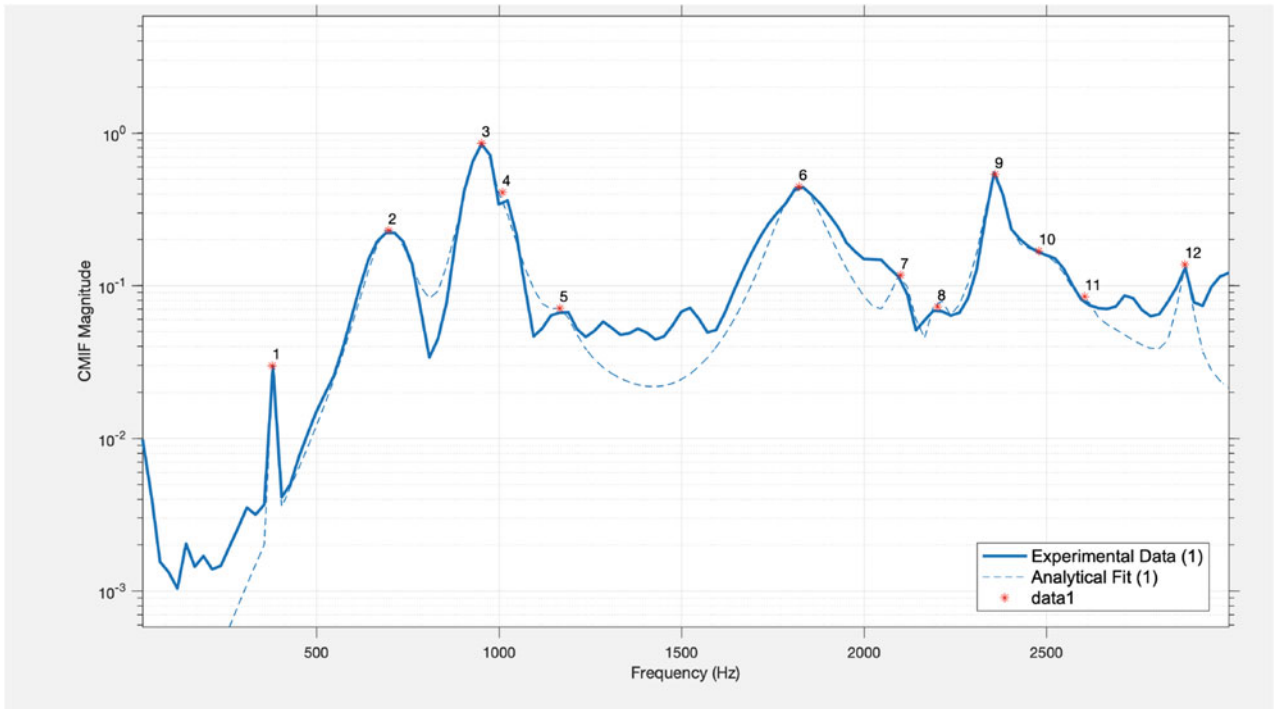

Fig. 4.8 CMIF and resynthesized CMIF of the low-level shock data

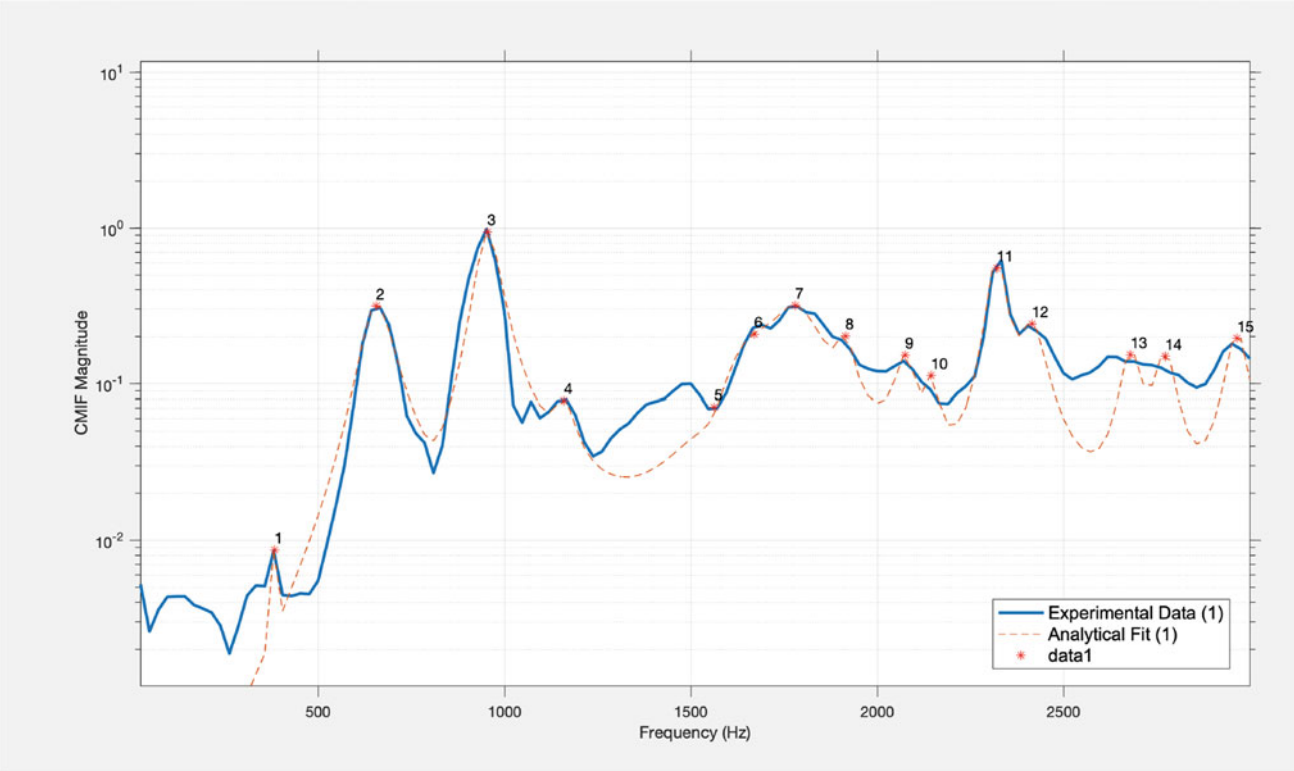

Fig. 4.9 CMIF and resynthesized CMIF of the high-level shock data

4.4 Conclusion

This chapter demonstrates the process of executing the SWAT-TEEM algorithm on a resonant plate test and that the force calculated from a test can be used to generate FRFs of sufficient quality to fit modal parameters. Having quality FRFs provides insight in the linearity, the natural frequencies, the damping, and the shapes of the test setup. This chapter compares the modal parameters acquired at experimental modal levels, low-level shocks, and high-level shocks to demonstrate that the resonant plate has varying degrees of nonlinearities per mode. The results show that there are physics present in the system that prevents the system from behaving linearly with respect to input force. The nonlinearities present, however, do not prevent the use of a linearized model that is calibrated to the dynamics present at shock type input loads.

Acknowledgments Sandia National Laboratories is a multi-mission laboratory managed and operated by National Technology and Engineering Solutions of Sandia, LLC., a wholly owned subsidiary of Honeywell International, Inc., for the U.S. Department of Energy's National Nuclear Security Administration under contract DE- NA-0003525.

References

1. Avitabile, P.: Modal Testing: A Practitioner's Guide. Wiley, Hoboken (2017)
2. Eriten, M., Kurt, M., Luo, G., McFarland, D.M., Bergman, L.A., Vakakis, A.F.: Nonlinear system identification of frictional effects in a beam with a bolted joint connection. Mech. Syst. Signal Process. **39**(1–2), 245–264 (2013)
3. Ewins, D.J.: Modal Testing: Theory, Practice and Application. Wiley, Hoboken (2009)
4. Ferri, B.A., Hopkins, R.N.: A Method for Determining Impact Force for Single and Tri Axis Resonant Plate Shock Simulations, pp. 65–71. Springer, Berlin (2020)
5. Heylen, W., Lammens, S., Sas, P., et al.: Modal Analysis Theory and Testing, vol. 200. Katholieke Universiteit Leuven, Leuven, Belgium (1997)

6. Hopkins, R.N., Sisemore, C.L.: Design of a resonant plate shock test for simultaneous multi-axis excitation. Report SAND2019-0777C, Sandia National Lab. (SNL-NM), Albuquerque, NM (United States) (2019)
7. Jacobson, E.M.: Using Frequency Based Substructuring to Optimize Multi-Axis Resonant Plate Shock Tests. Thesis (2019)
8. Schoenherr, T.F.: Calculating the impact force of supersonic hail stones using SWAT-TEEM. In: Shock & Vibration, Aircraft/Aerospace, and Energy Harvesting, vol. 9, pp. 67–79. Springer, Berlin (2015)
9. Sisemore, C., Babuska, V., Flores, R.: Multi-axis resonant plate shock testing evaluation and test specification development. Report SAND2020-10224, Sandia National Lab. (SNL-NM), Albuquerque, NM (United States) (2020)

Chapter 5
A Parameter Study of the Matrix Power Control Algorithm

Levi H. Manring, Brian P. Mann, and John F. Schultze

Abstract Environmental testing is very useful for qualifying components for their real-world use. To that end, random vibration testing is performed on component(s) in the laboratory in such a way as to mimic their real-world environment. This is particularly useful when testing a component in its real-world environment is time-consuming or costly. To accurately control, a random vibration test is not a simple challenge to meet, with issues arising such as lightly damped modes, signal noise, poorly conditioned frequency response functions (FRFs), and others. This chapter presents a parameter study on the performance of a random vibration control method called the Matrix Power Control Algorithm (MPCA). Additionally, this chapter shows that a simple modification to MPCA can result in improved stability and convergence. In particular, a proportional gain controller is used to change the control parameter for MPCA as a function of the error. Two simulation environments are used in this chapter: a single-input single-output (SISO) fixed-free cantilever beam with base excitation and a multiple-input multiple-output (MIMO) fixed–fixed beam with base excitation at both ends of the beam. Additionally, the Box Assembly with a Removeable Component (BARC) was used as a laboratory example illustrating the performance of MPCA and our modification in the laboratory.

Keywords Random vibration · Control · Matrix power · Convergence

5.1 Introduction

Random vibration testing is used to qualify components for their in-situ environment. This type of environmental testing is useful when real-world testing is costly or time-consuming, which is often the case. Random vibration testing is typically performed in a laboratory using an electrodynamic shaker(s) to excite the component in such a way as to mimic the vibration environment the component would experience during its real-use application. Sometimes multiple shakers are used to excite in different axes, as in MIMO testing. The usual target objective in SISO random vibration testing is to control the acceleration power-spectral density (PSD) at a desired location on the component. In the case of MIMO testing, the target objective is a power-spectral-density matrix (called the reference matrix) that includes the desired auto-spectra at the control locations on the diagonal of the matrix and the cross-spectra between outputs on the off-diagonal elements.

Achieving the target objective requires a control algorithm that uses the error between the reference matrix and the measured result and computes a modified control output to the shaker in such a way that convergence is achieved. One of the first control algorithms to achieve this is the Difference Control Algorithm (DCA) presented by Smallwood in reference [1]. However, this method has some numerical issues, such as scaling and potentially large control correction that can result in divergence. MPCA was introduced in reference [2], where the authors discuss their proposed algorithm in contrast to previous vibration control methods, such as DCA. In their paper, they demonstrate that MPCA has the ability to control both the cross-spectra and the auto-spectra of the reference matrix and achieve stable convergence. Additionally, MPCA relies on a single control parameter that can be used to tune the performance of the algorithm.

L. H. Manring (✉) · B. P. Mann
Department of Mechanical Engineering and Materials Science, Pratt School of Engineering, Durham, NC, USA
e-mail: levi.manring@duke.edu; brian.mann@duke.edu

J. F. Schultze
Los Alamos National Laboratory, Weapons Test Engineering E-14, MS C932, Los Alamos, NM, USA
e-mail: schultze@lanl.gov

C. Walber et al. (eds.), *Sensors and Instrumentation, Aircraft/Aerospace and Dynamic Environments Testing, Volume 7*,
Conference Proceedings of the Society for Experimental Mechanics Series, https://doi.org/10.1007/978-3-031-05415-0_5

Since the introduction of MPCA, some modifications have been made to the algorithm to add features or improve its performance. In particular, in reference [3], a method for controlling a non-Gaussian MIMO test was presented, which was used in parallel with MPCA to control both the auto-spectra of the reference matrix and the kurtosis of the response signals. The authors made a further modification in reference [4], where they included the ability to control cross-spectra of the reference matrix as well. In reference [5], the authors built on references [3, 4] and presented a method to control skewness, kurtoses, and power-spectral densities. The authors in reference [6] demonstrated non-stationary non-Gaussian random vibration control, where the power spectra were stationary and the root-mean-square and kurtosis distributions were moving. A Tikhonov filter was employed in reference [7] to improve control when the FRF matrix was poorly conditioned. The authors in [8] presented a modification to random vibration control that involved defining the reference matrix in such a way as to reduce the amount of drive power needed by the shaker to achieve the objective. For examples of progress in the field of random vibration control, an older summary was written by Smallwood in reference [9] and a more recent one by Underwood in reference [10].

While researchers have studied interesting problems in the area of random vibration control, particularly with regard to modifications or improvements to MPCA, there are no studies of the convergence of this control algorithm. This chapter will study how the control parameter for MPCA affects its convergence and propose a proportional control modification to improve convergence. In the following sections, this chapter will include a brief explanation of MPCA, provide random vibration simulation results from two different beam models (SISO and MIMO), and then provide some random vibration experimental results from using the BARC structure in a SISO configuration.

5.2 Explanation of MPCA

To achieve random vibration control using MPCA, the reference matrix, $\mathbf{R}_{YY}$, must first be defined. In practical terms, for n controlled outputs, $\mathbf{R}_{YY}$ is a $n \times n$ matrix with the desired auto-spectra on the diagonal and cross-spectra between outputs on the off-diagonal. This matrix $\mathbf{R}_{YY}(f)$ is defined as a function of frequency f. Once the reference matrix is defined, the desired $\mathbf{L}$, $\mathbf{L}_d$, can be obtained by means of the Cholesky decomposition:

$$\mathbf{R}_{YY} = \mathbf{L}_d \mathbf{L}_d^H \ . \tag{5.1}$$

The drive spectrum to control the shaker(s) and obtain the desired response at the control location(s) is

$$\mathbf{X}_k = \mathbf{H}^{-1} \mathbf{L}_k \mathbf{P}_k \ , \tag{5.2}$$

where k is the control loop iteration, $\mathbf{X}_k$ is the kth drive spectra, $\mathbf{H}$ is the FRF matrix between the control to the shaker and the controlled output measurements, $\mathbf{L}_k$ is the adjusted $\mathbf{L}$, and $\mathbf{P}_k$ is a randomized phase matrix. For the first control loop iteration, $\mathbf{L}_k = \mathbf{L}_d$. The response matrix is then measured for the kth control iteration, $\mathbf{S}_{YY_k}$. Ideally, the desired and measured spectra matrices would be identical, $\mathbf{R}_{YY} = \mathbf{S}_{YY_k}$. However, they are not due to inaccuracy from measuring the FRF matrix and from noise in the drive and measurement. The measured $\mathbf{L}$, $\mathbf{L}_{s_k}$, can be obtained by the Cholesky decomposition of the measured spectra matrix:

$$\mathbf{S}_{YYk} = \mathbf{L}_{s_k} \mathbf{L}_{s_k}^H \ . \tag{5.3}$$

The error at the kth control iteration, $\mathbf{E}_k$, is calculated in Eq. (5.4), and the updated $\mathbf{L}$, $\mathbf{L}_{k+1}$, is shown in Eq. (5.5).

$$\mathbf{E}_k = \mathbf{L}_d \mathbf{L}_{s_k}^{-1} \tag{5.4}$$

$$\mathbf{L}_{k+1} = \mathbf{E}_k^{\epsilon} \mathbf{L}_k \qquad 0 < \epsilon \leqslant 1. \tag{5.5}$$

It should be noted that for MPCA, there is a single tunable parameter, ϵ, which affects the rate of convergence of the algorithm. This chapter will consider the effect of this parameter on the rate of convergence of the control algorithm. A complete diagram of MPCA can be seen in Fig. 5.1.

In Fig. 5.1, the loop begins with two inputs—the reference matrix and the FRF estimate for the system. The FRF matrix is then inverted, and the Cholesky decomposition of the reference matrix is calculated. The initial $\mathbf{L}$ is $\mathbf{L}_d$, from which the drive spectrum is calculated using Eq. (5.2). This drive spectrum is then converted into the time domain using a time-domain

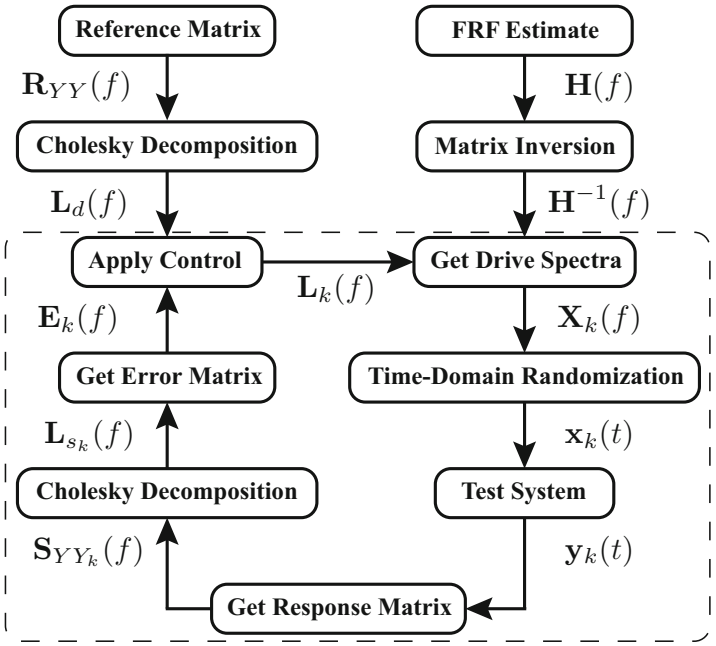

Fig. 5.1 Diagram showing the inputs and steps needed for the MPCA control loop (indicated by the dashed line)

randomization process outlined in reference [1]. The time domain drive, $\mathbf{x}(t)$, is then output to the shaker, and the output from the control location, $\mathbf{y}(t)$, is measured. From $\mathbf{y}(t)$, the response matrix $\mathbf{S}_{YY_k}$ is calculated, and the Cholesky decomposition is taken to obtain the measured $\mathbf{L}$, $\mathbf{L}_{s_k}$. Then the error is calculated between the reference and measured spectra matrices using Eq. (5.4), and the updated $\mathbf{L}$, $\mathbf{L}_{k+1}$, is calculated using Eq. (5.5). The dashed portion of Fig. 5.1 highlights the control loop of the algorithm, which continues until the test is complete. In Fig. 5.1, the designation of frequency domain f, or time domain t, is used to clarity.

The convergence of this algorithm is important. The measured spectrum, $\mathbf{S}_{YY_k}$, is the average of the measured power-spectral-density matrix. If in the first few iterations of the control loop, $\mathbf{S}_{YY_k}$ is not close to $\mathbf{R}_{YY}$ (i.e., convergence is slow), then the algorithm will have to run longer to eventually "average-out" the poor results. This can result in the overall poor performance of the algorithm, especially if there are lightly damped modes that are difficult to control.

5.3 Simulation Models

To test the convergence performance of MPCA, two beam models were simulated using random vibration testing. A fixed-free cantilever beam with base excitation was used for testing MPCA in a SISO configuration, and a fixed–fixed beam with base excitation at both ends of the beam was used for testing MPCA in a MIMO configuration. A diagram of each of these beam models can be seen in Fig. 5.2a and b, respectively.

In Fig. 5.2a and b, $V(x,t)$ is the relative motion of the beam response, $a(t)$ and $b(t)$ are the base excitations as a function of time t, x_1 and x_2 are the control locations, L is the length of the beam, and x is the spatial coordinate along the beam. These beams were modeled using Euler–Bernoulli theory, and the equations for $V(x,t)$ for the fixed-free beam and the fixed–fixed beam can be seen in Eqs. (5.6) and (5.7), respectively:

$$\ddot{V} + \frac{EI}{\rho A} V'''' + \ddot{a} = 0\,, \tag{5.6}$$

$$\ddot{V} + \frac{EI}{\rho A} V'''' + \frac{x}{L}\ddot{b} + \left(1 - \frac{x}{L}\right)\ddot{a} = 0\,. \tag{5.7}$$

In Eqs. (5.6) and (5.7), E is the modulus of elasticity of the beam material, I is the area moment of inertia of the beam cross-section, A is the area of the beam cross-section, and ρ is the density of the beam material. The over-dot notation ($\dot{}$)

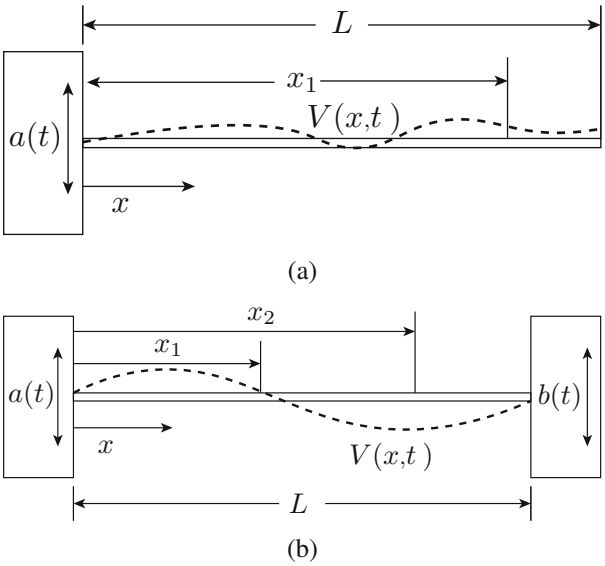

Fig. 5.2 Beam models for random vibration control simulation. (**a**) SISO fixed-free cantilever beam with base excitation. (**b**) MIMO fixed–fixed beam with base excitation at each end

indicates a derivative with respect to t, and the prime notation ($'$) indicates a derivative with respect to x. It should be noted that for the MIMO fixed–fixed beam model, there are two inputs to the beam: $a(t)$ and $b(t)$, as opposed to the SISO fixed-free model, which just has $a(t)$. For both of these beam models, a separable solution was assumed,

$$V(x,t) = \sum_{n=1}^{N} \psi_n(x) q_n(t) \ , \tag{5.8}$$

where $\psi_n(x)$ is the nth mode shape, $q_n(t)$ is the temporal response, and N is the number of modes included in the simulation. The mode shapes for each beam, $\psi_n(x)$, were obtained by assuming the form

$$\psi_n(x) = A_n \cos(\beta_n x) + B_n \sin(\beta_n x) + C_n \cosh(\beta_n x) + D_n \sinh(\beta_n x) \ , \tag{5.9}$$

and appropriate boundary conditions for the beams were used to reduce constants $A_n - D_n$ to a single constant that scaled the mode shape. The solutions for β_n for the fixed-free and fixed–fixed beams were found from Eqs. (5.10), and (5.11), respectively:

$$\cosh(\beta_n L)\cos(\beta_n L) + 1 = 0 \ , \tag{5.10}$$

$$\cosh(\beta_n L)\cos(\beta_n L) - 1 = 0 \ . \tag{5.11}$$

The spatial response, or mode shape $\psi_n(x)$, was related to the temporal response $q_n(t)$, by $\omega_n^2 = \frac{EI}{\rho A}\beta_n^4$, where ω_n is the nth modal frequency of the beam. The solution for $q_n(t)$ was obtained from a standard form:

$$\ddot{q}_n + 2\zeta_n \omega_n \dot{q}_n + \omega_n^2 q_n = F \ , \tag{5.12}$$

where ζ_n is the nth modal damping ratio and F represents forcing terms (in this case, base excitation(s)). Equations (5.13) and (5.14) show the expressions for F for the fixed-free and fixed–fixed beams, respectively:

$$-\frac{\int_0^L \psi_n(x)dx}{\int_0^L \psi_n^2(x)dx}\ddot{a}(t) \ , \tag{5.13}$$

$$-\frac{\int_0^L \psi_n(x)\left(1-\frac{x}{L}\right)dx}{\int_0^L \psi_n^2(x)dx}\ddot{a}(t) - \frac{\int_0^L \psi_n(x)\frac{x}{L}dx}{\int_0^L \psi_n^2(x)dx}\ddot{b}(t) \ . \tag{5.14}$$

5.4 Simulation Results

Random vibration control was applied to test the effect of control parameter ϵ on the convergence of MPCA (see Eq. (5.5)). For testing the SISO beam model (see Fig. 5.2a), base excitation $\ddot{a}(t)$ is the single input to the beam, and the response $\ddot{x}_1$ is the single output from the beam. The physical parameters that were used for the fixed-free beam model are shown in Table 5.1a, and the desired vibration profile is shown using discrete points in Table 5.1b that are interpolated using linear lines on the log scale. For this test, $x_1 = 0.6L$ and $\zeta_n = 0.025$.

The results from applying MPCA to the SISO fixed-free beam can be seen in Fig. 5.3. In particular, in Fig. 5.3a, the control results are depicted. The desired PSD profile, $\mathbf{R}_{YY}$, is indicated in light blue, with the ± 3 dB and ± 6 dB lines in dashed green and red, respectively. The average PSD response after 20 control loops, $\mathbf{S}_{YY}$, is indicated in blue. It can be seen that there is mode that is difficult to control at $\approx$70 Hz. This could be the result of light damping or potentially stubborn peak issues that are addressed in reference [7]. Aside from this modal frequency, the control converges t0 the desired PSD result.

In Fig. 5.3a, the effect of ϵ on the convergence of MPCA is demonstrated. The metric used to evaluate the convergence of MPCA is related to $\mathbf{E}_k$. For an ideal SISO system, $\mathbf{E}_k = 1$ at each frequency f. By taking the vector magnitude of the actual $\mathbf{E}_k(f)$ and scaling it by the ideal vector magnitude, the metric $|\hat{E}_k|$ is obtained. If $\mathbf{S}_{YY_k} = \mathbf{R}_{YY}$, then $|\hat{E}_k| = 1$, which is the control objective and is indicated by a red dashed line in Fig. 5.3b. It is desired that $|\hat{E}_k|$ converges to 1 in few control iterations. The effect of using different values for ϵ can be seen in Fig. 5.3b. For $\epsilon = 0.1$ (indicated by the green line), MPCA converges very slowly toward the red dashed line. For $\epsilon = 1$, MPCA overshoots but eventually converges near the control objective.

In general, a small ϵ resulted in a slow, steady, convergence, and a large ϵ resulted in overshoot of the control objective. To achieve faster convergence and reduce overshoot, a simple proportional controller was devised of the form:

$$\epsilon_k(f) = P(|\mathbf{E}_k(f)| - 1) \,, \tag{5.15}$$

Table 5.1 Settings for SISO random vibration control simulation using the fixed-free cantilever beam

(a) Fixed-free beam parameters

Parameter	Value
E	180 GPa
I	2.7749e–12 m^4
A	3.2258e–5 m^2
ρ	7750 kg/m^3
L	0.254 m

(b) Desired PSD profile for $\ddot{x}_1$

Frequency (Hz)	PSD value of $\ddot{x}_1$ (g^2/Hz)
20	1e–5
100	3e–5
200	3e–5
250	1e–5

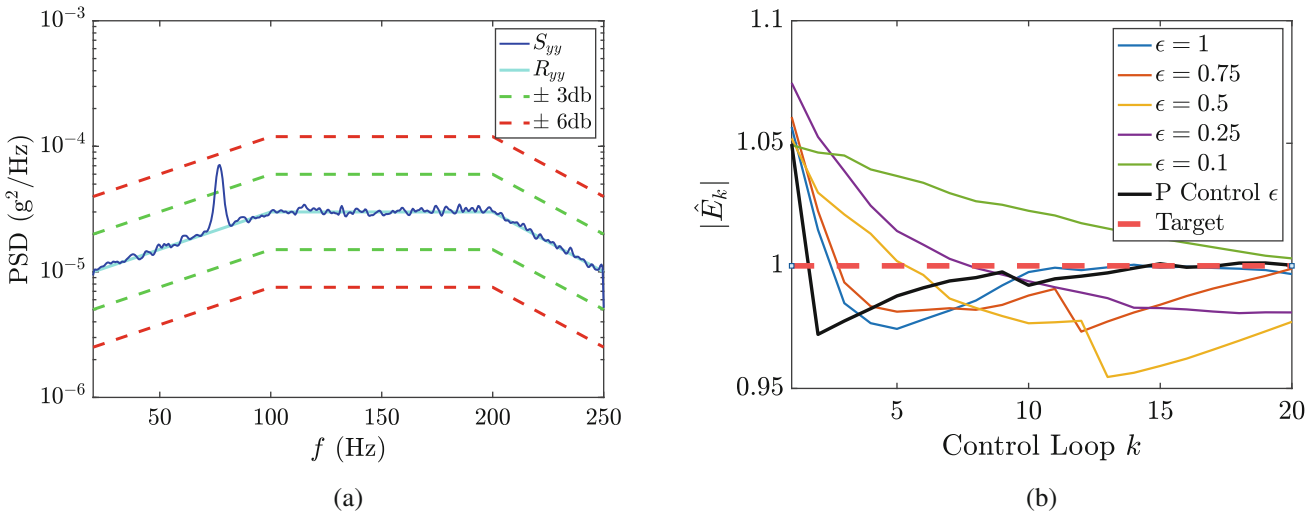

Fig. 5.3 Control results using the SISO fixed-free cantilever beam model. (**a**) PSD response at control location x_1 for SISO simulation. (**b**) Convergence of the SISO simulation using different ϵ

Table 5.2 Settings for MIMO random vibration control simulation using the fixed–fixed beam

Frequency (Hz)	PSD value of $\ddot{x}_1$ (g^2/Hz)	PSD value of $\ddot{x}_2$ (g^2/Hz)
5	1e–5	1e–5
50	4e–5	3e–5
100	4e–5	3e–5
125	1e–5	3e–5

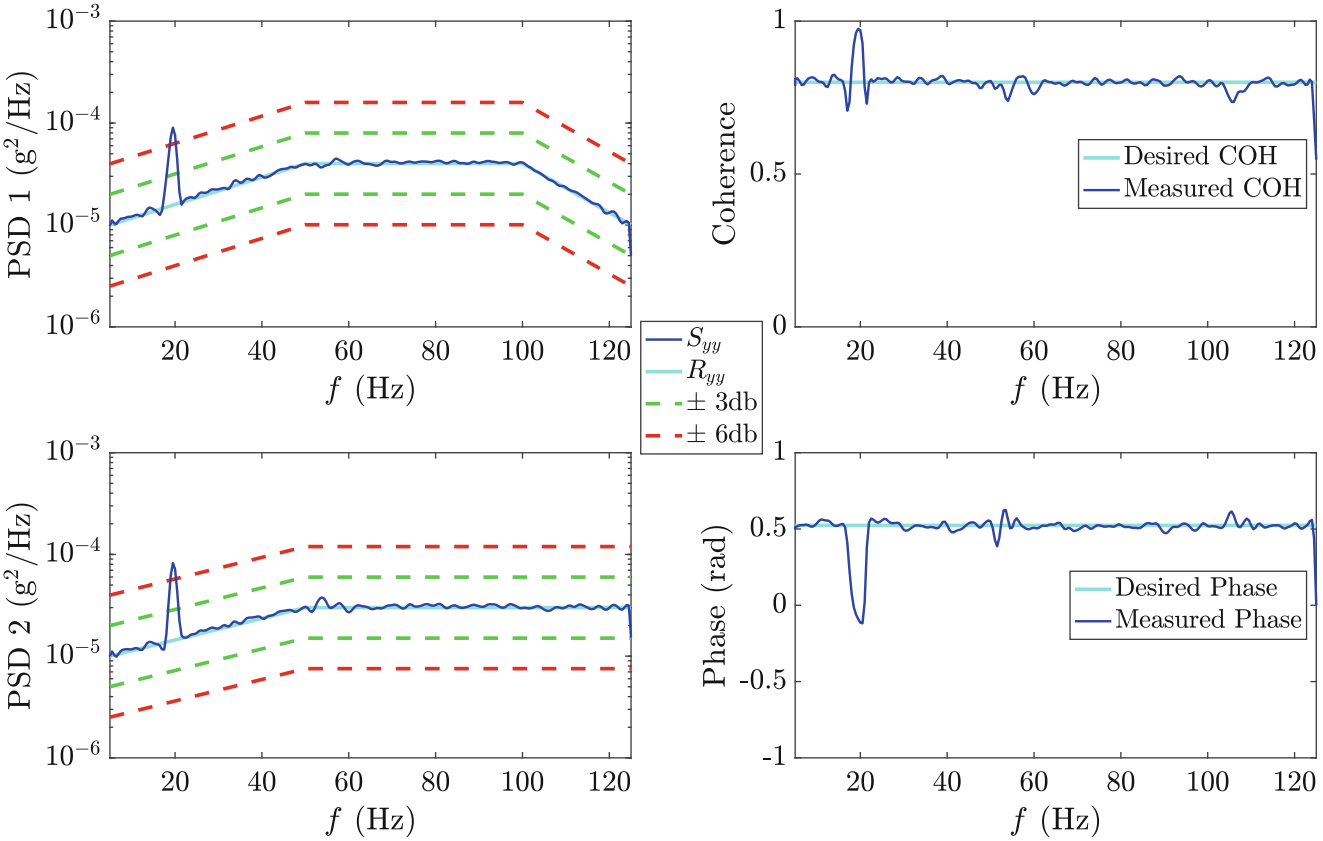

Fig. 5.4 PSD responses at control locations x_1 and x_2, phase and coherence for MIMO simulation

where P is a proportional gain that can be tuned. Instead of applying just ϵ as the control, $\epsilon_k(f)$ is applied, indicating that the proportional controller changes the value for ϵ at each spectral line f and at each control loop iteration k. It was enforced that $0 < \epsilon_k(f) \leqslant 1$. The black line in Fig. 5.3b shows the performance using a proportional controller. The proportional controller performed significantly better than any of the other values for ϵ by reducing overshoot and achieving quick convergence toward the control objective.

To further examine the convergence performance of MPCA, random vibration control was applied to the MIMO fixed–fixed beam (see Fig. 5.2b). For this simulation, the inputs to the system were $\ddot{a}(t)$ and $\ddot{b}(t)$, and the outputs were $\ddot{x}_1$ and $\ddot{x}_2$. The physical parameters used in this simulation were the same as listed in Table 5.1a with the exception of L, which in this case $L = 0.508$ m. The desired vibration profiles for outputs $\ddot{x}_1$ and $\ddot{x}_2$ are shown in Table 5.2, and the phase and coherence between outputs was set to $\pi/6$ radians 0.8, respectively. The locations of the outputs were $x_1 = 0.45L$ and $x_2 = 0.6L$.

The controlled results for the fixed–fixed beam simulation can be seen in Fig. 5.4. It can be seen that MPCA did a good job controlling the desired PSDs at both output locations (left plots of Fig. 5.4) and the coherence and phase between outputs (right plots of Fig. 5.4). The exception was a low-frequency mode at $\approx$ 20 Hz that was difficult to control and slightly exceeded the +6 dB lines.

The convergence of the MIMO simulation for different values of ϵ can be seen in Fig. 5.5. The performance of MPCA exhibited similar behavior for the MIMO simulation as it did for the SISO, with small values of ϵ achieving slow, steady

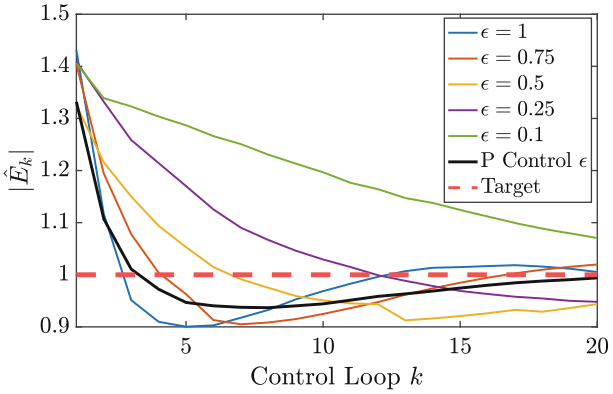

Fig. 5.5 Convergence of the MIMO simulation using different ϵ

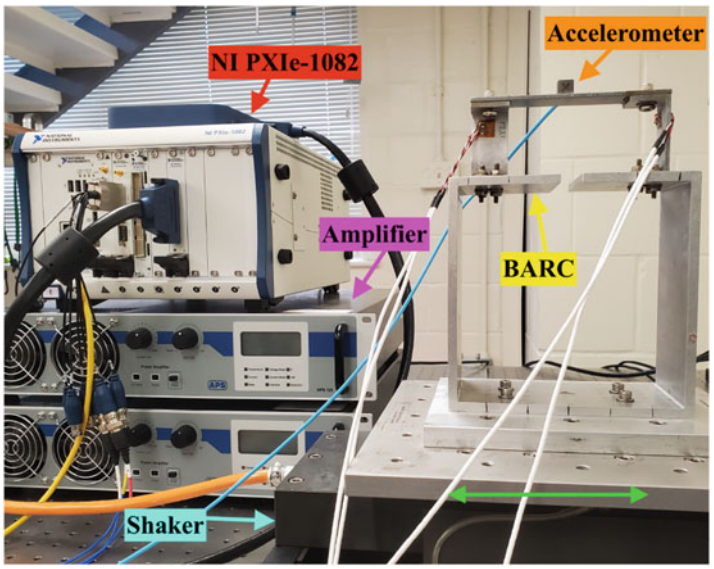

Fig. 5.6 Experimental setup

convergence, and larger values of ϵ overshooting the control objective. As with the SISO simulation, the proportional controller shown in Eq. (5.15) was applied, and the black line in Fig. 5.5 illustrates the improved performance that was achieved using this modification.

5.5 Experimental Results

To verify the convergence results that were obtained using simulation, a lab experiment was performed using the BARC in a SISO configuration. To implement a user-defined control loop, LabVIEW was used to build the MPCA control architecture and deploy on a National Instruments (NI) PXIe-1082 chassis. The experimental setup can be seen in Fig. 5.6, with the BARC mounted on a shaker table, the NI controller, amplifier, and accelerometer measurement. The accelerometer measurement at the top of the BARC was used as the control location, measuring in the axis of shaker excitation. The direction of motion for the shaker is shown by the green arrow. The desired vibration profile is shown in Table 5.3.

Table 5.3 Settings for SISO random vibration control experiment using the BARC

Frequency (Hz)	PSD value of control location (g^2/Hz)
30	1e–7
100	1e–6
500	1e–6
750	1e–7

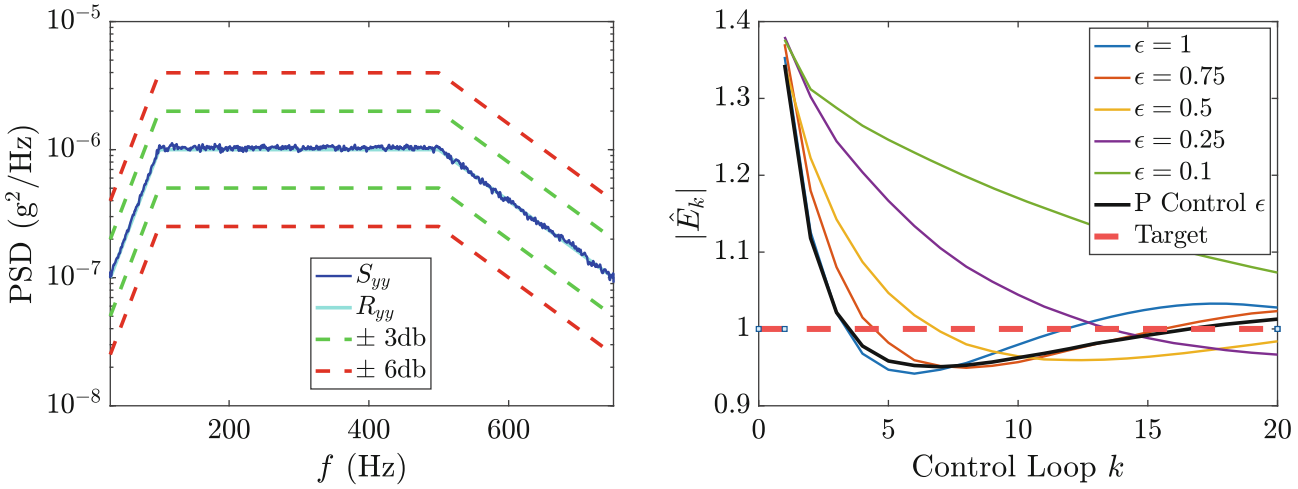

Fig. 5.7 Control results using the SISO BARC lab experiment. (**a**) PSD response at the control location on the BARC. (**b**) Convergence of the SISO experiment using different ϵ

The control results from the lab experiment are shown in Fig. 5.7a. The implementation of MPCA in the lab performed very well, achieving good control at the measurement location. No spectral lines came close to the ±3 dB or ±6 dB lines. The convergence results using different values for ϵ are shown in Fig. 5.7b. The lab experiment exhibited similar behavior to both the SISO and MIMO simulation convergence results (see Figs. 5.3b and 5.5). The application of a proportional control improved the performance of MPCA as it did in simulation. The proportional control reduced the overshoot effect and provided steady convergence toward the desired target.

5.6 Conclusion

This chapter has examined the convergence of MPCA. Using two simulated beam models, a fixed-free cantilever beam and a fixed–fixed beam, both SISO and MIMO random vibration control were examined. Simulation results demonstrated the significance of the control parameter ϵ on the convergence performance of MPCA. Additionally, using a proportional controller, the convergence performance was improved significantly.

To verify the simulated beam results, the BARC was also tested in the lab in a SISO configuration. MPCA was implemented on a NI chassis using LabVIEW, and the convergence dependence on the control parameter ϵ was similarly observed in experiment. The proportional control also improved the convergence of MPCA in the lab. While this chapter has provided a modification to MPCA that improves convergence, future work will examine whether or not there is a benefit to additional control structure complexity in controlling the parameter ϵ to achieve improved convergence.

Acknowledgement Funding from the Los Alamos National Laboratory is gratefully acknowledged.

References

1. Smallwood, D.O.: A random vibration control system for testing a single test item with multiple inputs. SAE Trans. **91**., Section 4: 821158–821559, 4571–4577 (1982)
2. Xuli, C., Huaihai, C., Xudong, H., Jiang, S.: Matrix power control algorithm for multi-input multi-output random vibration test. Chin. J. Aeronaut. **24**(6), 741–748 (2011)
3. Zheng, R., Chen, H., He, X.: Control method for multiple-input multiple-output non-Gaussian random vibration test. Packag. Technol. Sci. **30**(7), 331–345 (2017)
4. Zheng, R., Chen, H., He, X.: Control method for multi-input multi-output non-Gaussian random vibration test with cross spectra consideration. Chin. J. Aeronaut. **30**(6), 1895–1906 (2017)
5. Zheng, R., Chen, H., Vandepitte, D., Luo, Z.: Multi-exciter stationary non-Gaussian random vibration test with time domain randomization. Mech. Syst. Signal Process. **122**, 103–116 (2019)
6. Zheng, R., Chen, H., He, X., Vandepitte, D.: Multiple-input multiple-output non-stationary non-Gaussian random vibration control by inverse system method. Mech. Syst. Signal Process. **124**, 124–141 (2019)
7. Cui, S., Chen, H., He, X., Zheng, W.: Multi-input multi-output random vibration control using Tikhonov filter. Chin. J. Aeronaut. **29**(6), 1649–1663 (2016)
8. D'Elia, G., Musella, U., Mucchi, E., Guillaume, P., Peeters, B.: Analyses of drives power reduction techniques for multi-axis random vibration control tests. Mech. Syst. Signal Process. **135**, 106395 (2020)
9. Smallwood, D.O.. Multiple shaker random vibration control–an update. Technical Report, Sandia National Labs, Albuquerque, NM (US) (1999)
10. Underwood, M.A., Keller, T., Ayres, R.: Multi-shaker control: a review of the evolving state-of-the-art. Sound Vibr. **51**(8), 8–16 (2017)

Chapter 6
Acoustic Resonance Testing on Production Lines with the Smart Impulse Hammer WaveHit^{MAX}

Yaron Brauner, Daniel Herfert, Andreas Lemke, and Maik Gollnick

Abstract Acoustic resonance testing (ART) is a method for efficient and objective serial testing of workpieces. It nondestructively detects smallest variations in geometry, weight, and bonding and can identify holes, cracks, and other structural defects. In ART, a fully automated impact excitation is fundamental. Fully automatic, in this context, means an excitation point search and an adjustment of the excitation force controlled directly in the hammer. Moreover, it is essential to perform this excitation in a precisely reproducible process and in large series. No manual configuration steps are necessary for the user. For nondestructive ART on production lines, changes in the position of the test object must also be compensated.

To demonstrate the suitability and the advantages of the first smart impulse hammer in series testing, an ART was carried out on floor tiles on production line. For evaluation, the force sensor signal of the hammer and additionally a measuring microphone were used. Artificial intelligence and signal processing methods were used for classification. The system and results of the ART are presented in this chapter.

Keywords Impulse hammer · Acoustic resonance testing · Excitation techniques · Sensors and instrumentation · Artificial intelligence

6.1 Introduction

Manual acoustic resonance analysis, or sound testing, is one of the oldest nondestructive testing methods, along with visual inspection [1]. It is commonly used for manual inspection of tableware and glassware. In series production, however, this method cannot be performed by human inspectors. Fully automated testing is necessary. Computer-aided ART can fill this role while ensuring increasing quality requirements.

In ART resonance, frequencies are evaluated as the test object vibrates. The resonances are an acoustic fingerprint of the vibrating structure and thus the "voice" of the structure, so to speak. They depend on the material, geometry, and aging condition of the structure. If these structural properties change, for example, due to aging or damage, deviations occur in the fingerprint describing these properties. Therefore, resonance analysis can be used to detect faulty of damaged workpieces.

Using ART for this task has a number of advantages:

- Entire structure is included, and damage location does not have to be known.
- Reproducible.
- Objective
- Sensitive/high resolution.
- Can be automated.
- Environmentally friendly.
- Fast.
- Inexpensive.

Y. Brauner · D. Herfert (✉) · M. Gollnick
Society for the Advancement of Applied Computer Science, Department of Structural Dynamics/Pattern Recognition, Berlin, Germany
e-mail: herfert@gfai.de

A. Lemke
System Development and Software Engineering Andreas Lemke, Schöneiche, Germany
e-mail: info@systementwicklung-lemke.de

C. Walber et al. (eds.), *Sensors and Instrumentation, Aircraft/Aerospace and Dynamic Environments Testing, Volume 7*,
Conference Proceedings of the Society for Experimental Mechanics Series, https://doi.org/10.1007/978-3-031-05415-0_6

6.2 Background

When performing an ART, both the excitation of the structure and the measurement of the structural response are fundamentally important.

The excitation must be reproducible to do reliable serial testing. Impulse excitation using an impulse hammer is usually the preferred excitation method in ART. It is fast and no fixation to the test object is necessary. Furthermore, it is advantageous if the instrumentation of the excitation can be adapted to the specific problem. This allows adjusting the characteristics of the excitation, such as height and width of the pulse and the frequency range, accordingly. Choosing the right instrumentation for a given problem is substantial for the quality of the ART and the subsequent classification. Instrumentation comprises the selection of hammer tips, additional weights, and force sensors. The structural response is recorded using a microphone. Both the selection of the microphone and its positioning play an important role. The way in which the test object is mounted also influences the ART.

6.3 Technical Implementation

The implementation of ART listed in Fig. 6.1 can be installed on production lines for end-of-line testing. Within the scope of the publication, a white floor tile with dimensions of 20.3 cm × 20.3 cm was reproducibly investigated. The demonstrated setup, however, is easily transferable to other applications.

The smart impulse hammer WaveHit^{MAX} for reproducible impulse excitation was used to excite the tiles. The introduction of the first intelligent impulse hammer offers new possibilities of mechanical excitation for ART applications [2, 3]. It guarantees fully automatic, reproducible, and highly precise bounce-free excitation of a test object. Important parameters such as impact force and pulse width can be adjusted within wide limits.

"Smart" means the device is able to do internal signal processing. The advantages of internal signal processing are as follows:

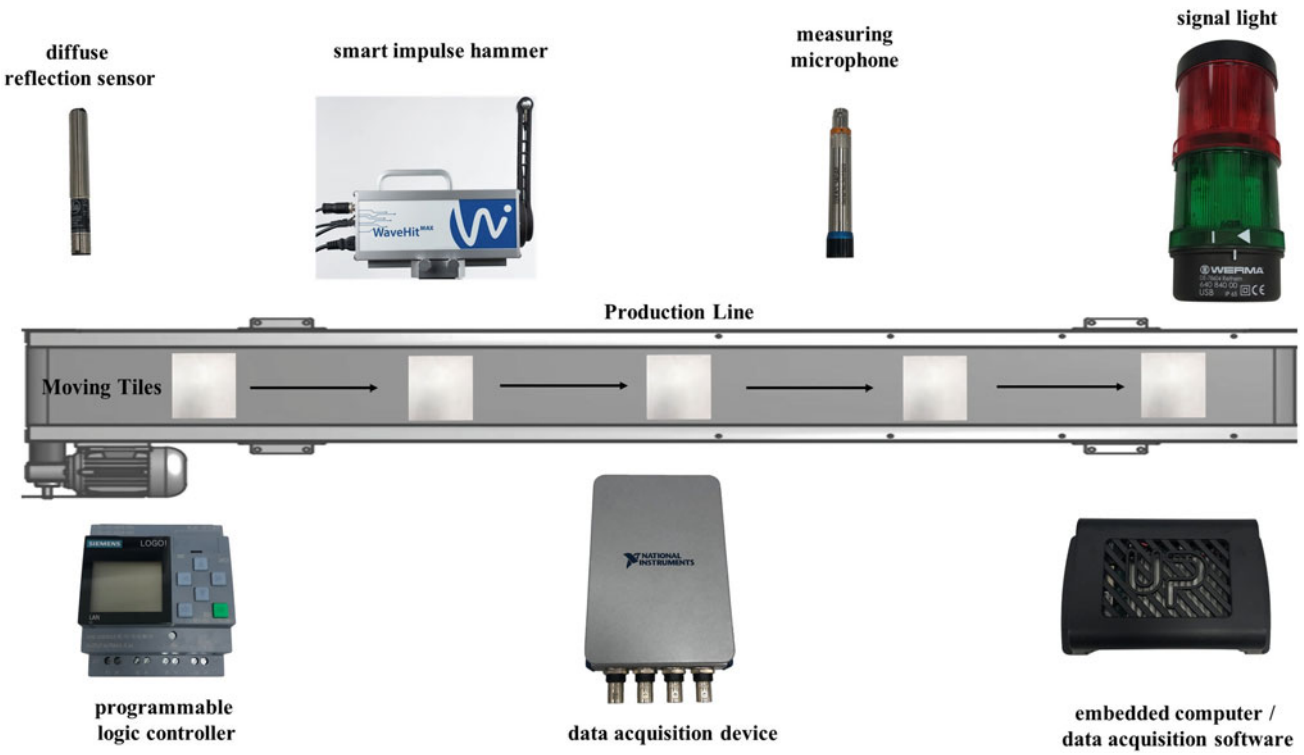

Fig. 6.1 Overview of all components for ART

- Guarantees fully automatic, reproducible, and high-precision single hit excitation of a test object.
- Automatic calibration to user-defined impact force.
- Automatic excitation point search.
- Changes in position and height differences from test object are automatically anticipated.
- Internal quality assurance.
- Manual adjustment by the user is no longer necessary.
- Control via programmable logic controller possible.

This impulse hammer can be fitted with four different tips, two different additional weights, and two different force sensors. The effects of these different instrumentations on ART are discussed below.

An ifm electronic OF5027 diffuse reflection sensor was used to trigger the hammer impact. This sensor notifies with a signal edge with signal state high when the beginning of a tile is located below. The Siemens LOGO! 24 CE programmable logic controller provided the possibility to use different production line speeds, tile dimensions, and distances between the diffuse reflection sensor and the point of excitation. With this controller, the impulse hammer can be triggered or controlled autonomously. Furthermore, all settings on the hammer, such as impact force and the selected instrumentation, can be set directly on the menu of the hammer. No PC is required to operate the hammer. The NI-9234 measuring card from National Instruments was used to record the measurements. The GRAS 146AE 1/2″ CCP free-field microphone was used as the measurement microphone. An embedded PC was used for data acquisition and analysis. An industrial traffic light was used to display the results of the ART.

6.4 Measurement Setup

In this section, the measurement setup for performing ART is shown. A floor tile of the type Rytmo was examined. The fine stone tiles came from two different production charges. The measurement was performed on a running production line. No changes to the production process were necessary for the integration of the ART system. The aim of the application was to distinguish between tiles in good condition (IO) and defective tiles (NIO). This application is challenging, because the tiles have a very strong damping (after an impulse excitation of 1 kN, the tile is back in resting position after 0.05 s) in spite of a suitable elastic mounting. Furthermore, in good condition the tiles show significant differences in their mass (range 717–740 [g]), stiffness, and height. For this reason alone, there are large differences in the determined resonances and associated damping (see Fig. 6.2). Height differences between the test objects further complicate the process. As the backward movement of the impulse hammer varies, reproducible single impacts become significantly more difficult.

In the context of ART, the measurement setup (see Fig. 6.3) is of fundamental importance for the subsequent analysis. The following aspects are essential: elastic mounting of the test object, location of the excitation, instrumentation of the excitation, and location of the microphone.

For the tiles, the aim was close to free vibration without any boundaries. It was achieved by elastically mounting them only at their corners. They were excited at the edge to generate as many resonances as possible. In order to excite a wide frequency range, the metal tip and the 12 g additional weight were chosen for the smart impulse hammer. To find the right instrumentation, different options were tested, validated, and compared to the results of the sound tests (see Fig. 6.4). The choice of instrumentation has a major impact on the subsequent ART. To ensure an energy input over the entire surface and excite the essential frequency range of the tile, an impact force of 1 kN was chosen. The impulse hammer then adjusted to this force automatically.

The structure response measurement was taken at the edge of the tile opposite to the excitation point. It was recorded with a measuring microphone at a distance of 15 cm perpendicular to the test specimen. The sampling rate of the measurement was set to 48 kHz.

Consistency of the measurement setup is essential, since changes in the measurements can have a direct influence on the subsequent ART and lead to poorer classification results. For the test, 50 tiles in good condition and 5 tiles with damage were available. The defective tiles (see Fig. 6.5) were damaged manually. However, damage patterns from production were used as a guide. Different degrees of damage were introduced to evaluate the sensitivity of the ART. The NIO tiles were recorded several times to account for different damage locations. For this purpose, the tiles were always shifted by 90 degrees and recorded again, so that each damage was recorded at four different locations.

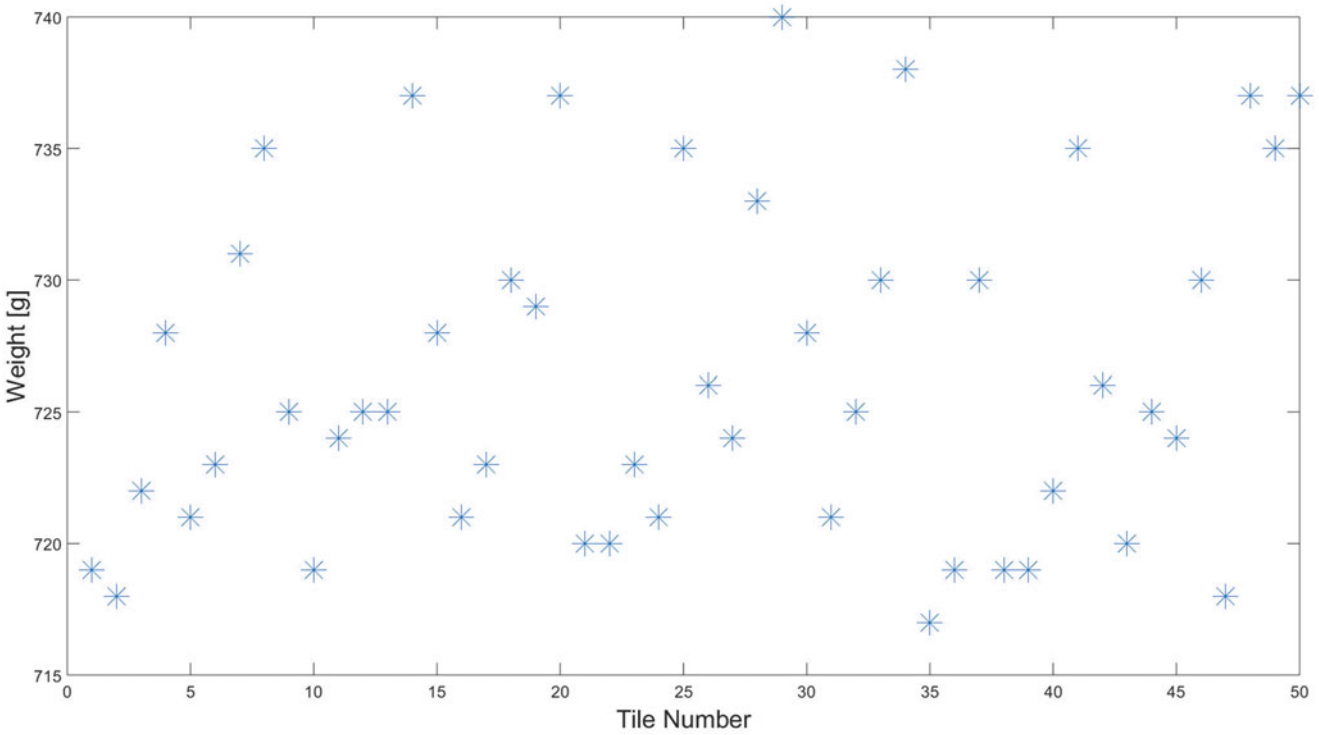

Fig. 6.2 Weight of all good tiles

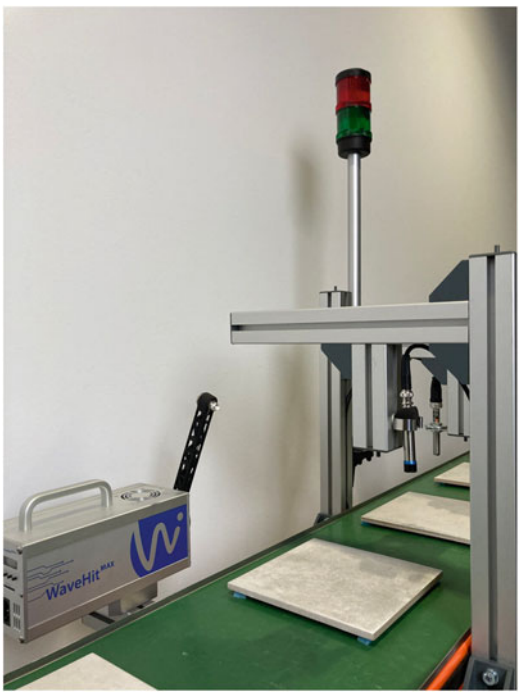

Fig. 6.3 Overview of the measurement setup and the overall system for ART

6.5 Analysis

The software WaveImage [4] offers an automated and real-time functionality to evaluate and analyze measurement data for ART. A modular system consisting of three components (feature extraction, feature selection, classification) provides universal applicability. The modular components can be combined individually to find an adequate approach to the given

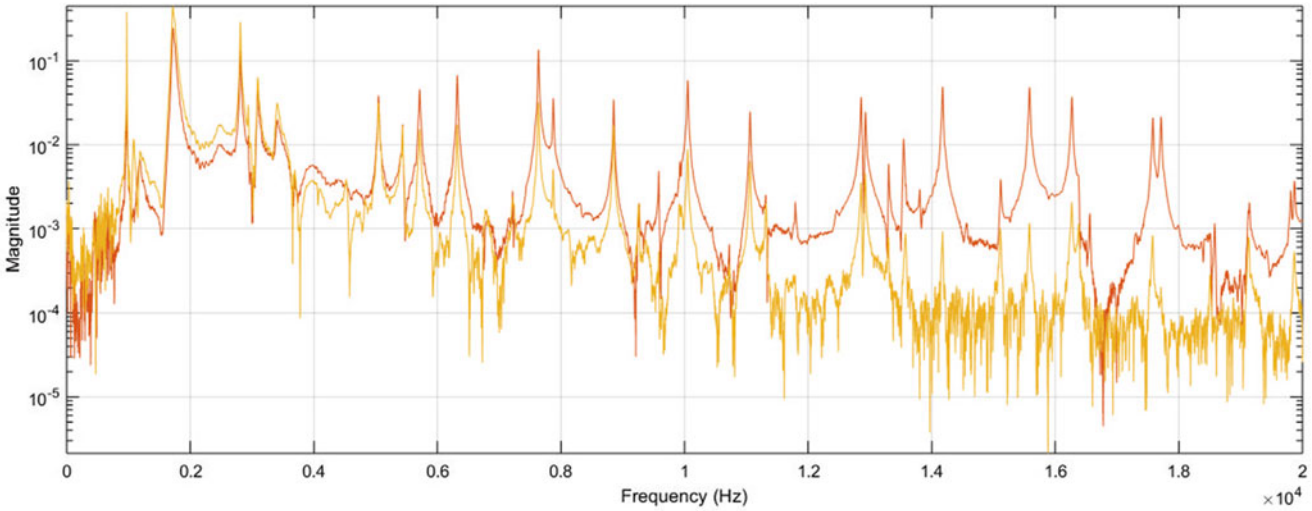

Fig. 6.4 Comparison of the response behavior of the test object with two different hammer tips: metal tip (red) and plastic tip (yellow)

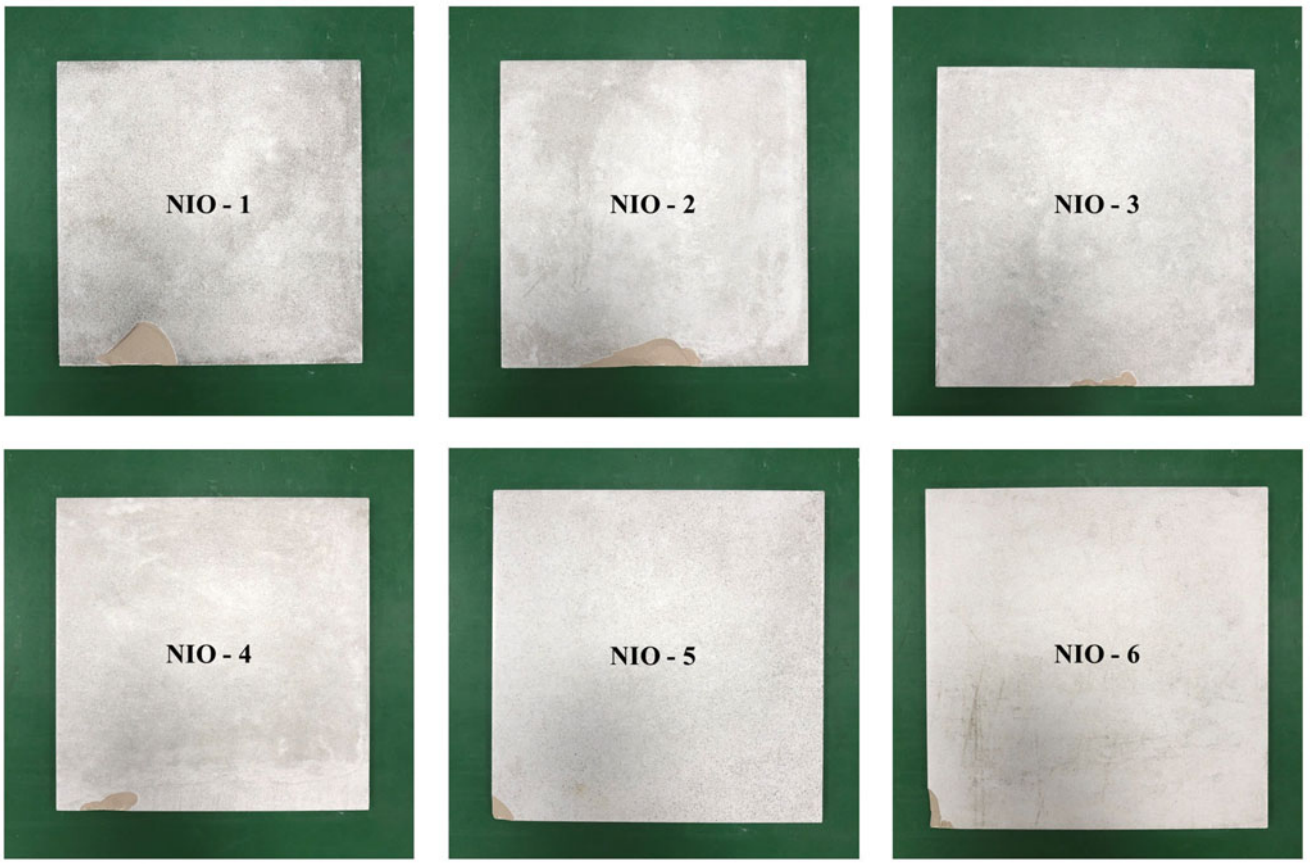

Fig. 6.5 Comparison of the defective tiles. Sorted according to the severity of the damage

problem. Together with state-of-the-art methods from the complementary fields of artificial intelligence, signal processing, and modal analysis, this enables a wide range of applications.

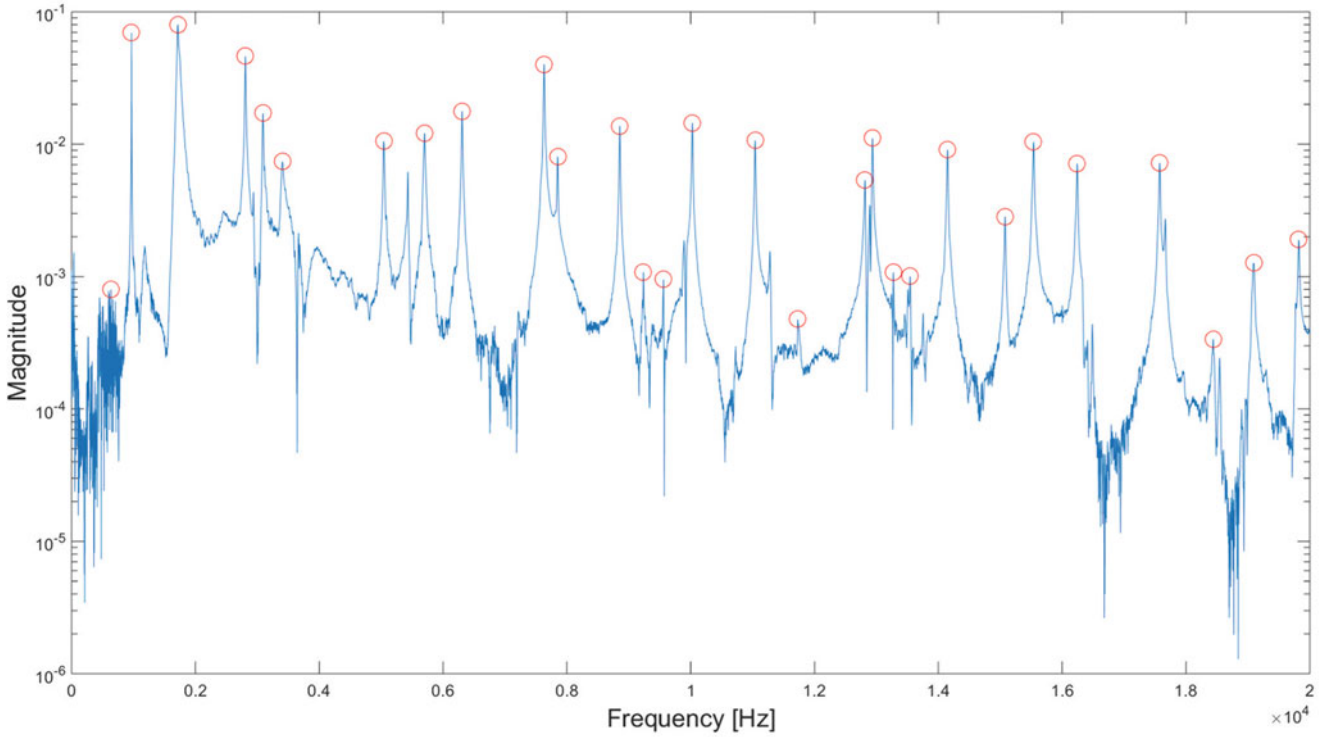

Fig. 6.6 Response frequency spectrum (blue) of a tile with automated determination of resonance frequencies (red)

6.5.1 Feature Extraction

Feature extraction is performed at the beginning. The feature extraction component includes current methods of filtering (high-pass, low-pass, or band-pass), noise removal, and background noise removal. In the demonstrated use case, feature extraction was not necessary due to the good measurement setup.

6.5.2 Feature Selection

The next component uses the pre-processed sensor data for the characterization of significant features. This enables the best possible separation between the classes (e.g., damage, no damage). Methods from time domain analysis (e.g., statistical indices, such as the kurtosis, variance, maximum value, or the attenuation of the overall system) and frequency domain analysis (spectrum, octave spectrum, psychoacoustic features) can be utilized.

For the application of ART on tile testing, an algorithmic approach was implemented, which requires no prior knowledge and can be highly automated. Only the response spectrum of the microphone was used. Features for the subsequent classification were determined in the response spectrum by means of "intelligent" identification of modal parameters (see Fig. 6.6) [5]. This search algorithm is designed to locate and select extreme values in function graphs. The developed method for automatic modal parameter identification is based on pattern recognition and artificial intelligence techniques and does not require any further parameters or expert knowledge to use. The values of the indicator functions are represented by a simple feature vector with small dimensions and are classified by a "support vector machine" (SVM). Since the features already describe the function course, they are independent of measurement parameters such as sampling rate or frequency spacing. In order to increase robustness, existing methods from the field of computer vision were adapted and extended.

After the resonant frequencies have been found automatically and without prior knowledge (see Fig. 6.6), the corresponding damping ratios are calculated using the half-power bandwidth method. Then a feature vector is calculated whose dimension corresponds to the number of frequency lines. It contains a value for each frequency in the observed frequency range. If a resonance was found at a frequency, the value at this frequency is set to the damping ratio associated with the resonance frequency. Due to mass or stiffness differences, the same resonances may be shifted by some frequency

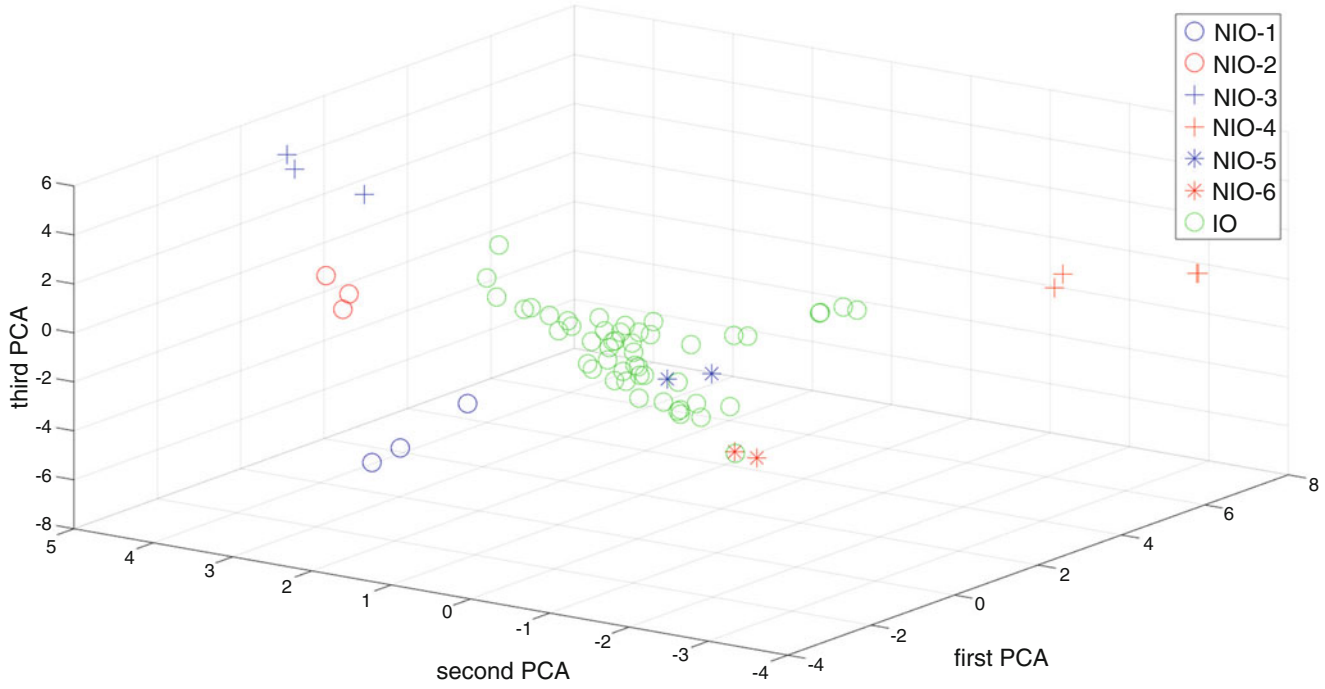

Fig. 6.7 Illustration of the first three main components for separating good (IO) and damaged (NIO) tiles

lines for different tiles. In order to identify such similar resonances to each other, the frequencies in an interval around each resonance frequency are given the same damping value multiplied by a decay factor. These decay factors are calculated in the following way:

Consider a number of frequency lines $f_{-M}, f_{-M+1}, \ldots, f_{-1}, f_0, f_1, \ldots, f_{M-1}, f_M$, where f_0 is the resonance frequency and M is left and right neighbor frequencies which are to be given decay factors; then the i-th decay factor d_i corresponding to frequency f_i is calculated as follows: $d_i = \frac{1}{\exp(|i|)}$ with $i = -M, \ldots, -1, 0, 1, \ldots, M$. All other elements of the feature vector receive the value 0.

The introduction of the decay function led to an improvement of the ART, since slightly shifted identical resonance frequencies were now also considered with an attenuated damping. Including both the damping and the resonant frequencies led to the best results. To reduce the dimension of the feature space for the subsequent classification, principal component analysis (PCA) is used [6]. This requires no prior knowledge about the test object and can be performed automatically. PCA structures large data sets by using eigenvectors of the covariance matrix. This allows data sets to be simplified and illustrated by approximating a large number of statistical variables by a smaller number of linear combinations (the principal components) that are as meaningful as possible.

For the given classification problem, the first eight principal components were used, since these show sufficient variance. In Fig. 6.7 only, the first three are shown for reasons of clarity. However, a clear separation between damaged and non-damaged tiles can already be seen with three components. It is clear from the results that depending on the severity of their damage, the damaged tiles are further away from the non-damaged tiles. The most damaged tiles are farthest from the good group. The good tiles continue to be in a very dense cluster, which is desirable. This is despite large variations in their height, mass, and stiffness. NIO-5 and NIO-6 tiles are close to the edges of the good cluster, because their damage introduces similar differences in mass and stiffness as is already present within the distribution of the good tiles. The location of the damage does not have a great influence on the classification quality. The feature vector could be generated automatically without any prior knowledge and provided very promising results. This approach is also suitable for other ART applications.

6.5.3 Classification

The selected features are then used to construct the classifier (single- or multi-class classifier possible). The following methods are supported for classification:

- Support vector machines
- Hidden Markov models
- Distance-based classifiers (K-means, fuzzy C-means, ellipsoid)
- Distribution-based classifier (Bayes classifier)
- Density-based classifier (k-nearest neighbors)
- Neural networks

In the near future, classification for one (only good) and two classes will be performed using the features shown and using support vector machines.

6.6 Conclusion

The introduction of the first smart impact hammer introduces new possibilities of mechanical excitation for acoustic end-of-line testing. Smart means the device handles signal processing internally. The WaveHit^{MAX} guarantees fully automatic, reproducible, and high-precision excitation of a test object without double hits on moving production lines. All presettings like zero point search or impact force search are performed automatically by the hammer. Manual adjustment by the user is no longer necessary. If the test object is on a moving base, the WaveHit^{MAX} can easily compensate height differences between hammer and test object without new calibration. This fact is significant for automatic end-of-line testing. The possibility to change the instrumentation (tip, additional weight, force sensor), its autonomous operation, and the ability to be operated via a programmable logic controller make this impulse hammer a perfect tool for ART. All these features could be validated during the demonstrated application of ART to end-of-line testing of fine stone floor tiles. The results of the investigated use case were promising despite the high variance of geometrical and structural parameters within the non-damaged tiles.

The design of the measurement setup and the execution of the measurement were carried out as part of the bachelor thesis of Yaron Brauner in cooperation with the Department of Structural Dynamics and Pattern Recognition. The entire ART was performed with the software WaveImage. The obtained results are very promising and could be built upon in the future. Further apps of art in the described setup are planned in the future.

References

1. Hertlin, I., Herkel, T.: Riss- und Gefügeprüfung mit akustischer Resonanzanalyse im Schall- und Ultraschallbereich für Kfz-Sicherheitsteile. DGZfP-Jahrestagung, 2003
2. Lemke, A., Herfert, D.: WaveHit^{MAX} – Sensor-Based System for Impulse, Bounce-Free Excitation of Macroscopic Solid Structures, https://wave-hit.com. GFaI e.V., Berlin (2021)
3. Herfert, D., Lemke, A.: WaveHit – The First Smart Impulse Hammer for Fully Automatic Impact Testing, Proc. 39th Intl. Modal Analysis Conf. Springer Verlag, Cham (2021)
4. Product Page of the WaveImage Software. https://wave-image.com/?lang=en. 2021
5. Gollnick, M., Heimann, J., Herfert, D.: Automatic Modal Parameter Identification with Methods of Artificial Intelligence. 38. International Modal Analysis Conference, 2020
6. Jolliffe, I.: Principal component analysis. In: Lovric, M. (ed.) International Encyclopedia of Statistical Science. Springer, Berlin, Heidelberg (2011)

Chapter 7
Techniques for Modifying MIMO Random Vibration Specifications

Ryan Schultz and Garrett Nelson

Abstract While research in multiple-input/multiple-output (MIMO) random vibration testing techniques, control methods, and test design has been increasing in recent years, research into specifications for these types of tests has not kept pace. This is perhaps due to the very particular requirement for most MIMO random vibration control specifications – they must be narrowband, fully populated cross-power spectral density matrices. This requirement puts constraints on the specification derivation process and restricts the application of many of the traditional techniques used to define single-axis random vibration specifications, such as averaging or straight-lining. This requirement also restricts the applicability of MIMO testing by requiring a very specific and rich field test data set to serve as the basis for the MIMO test specification. Here, frequency-warping and channel averaging techniques are proposed to soften the requirements for MIMO specifications with the goal of expanding the applicability of MIMO random vibration testing and enabling tests to be run in the absence of the necessary field test data.

Keywords MIMO · Random vibration · Vibration testing · Environment specifications · Multi-degree of freedom testing

7.1 Introduction

The objective of laboratory vibration testing should be to cause the laboratory test system to respond as it would in a service or field environment. That is, the acceleration response in the laboratory test should match the acceleration response of the same system subject to all the loads and boundary conditions found in the field environment.

Multiple-input/multiple-output (MIMO) vibration testing can provide a laboratory test response which accurately replicates response of a system in a service or field environment. Conducting a MIMO test requires a specification at multiple accelerometer channels or output degrees of freedom (DOF). Ideally, this specification is derived directly from measurements of the system in a field environment, meaning the unique responses at individual DOF as well as the DOF to DOF relationships are captured in the specification. With a good specification and adequate excitation approach (i.e., shaker locations and directions), a MIMO test can be conducted which accurately matches that specification and thus mimics as closely as possible the response of the system in the field environment.

Performing such a test requires several key things to work properly: output DOF to allow the laboratory system to be controlled, sufficient input DOF to cause the system to respond, and a specification which is appropriate for the system being tested and represents the field environment response. However, often one or more of these necessary components are different from the idealized scenario or are missing altogether.

Consider this common scenario: a new system, system B, is being developed and laboratory vibration testing is needed for development and qualification of the system. However, because this is a new system, there is no field test data available for a MIMO test specification. There is some field test data from an old system, system A, but that system is a bit different, and it has accelerometers in different locations. These are relatively minor changes from the perspective of a systems engineer – small changes in the design, construction, and instrumentation between the old and new systems – but this can mean big problems for the test engineer as now the dynamics are different, the DOF are different, and there is no specification that can be directly leveraged for the new system test.

R. Schultz (✉) · G. Nelson
Sandia National Laboratories, Albuquerque, NM, USA
e-mail: rschult@sandia.gov

C. Walber et al. (eds.), *Sensors and Instrumentation, Aircraft/Aerospace and Dynamic Environments Testing, Volume 7*,
Conference Proceedings of the Society for Experimental Mechanics Series, https://doi.org/10.1007/978-3-031-05415-0_7

The test must be conducted, so what can be done?

1. Use a generic straight-line specification from a published standard.
2. Apply the specification from system A to system B.
3. Modify the specification from system A to account for differences in dynamics between A and B.

Naturally, these options each have pros and cons. Picking a generic specification ignores the system dynamics and the field environment loads, so it will not match the field response well and will not be a very good test. Similarly, simply applying the system A specification to system B, perhaps by picking the nearest accelerometers A to B, could work, but it again ignores the difference in dynamics and will be trying to force the response at a location on B to respond like a different location on A, which will not be a very good test.

This chapter presents some alternative methods where the system A specification is modified to account for the differences in dynamics and accelerometer locations, adding needed flexibility in the MIMO testing process. None of these methods are perfect, but they do provide some options when the test engineer is in the position of needing to run a test with imperfect or missing specification data while still meeting the intent of the test: to cause the laboratory test system to vibrate as it would in the field environment.

7.2 Typical MIMO Testing Process

For general MIMO random vibration testing, there are typically two tests: the field environment test which provides the necessary data to generate the specification and the laboratory test which is used for system evaluation, development, and qualification. The field environment test would ideally provide rich response time history data at many locations throughout the system. The field test response is then used as the specification for a subsequent laboratory MIMO test, often on a different system or version of the system. This is shown on an example set of hardware in Fig. 7.1.

The laboratory system is setup with accelerometers to measure the dynamic response and excited by mounting the system to a 3- or 6-DOF table or by attaching several shakers directly to the system. Once setup, the test is conducted using a MIMO controller which runs several steps. The first step is to measure the laboratory system input-output relationship, which is often called the system identification (system ID) or buzz test [1, 2]. Next, the specification is loaded in, and the controller makes a prediction, determining what the inputs need to be to best match the specification outputs. At this point the test can be run using the inputs determined in the prediction step.

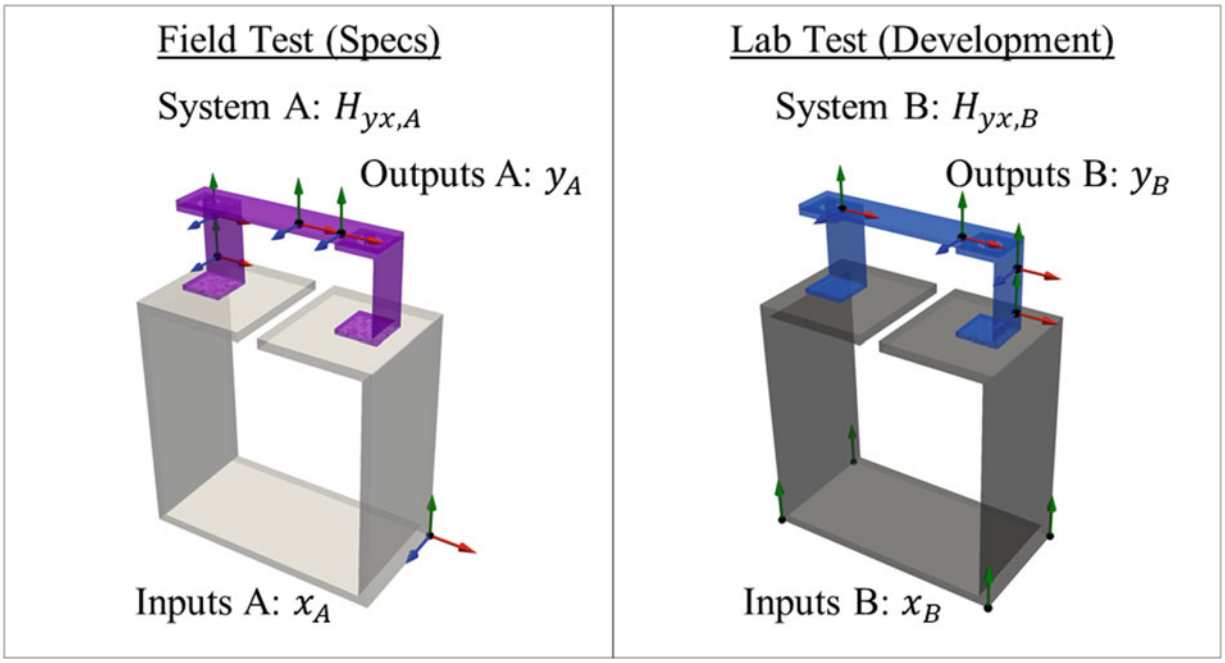

Fig. 7.1 Field test with original dynamics, system A, vs. laboratory test with different dynamics, system B

Generally, a MIMO random vibration test is defined and conducted using narrowband cross-power spectral density (CPSD) matrices for outputs and inputs and narrowband frequency response functions (FRFs) relating the outputs and inputs. As the MIMO control solution is evaluated inside the controller using those narrowband CPSD and FRF matrices, the specification must be defined as a narrowband, Hermitian, positive-definite CPSD matrix [3]. For ideal test conditions, this works well and is not much trouble. However, this does limit the possibilities in terms of conducting a MIMO test using non-ideal specification – any modifications to the specification must still result in a narrowband, Hermitian, positive-definite CPSD matrix. The goal in this work is to make modifications to the specification which still follow those rules so the specification can be imported into any typical MIMO controller and the test can be run as usual.

7.3 Options for MIMO Response-Control Specifications When Data Is Not Available

As mentioned in the previous section, there are some options available to create a MIMO test specification when sufficient field test data is not available for the system being tested. None of these are ideal and will generally result in the laboratory system response being different from the field response, but the goal is to choose some method which minimizes this difference. The following subsections describe the pros and cons of each method.

7.3.1 Use a Generic Straight-Line Specification from a Standard

Single-axis base-control vibration testing often uses straight-line specifications such as MIL-STD-810 [4]. This works well for many types of test articles and environments, but in general is not applicable to MIMO response-control testing because the straight-line specifications do not reflect the peaks and valleys in the response at each DOF and would not account for the differences in response at one DOF vs. another as they all have the same specified response. Further, there is no cross-term (coherence and phase) information available. However, since no field test is needed to define the environment, it is easy to implement. In general, generic straight-line base-control specifications applied to MIMO response-control tests will likely result in inaccurate system response not reflective of the field environment and will not be considered further in this chapter.

7.3.2 Apply the Specification from the Old System to the New System

If data exists for a previous field test of system A, it could be used as the specification for system B. This ignores any differences in dynamics between systems A and B, essentially forcing system B to vibrate like system A. If the dynamics and output DOF of A and B are quite similar, then this is a reasonable approach. However, if either the dynamics or output DOF are different, the laboratory test of system B will not be representative of the actual field environment response of system B. If the dynamics are quite different, the controller will simply be trying to force the system B to respond like system A. If the output DOF are different, the specification at a system A DOF could be assigned to the nearest system B DOF. This should be done carefully as mapping an A DOF to a B DOF which are in different locations or directions could result in large errors in the system response. This limitation is problematic if there are not many DOFs which match up as the MIMO controller needs some minimum number of control DOF.

7.3.3 Modify the Specification to Account for the Differences Between A and B

For cases where the dynamics or output DOF are different, ideally the specification should be modified to allow the test of system B to represent the field response of system B instead of the field response of system A. The goal is to add some flexibility in how the specification is defined while maximizing the use of the system A specification (i.e., not throwing away DOFs that do not match). The techniques presented here rely on frequency or DOF averaging, which help to reduce the effects of mismatches in the system dynamics and DOF locations and directions. The next section will present several possible specification modification techniques.

7.4 Techniques for Specification Modification

This section presents techniques for modifying MIMO random vibration specifications for applications when either the system dynamics are different or when the output DOF are different. All techniques assume some auto-power spectral density (APSD) data is available from a field test of the old system. Frequency averaging or modification could be used when the output DOF are the same but the new system dynamics are somewhat different than the old system. DOF averaging could be used when the output DOF of the new system are different from the old system and when there are differences in the dynamics as well.

7.4.1 Frequency Averaging and Frequency Modification

Frequency modification aims to alleviate the effects of differences such as small mode frequency shifts between system A and B. Large changes in dynamics will be difficult to account for and will not be considered here. Two techniques are considered: averaging the specification over some frequency band and modifying (by stretching or warping) the frequency axis to shift peaks or other features in the system A specification to match similar features in the system B dynamics. System B's dynamics can be viewed by looking at the system ID test response.

Frequency averaged specifications can be made by applying a moving average to each DOF's APSD, averaging together the APSD values of several frequency lines and smoothing the APSD curve for each DOF. The size of the moving average window is user-specified and should be made based on the differences in dynamics between A and B. Generally, differences are larger and more complicated at higher frequency so the window size can be made frequency dependent, getting wider at higher frequency.

Frequency modification stretches or compresses the frequency axis of the specification APSDs by changing the frequency resolution (*df*) in frequency bands. The test engineer selects frequency bands for system A based on the features (e.g., peaks) in the specification and for system B based on the features in the response of a system ID test. The idea is to move a peak in the specification to a new frequency based on a similar peak in the system ID response of system B, as shown in the colored lines in Fig. 7.2. The frequency modification process is as follows:

- Obtain narrowband specification data for system A.
- Measure the response for system B in a laboratory system ID test.
- Plot the mean specification for system A on the same plot as the mean system ID response for system B, adjusting scales as needed to allow for visual comparison.
- Identify features in the system A and system B plot to match up. For example, in Fig. 7.2, we want to shift the first peak in the system A specification (blue solid line) to the first peak in the system ID response of system B (blue dotted line), so those peaks are chosen as the upper limit of the first band.
- Continue selecting features for the rest of the bandwidth, choosing similar features in A and B to define the band limits across the entire test frequency range.
- For each frequency band, move the specification APSD at each frequency line in the system A band to match the system B band by adjusting the frequency spacing, *df*. The result is the same specification APSD values but at slightly different frequencies due to the stretching or compressing needed to match the band limits of A to the band limits of B.
- Interpolate the unevenly spaced specification APSDs back to evenly spaced frequencies, resulting in a modified set of specification APSDs.

An example is shown in Fig. 7.3 where the specification has the same overall shape, but is moved to better align with the peaks in the system B system ID response. Note that these methods could be applied to the cross-terms (coherence and phase) as well, though care should be taken to ensure the averaged or modified CPSD remains positive-definite. If modifying the APSDs only, then the cross-terms for a complete specification CPSD can be taken from the coherence and phase of the system ID or buzz test.

7.4.2 DOF Averaging

In the more extreme case where the system dynamics are different and the output DOF are different, further modification of the specification is needed. While techniques are available to map response from one system to another or to infer response

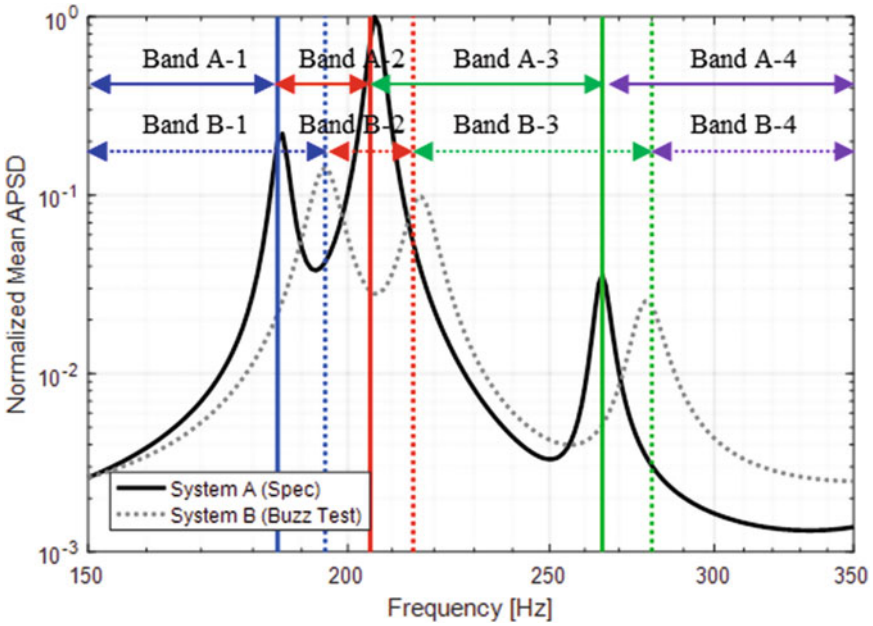

Fig. 7.2 Example frequency band limits shown in colored lines at peaks in the system A specification and system B system ID response

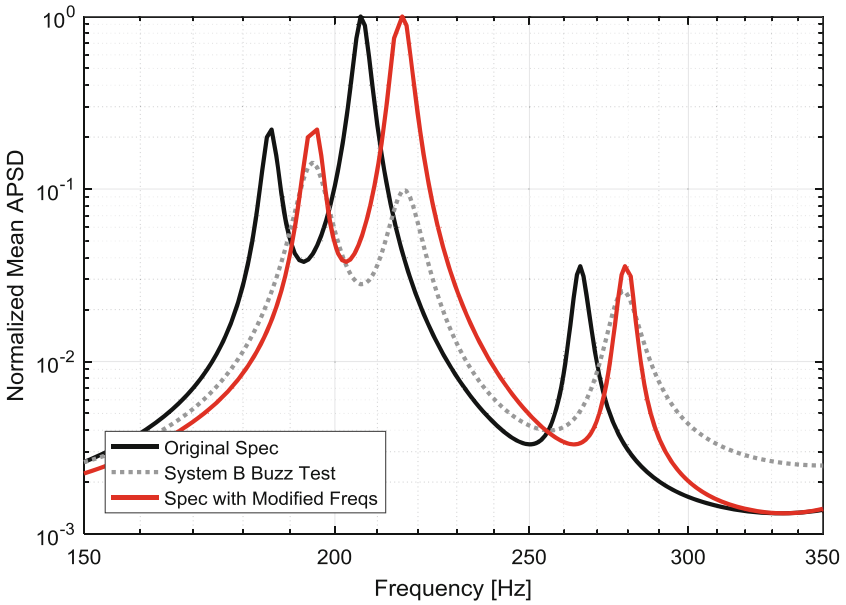

Fig. 7.3 Original system A specification (solid black) and the modified specification (solid red) which better matches the dynamics of system B (dotted gray)

at un-measured locations [5, 6], here simple DOF averaging is used as it does not require additional processing or knowledge of the system modes.

The basic premise is to get the averaged response of the laboratory test system, B, to match the averaged response of the specification from system A. Averaging the response simply entails averaging the APSDs for each DOF. To account for differences in the dynamics, such as peaks shifting, the APSDs can be averaged over frequency as well using octave averaging or some other band-wise frequency averaging method. The DOF to use in the average for each system should be chosen so the sets are generally similar, that is, have approximately the same number of DOF in similar locations and directions in each system. If they are different, for example, if system A has many DOF near the front and in the *X* direction but system B has many DOF near the back and in the *Y* direction, the averaged responses of the two DOF sets are incompatible and will not

result in a sensible test. Averaging the DOF will account for the exact location and direction differences, but care should be taken to make the system A and B DOF sets similar.

Averaging can be done over all DOF in the set, trying to match a single averaged APSD from A to a single averaged APSD from B. The process is as follows:

- Select the DOF from A and B to use in the average, choosing a similar number of DOF in similar locations and directions if possible.
- Frequency average the APSDs from the system A specification using octave or other frequency band averaging.
- Run a system ID test on system B in the laboratory and frequency average the APSDs from this test using the same frequency band averaging.
- Average the APSDs from A and B to create a single averaged APSD for A and for B.
- Take the ratio of A to B to give a set of scale factors at each frequency band which says how much the system ID input needs to change to get the averaged response of B to match the specification from A.
- Interpolate these scale factors from band center frequencies to narrowband frequencies.
- Scale the narrowband system ID response by the narrowband scale factors to give a set of scaled, narrowband APSDs.
- Use the scaled system ID APSDs along with the system ID coherence and phase to create the modified laboratory test specification CPSD.
- Run the MIMO test.

Alternatively, averaging can be done over groups of DOF. These groups could be chosen by region (e.g., front, back, top, bottom) and/or by direction (e.g., *X*, *Y*, *Z*). Each group can have one or more DOF depending on what is available or how much emphasis is placed on a particular DOF or set of DOF. Then, the group averaged APSDs can be used to create scale factors as described above, except that there will be a different set of scale factors for each group of DOF. Note that the average of these scale factors for each group will not equal the overall average scale factor due to the relative influence of individual DOF based on the number of DOF per group. The scale factors are interpolated to narrowband frequency lines and applied to the system ID response APSDs group-by-group to yield a set of scaled system ID APSDs which can be combined with the system ID coherence and phase to create the test specification CPSD.

7.5 Example Using the BARC

These techniques will now be demonstrated using a structural dynamics model of a system known as the BARC [7, 8]. FRFs are synthesized from modes of the model over the bandwidth 90–900 Hz, a bandwidth that comprises several different modes and has interesting dynamics. To simulate dynamic differences between field and laboratory systems and to have two sets of output DOF, three versions of this system are created:

- System A: nominal dynamics, original output DOF
- System B: different dynamics, original output DOF
- System C: different dynamics, new output DOF

The dynamics were changed by modifying the mode frequency and damping prior to synthesizing FRFs. The changes for B and C are the same: modes 7–10 were made 5% stiffer, and modes 11–14 were made 5% softer. This causes mode 10 at 440 Hz to swap with mode 11 at 468 Hz. Modal damping was changed from 1% for all modes in system A to 2% for modes 7–10 and 0.5% for modes 11–14 for systems B and C. While these are not physical changes, they do create useful differences in system dynamics as shown in the FRF magnitude sum in Fig. 7.4. Output DOF are the same for A and B, with two triaxial accelerometers on the top and two on the left leg of the component. Output DOF for C are different, with a different triaxial on the top and two on the right leg of the component. Accelerometer 110 is the same between all three systems as shown in Fig. 7.5.

A field environment is simulated using uncorrelated inputs at one location in three directions *X*, *Y*, and *Z* at the base of each system A, B, and C as shown in Fig. 7.6. The response from the simulated field environment is what should be replicated, as closely as possible, in a laboratory test of B and C. Inputs for the laboratory tests are different from the field test, using four inputs in the *Y* direction. A comparison of input DOF is shown in Fig. 7.6. The specifications for the laboratory tests are derived from the field response from system A only. Specification modification techniques are used to modify the specification from A to account for the differences in dynamics between system A and B and the differences in both the dynamics and DOF between system A and C.

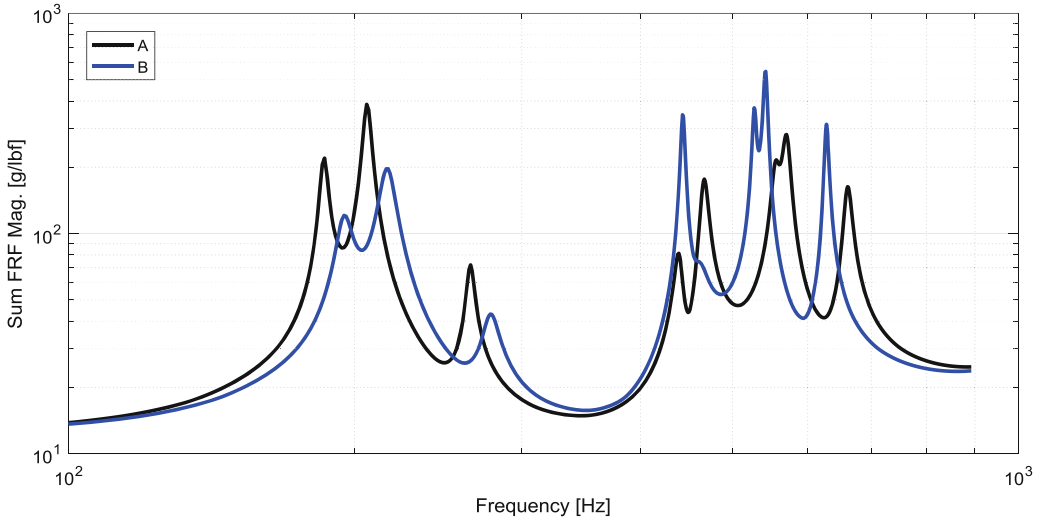

Fig. 7.4 FRF magnitude sum comparing the dynamics in A vs. B

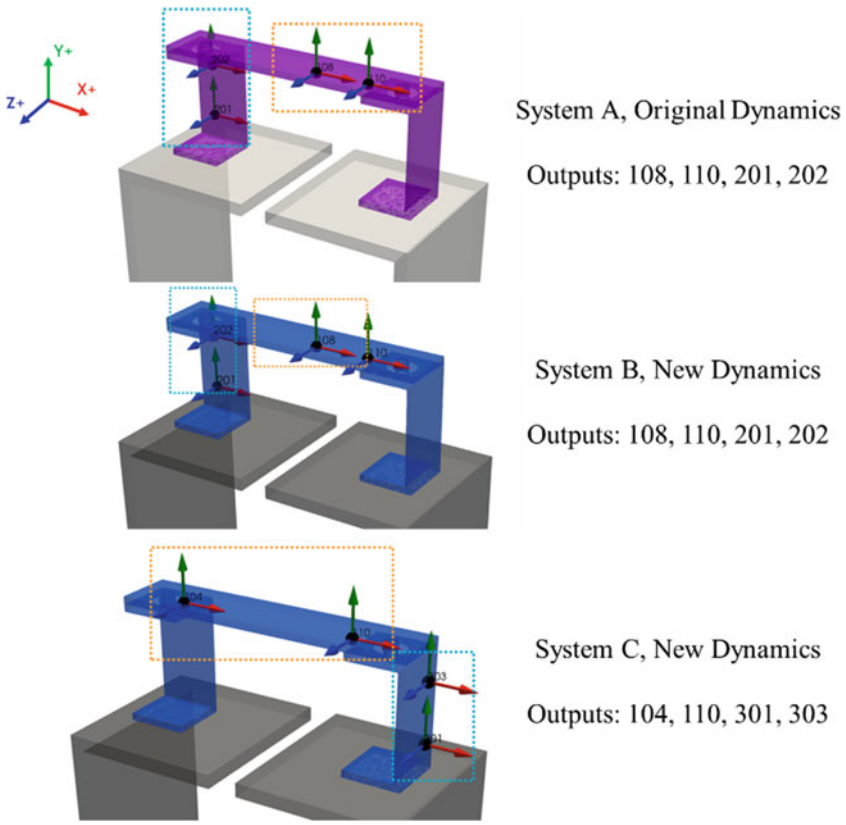

Fig. 7.5 Output DOF locations for each of the three systems. DOF groups shown in dotted line boxes

Laboratory MIMO tests are simulated first using the traditional MIMO specification approach where the field response from A was applied directly as the specification for a MIMO test of B and C. For C, because the output DOF do not match exactly, the nearest DOF was chosen. This introduces errors as there is significant mismatches between the locations of some of the A and C DOF.

Next, laboratory MIMO tests are simulated using the different specification modification methods described above. For system B, frequency averaging and frequency modification are applied to account for the differences in dynamics between A and B. For system C, DOF averaging is applied as an average of all DOF and then as an average of groups of DOF. The two

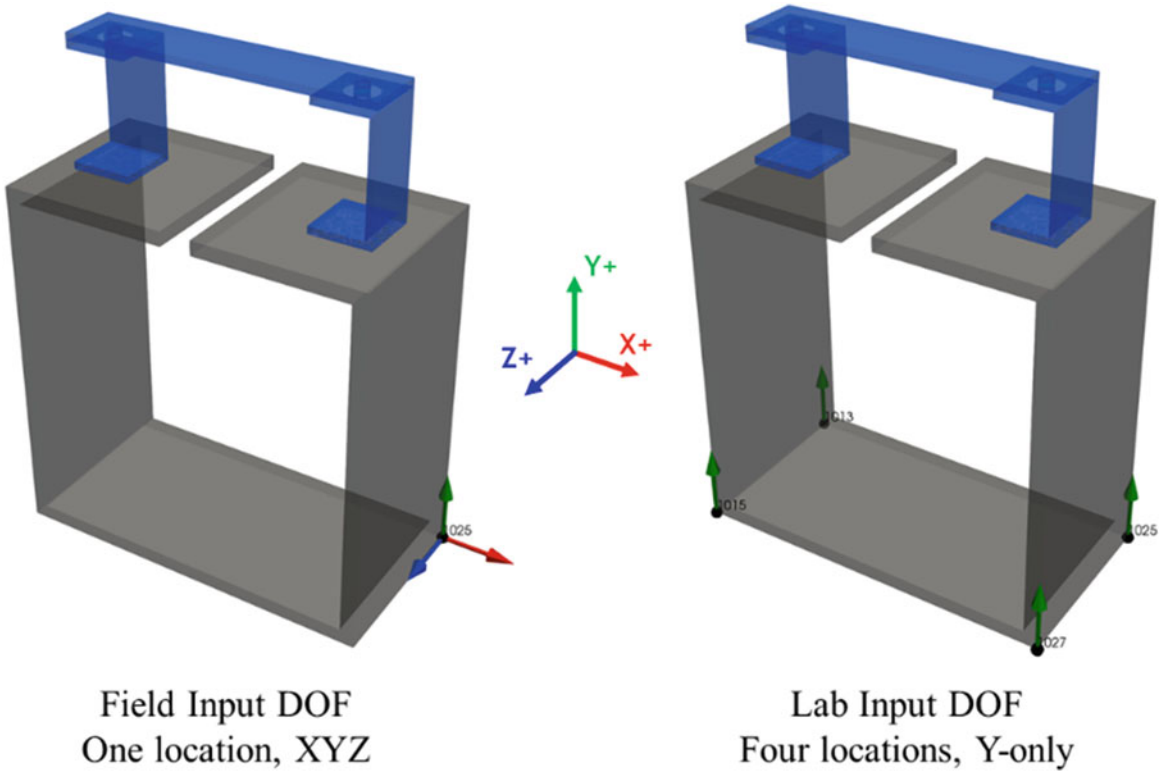

Fig. 7.6 Input DOF locations for the field and laboratory tests shown as arrows in *X* (red), *Y* (green), and *Z* (blue)

triaxial accelerometers on the top of the component formed one group (108, 110 and 104, 110), and the two accelerometers on a leg of the component formed a second group (201, 202 and 301, 303). These DOF groups are shown as dotted line boxes in Fig. 7.5.

7.6 Observations

Results of the simulated laboratory MIMO tests for each of the four modified specification methods are shown in this section. Comparisons are made between the modified and original (traditional) specification cases. These simulated tests result in response CPSDs with all 12 output DOF and 4 input DOF, but for simplicity the results are shown as four plots: the output APSD for one DOF, 110Y+, a comparison of the mean input and output APSD, and the dB error of 1/6th octave-average APSDs. The dB error is with respect to the field environment response of system B and C, the actual response that should be replicated by one of the laboratory tests. A "good" test should match the actual environment response well at each DOF (meaning the dB error should be near zero), and the overall system response should match (meaning there is little bias error in the mean response). Further, as many random vibration service environment loads are smooth functions of frequency (i.e., there are not significant tones or jumps between frequency lines), the inputs in a test should also be smooth functions of frequency. These plots should provide a sufficient view into the DOF-by-DOF response accuracy, the overall system response accuracy, and the input spectrums and levels.

A general trend in these results is an over- or under-test at some frequencies, which is in part due to the damping shift applied between system A and systems B and C. As the specification in all cases is based on the system A field response, there will naturally be some error in the response amplitude near modes where the damping was higher (modes 7–10, 195–461 Hz) or lower (modes 11–14, 443–627 Hz). The expected error is an over-test at low frequency and an under-test at high frequency due to this damping error, which is what is seen in each of the four cases. If the damping changes were smaller, this amplitude error would be smaller. The damping differences were included as it is a typical system-to-system difference encountered in real testing.

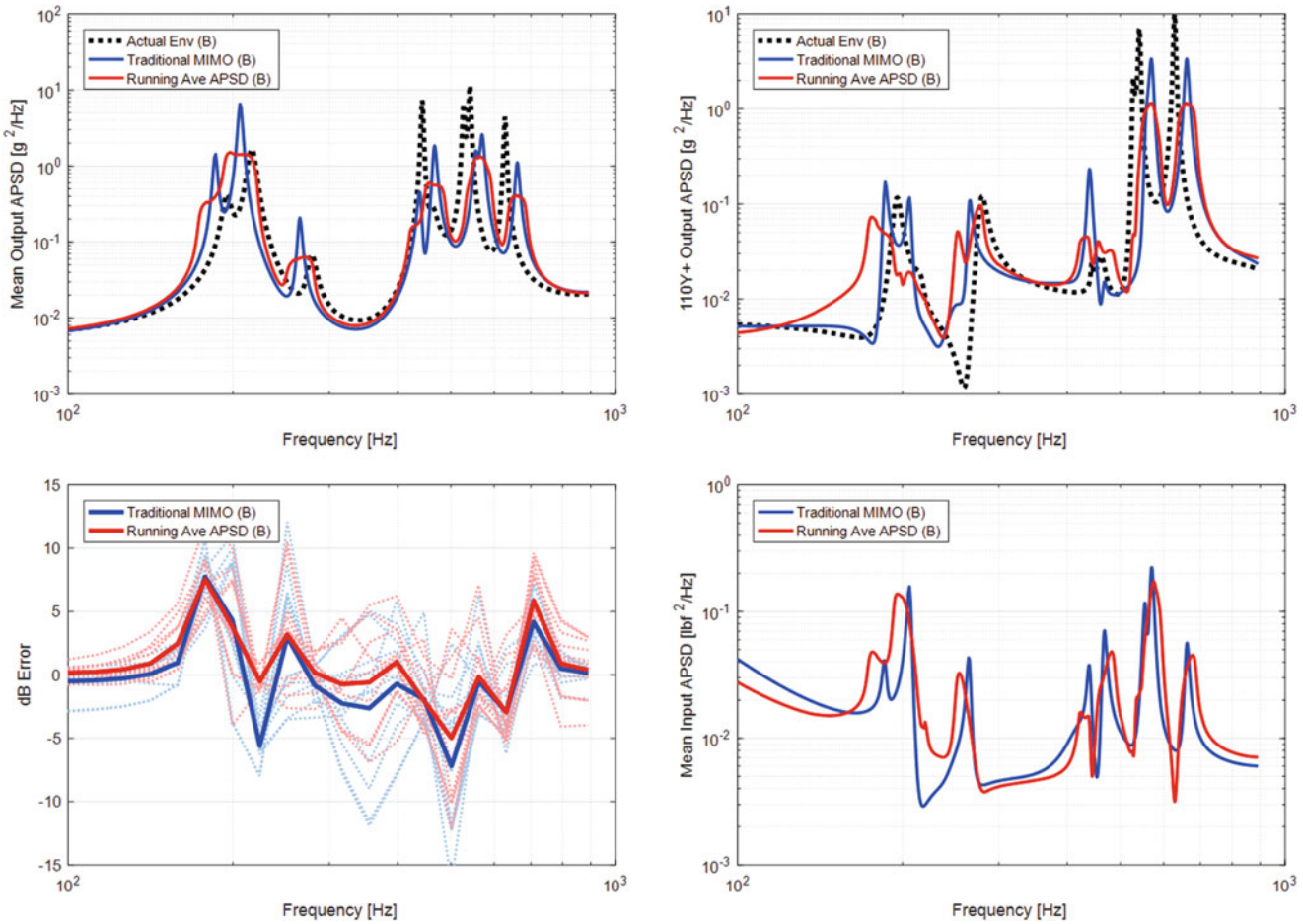

Fig. 7.7 Results of simulated laboratory MIMO test using traditional and frequency averaged specifications. Top left: mean APSD over all 12 output DOF. Top right: APSD for one DOF, 110Y+. Bottom left: dB error in 1/6th octave APSD relative to the field response. Dotted lines: individual DOF. Solid lines: mean over all 12 DOF. Bottom right: mean input force APSD

7.6.1 Frequency Averaged Specification

As expected, the frequency averaged specification results in response with flatter peaks with response energy distributed over a wider frequency range (Fig. 7.7). This helps account for peak shifts to some degree but does not completely adjust the specification to match the laboratory system dynamics. The result, overall, is a spreading of input and output energy over a wider frequency range, which could be useful in cases where there are lightly damped and closely spaced modes.

7.6.2 Frequency Modified Specification

The frequency modified specification does cause the laboratory system response to match the field response more closely than both the traditional specification and frequency averaged specification as shown in Fig. 7.8. As intended, frequency bands selected to stretch and compress the specification frequency axis seem to be effective in moving the specification and aligning to features in the system B dynamics. The result is a good match to the overall output APSD and individual DOF APSD. The dB error plot shows that the mean error is near zero over the entire frequency range and the spread in error among all individual DOF is small, indicating the overall system response is accurately replicated by the test. The input APSDs are smoother and flatter than the traditional test, which is sensible since the actual environment was smooth and flat. This indicates that the MIMO controller does not have to put energy in or take energy away at frequencies where there is a mismatch between the specification and laboratory system dynamics.

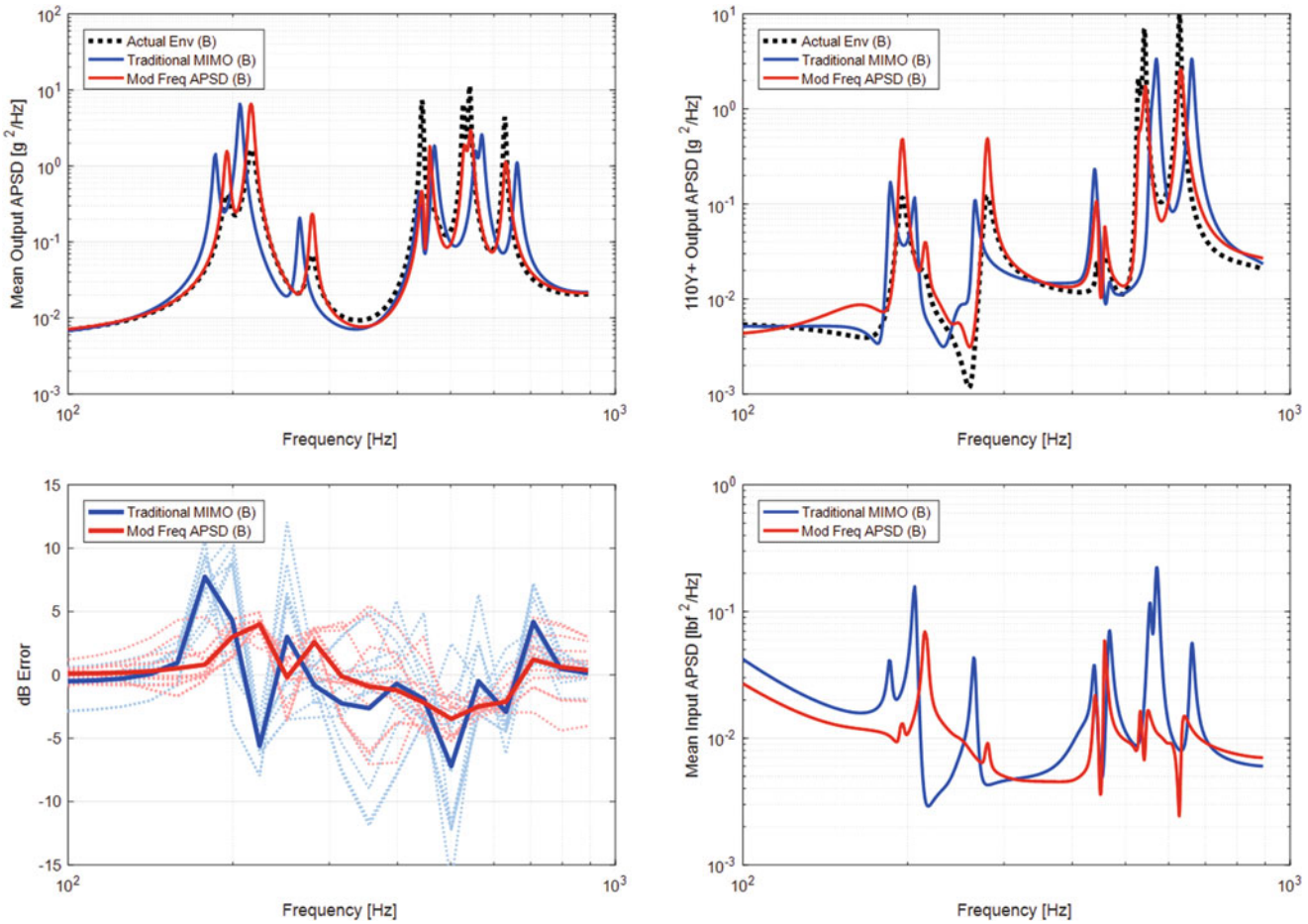

Fig. 7.8 Results of simulated laboratory MIMO test using traditional and frequency modified specifications. Top left: mean APSD over all 12 output DOF. Top right: APSD for one DOF, 110Y+. Bottom left: dB error in 1/6th octave APSD relative to the field response. Dotted lines: individual DOF. Solid lines: mean over all 12 DOF. Bottom right: mean input force APSD

7.6.3 All DOF Averaged SPEC

Despite averaging over all DOF and also over frequency bands, the all DOF averaged specification worked quite well in this case (Fig. 7.9). The output APSD matches the actual response well, and better than the traditional test, meaning the averaged specification allowed the laboratory system to vibrate as it naturally should. The input APSDs are very smooth over the frequency range, indicating the controller is not having to fight the system dynamics to match the specification at individual frequency lines. Both the overall error and the spread in error among all the individual DOF is small, indicating the system response is accurate.

It should be noted that the quality of the test from this averaged specification approach is dependent on the test setup. Shakers in different locations or directions could provide a different result, which could be quite bad in some cases. Care should be taken to design the test with boundary conditions and shaker input locations to mimic the field conditions as closely as possible.

7.6.4 Group DOF Averaged SPEC

Averaging the DOF by groups of gauges on the top and on the legs of the component changes the results slightly vs. averaging over all the DOF (Fig. 7.10). Generally, the test works well and provides a more accurate result vs. using a traditional

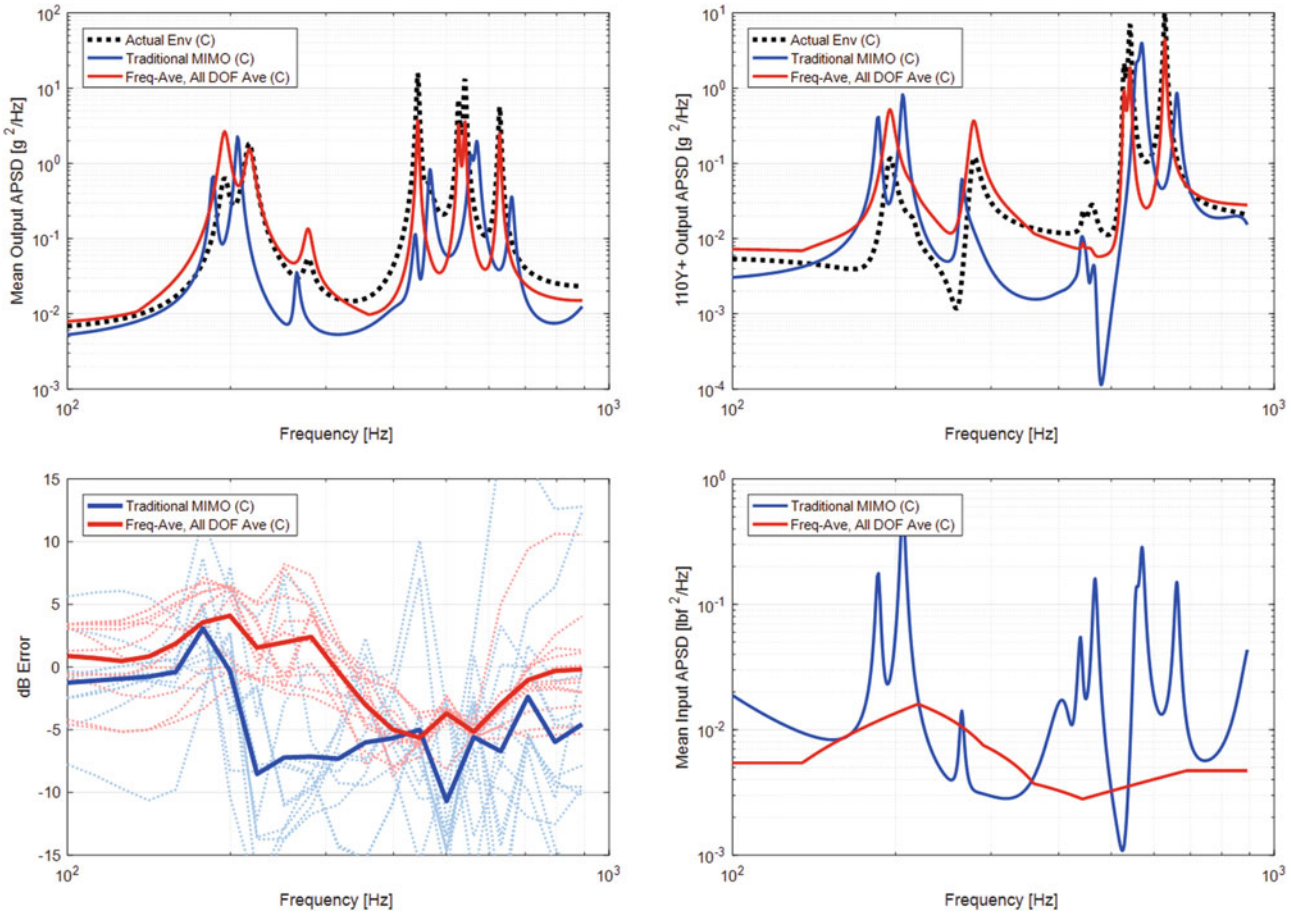

Fig. 7.9 Results of simulated laboratory MIMO test using traditional and all DOF averaged specifications. Top left: mean APSD over all 12 output DOF. Top right: APSD for one DOF, 110Y+. Bottom left: dB error in 1/6th octave APSD relative to the field response. Dotted lines: individual DOF. Solid lines: mean over all 12 DOF. Bottom right: mean input force APSD

specification and trying to force dissimilar DOF to match. The response error is marginally worse than averaging over all the DOF, and the inputs APSDs are less smooth.

7.7 Conclusion

MIMO vibration testing has several advantages over traditional single-axis testing, but it comes at the cost of added complexity in the test setup, control, and specification. While there have been many advances in test setup and control over the years, specification approaches have remained fairly standard, relying on field-measured narrowband CPSD data. This greatly constrains the applicability of MIMO testing for new systems or systems for which field data does not exist.

This work presents techniques to modify MIMO random vibration specifications to account for differences in system dynamics and measurement DOF (locations and directions) using averaging over frequencies and DOF or warping the frequency axis. Different conditions may require one technique over the other depending on how different the laboratory system is from the field-tested system. All techniques rely on readily available FRF data, and all techniques result in a fully populated CPSD specification which can be imported into any typical MIMO vibration controller. This should enable MIMO testing of more systems by relaxing the strict requirements of the specification and providing needed flexibility in modifying the specification to accommodate the dynamics of the laboratory test system.

Future efforts could focus on DOF mapping and averaging methods which account for differences in dynamics of the field and laboratory systems and differences in DOF locations. Transfer path analysis or expansion may be tools that could be applied for this purpose. The frequency modification technique presented here relies on manual selection of the frequency

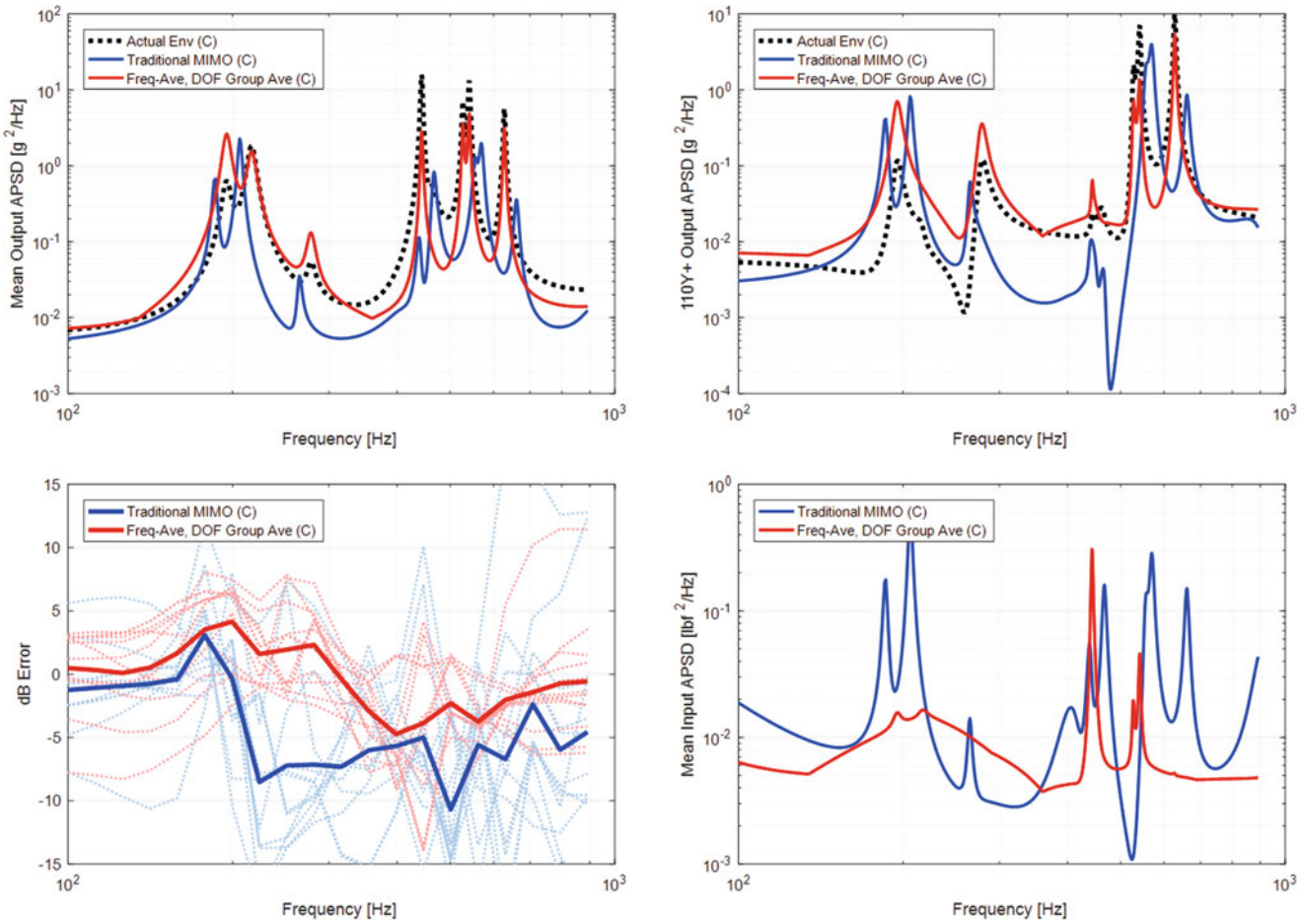

Fig. 7.10 Results of simulated laboratory MIMO test using traditional and DOF group averaged specifications. Top left: mean APSD over all 12 output DOF. Top right: APSD for one DOF, 110Y+. Bottom left: dB error in 1/6th octave APSD relative to the field response. Dotted lines: individual DOF. Solid lines: mean over all 12 DOF. Bottom right: mean input force APSD

bands. This could be automated using deflection shape matching between the specification and the system ID data sets. In this work, the DOF averaged specification methods rely on scaling of the system ID test responses, which used flat, uncorrelated inputs. It would be possible to use partially correlated, shaped inputs for this initial test, which could better mimic the field environment response and provide a more accurate result. Investigating how to determine appropriate correlation and shaping of the initial test would be useful.

Acknowledgments Sandia National Laboratories is a multimission laboratory managed and operated by National Technology and Engineering Solutions of Sandia, LLC., a wholly owned subsidiary of Honeywell International, Inc., for the US Department of Energy's National Nuclear Security Administration under contract DE-NA0003525.

References

1. Daborn, P.M.: Smarter Dynamic Testing of Critical Structures, PhD Thesis, University of Bristol, 2014
2. Daborn, P.M., Roberts, C., Ewins, D.J., Ind, P.R.: Next-generation random vibration tests. In: Proceedings of IMAC XXXII, the 32nd International Modal Analysis Conference, Orlando, FL, 2014
3. Musella, U., D'Elia, G., Manzato, S., Peeters, B., Guillaume, P., Marulo, F.: Analyses of target definition processes for MIMO random vibration control tests. In: Proceedings of IMAC XXXV, the 35th International Modal Analysis Conference, 2017
4. Department of Defense Test Method Standard, MIL-STD-810G, Environmental Engineering Considerations and Laboratory Tests, Department of Defense, 2008
5. van der Seijs, M.V., de Klerk, D., Rixen, D.J.: General framework for transfer path analysis: history, theory and classification of techniques. Mech. Syst. Signal Process. **68-69**, 217–244 (2016)

6. O'Callahan, J., Avitabile, P., Riemer, R.: System Equivalent Reduciton Expansion Process (SEREP). In: Proceedings of IMAC VII, the 7th International Modal Analysis Conference, Las Vegas, NV, 1989
7. Schoenherr, T., Skousen, T., Jones, R., Soine, D.: Boundary Conditions in Environmental Testing Challenge Problem, 2018. [Online]. Available: https://connect.sandia.gov/sites/TestBoundaryConditions
8. Schultz, R., Schoenherr, T.F., Owens, B.C.: A proposed standard random vibration environment for BARC and the boundary condition challenge. In: Proceedings of IMAC XXXIX, the 39th International Modal Analysis Conference, 2021

Chapter 8
On the Selection of Mode Shapes Used in Optimal Sensor Placement

Kultigin Demirlioglu, Semih Gonen, and Emrah Erduran

Abstract Structural health monitoring (SHM) is gaining more attention, particularly for bridge structures to continuously evaluate their structural performance and assure their serviceability and safety throughout their service life. To assure reliable SHM systems, optimal sensor placement (OSP) is a cornerstone since it directly influences the quality of obtained data and, thus, the accuracy of the diagnosis. Hence, determining the optimal sensor configuration is a critical step to acquire the maximum information on the structural behavior. Of the available OSP methods, the effective independence method (EFI), which aims to assure that the mode shapes identified from the recorded vibrations are orthogonal to each other, is popular and widely used in literature. Despite its popularity, there are no clear guidelines on how to select the modes that will be included in the OSP application. This chapter evaluates the impact of various parameters including the selected number of mode shapes and sensors on the results of OSP using EFI.

Keywords Optimal sensor placement · Effective independence method · Structural health monitoring · Finite element modeling · Modal mass participation

8.1 Introduction

During their lifetime, structures are exposed to various environmental conditions, natural hazards, and excessive loads. This exposure can lead to structural degradation, poor structural performance, and, in extreme cases, extensive damage or even failure in structures. Structural health monitoring (SHM) plays a crucial role in early detection and prevention of possibly dangerous scenarios to extend the service life of structures. A cost-effective and functional SHM application can be realized by installing the minimum number of sensors that provide the maximum information. In essence, optimal sensor placement (OSP) enables a robust system that minimizes the cost and assures the accuracy of structure's health diagnosis without compromising the quality. Herein, the primary concern is to determine the number and location of sensors to obtain the most meaningful information for the identification of dynamic behavior of the structure [1]. Optimizing the number and location of the sensors is likely to increase the reliability of various SHM applications such as system identification, finite element model updating, and structural damage detection.

In literature, various optimization algorithms have been developed for OSP, such as effective independence method (EFI) [2], Guyan reduction [3], driving point residue [4], and kinetic energy [5] methods. In a study, these methods were compared for on-orbit modal identification of space platforms [6]. The OSP methods have also been applied on civil engineering structures, particularly bridges. The efficiency of different sensor placement criteria, based on a comparison of the numerical mode shapes for long-span bridges, was investigated using modal expansion techniques [1, 7]. Castro-Triguero et al. [8] carried out a comparative study to evaluate how parametric uncertainties affect the OSP algorithms including the Fisher information matrix and energy matrix rank optimization for the modal analysis of a truss bridge. Several numerical studies were also conducted to determine sensor configurations for modal parameter identification of bridges [9–11].

Of these methods, the effective independence method is arguably the most used method for optimal sensor placement in bridge structures [12]. The effective independence (EFI) method was introduced by Kammer [2], and it seeks the optimal set of degrees of freedom (DOFs) to place the sensors among all the candidate locations on the structure. The candidate measurement locations are provided by the user. The optimal sensor configuration is determined based on the principle

K. Demirlioglu · S. Gonen (✉) · E. Erduran
Department of Civil Engineering and Energy Technology, Oslo Metropolitan University, Oslo, Norway
e-mail: kultigin@oslomet.no

C. Walber et al. (eds.), *Sensors and Instrumentation, Aircraft/Aerospace and Dynamic Environments Testing, Volume 7*,
Conference Proceedings of the Society for Experimental Mechanics Series, https://doi.org/10.1007/978-3-031-05415-0_8

of linear independence of the mode shapes included in the analysis. Although widely used in practice, there are no clear guidelines on how to determine the number of mode shapes that will be used in the EFI algorithm nor on the selection of the mode shapes. In addition, experimental investigations provide only a limited number of structural modes due to various limitations in equipment and identification methods. In this context, the following question remains unanswered: How many of the structural modes should be considered in the analysis to determine the optimal sensor configuration using the EFI method, and which of the available mode shapes should be selected? Further, what is the impact of these parameters on the results of the EFI algorithm?

In order to provide a first insight to these questions, a numerical study has been carried out. For this purpose, a five-span continuous bridge situated on the railway network between the cities of Oslo and Trondheim in Norway is used. A three-dimensional (3D) finite element model of the bridge was generated, and the representative values for the unknown boundary conditions were determined with the help of a sensitivity study. The required modal information was extracted from the numerical model to provide data for OSP analysis. The effective independence method was adopted as the OSP algorithm and applied to determine 8, 12, and 18 sensor locations for 4 separate cases, each with a different set of target modes. The impact of the number of mode shapes included in the EFI algorithm on the location of the sensors was evaluated.

This chapter is structured as follows: First, the railway bridge used in the study is described, and details about the numerical model are provided. Second, the theoretical formulation of the EFI method is provided. The next section summarizes the application of the EFI algorithm for 12 different cases, and the final sensor configurations for each case are presented. Lastly, the main conclusions of this study and recommendations for future work are presented.

8.2 The Railway Bridge and Numerical Modeling

The railway bridge investigated in this study is a five-span prestressed concrete continuous bridge with a total length of 48.6 m. It has an unusual geometric shape with an extension of 4.5 m in each direction from both abutments. Due to the bridge's complex geometry and boundary conditions, its structural behavior is more complicated than characteristic bridges. Further details about the analyzed bridge are summarized in detail in [13].

A 3D finite element model of the bridge was generated using SAP2000 software (Fig. 8.1a). Shell elements with four nodes were used for modeling the reinforced concrete (RC) bridge deck, which has a thickness of 0.5 m and a width of 5.8 m. The wing walls of the bridge deck have a thickness of 0.70 m and a height of 0.95 m on the deck's edges. The pier caps, which are directly attached to the prestressed concrete deck, have a diameter of 5.6 m, and their thickness ranges from 0.50 to 0.85 m. The wing walls and pier caps were also modeled with shell elements. The mesh size of the FEM model was optimized as 0.45 $\times$ 0.55 m rectangular shell elements for computational efficiency. The piers that have a cylindrical shape and diameter of 1.4 m positioned at the 18.2 m and 37.0 m of the bridge were modeled using elastic Bernoulli beam-column elements. Elastic bearings that are located 4.5 m away from the bridge's ends were defined using three translational elastic springs, K_v, K_t, and K_l in the vertical, transverse, and longitudinal directions, respectively. Although there is a physical gap between the bridge deck and the rest of the railway at both ends of the bridge, the railway infrastructure consisting of rails, sleepers. and 40-cm-thick ballast is likely to provide resistance in both longitudinal and vertical directions as well as rotational resistance about the transverse axis. This resistance is modeled using linear springs at both ends of the bridge: Fig. 8.1b, c.

One of the biggest challenges related to the developed FE model is the large uncertainties associated with the stiffness of the springs that represent the resistance of the railway infrastructure at the ends of the bridge. The stiffness properties of the springs could not be computed from material and geometry information as such information is not provided in the design drawings and cannot be easily deducted from inspections. In order to overcome this shortcoming, a comprehensive sensitivity analysis was conducted to determine the upper and lower bound values of the springs assigned at the boundaries of the bridge. The vertical, longitudinal, and rotational spring coefficients, separately, were increased incrementally from zero (the lower bound value) until a maximum value where the modal properties of the bridge become insensitive to this coefficient, and no change was observed in the modal properties corresponding to a further increase in the stiffness. The maximum values of the vertical, longitudinal, and rotational spring coefficients for the bridge ends (see Fig. 8.1c) were obtained as 825,000 kN/m, 1,925,000 kN/m, and 27,500,000 kN.m/rad, respectively. As the effects of the number of mode shapes on OSP are being investigated in the context of this study, these parameters are given a final value, and only a single FE model is generated to determine the bridge's dynamic properties. The final values of the modeling parameters are determined as the median values obtained from the sensitivity study. The values of the parameters used in the final FE model are summarized in Table 8.1.

The dynamic behavior of the bridge in the vertical direction is of primary concern in this study; thus, the horizontal and transverse behavior is not investigated. As a result of the eigenvalue analysis conducted on the numerical model, the first

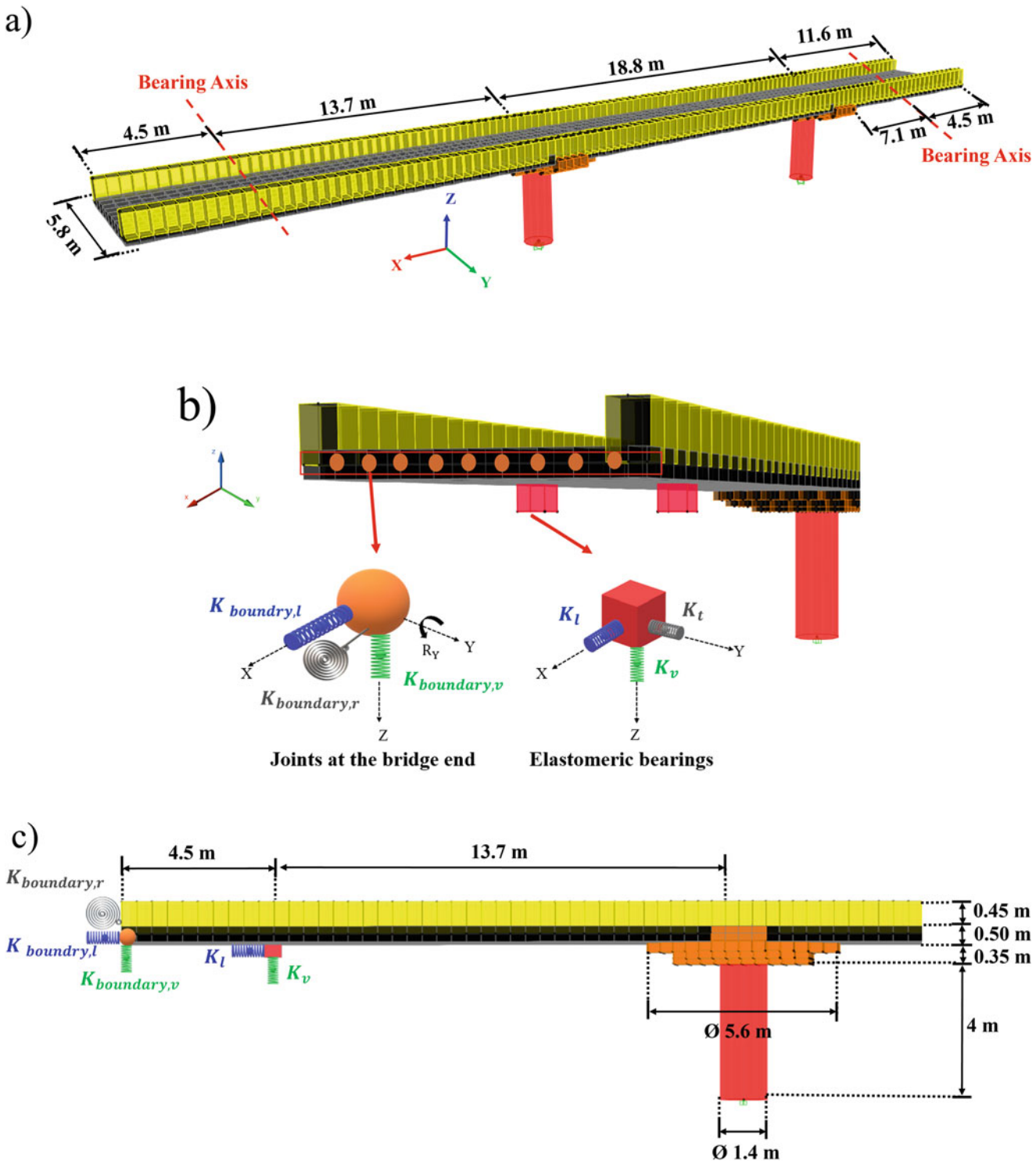

Fig. 8.1 FE model of the bridge (**a**) 3D view, (**b**) springs used for defining the boundary conditions and the elastomeric bearings, and (**c**) elevation view

eight vertical mode shapes and their modal mass participation ratios (MMP) were obtained and are presented in Fig. 8.2. It should be noted that the modal mass participation factor indicates the degree of the participation of individual modes to the total dynamic behavior [14], and they are also presented in this study as additional information. The modal frequencies range from 8.40 to 35.68 Hz, while the total MMP ratio reaches to 82% when all eight modes are considered. The first three modes,

Table 8.1 Parameters used in the benchmark numerical model

Parameter	Value
Young's modulus of concrete, E_c,	38,000 MPa
Spring constant in vertical direction,Elastomeric bearing (K_v)	815,000 kN/m
Spring constant in horizontal directions,Elastomeric bearing (K_l & K_t)	1500 kN/m
Boundary condition,Vertical spring stiffness, $K_{boundary,\ v}$	440,000 kN/m
Boundary condition,Longitudinal spring stiffness, $K_{boundary,\ l}$	1,100,000 kN/m
Boundary condition,Rotational spring stiffness, $K_{boundary,\ r}$	2,750,000 kN.m/rad

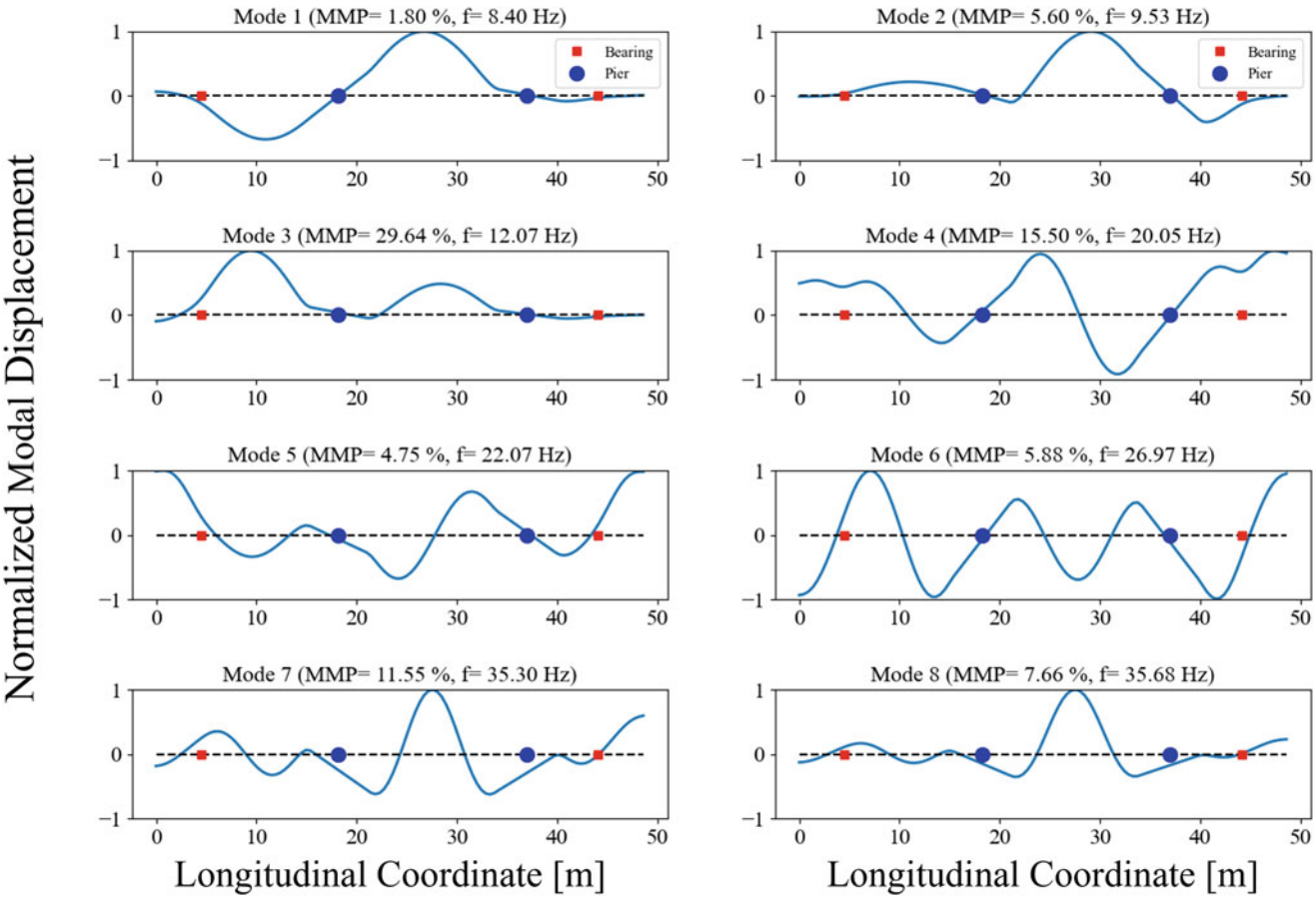

Fig. 8.2 Normalized vertical mode shapes – side view

accounting for a total MMP of 37%, have substantial modal displacements at the mid spans of the bridge deck. Starting from the fourth mode, higher modal displacements are detected at the outer spans before and after the elastomeric bearings.

8.3 Application of the EFI Method and the Optimal Sensor Placement

The EFI method ranks the possible sensor locations based on the linear independence of the mode shapes. The first step in this method is to establish the mode shape matrix ($\mathbf{\Phi}$) of the structure. For this, the target modes are manually selected considering factors such as their contribution to the dynamic behavior, natural vibration frequency of the mode, and the feasibility of detecting them experimentally. The rows of the mode shape matrix represent the degrees of freedoms of the candidate locations, while each column of the matrix provides the modal displacements for each of the mode shapes considered.

The second step of the EFI method is to compute the Fisher information matrix (**FIM**), defined as the product of the mode shape matrix and its transpose; see Eq. 8.1:

$$\mathbf{FIM} = \boldsymbol{\Phi}^T \boldsymbol{\Phi} \tag{8.1}$$

The EFI method aims to determine the sensor configuration that maximizes the determinant of the **FIM** for a given number of sensors. This can be achieved in an iterative way by eliminating DOFs that contribute least to the linear independence of the mode shapes at each iteration. Hence, in the next step, the number of sensors (DOFs) is reduced iteratively by means of the orthogonal projection matrix, $\boldsymbol{E}$, that is defined as the product of the mode shape matrix, the inverse of the **FIM**, and the transpose of the mode shape matrix, given in Eq. 8.2.

$$\boldsymbol{E} = \boldsymbol{\Phi}\, \mathbf{FIM}^{-1}\, \boldsymbol{\Phi}^T \tag{8.2}$$

The fractional contribution of the ith DOF to the rank of the $\boldsymbol{E}$ matrix is represented by each member of the diagonal of the matrix [7]. When the diagonal of the matrix $\boldsymbol{E}$ is sorted from the highest value to the lowest, the DOF with the lowest value, i.e., the DOF that contributes to the linear independence of the mode shapes the least, is determined and removed from the mode shape matrix. This elimination process is repeated until the desired number of sensors is acquired.

In this study, the candidate DOFs where the sensors can be placed are determined as follows: five longitudinal axes parallel to each other, dividing the bridge width at approximately equal distance, were utilized. Then, by setting the candidate sensor locations at 1.25 m intervals, a total of 38 DOFs were determined on each longitudinal axis along the 48.6 m bridge span. Hence, in total, 190 locations, i.e., 38 equally spaced locations at each of the 5 longitudinal axes, were selected as candidate locations for sensor placement. Once the candidate locations were determined, a comparative study was carried out to investigate the effects of the number of mode shapes and the total modal mass participation of the modes used in the EFI algorithm on the optimal sensor configuration. For this, four different cases were considered, where the mode shapes used in the EFI algorithm were selected as the first three, four, six, and eight vertical modes, respectively. The number of sensors was also varied between 8, 12, and 18 to observe whether the sensor configuration changes significantly when the number of sensors is increased. Thus, the OSP analyses were repeated for 12 separate cases: combination of three different number of sensors (8, 12, and 18) and four different set of modal shapes (3, 4, 6, and 8 modes).

For example, when the first eight vertical modes were used, the EFI algorithm was applied as follows: First, a mode shape matrix with 190 rows and 8 columns was constructed. Here 190 is the number of candidate locations, and 8 is the number of mode shapes used. Applying Eqs. 8.1 and 8.2, a 190 by 190 orthogonal projection matrix ($\boldsymbol{E}$) was obtained in the first iteration. In the diagonal of the matrix $\boldsymbol{E}$, the DOF with the lowest value, i.e., the one that contributes the least to the linear independence of the target mode shapes, was deleted from the mode shape matrix. Therefore, in the second iteration, a 189 by 8 mode shape matrix was used. Consequently, the mode shape matrix was updated as the DOF corresponding to the lowest diagonal value of the $\boldsymbol{E}$ was eliminated at each iteration. This iterative process was repeated until 8-, 12- and 18-sensor configurations were attained, as illustrated in Figs. 8.3, 8.4, and 8.5, respectively. Also depicted in these figures is the location of the sensors that are computed using three, four, and six mode shapes.

Figures 8.3, 8.4, and 8.5 show that the optimal sensor distribution computed using only the first three vertical mode shapes concentrated in the middle spans, i.e., spans two and three. From Fig. 8.2, it can also be observed that the modal displacements of these three mode shapes are the highest in these two spans. Since the modal displacements in the exterior spans are very low for all the three mode shapes considered, the algorithm struggles to select any of the locations in the exterior spans as it cannot confirm the linear independence of the mode shapes at these locations. The first and fourth spans do not get any sensors even for the 18-sensor configuration if only the first 3 or 4 mode shapes are considered in the analysis; see Fig. 8.5c. This shows the dominance of certain spans when a limited number of mode shapes are considered in the EFI algorithm.

When the number of modes shapes is increased to six, the distribution of the sensor locations becomes evenly distributed over the length of the bridge. However, the picture changes once again when the number of mode shapes considered is increased to eight (Fig. 8.3). While at least one sensor is located at each span when six mode shapes are considered in the analysis, the sensor locations remain concentrated at the third span when the number of mode shapes considered is increased to eight with the fourth span getting no sensors. This also stems from the low modal displacements at the fourth span in the seventh and eight mode shapes. It should be noted that an increase in the number of mode shapes used in a structural dynamics application leads to improved accuracy and results. However, in the case of application of the EFI algorithm on this bridge, it can be argued that including eight modes instead of six leads to an arguably inefficient sensor configuration. This argument is based on the expectation that a more evenly distributed sensor configuration provides better information on the mode shapes and the dynamic properties of the bridge. Since including eight modes in the algorithm leads to a more concentrated sensor layout than its counterpart obtained using six modes, it leads to a more inefficient layout as far as getting the most information from a sensor setup is concerned.

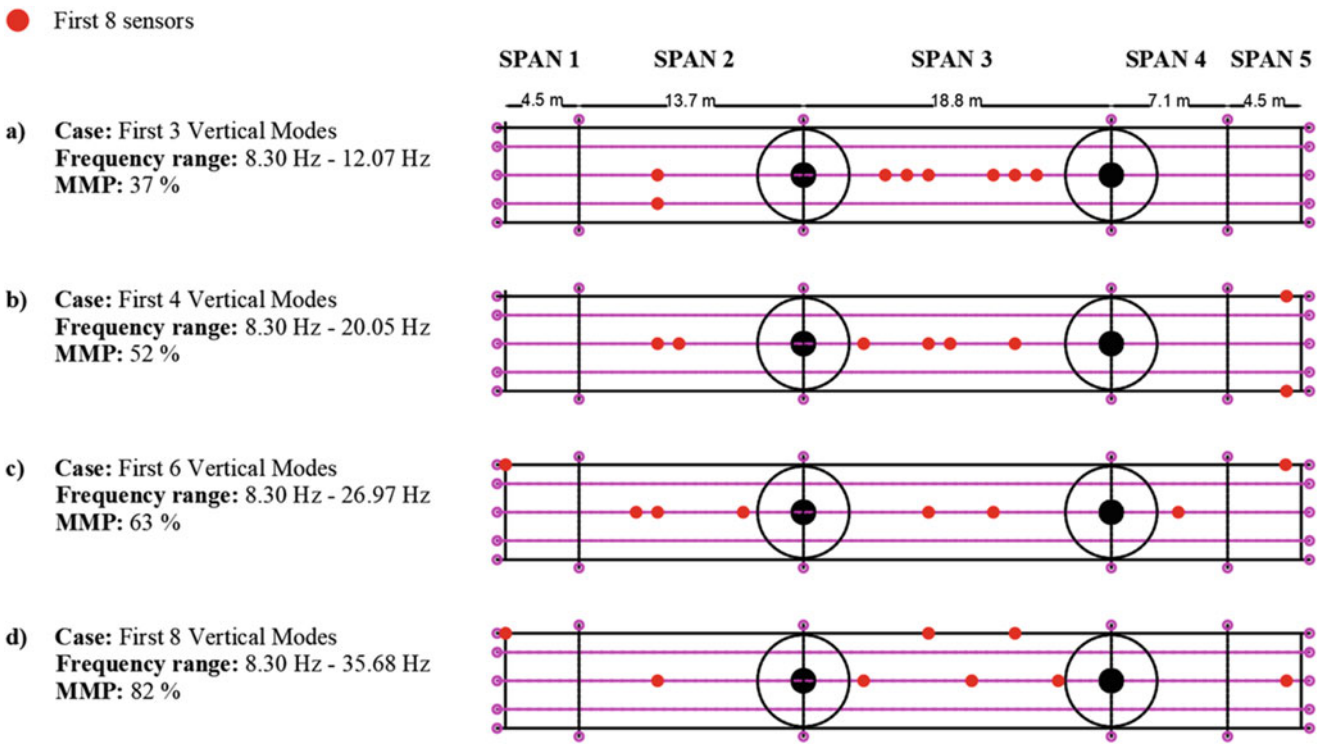

Fig. 8.3 Illustration of eight-sensor layout: (**a**) first three vertical modes, (**b**) first four vertical modes, (**c**) first six vertical modes, and (**d**) first eight vertical modes

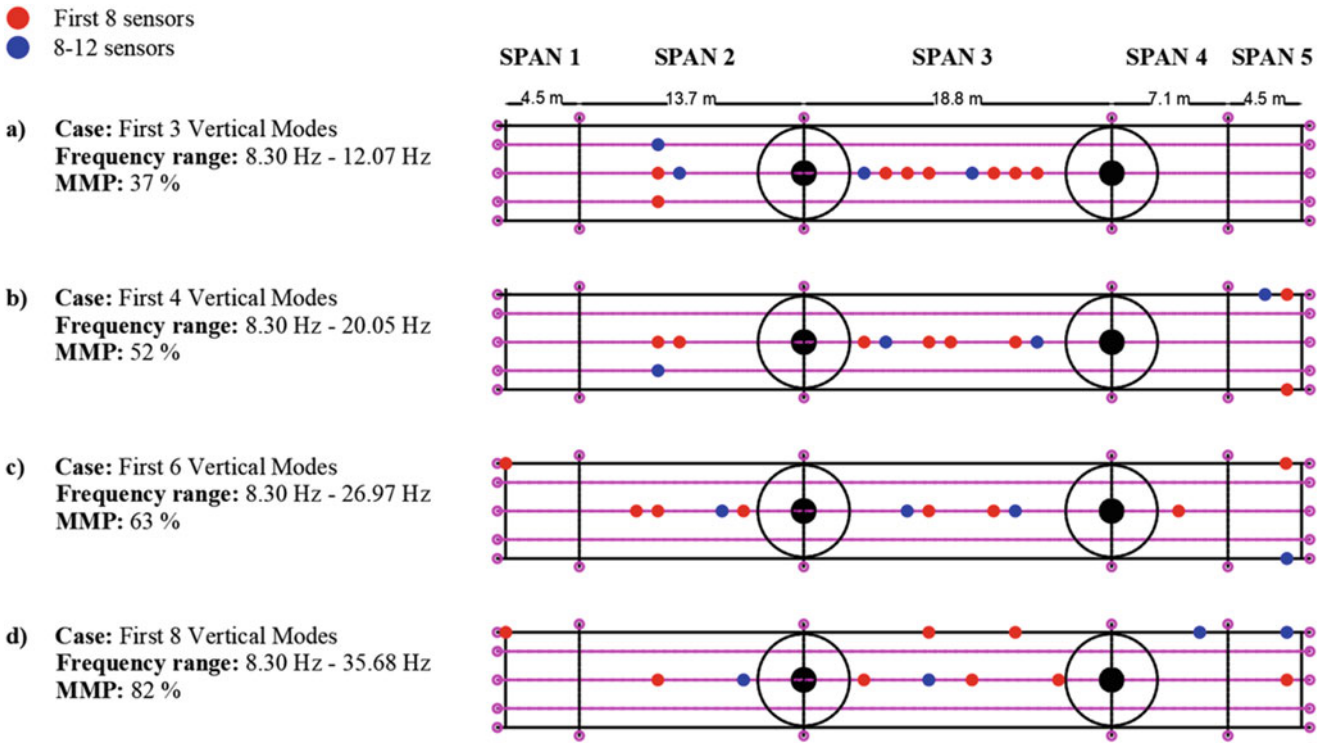

Fig. 8.4 Illustration of 12-sensor layout: (**a**) first 3 vertical modes, (**b**) first 4 vertical modes, (**c**) first 6 vertical modes, and (**d**) first 8 vertical modes

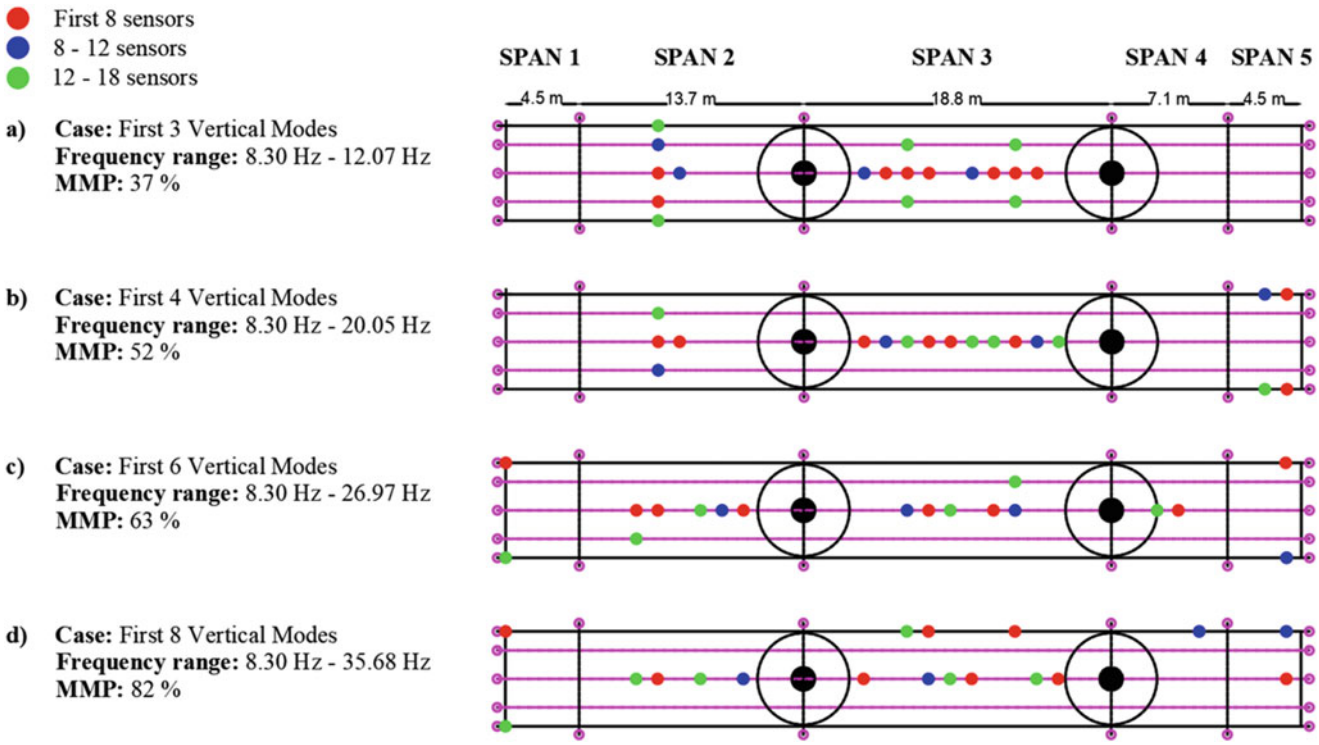

Fig. 8.5 Illustration of 18-sensor layout: (**a**) first 3 vertical modes, (**b**) first 4 vertical modes, (**c**) first 6 vertical modes, and (**d**) first 8 vertical modes

8.4 Conclusion

This chapter investigates the influence of the number of mode shapes included in the effective independence method for optimum sensor placement. The data that feed the EFI algorithm has been collected from a 3D FE model of the bridge. A comparative study has been conducted based on the selection of different target modes including the first three, four, six, and eight vertical modes of vibration. For each target mode scenario, 8-, 12-, and 18-sensor configurations were determined using the EFI algorithm.

The results reveal that the OSP algorithm with the mode shape matrix constructed using only the first few modes is not able to capture the complete structural behavior of the bridge since it places the sensors mainly at the middle spans of the bridge. By increasing number of vibration modes used in the EFI method to six, a more uniform distribution of sensors has been achieved. However, increasing the number of mode shapes to eight led again to a sensor layout that is more concentrated at the middle spans. In other words, considering that a more evenly distributed sensor layout is more likely to provide improved information about the dynamic behavior of the structure, increasing the number of mode shapes from six to eight leads to a less efficient sensor configuration. This observation is counterintuitive because, in general, increasing the number of mode shapes used in a structural dynamic application is expected to increase the accuracy of the results. Therefore, the results presented in this study show the complexity of the sensor optimization problem and highlight the need for further research to develop a methodology that is consistent and can systematically be applied to a wide range of structures.

Acknowledgments The authors acknowledge the collaboration with the Norwegian Railway Authority (Bane NOR).

References

1. Meo, M., Zumpano, G.: On the optimal sensor placement techniques for a bridge structure. Eng. Struct. **27**(10), 1488–1497 (2005)
2. Kammer, D.C.: Sensor placement for on-orbit modal identification and correlation of large space structures. J. Guid. Control. Dyn. **14**(2), 251–259 (1991)
3. Guyan, R.J.: Reduction of stiffness and mass matrices. AIAA J. **3**(2), 380 (1965)

4. Parker, G.R., Rose, T.L., Brown, J.J.: Kinetic energy calculation as an aid to instrumentation location in modal testing. In: Proceedings of the 1990 MacNeal-Schwendler Corporation World Users Conference, Los Angeles, CA, 28–30 Mar 1990
5. Heo, G., Wang, M.L., Satpathi, D.: Optimal transducer placement for health monitoring of long span bridge. Soil Dyn. Earthq. Eng. **16**, 495–502 (1997)
6. Glassburn, R.S., Smith, S.W.: Evaluation of sensor placement algorithms for on-orbit identification of space platforms. In: Master's thesis, University of Kentucky, 1994
7. Soman, R.N., Onoufrioua, T., Kyriakidesb, M.A., Votsisc, R.A., Chrysostomou, C.Z.: Multi-type, multi-sensor placement optimization for structural health monitoring of long span bridges. Smart Struct. Syst. **14**(1), 55–70 (2014)
8. Castro-Triguero, R., Murugan, S., Gallego, R., Friswell, M.I.: Robustness of optimal sensor placement under parametric uncertainty. Mech. Syst. Signal Process. **41**(1–2), 268–287 (2013)
9. Qin, Q., Li, H., Qian, L.Z., Lau, C.K.: Modal identification of Tsing Ma bridge by using improved eigensystem realization algorithm. J. Sound Vib. **247**(2), 325–341 (2001)
10. Conte, J.P., He, X., Moaveni, B., Masri, S.F., Caffrey, J.P., Wahbeh, M., Tasbihgoo, F., Whang, D.H., Elgamal, A.: Dynamic testing of Alfred Zampa memorial bridge. J. Struct. Eng. **134**(6), 1006–1015 (2008)
11. Weng, J.H., Loh, C.H., Lynch, J.P., Lu, K.C., Lin, P.Y., Wang, Y.: Output-only modal identification of a cable-stayed bridge using wireless monitoring systems. Eng. Struct. **30**(7), 1820–1830 (2008)
12. Friswell, M.I., Castro-Triguero, R.: Clustering of sensor locations using the effective independence method. AIAA J. **53**(5), 1388–1391 (2015)
13. Erduran, E., Demirlioglu, K., Lau, A., Aziz, K., Willoughby, I., Hyldmo, E., Arsenovic, T., Martinelli, E.: Stange overpass: Finite element model updating of an unconventional railway bridge. In: International Workshop on Civil Structural Health Monitoring, pp. 889–901. Springer (2021)
14. Chopra, A.K.: Dynamics of structures. 13 Prentice Hall, 2016, ISBN: 9780134555126

Chapter 9
Thoughts on Automatic Impulse Hammer Parameters and Sensor Fixation Methods

Johannes Maierhofer, Max Gille, and Daniel J. Rixen

Abstract The majority of data acquisition in experimental structure dynamics are conducted using impulse excitation and acceleration sensors. As the shape of the impulse in time domain is the crucial basis for the frequency content calculated from the impulse, mechanical parameters of the automatic modal impulse hammer (AMimpact) are discussed that have an influence on the impulse function. Using minimal models, the individual effects of the parameters are theoretically discussed and shown in experiments. Mounting the sensors to the structure is a critical step towards achieving good measurement quality. This investigation presents an overview and compares several, feasible methods for fixing acceleration sensors to metal (aluminum) structures. The methods are discussed regarding their effort, their positional precision, and their repeatability. The various methods are discussed in terms of their positional precision and their repeatability. The experiments are conducted and analyzed on an academic aluminum test structure and the automatic modal hammer (AMimpact). One difficulty is the lack of any ground truth, for which reason two sensors are stacked together to compare frequency response functions. These FRFs are obtained in two directions to enable the sensor fixation to be loaded in normal and tangential direction. The conclusion of the paper states that the fixing methods used for acceleration sensors are not critical in the normal direction but can have a non-negligible influence on measurements in the tangential direction. This effect should therefore be considered at an early stage of a measurement campaign.

Keywords Sensor fixation · Testing equipment · Automatic modal hammer · AMimpact · High-quality FRF

9.1 Introduction

Devising the instrumentation of test rigs is an art in itself. It is necessary to discriminate between the actuation of structures on the one hand and sensing outputs on the other. In experimental structural dynamics, impact hammers and acceleration sensors are employed in the vast majority of tasks, such as experimental modal analysis (EMA), determining frequency response functions (FRFs) for substructuring techniques, as well as for measuring operational signals for operational modal analysis (OMA) or monitoring purposes. The first topic in this paper is devoted to the influences of various mechanical parameters of the automated impulse hammer AMimpact, which is used to excite the structure. The following parameters are examined:

The first topic in this paper is devoted to the influences of various mechanical parameters of the automated impulse hammer *AMimpact*, which is used to excite the structure. The following parameters are examined:

- Tip material
- Mass of the hammer
- Spring strength (stiffness and preload)

A lot of effort is put into selecting the right sensors and placing them at the best possible position for gaining the best results for the measurement task. However, mounting a sensor is a critical step. In structural dynamics, acceleration sensors must be mounted to the surface of a structure. This surface can be of various shapes and have different properties stemming from its material, surface treatment, or lacquer. Depending on the operator's abilities and the possibilities available in the workshop, a number of sensor fixation methods may be feasible for mounting the sensor on the surface.

J. Maierhofer (✉) · M. Gille · D. J. Rixen
Chair of Applied Mechanics, TUM School of Engineering and Design, Technical University of Munich, Garching, Germany
e-mail: j.maierhofer@tum.de; max.gille@tum.de; rixen@tum.de

C. Walber et al. (eds.), *Sensors and Instrumentation, Aircraft/Aerospace and Dynamic Environments Testing, Volume 7*,
Conference Proceedings of the Society for Experimental Mechanics Series, https://doi.org/10.1007/978-3-031-05415-0_9

The second part of this chapter investigates different mounting techniques and their influence on the resulting measurements:

- Petro Wax
- Cyanoacrylate (Super Glue)
- Hot Glue
- Double-sided tape

9.2 Automated Impulse Hammer Parameters

9.2.1 System Description

To obtain a repeatable, good quality impact, the automated impulse hammer *AMimpact* (developed at the Chair of Applied Mechanics, [1]) was used. Further reflections on the subject of impulse hammering can be found in [2].

The system consists of a linear sliding bolt, which is attracted by a reluctance electromagnet. The bolt is retracted back to its rest position by a spring. A force sensor (PCB Model 086E80) is glued to the tip of the bolt to measure the impact force. The system is packed into a compact device (Fig. 9.1a) controlled via a USB interface or a WiFi connection in conjunction with a web app running on a smartphone. The device is positioned with a magnetic stand (Fig. 9.1b). The actuator is only active up to the point where the force sensor tip approaches the structure. The actuator is then deactivated, so the impact is purely ballistic (free-flight phase) without the driving force of the magnetic actuator. This ensures a single impact (for the majority of target structures; for exceptions, see [2]).

The shape of the force impulse in the time domain can be influenced by various parameters. The two most important once are the impact velocity and the material pairing between force sensor tip and target. A higher impact velocity (corresponding to a higher kinetic energy of the bolt) results in a higher peak force. The stiffer the material pairing, the shorter (and in result also higher) is the peak. In Fig. 9.2, two series of impacts are shown that differ in the material of the force tip, namely steel (red) and vinyl (gray). Within one series (the same material pairing), different levels of force amplitude are excited. The force amplitude is adjusted by varying the time for which the acceleration force F_{actuator} is applied to the bolt. With increasing time, the force amplitude increases. The difference between two curves is a constant 1 ms increase of actuation time.

The problem is that there are situations in which an appropriate choice of parameters cannot be made that will achieve the desired frequency range. In particular, the material pairing is often fixed, as the target material cannot be changed without affecting the system dynamics. This is an important issue, for example, in systems made from plastics or even wood. That low stiffness of these target materials means that the force peak softens considerably and the frequency range drops rapidly (cf. Fig. 9.3).

For the AMimpact, there are two parameters left, which can be tuned to modulate the impulse shape within a certain range and which can therefore overcome certain difficult excitation situations. First, the influence of the bolt mass can be

Fig. 9.1 Tools for automated impulse excitation. (**a**) The Automated Impulse Hammer, *AMimpact*. (**b**) Magnetic stand to orientate and fix the *AMimpact* [3]

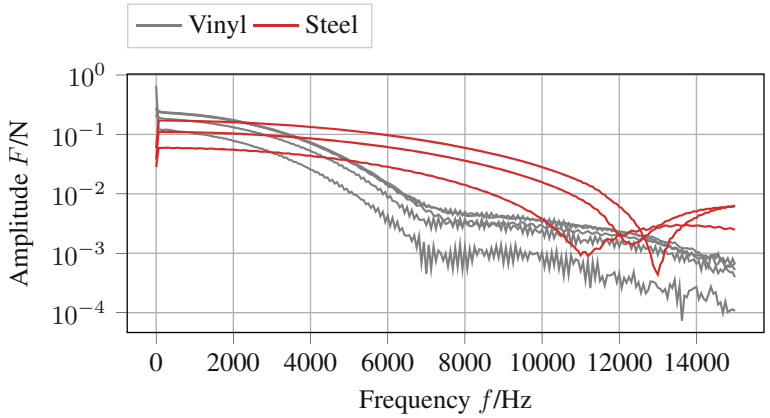

Fig. 9.2 Influence of different material pairs

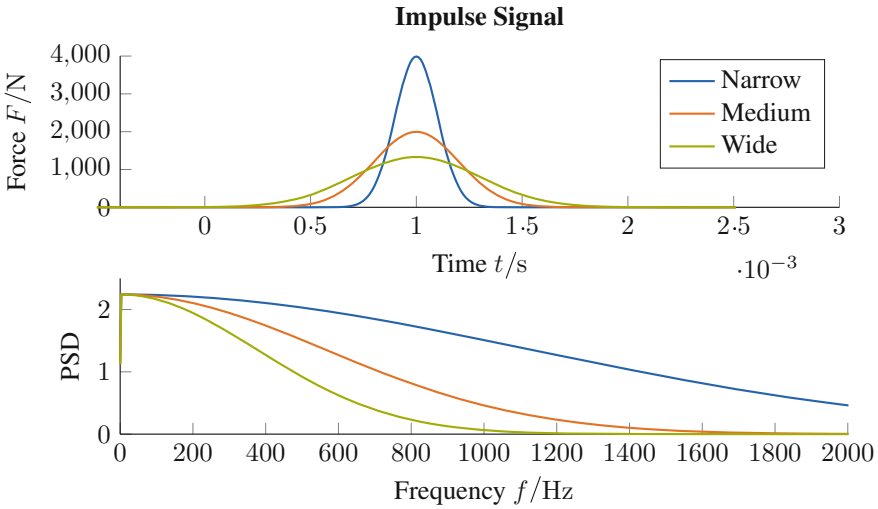

Fig. 9.3 Different impulse shapes show the frequency content of the excitation

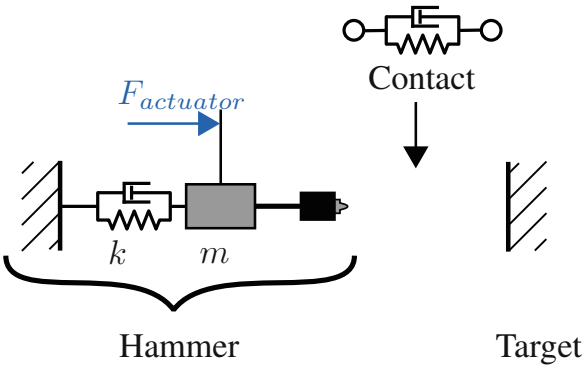

Fig. 9.4 Minimal model of the *AMimpact* system against a rigid target

varied, followed by the spring strength. A simple explanatory model is shown in Fig. 9.4. The actuator force F_{actuator} is not influenced by the variation of the mass m or the stiffness k. The losses due to friction of the mechanism are embedded in the unknown (and not further investigated) damping. The sequence of the hammer being in contact is modeled with an additional spring/damper element due to the Hertzian contact theory, see [1].

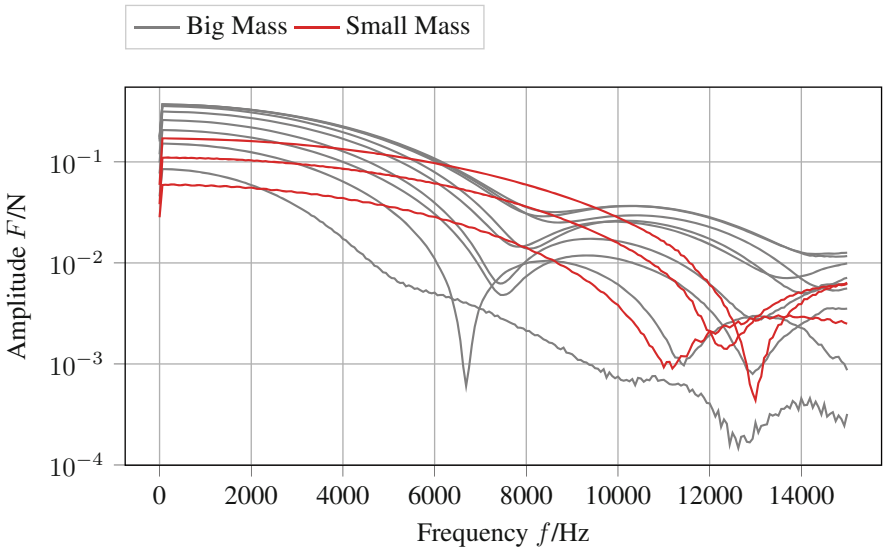

Fig. 9.5 Influence of a mass increase of factor 2.5

9.2.2 Influence of the Bolt Mass

Increasing the movable mass m in turn causes the inertia to increase. This leads to a longer contact phase which means a wider force peak that results in a lower cutoff frequency. On the other hand, a greater mass allows much better control of the impact energy. As the actuator is regulated with a bang-bang limit controller, a small timing error is less significant. Additionally, the distance of the free flight phase is less critical, as the effects of friction play a smaller role.

Figure 9.5 shows two series of impacts with different energy levels. The two series differ in the mass m of the movable hammer. The red series has no additional mass, so the conclusion is as previously discussed in theory that the lighter the hammer, the wider the excitable frequency spectrum. But it can also be seen that the steps of the force levels in the series are bigger (the actuation time still increases by 1 ms per graph) than in the heavier system (depicted in gray). The two mass configurations differ by a factor of about 2.5.

Intermediate conclusion: For the lab worker, a higher mass is always preferable. After checking material parings with different force sensor tip materials, the mass of the bolt can be lowered to achieve a higher excitation frequency range, if required.

9.2.3 Influence of the Spring Stiffness

In this section, a medium mass is attached to the bolt to fix this parameter. Changing the spring strength is effected in one of two subparameters: Either by changing the prestress of the spring and maintaining the spring stiffness, or changing the spring stiffness itself. Theoretically, a stronger pull-back force will result in a shorter contact phase, leading to a wider frequency spectrum. Both of these subparameters can only be varied within rather narrow limits to maintain the device in an operable state. The effect is shown in Fig. 9.6, in which the spring has been completely detached for the second series (red). The plunger is pulled back manually before each new impact, but the experiment shows only minimal changes in the frequency behavior. The effect of the spring is therefore more important for the handling and robustness of the device's operation.

Intermediate conclusion: The effect of spring stiffness on the excitation frequency range is negligible. The spring should be adjusted such that a secure retraction of the bolt is ensured and the magnet has sufficient force to enable controlled acceleration of the plunger.

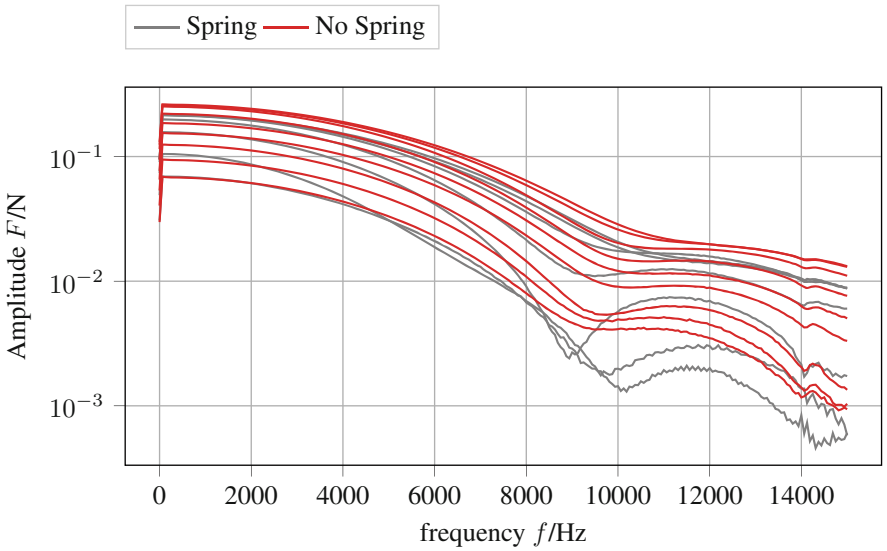

Fig. 9.6 Difference in the force spectrum with the both extrema: spring and no spring

9.3 Sensor Fixation Parameters

The counterpart of structure actuation is motion sensing. The use of familiar acceleration sensors raises the question of how to mount these sensors to the structure.

9.3.1 Technical Properties of Fixation Methods

This section discusses the mechanical and application properties of the various fixation methods. A little chemical background is provided for the different adhesives to enable the reader to gain a feeling for their correct use. The order is already in a way that represents the feasibility of the fixation method.

Wax The most traditional way of mounting acceleration sensors to a structure is to use wax. Originally beeswax was used and indeed it sometimes still is today. One drawback is that the cohesive forces are very small, so that the sensor can be moved out of position with very little force from the outside. On the other hand, removing the sensor is not a problem, as the wax retains its kneadable consistency. The sensor and structure can be cleaned with turpentine. In most cases, no damage to any surface is to be expected. PCB Petro Wax is used throughout this investigation.

Cyanoacrylate Once the polymerization process has started by way of hydroxide ions present in the moisture of the air, initial solidity is attained in a few seconds and full strength within a range of few hours. Cyanoacrylate glues are also available in high viscous gel formulations. This makes them easy to apply in non-horizontal positions. Also, small gaps up to 0.1 mm can be evened out. The high adhesive forces for surfaces with high surface energy (such as metals and duroplasts) produce a stable sensor attachment but are problematic when it comes to dismantling. This has to be done carefully so as not to damage the sensor or the object being measured. To clean the sensor, acetone can be used as it dissolves the glue. The product used in this investigation is LOCTITE 408.

Hot Glue Classic hot glue is an ethylene-vinyl acetate copolymer. A problem occurs when trying to use it to glue metal parts: Due to the high thermal conductivity of, in particular, aluminum, the heat is extracted from the glue so quickly, that the glue hardens before it can bind to the surface. The result is that there is little or no adhesion. Moreover, it is not suitable for plastics like PE, PP, and PTFE. The application itself is very simple and the joint can be subjected to use after a maximum of 2 min. Here, Pattex Hotmelt Sticks are used.

Double-Sided Tape Two acrylic bonding sheets envelop a thin foil of 10–100 µm. A drawback of this fixation method becomes apparent when the surface is not flat. Due to the thin foil carrier, the tape is not able to even out any geometric

curvatures. The sensor would have near-line contact, which is of course not acceptable. After pulling off the tape, the residues can be cleaned with acetone. The product used in this case is *Tesa*.

Magnetic Bond A neat way of mounting sensors which enables them to be easily repositioned and without effort to structures is to use magnetic adapters. However, there are two major issues. As only ferromagnetic structures are attracted by a magnet, neither aluminum nor plastic of any type can be instrumented. Also, the dimensions and weight of the magnets are not negligible. For these reasons, this method is not considered further during this work.

Direct Screw Mount Some sensors have a thread in the housing which enables the sensor to be screwed directly to the surface. The major drawback here is the fact that the surface has to be bored and an opposing thread must be created. This is not possible in most applications. It is therefore not considered here.

9.3.2 Experimental Setup

The test structure used in this work is a monolithic L-shaped aluminum beam welded to an aluminum base plate which is screwed to the ground. This structure was already used in [4] to perform various procedures to obtain FRFs to be used in the field of experimental substructuring. Two sensors are mounted to the structure in a vertical stack. The lower sensor is fixed to the structure with a thin layer of wax as this seems to be the common practice. The fixing layer between the two sensors is varied. The lower sensor 1 therefore always has the same position and orientation, while the fixing of the top sensor 2 may vary between a very thin wax layer (<0.1 mm), a thick wax layer (1 mm), double-sided tape, or an adhesive bond of hot glue and cyanoacrylate glue (Loctite 408).

Excitation is then performed in two directions using the AMimpact as shown in Fig. 9.7. This causes the fixation layer to be loaded in line with two different regimes: normal forces and tangential forces. The received frequency response functions (FRFs) are so called driving point FRFs, from which follows that each resonance necessarily has to be alternated by an antiresonance.

The measurements are made using a Siemens LMS device and processed to FRFs with the LMS software. Each measuring run consists of five averaged impacts by the AMimpact, using the inbuilt automatic timing function. The results are presented in two sections for the two directions (Fig. 9.8).

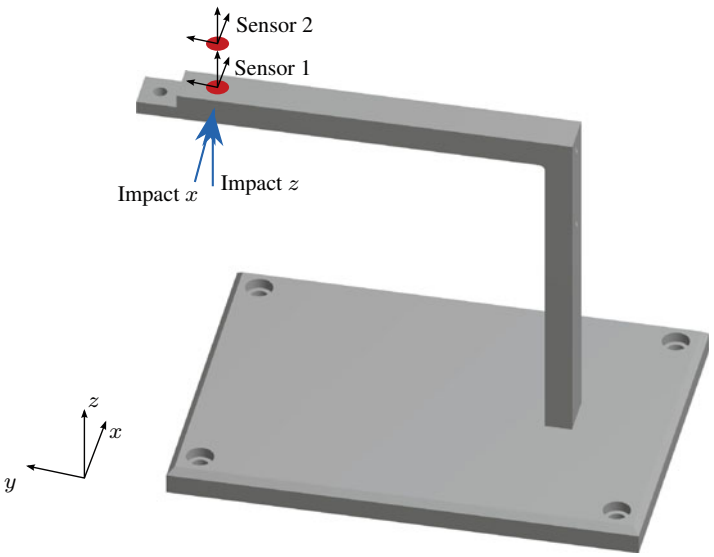

Fig. 9.7 Academic test structure with marked positions of sensors and impacts applied during the measurements

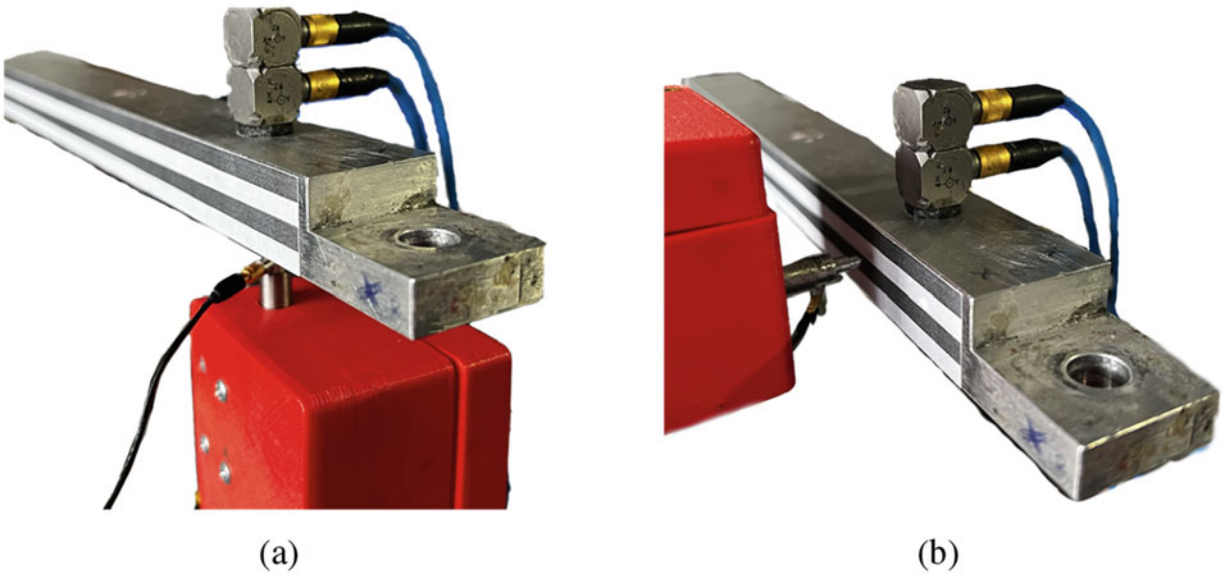

Fig. 9.8 Two sensor experimental setups. (**a**) z-direction. (**b**) x-direction

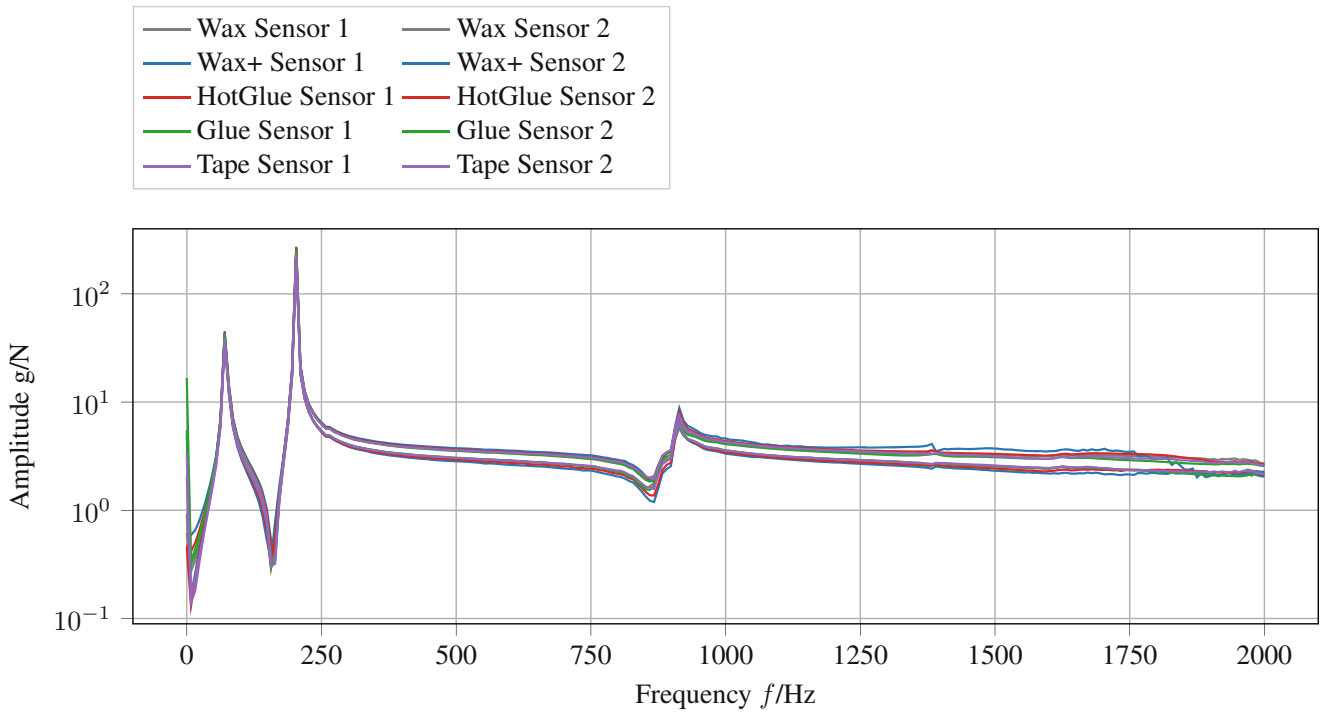

Fig. 9.9 Frequency response functions for both sensors and all fixations. No outliers are found

9.3.2.1 Normal Direction

In this setup, the fixing layers are loaded in the normal direction. Figure 9.9 shows all FRFs for both sensors and all fixation methods. No outliers are detected in the observed frequency range. The resonances are captured very well with all configurations. It can be seen that the second sensor deviates in the frequency range from 250 Hz onwards. The origin of this behavior is assumed to be in the different z-position of this sensor in relation to the reference sensor 1. Therefore, a different amplitude is expectable for modes that have a major rotational portion at the sensor's position. According to [4], the 5th mode is around 900 Hz. This mode's shape is in the plane of the L-shape and has a node very close to the point where the sensor stack is mounted. Consequently, this point undergoes a rotational motion. As sensor 1 is closer to the neutral line, the

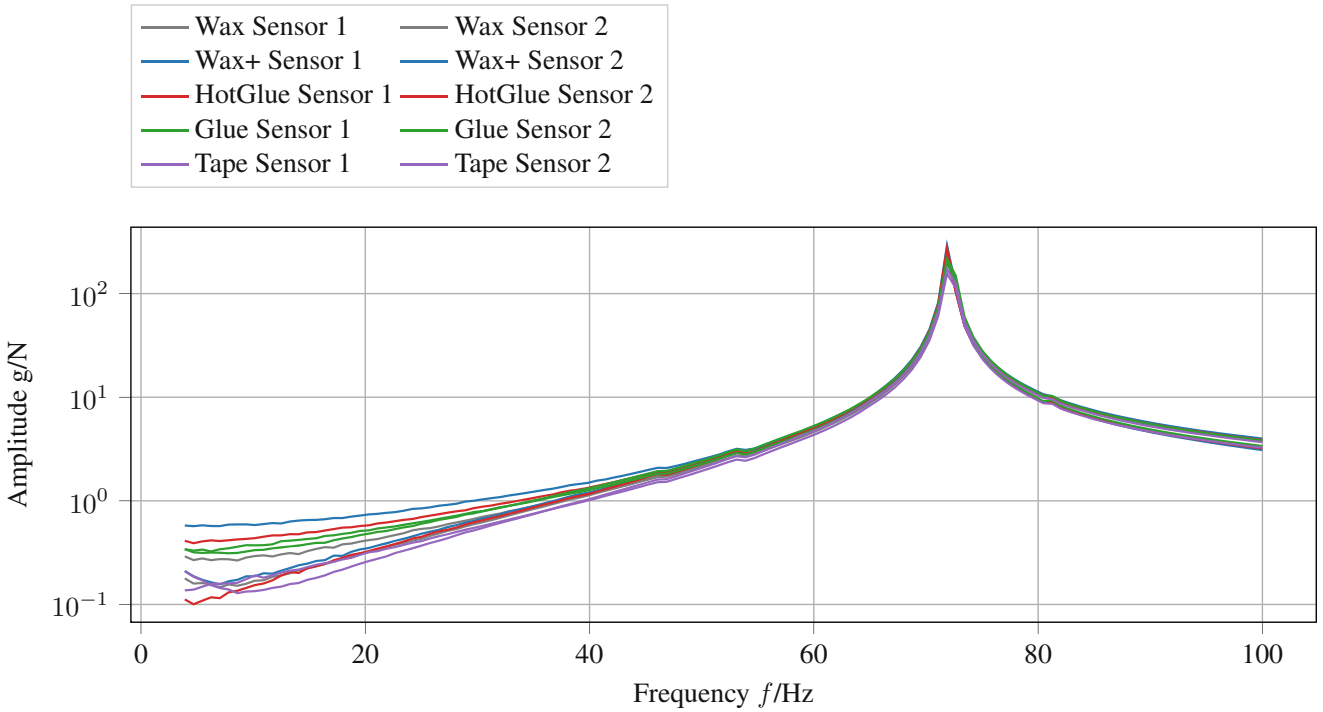

Fig. 9.10 Detail of the low frequency range. The softer the interface between the two sensor, the higher the amplitude for the low end of the frequency range

parasitic z motion is smaller than for sensor 2. Concluding, the offset of the two sensors is explained by a pure geometrical effect.

Differences can be observed in the first 50 Hz. This section has been zoomed out in Fig. 9.10, starting at 5 Hz to avoid confusion in the zone in which the sensor is not reliable. Any higher amplitudes from one fixing method always arise from sensor 2, i.e., the upper of the two sensors. It can be observed from the graph that fixation methods that have a rather thick and elastic nature seem to diverge in the very low-frequency range. This is especially the case with hot glue (red), thick wax (blue), and thin wax (gray). Thin and very stiff interface connections such as cyanoacrylate glue (green) and tape (purple) are very close together.

Intermediate conclusion: The thin wax, tape, and glue configurations show similar behavior for both sensors and are therefore to be preferred whenever possible.

9.3.2.2 Tangential Direction

The differences to the previous setup are that the fixing layer is now loaded tangentially. Figure 9.11 reveals several differences in the higher frequency range. As sensor 1 does not change its behavior, it is displayed gray, so the focus is on sensor 2, which displays a number of significant variations in frequencies above 500 Hz.

Again two fixation methods stand out: thick wax (blue) and hot glue show an amplitude magnification at various frequencies between 500 and 1250 Hz that does not seem to stem from the physical properties of the test structure. Close together are the methods: thin wax and cyanoacrylate glue. Tape is between the rigid and the soft interface connections. All in all, this tangential experiment is clearly more sensitive to the sensor-structure interface. Unfortunately, it was not possible to explain the effects for the higher frequency range above 1500 Hz. This will require deeper investigation.

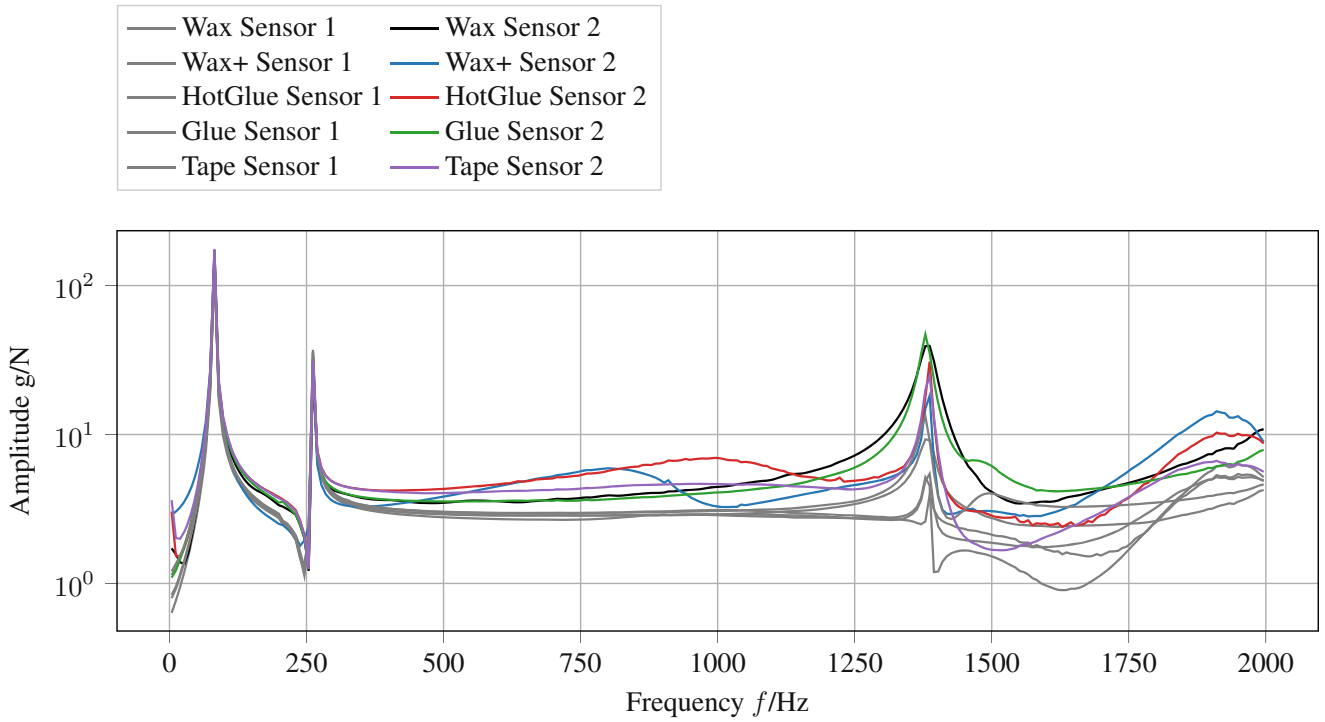

Fig. 9.11 All fixation method FRFs in x-direction

9.4 Summary

They depend very much on the experimental limits of the setup and the degrees of freedom that are available. Starting with the excitation mechanism, in this case, the automated impulse hammer AMimpact, the operator has the choice between a robust, easily controllable configuration or a less robust configuration that offers a broader excitation frequency range. Easily controllable in this context means that the energy content of the bolt and therefore the peak force is readily adjustable by the activation time of the actuator in milliseconds. The friction loss should be small in relation to the kinetic energy of the bolt. Second, the fixation of the sensors has to obey the requirements of practicability and a well-defined signal quality. Regarding the sensor fixing, we found that the practical aspects outweigh the different signal qualities, as there is as yet no clear winner or loser. As for practicability, we would suggest using petro wax if the components will not be experiencing any large movements or do not have to be assembled or disassembled during a measuring run. In such cases, cyanoacrylate glue is recommended, in order to avoid misalignment of sensors during handling. The increased effort involved in cleaning the sensor and the component must be borne in mind. For the future, a more complex experimental setup may be employed to investigate the signal quality in higher frequency ranges and to determine whether there are any differences between the fixation methods. For now, it can be said that the positioning and orientation of the sensor are far more important than the fixing method itself.

References

1. Maierhofer, J., Mahmoudi, A.E., Rixen, D.J.: Development of a low cost automatic modal hammer for applications in substructuring. In: Conference Proceedings of the Society for Experimental Mechanics Series, pp. 77–86. Springer International Publishing, Cham (2019). https://doi.org/10.1007/978-3-030-12184-6_9
2. Maierhofer, J., Rixen, D.J.: Development of an electrodynamic actuator for an automatic modal impulse hammer. In: Dynamic Substructures, pp. 189–199. Springer International Publishing, Cham (2020). https://doi.org/10.1007/978-3-030-47630-4_18.
3. Hörger & Gässler OHG: Hydraulisches Messstativ (2021). http://www.hoerger-gaessler.de/
4. Trainotti, F., Berninger, T.F.C., Rixen, D.J.: Use of laser vibrometry for precise FRF measurements in experimental substructuring. In: Proceedings of the 37th IMAC, A Conference and Exposition on Structural Dynamics (2019)

Chapter 10
Modal Correlation of Complex Aerospace Joints Using Automated Variable Substitution

James P. Winkel, Peter A. Kerrian, and Theodore J. Bartkowicz

Abstract A critical task involved with being able to predict flight loads accurately in aerospace finite element models (FEMs) is the prior verification of the FEMs by conducting modal survey testing (MST). Experience comparing dynamic response of initial FEMs to MST data tends to demonstrate that FEMs can have unacceptable accuracy even when best modeling practices are followed. One inherent source of inaccuracy in linear dynamic FEMs is the modeling of nonlinear joints with mechanisms such as spherical bearings. These joints are usually designed to freely translate or rotate under the high levels of loading experienced in flight. Engineers who create linear FEMs conventionally model these joints without any stiffness in the mechanism degrees of freedom to meet this design intent. However, inaccuracy is observed during test validation of these FEMs, which usually relies on low-level force excitation orders of magnitude below flight load levels. This low-level modal test rarely overcomes the joint friction that is present, and thus the mechanism joints are able to react loads. This divide between the test results and the FEM creates a significant challenge to the engineer who is performing the correlation, in that the engineer has no basis for what stiffness value should be used to make the FEM match the test results. A compounding challenge is that complicated built-up aerospace structures commonly have multiple joints through a load path where each joint will "stick" and "slip" at different levels of force input. Explicitly matching the dynamics of a system containing these nonlinear mechanisms would require a nonlinear FEM, which is prohibitively costly for dynamic simulations of most aerospace systems. The objective of this chapter is to present a workflow that can efficiently cycle through many iterations of a FEM, allowing a Monte Carlo–style examination of the design space to identify candidate stiffness values for nonlinear mechanism joints. The outlined approach is specific to MSC Nastran and utilizes MSC Nastran's symbolic substitution capabilities, coupled with the IMAT™ and Attune™ software packages developed by ATA Engineering, Inc. (ATA). The workflow is demonstrated with a case study from the correlation effort for The Boeing Company's Crew Space Transportation (CST)-100 Starliner FEM.

Keywords Correlation · MSC Nastran · IMAT™ · Attune™ · Finite element model · Modal testing

Nomenclature

AMRV	Augmented modes residual vectors
ATA	ATA Engineering, Inc.
Boeing	The Boeing Company
CG	Center of gravity
CM	Crew module
CST	Crew Space Transportation
DMAP	Direct matrix abstraction program
DOF	Degree of freedom
FEM	Finite element model

J. P. Winkel (✉)
NASA Langley Research Center, Hampton, VA, USA
e-mail: james.winkel@nasa.gov

P. A. Kerrian
ATA Engineering, Inc., San Diego, CA, USA

T. J. Bartkowicz
The Boeing Company, Houston, TX, USA

C. Walber et al. (eds.), *Sensors and Instrumentation, Aircraft/Aerospace and Dynamic Environments Testing, Volume 7*,
Conference Proceedings of the Society for Experimental Mechanics Series, https://doi.org/10.1007/978-3-031-05415-0_10

IMAT	Interface between MATLAB, analysis, and test
MST	Modal survey test
NASA	National Aeronautics and Space Administration
SM	Service module
SP	Seat pallet
SSH	Secure shell

10.1 Introduction

Updating finite element models (FEMs) of complicated structures to correlate analysis modes to low-level modal test results is a common technique for validating a FEM. The first two critical steps of any correlation are ensuring that the FEM accurately represents the as-built hardware geometry and that the mass and center of gravity (CG) agree with the measured test values. The goal should always be to maintain a physics-based FEM. The remaining correlation effort is often focused on making local changes to the FEM to improve the correlation of individual modes. Utilizing engineering judgment, element properties are selected as design variables based on an assumption that they will have an influence on the modal behavior of a component. Multiple optimization algorithms have been developed for use as a final step in the correlation process to make small changes to multiple design variables at once to solidify the correlation. Challenges arise when certain optimization algorithms are used when significant uncertainty in the initial value exists. Because the FEM might not be sensitive to the design variable in question, the algorithm may produce positive correlation results by making unrealistic changes to other design variables.

One example in the aerospace community where one might experience this scenario is the correlation of spherical ball joints, such as the example shown in Fig. 10.1. The FEM representation of these mechanisms is commonly a coincident node CBUSH, with the stiffness values associated with the rotation degrees of freedom (DOFs) set to zero. During high levels of dynamic excitation, such as a rocket launch or aircraft takeoff, friction forces will be exceeded, and the joint will "slip." As a result, a zero rotational stiffness representation of the mechanism is a good approximation. However, modal survey tests (MSTs) are conducted at significantly lower levels of excitation – often not enough to overcome the friction in the joints. As a result, the spherical ball joint may "stick," causing a significant increase in joint stiffness. From the perspective of fundamental principles, answering the stick/slip dichotomy is essential to accurately capturing the behavior of the joint for the correlation process. The challenge in the correlation is determining the appropriate stiffness value for the joint to match the test results. Commonly there are multiple joints in a complicated system, which compounds the problem because each joint will stick and slip at different levels of force input.

Fig. 10.1 Example spherical rod end joint. (From http://www.grainger.com)

Explicitly matching the dynamics of a system containing these nonlinear mechanisms would require a nonlinear FEM, which is uncommon for commercial aerospace dynamic simulations. The objective of this chapter is to present a workflow that can efficiently cycle through many iterations of a FEM to allow a Monte Carlo–style examination of the design space to identify candidate stiffness values for nonlinear mechanisms. Traditional optimization algorithms can subsequently be used to finalize the correlation of the FEM. A similar workflow, augmented modes residual vectors (AMRV), has been previously published [1] for use with Simcenter Nastran. Compatibility issues between Simcenter and MSC Nastran currently preclude the use of that technique with FEMs developed with MSC Nastran, so the approach outlined herein is specific to MSC Nastran and utilizes MSC Nastran [2–4] symbolic substitution capabilities coupled with the IMAT™ and Attune™ software packages developed by ATA Engineering, Inc. (ATA).

A case study of this correlation process being utilized on The Boeing Company (Boeing) Crew Space Transportation (CST)-100 Starliner FEM has been provided. ATA was contracted to conduct an MST of the crew module (CM), with the primary objective of characterizing the modes of the seat pallet (SP). The presented workflow was developed during the joint Boeing/NASA/ATA correlation effort to characterize stiffness values at the MST force levels for the nonlinear joints. Given the design of the joints of the SP, a significant number of nonlinearities were present in the test, which posed a challenge for successfully correlating the SP FEM. The CST-100 Starliner FEM had to be accurately verified in order to ensure the crew and structural integrity of the vehicle was maintained in all phases of the required mission profile.

10.2 Analysis Approach

The use of a single “common” FEM to predict loads, dynamic environments, and stresses is becoming an increasingly prevalent occurrence in the aerospace industry. In the past, each discipline would have to develop their own model and verify it to be accurate by different means. A single common FEM of a crewed space capsule has to be able to accurately predict loads, dynamic environments, and stresses caused by liftoff, potential abort scenarios, on-orbit operations, and landing. In addition to ensuring the structural integrity of the vehicle is maintained in all phases of flight, one also has to certify the health and safety metrics for the crew are maintained. The task of guaranteeing a single FEM accurately predicts all these different environments is a very significant challenge. The reliance on a physics-based model updating approaches becomes a necessity as this model is employed in verification analysis to ensure safety and structural integrity. When this single common FEM technique is utilized, extra emphasis must be placed on its accuracy because it is the one and only prediction tool that a project has to show in the entire mission profile can be safely carried out.

A fundamental prerequisite in the verification of these common FEMs is ensuring that what is modeled in the FEM is what is actually in the as-built design. There is no benefit in going any further in a verification process if this work has not already been completed. The added benefit of this exercise is the engineering team gains a fundamental awareness of how the FEM was constructed and simplified assumptions were made and where sources of structural nonlinearity could be present. It may seem trivial, but this knowledge helps to guard against a FEM correlation effort from becoming an artificial manipulation of the structural and material properties. The workflow described in this chapter assumes that these prior steps have taken place prior to utilizing it.

To keep the workflow compatible with traditional model updating software, the Nastran SOL200 design sensitivity and optimization solver is used in conjunction with ATA’s Attune direct matrix abstraction program (DMAP). The advantage of these existing tools is their built-in ability to efficiently generate the information needed to compute the standard model validation comparison metrics, such as the cross-orthogonality matrix. Because the workflow relies on the Attune standard design optimization package, an overview of the process for setting up a model correlation with Nastran design variables is provided below.

10.2.1 Design Variable Definition

First, element or material properties are identified as potential tuning knobs based on an engineering judgment review of the FEM. The joints between structural members are common areas where assumptions were made during the creation of the FEM that may be invalidated based on the test data. Utilizing strain energy density for each mode is an excellent way to identify and zero in on FEM components that are sensitive to perturbations. Successfully identifying the critical elements or material properties is essential to a successful correlation; failure to identify enough tuning knobs will cause the software

```
$-------><------><------><------><------><------><------><------><------>
DESVAR    1       SPRG1   1.0
DVPREL1   1       PBUSH   3011001 K1
          1       100000.
$--------
DESVAR    2       SPRG2   1.0
DVPREL1   2       PBUSH   3011002 K2
          2       50000.

$--------
DESVAR    3       SPRG1   1.0
DVPREL1   3       PBUSH   3011003 K3
          3       20000.

$--------
DESVAR    4       SPRG4   1.0
DVPREL    4       PBUSH   3011001 K4
          4       100.
DVPREL    5       PBUSH   3011002 K4
          4       100.
DVPREL    6       PBUSH   3011003 K4
          4       100.
```

Fig. 10.2 Example MSC Nastran SOL200 design variable definition

package to try to force unrealistic changes to other properties that have little influence on the mode in question. In contrast, including too many tuning knobs in the design space will result in changes to the FEM with no engineering justification.

After the element or material properties are identified, Nastran DVPREL1 cards containing the associated FEM attributes, such as property type, ID, name, and value, are generated for use in the SOL200 optimization solver. Nastran design variable DESVAR cards contain the assigned name and scalar value that will be applied to the FEM attributes associated with the DESVAR. The DVPREL1 cards can either be assigned to separate DESVAR cards or grouped together into a single DESVAR card to change consistent properties by the same amount. The Attune software is capable of exporting the required DVPREL1 and DESVAR cards. Alternatively, custom MATLAB scripts can be developed to take properties and design variables from Microsoft Excel and export them in Nastran format. The final outcome should look similar to the generic example shown in Fig. 10.2. Additional details on setting up the optimization cards can be found in the *MSC Design Sensitivity and Optimization User's Guide* [4]. The modified workflow diverges from the standard Attune workflow after this point.

10.2.2 Symbolic Substitution

The user now needs to identify the subset of those DESVAR variables that are likely to be off by several orders of magnitude. These areas are usually joints designed to act a specific way during flight but which will not behave the same way during low-level modal tests. As mentioned, prime candidates are spherical ball joints or sliding mechanisms that are constrained by friction that would be overcome by in-flight loading. When that subset is identified and separated out of the original DVSET file, the user needs to create the framework necessary for MSC Nastran to perform the variable swapping.

Within all the DESVARs, the user will need to replace the fourth column of the DESVAR with a custom variable name. The authors prefer to keep it simple and just name each variable "DV00##," where the ## is the number of the DESVAR, for easy tracking purposes. Next, it is strongly recommended that the user modify any of the bulk data cards that contain this custom variable name to utilize the free-field format (comma separated) instead of the more standard small-field format (eight-character spacing). The reason for this modification is twofold: first, if the user chooses to make custom variable names longer than eight characters, MSC Nastran will be able to handle this situation with the free-field format being utilized. Second, the free-field format will prevent most issues related to the length of the value being substituted. The next section includes more discussion on the length and formatting of the values. MSC Nastran provides sufficient documentation in the *MSC Nastran Quick Reference Guide* [2], specifically the "Symbolic Substitution" section, on the different ways to modify the rules relating to the symbolic substitution, but it is not the focus of this chapter, and the authors deem it unnecessarily complicated for this approach (Fig. 10.3).

```
$---1--><---2--><---3--><---4--><---5--><---6--><---7--><---8--><---9-->
DESVAR,1,SPRG1,%DV0001%
DVPREL1  1       PBUSH   3011001 K1
         1       100000.
$-------
DESVAR,2,SPRG2,%DV0002%
DVPREL1  2       PBUSH   3011002 K2
         2       50000.
$-------
DESVAR,3,SPRG3,%DV0003%
DVPREL1  3       PBUSH   3011003 K3
         3       20000.
$-------
DESVAR,4,SPRG4,%DV0004%
DVPREL1  4       PBUSH   3011001 K4
         4       100.
DVPREL1  5       PBUSH   3011002 K4
         4       100.
DVPREL1  6       PBUSH   3011003 K4
         4       100.
```

Fig. 10.3 Example symbolic substitution variable modification

```
DV0001=(1.-3 1.+3 1.00 1.00 1.00 1.00 1.00 1.00)
DV0002=(1.00 1.00 1.00E-4 1.00E+4 1.00 1.00 1.00 1.00)
DV0003=(1. 1. 1. 1. 0.001 1000.0 1. 1.)
DV0004=(1.00 1.00 1.00 1.00 1.00 1.00 1.000E-01 10.000E+06)
```

Fig. 10.4 Nastran variable substitution iteration definition array

10.2.3 Iteration Value Assignment

Once this subset of DESVARs is assigned, the user will need to decide on the upper and lower limits of the divergence from the original value and whether any steps should be taken between these limits. Remember that the point of this process is not to identify the exact value but rather to estimate a good starting value to be used during fine-tuning of the FEM. Also, it is best to vary one value at a time in most cases to allow the engineer to truly understand how each variable influences each of the target modes of the correlation. When a variable is not being modified, simply place a 1.0 in the column; the final product is a numeric matrix that should be equivalent to the number of variables (rows) by the sum of the number of steps taken for each variable (columns). A simple example matrix is shown in Fig. 10.4 for reference. This example has its values modified differently on purpose to demonstrate that the formatting of the values does not matter as long as the free-field format is utilized. In the case, as shown for DV004, where the user has values longer than eight characters, MSC Nastran will handle them by converting those to the large-field format in the analysis. The correct substitution can also be confirmed by turning on the echo command in the case control and reviewing the results. Accuracy is not lost unless the value exceeds 16 characters. It is always best to stay consistent with the same type of formatting throughout the entire variable substitution list.

10.2.4 Nastran SOL200 Deck Setup

While going through the process of creating custom variable names, the user should be creating a separate list of these custom variable names along with the original values for use in the next step of the process. Take the separate list of the custom names, and concatenate %defrepsym to the front of each. This list then needs to be placed in the executive control section of the Nastran SOL200 run deck. Examples of these statements can be found on lines 4–7 of Fig. 10.5. The list can also be stored in a separate include file and called into the SOL200 run deck by use of the include statement if desired. MSC Nastran has the capability to perform the value swaps inside of the Nastran SOL200 run deck; however, the authors deem this process too cumbersome for this application, and it does not readily lend itself to automation. The key benefit of using the defrepsym capability in this workflow is that the variable that needs to be changed only exists in one location at the top of the

Nastran deck within the executive control section and then that modified value will flow throughout the entire bulk data and will be changed everywhere it is found, without any additional files being modified. This fact makes it extremely easy to use in conjunction with automation tools outside of Nastran because now only one file needs to be changed every time and the output files can be easily managed as well. The workflow defined in this chapter utilizes shell scripting in conjunction with a secure shell (SSH) client software such as XWIN32 or PuTTY. A shell script is simply a series of Linux commands housed inside a file that can be interpreted by a command line interface installed on a remote server. This is a common way many Nastran users already access and submit their large Nastran runs on remote servers. The reader should not be concerned if they do not have any knowledge of shell scripting, as only a few basic commands are used and they are discussed in the next section.

The additional key features in this SOL200 deck that need to be set to take advantage of the Attune DMAP are formatted in bold text in Fig. 10.5. First and foremost, the Attune DMAP needs to be included in the deck. Second, there are two commands that follow after the CEND statement that should also be present. Finally, there are specific parameters that should be set up in the bulk data section. Detailed information on what the DMAP settings do can be found inside the Attune DMAP file.

10.3 Shell Automation Script

The next step of the defined workflow utilizes a shell script to automate the initiation of the Nastran runs in conjunction with the variable swapping. As previously mentioned, a shell script is simply a series of Linux commands housed inside a file that can be interpreted by a command line interface installed on a remote server. It should be stated that the authors had no working knowledge of shell scripts or programming with Linux commands prior to defining this workflow process; all commands utilized in this workflow are very basic, and further information on them can be easily found via web search. Even the engineer who has no working knowledge on shell scripting should be able to use the material provided below to implement this workflow. The authors developed a shell script that contains the commands necessary to set the working directory and loop through a defined number of cases. Each step of the loop will make the required value substitutions from the numeric matrix created earlier, run each Nastran run, and store the necessary results files without any user input. Shell scripts can be created using any text editor and are generally saved with the file extension *.sh. The generic example shell script is shown in Fig. 10.6. The subsequent sections provide more detail on each individual line of code in Fig. 10.6.

10.3.1 Initial Script Setup

To start with, the shell script must define any variables that are intended to be used at some point inside the script, in addition to supplying the information to point to the folder on the remote server where the Nastran runs will occur. Setting the working directory folder can be done using the "cd" statement followed by the variable where the filepath is stored. Line 4 (shown in Fig. 10.7) assigns the name "Generic_Study" to the variable name workdir, and then line 7 actually runs the command to change the working directory to the folder called "Generic_Study." This example assumes that there is a folder called Generic_Study within the home directory of the remote server. The command "ls" can be used to see what folders currently exist on the home directory of a remote server. While using a variable to store the filepath is not required, it is the authors' preference. In shell scripting, calling variables is done by using "$" in front of the variable name. Any desired comments can be placed in the shell script by using "##" in front of the comment. The optional "echo" statement is simply used to print out on the command line prompt what the directory is.

After this initial portion, the next part of the script is the matrix of values that the user created earlier. Depending on its size, it can be manually assembled or written out using the program of the user's choice (MATLAB, Python, etc.). A simple example of the output matrix is presented in Fig. 10.8.

10.3.2 Iteration Loop Definition

The loop that performs the variable swapping is contained within lines 16 through 29 of Fig. 10.9. It is a part of the script the user may wish to have in a separate code format and write out if the number of variables becomes too extensive.

```
$----------------------------------
$ Executive Control
$----------------------------------
%defrepsym DV0001=1.0
%defrepsym DV0002=1.0
%defrepsym DV0003=1.0
%defrepsym DV0004=1.0
$
SOL 200
DIAG 8,47,56
GEOMCHECK, NONE
INCLUDE 'attune23.dmap'
CEND
DSAPRT(END=SENS) = ALL
ANALYSIS = MODES
$
$----------------------------------
$ Case Control
$----------------------------------
$ Output Requests
ECHO = NONE
TITLE = Sensitivity Study
AUTOSPC(NOPRINT,PUNCH,SID=101,EPS=1.E-8)=YES
MEFFMASS(PARTFAC,MEFFW,FRACSUM,SUMMARY)=YES
DISP(PLOT) = ALL
METHOD = 1
SPC = 1
$
BEGIN BULK
$
$ User Specific Parameters
PARAM,POST,-1
PARAM,WTMASS,0.002588
PARAM,K6ROT,1.0
PARAM,MAXRATIO,1.E8
PARAM,OUGCORD,GLOBAL

$ Attune™ Specific Parameters
PARAM,MREDUC,USET
PARAM,KREDUC,USET
PARAM,OUTDRM,NO
PARAM,OUTFORM,OP2
PARAM,REDMETH,STATIC
PARAM,POSTEXT,YES
$
$---1--><---2--><---3--><---4--><---5--><---6--><---7--><---8--><---9-->
EIGRL          1         MAXFREQ                                    mass
$
$ FEM Configuration
INCLUDE 'Desired Files'
$
$ Test Instrumentation Set
INCLUDE 'TEST_USET.blk'
$
% Design Variables from Fig. 3
INCLUDE 'DESVARS.blk'
$
ENDDATA
```

Fig. 10.5 Example SOL200 deck setup with Attune™ DMAP

Line 17 shows the statement needed to copy the “SOL200_ModelName_Original.dat” from the remote server’s home directory to a new filename in the previously assigned working directory. A “~/” always refers to the home directory and “./” refers to the current working directory. The new filename is the pre-assigned variable “filename” followed by the iteration

```
1  ## Must run chmod +x SOL200_Auto_Generic.sh prior to running this script.
2  ## To run script, type nohup ./SOL200_Auto_Generic.sh & in command line.
3
4  workdir="Generic_Study"
5  filename="SOL200_ModelName_Case"
6  echo $workdir
7  cd $workdir
8
9  ## Variations
10 ## (Case1 Case2 ... CaseN)
11 DV0001=(1.-3 1.+3 1.00 1.00 1.00 1.00 1.00 1.00)
12 DV0002=(1.00 1.00 1.00E-4 1.00E+4 1.00 1.00 1.00 1.00)
13 DV0003=(1. 1. 1. 1. 0.001 1000.0 1. 1.)
14 DV0004=(1.00 1.00 1.00 1.00 1.00 1.00 1.000E-01 10.000E+06)
15
16 for t in ${!DV0001[@]}; do
17   cp -r ~/SOL200_ModelName_Original.dat ./$filename$t.dat
18   sed -i "s/%defrepsym DV0001=1.0/%defrepsym DV0001=${DV0001[$t]}/" $filename$t.dat
19   sed -i "s/%defrepsym DV0002=1.0/%defrepsym DV0002=${DV0002[$t]}/" $filename$t.dat
20   sed -i "s/%defrepsym DV0003=1.0/%defrepsym DV0003=${DV0003[$t]}/" $filename$t.dat
21   sed -i "s/%defrepsym DV0004=1.0/%defrepsym DV0004=${DV0004[$t]}/" $filename$t.dat
22   nohup /usr/local/msc/mscnastran-2016.0/bin/nast20160 MEM=20gb SMEM=10GB SMP=8
23         mode=i8 REPINFO=3 $filename$t.dat bat=no
24   sleep 2
25   mv $filename$t.op2 $filename$t.f06 ./Study_Results
26   sleep 5
27   rm $filename$t*
28   sleep 5
29 done
```

Fig. 10.6 SOL200 automation shell script

```
1  ## Must run chmod +x SOL200_Auto_Generic.sh prior to running this script.
2  ## To run script, type nohup ./SOL200_Auto_Generic.sh & in command line.
3
4  workdir="Generic_Study"
5  filename="SOL200_ModelName_Case"
6  echo $workdir
7  cd $workdir
8
```

Fig. 10.7 Working directory setup

```
9  ## Variations
10 ## (Case1 Case2 ... CaseN)
11 DV0001=(1.-3 1.+3 1.00 1.00 1.00 1.00 1.00 1.00)
12 DV0002=(1.00 1.00 1.00E-4 1.00E+4 1.00 1.00 1.00 1.00)
13 DV0003=(1. 1. 1. 1. 0.001 1000.0 1. 1.)
14 DV0004=(1.00 1.00 1.00 1.00 1.00 1.00 1.000E-01 10.000E+06)
15
```

Fig. 10.8 Design variable variation array

number of the loop. Remember that shell scripts start counting from 0 rather than 1, so the first iteration of this loop will create a file named “SOL200_ModelName_Case0.dat.”

Lines 18 through 21 contain the statements that perform the variable swapping in the new Nastran file. The command “sed” is short for stream editor, and it edits the file without needing to open it. It searches through the document and finds/replaces the instances of text within the function. Again, it is recommended that the “sed” command lines be created using some sort of script automation to prevent mistakes.

Line 22 is the statement that actually submits the Nastran run. This statement will be different depending on where Nastran is installed on the remote server, what version the user intends to run, and the setting of any user-specific Nastran keyword assignments. The reader should refer to the *MSC Nastran Quick Reference Guide* [2] for more information on what keyword

```
16  for t in ${!DV0001[@]}; do
17    cp -r ~/SOL200_ModelName_Original.dat ./$filename$t.dat
18    sed -i "s/%defrepsym DV0001=1.0/%defrepsym DV0001=${DV0001[$t]}/" $filename$t.dat
19    sed -i "s/%defrepsym DV0002=1.0/%defrepsym DV0002=${DV0002[$t]}/" $filename$t.dat
20    sed -i "s/%defrepsym DV0003=1.0/%defrepsym DV0003=${DV0003[$t]}/" $filename$t.dat
21    sed -i "s/%defrepsym DV0004=1.0/%defrepsym DV0004=${DV0004[$t]}/" $filename$t.dat
22    nohup /usr/local/msc/mscnastran-2016.0/bin/nast20160 MEM=20gb SMEM=10GB SMP=8
23          mode=i8 REPINFO=3 $filename$t.dat bat=no
24    sleep 2
25    mv $filename$t.op2 $filename$t.f06 ./Study_Results
26    sleep 5
27    rm $filename$t*
28    sleep 5
29  done
```

Fig. 10.9 Example iteration loop

assignments the user should or should not set. Only one of the Nastran keyword assignments is directly applicable to this workflow: "REPINFO = 3." When "REPINFO = 3" is placed into the run command line, a detailed listing of the variables that were swapped, how many times they were swapped, and the value used in the swapping will be placed at the bottom of the *.f06 file generated for each run. Refer to the *MSC Nastran Quick Reference Guide* [2] to better understand the different settings for the REPINFO optional keyword. The "nohup" at the beginning of this statement ensures that the Nastran run will not stop running if the connection to the remote server is closed out.

Finally, the statements between lines 24 and 28 handle the results files before another run is started. The "sleep" statements ensure that for large results files, everything is completed prior to the next command being carried out. The "mv" command is what moves the specified results files to a new folder called "Study_Results." The last step before going onto the next loop is to clean up all the unnecessary files generated from the Nastran run, using the "rm" command. The "*" is a catch-all statement; therefore, the way it is used in line 27 is to remove any files, no matter the file extension, that have the filename "SOL200_ModelName_Case#."

10.3.3 Shell Script Execution

Now that the shell script has been created, the user is ready to run the shell script. First, the user will need to access the remote server. This is typically done using some sort of shell client software such as X-Win32 or PuTTY, which will connect the user's local computer to the remote server. Once the connection is made, the next step is to make sure the shell script and all the required Nastran files are placed onto the remote server and any necessary folders are created. Next, the custom shell script needs to be set as "executable" on the remote server. To do this, the user simply needs to type **chmod +x SOL200_Auto_Generic.sh** into the command line prompt, where the "SOL200_Auto_Generic" is the saved filename of the custom shell script. The notes on line 1 of Fig. 10.6 inform the user on how this is to be done. Finally, to execute the shell script, the user needs to type **nohup ./SOL200_Auto_Generic.sh &** into the command line prompt.

10.3.4 Output Review

After all the iterations have completed, a review of the results can be undertaken. First, as always, it is good to ensure that the simulation performed the variable swapping as intended. This outcome can be checked at the bottom of the *.f06 file that was generated for each Nastran iteration.

Once checked, the *.op2 files can be read into the ATA IMAT software, and the cross-orthogonality matrices can be generated. This process can easily be automated with scripting. Ultimately, the final outcome is a single spreadsheet that contains the cross-orthogonality matrix for each iteration in a different tab, which allows the user to quickly sort through iterations and see the influence each individual design variable can have on each mode, and it will offer several key insights. First, it will show whether the selected variable has any influence on any of the modes: if changing the variable by an order of magnitude or more does not have a significant impact on any of the modes, that variable can readily be eliminated from the study. Secondly, if the variable does have a significant impact, the user can clearly see which modes it will affect. Finally,

a new value can be assigned to the variable that should be closer to what it will need to be to correlate the FEM. This process can then be repeated as necessary. The elegance of this process is that the original FEM has not been changed at any point in the workflow, greatly simplifying the correlation process where it can be common for numerous iterations of FEMs to be created in the process of finding the "best fit." As a reminder, the goal of this workflow was not to get the "best fit" value for each variable but more to find a close ballpark starting value that can then be carried into a more traditional correlation process such as Attune. Because the framework of files needed for an Attune correlation study is nearly the same as what is required for this workflow, the transition back to Attune is seamless.

10.4 Case Study

Boeing has developed the CST-100 Starliner to transport astronauts to the International Space Station. The CST-100 Starliner consists of two primary components: the Crew Module (CM), which can support up to five people on the primary seat pallet (SP), and the Service Module (SM). Validating the FEM of the CST-100 is a mission critical task because the analysis predictions provide confidence in ensuring a safe dynamic environment in all stages of flight for the health of the crew. ATA was hired to conduct a MST of the CM with an emphasis on the modes of the SP because the SP modes would have the biggest impact on the dynamic environment experienced by the crew during flight. In July 2020, ATA successfully completed the MST of the CM isolated with a soft suspension system, utilizing 3 shakers and approximately 400 accelerometers. Figure 10.10 shows the CST-100 Starliner CM in the test configuration. Two shakers were attached to exterior structural components of the CM, and the third shaker was placed in an isolation cage inside the CM to directly excite the SP. The SP was mass loaded with sandbags to represent the predicted as-flown configuration. Approximately 50 modes of the CM and SP were extracted up to 100 Hz.

The primary focus of the posttest model correlation, which was joint effort between ATA, Boeing, and NASA, was ensuring the model quality of the SP. The single 2.4 million DOF common FEM of the CST-100 is used for load and stress predictions at multiple phases of flight including liftoff, in-orbit, descent, and landing, and the boundary condition of the vehicle changes from fixed to the launch vehicle, combined CM/SM, and CM in a free-free configuration. As a result, the

Fig. 10.10 Boeing CST-100 Starliner CM in the test configuration

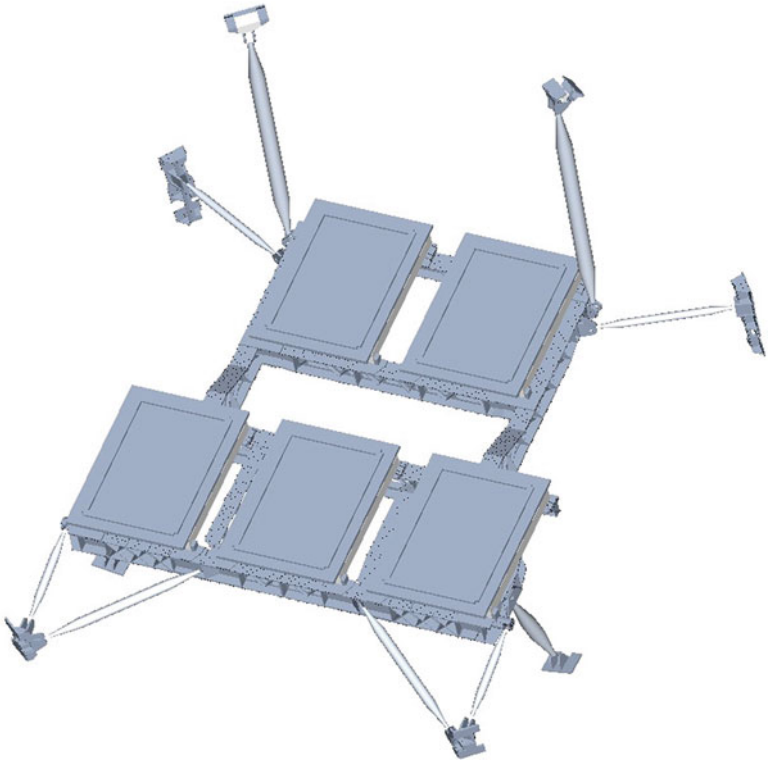

Fig. 10.11 Representation of SP FEM showing strut attachments to CM

model correlation effort focused on keeping a physics-based approach as opposed to simply adjust model parameters to make the FEM match a single set of test modes.

The SP is attached to the CM pressure dome with ten struts that have spherical ball joints at both ends. Figure 10.11 shows the primary geometry and attachment locations of the SP relative to the CM with cargo shelves attached at each of the seat positions. The attachment mechanisms of the cargo shelves to the SP exhibited the same uncertain nonlinear behavior as the spherical ball joints of each strut. Attempting to adjust the stiffness values of these joints was the motivation for the development of the previously discussed workflow. A linearity study of the SP conducted during the MST confirmed the nonlinearity of these joints. The stiffness values in question were the rotations and axial translations of the strut joints, as well as the majority of the stiffnesses of the cargo adapter joints. After all the meshes were verified as representing the desired load paths, and with a basic understanding of how primary joint stiffness affected the target modes of interest, a limited Monte Carlo–style analysis was performed to identify a set of PBUSH values that could be used in Attune to further improve the correlation.

The objective of the following case study is to demonstrate the value of the developed workflow, rather than to present a study of the CST-100 Starliner's structural dynamic behavior. As such, mode shape descriptions and explicit changes made to the FEM are not discussed. To protect proprietary design data, the presented data does not represent initial or final results nor does it comprise a complete data set. Adjustments have been made to all the cross-orthogonality matrices to remove unnecessary information, including off-diagonal terms, frequencies, and modes associated with non-flight configuration components.

Figure 10.12 shows the cross-orthogonality matrix between the test mode shapes and FEM mode shapes that are the starting point for the workflow demonstration. The modes of interest for the study are test and FEM modes highlighted in blue. After multiple attempts to manually diagonalize test modes 6 through 8, the correlation team had a good understanding of how the modes in question were sensitive to each of the elemental physical properties. The challenge arose that improvements in orthogonality were usually accompanied by an unacceptable change in frequency. The conclusion was that other spring stiffness variables were incorrect by a significant factor. The PBUSH properties were grouped into four design variables based on engineering judgment. Fundamentally, the groups were based on strut end rotations as well as different combinations of cargo adapter spring stiffness translations and rotations. A Monte Carlo simulation was run with

Test Shapes	FEM Shapes 1	2	3	4	5	6	7	8	9	10	11	12	13
1	98												
2		95											
3			100										
4				96									
5					99								
6							75	39					
7							62	81					
8						95							
9									56				
10										98			
11											96		
12												78	46
13												43	72

Fig. 10.12 Snapshot of initial cross-orthogonality matrix associated with coupled mode pairs

Table 10.1 Summary of DESVAR permutations

DESVAR	Automated substitution scaling			
A	0.01×	0.1×	10×	100×
B	0.01×	0.1×	10×	100×
C	0.01×	0.1×	10×	100×
D	0.1×	10×	100×	1000×

the above workflow, varying the DESVARs one at a time by 4 different orders of magnitude, summarized in Table 10.1, totaling 16 unique runs. Cross-sensitivity was not examined directly.

Figure 10.13 contains an excerpt of the resulting cross-orthogonality matrices from the Monte Carlo simulation for DESVARs A and D at three different values. The shown matrices were selected to illustrate the relative changes observed for the four design variables. Figure 10.13a indicates that dropping DESVAR A by two orders of magnitude is most likely too significant of a change, because two additional modes appear. Figure 10.13b indicates that reducing DESVAR A by one order of magnitude increases the on-diagonal and decreases the off-diagonal values of modes 7 and 8, indicating that DESVAR A should be lowered. Figure 10.13c shows that increasing DESVAR A by one order of magnitude diagonalizes modes 7 and 8 in reverse order and significantly decreases the orthogonality of modes 12 and 13. Figure 10.13d–f indicate that changing DESVAR D by multiple orders of magnitude has little effect on the overall correlation value and, as such, the original value should be retained for the subsequent correlation effort.

DESVAR B exhibited behavior similar to DESVAR A, indicating that it should also be reduced by an order of magnitude, and like DESVAR D, DESVAR C indicated that it should remain unchanged. However, the changes in magnitude of DESVAR C exhibited the same behavior of additional modes and misaligned diagonalization as DESVAR A. With these adjustments in mind, the design variables A and B were reduced based on the Monte Carlo results, and the model was passed through Attune for further refinement of design variables. Figure 10.14 shows the resulting cross-orthogonality matrix. Test modes 6 and 7 have now diagonalized with FEM modes 7 and 8 with significantly lower off-diagonal terms. Additionally, test/FEM modes 12 and 13 were improved, with higher on-diagonals and lower off-diagonals. While not explicitly reported here, the frequency difference of the first mode pair saw limited improvement after the described workflow was utilized. Additionally, the second mode pair did see a noticeable improvement in the frequency error of mode 12.

As previously stated, the purpose of the case study is to demonstrate the effectiveness of the method on an actual model correlation. The workflow was effective in reducing the amount of time required to iterate through different DESVAR orders of magnitude and helped to identify a better range for physical properties that may not be the primary turning knob for a particular mode. From a larger perspective, however, the role of the engineer in understanding the results and justifying changes to the model was not altered. The final correlation of the CST-100 produced a physics-based model that accurately captures the dynamics of the test configuration up to 50 Hz. As a result, Boeing and NASA had a grounded model that could be used for subsequent analysis to ensure the safety of the crew and the structural integrity of the vehicle.

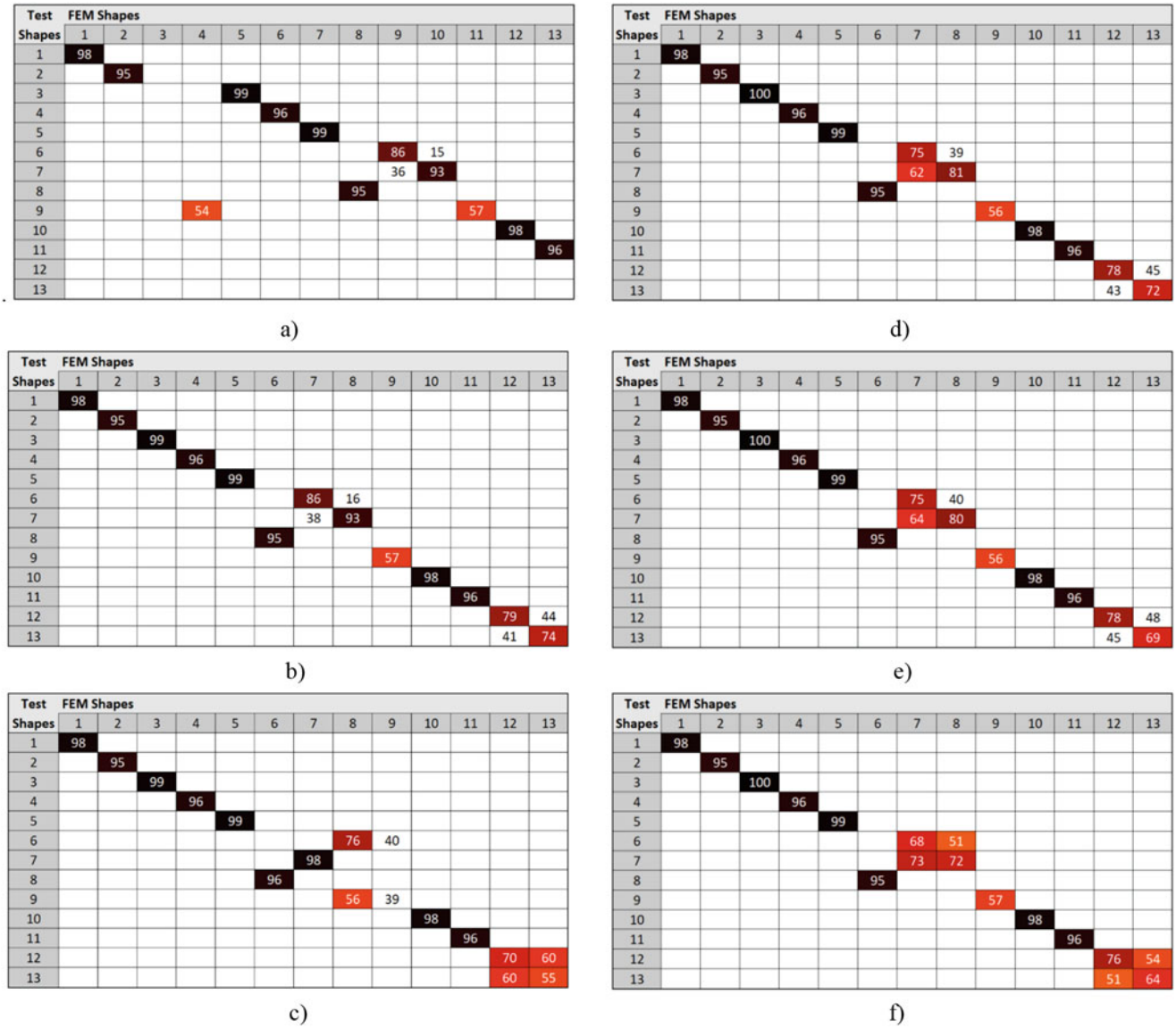

Fig. 10.13 Cross-orthogonality matrices outputted from Monte Carlo simulation. (**a**) DESVAR A × 0.01. (**b**) DESVAR A × 0.1. (**c**) DESVAR A × 10. (**d**) DESVAR D × 0.1. (**e**) DESVAR D × 10. (**f**) DESVAR D × 100

10.5 Conclusion

The objective of this chapter was to present a workflow for use in model correlation to expedite the examination of the design space by automating MSC deck generation. The technique proved useful in finding improved stiffness ranges for joints that are not easily modeled with linear finite elements. While this chapter focused on the application of model correlation, the technique can also be used for MST pretest analysis to better understand FEM sensitivities or for variational design sensitivity studies.

Test Shapes	FEM Shapes 1	2	3	4	5	6	7	8	9	10	11	12	13
1	98												
2		95											
3			100										
4				96									
5					100								
6							89	0					
7							19	98					
8						96							
9									57				
10										94			
11											97		
12												84	12
13												18	92

Fig. 10.14 Snapshot of cross-orthogonality matrix after Monte Carlo and Attune™ associated with coupled mode pairs

References

1. Stewart, E., Blelloch, P., Coppolino, R.: Improving accuracy of structural dynamic modification with augmented modes residual vectors. In: AIAA Scitech 2019 Forum
2. The MSC Software Corporation. Quick Reference Guide. Newport Beach (2019)
3. The MSC Software Corporation. Reference Guide. Newport Beach (2019)
4. The MSC Software Corporation. Design Sensitivity and Optimization User's Guide. Newport Beach (2019)

Chapter 11
Multi-Shaker Testing at the Component Level

William Larsen, Ryan Schultz, and Brandon Zwink

Abstract Unlike traditional base excitation vibration qualification testing, multi-axis vibration testing methods can be significantly faster and more accurate. Here, a 12-shaker multiple-input/multiple-output (MIMO) test method called intrinsic connection excitation (ICE) is developed and assessed for use on an example aerospace component. In this study, the ICE technique utilizes 12 shakers, 1 for each boundary condition attachment degree of freedom to the component, specially designed fixtures, and MIMO control to provide an accurate set of loads and boundary conditions during the test. Acceleration, force, and voltage control provide insight into the viability of this testing method. System field test and ICE test results are compared to traditional single degree of freedom specification development and testing. Results indicate the multi-shaker ICE test provided a much more accurate replication of system field test response compared with single degree of freedom testing.

Keywords MIMO · Experimental · Dynamic environments testing · Intrinsic connection excitation

11.1 Introduction

Single-axis, base excitation vibration testing has long been considered an overly conservative and robust testing method. Recent research thrusts have shifted to consider multi-axis testing and boundary conditions in an attempt to advance this testing [1–3]. This should provide better test accuracy which would improve margin assessments, reduce overconservatism, and ultimately reduce overdesign. The test time should decrease by performing all testing in one test setup rather than three independent test configurations for each axis. Also, lower initial cost of entry should allow more access for more facilities and industries to perform multi-axis testing, which will allow more advancement in related areas.

The overall goal of this work is to demonstrate these vibration testing improvements by performing a component-level multi-shaker test utilizing a test technique called intrinsic connection excitation (ICE) [4]. This method assumes that the required number of control degrees of freedom must match or exceed the number of connection degrees of freedom of the unit, which should allow for appropriate control of a component to a field environment. A test fixture and setup were designed and created to minimize input forces required to appropriately excite a component [5]. Although this is a demonstration of a random test, there is certainly validity in expanding this concept to shock or other testing environments [6].

Although many tests were performed, parameters of interest of the ICE test method that will be presented here include ICE setup linearity, fixture control, accuracy of uncontrolled degrees of freedom, voltage control, force control, and setup repeatability. All of these should provide insight into scalability of this technique, future specification options, accuracy of full-field test recreation, and sensitivity to unit mounting. Single-excitation axis tests will be compared using current common practice techniques with enveloped system data as well as narrowband control, which should compare the traditional method's ability to replicate the field environment dynamics of the component in a laboratory test.

Sandia National Laboratories is a multimission laboratory managed and operated by National Technology and Engineering Solutions of Sandia, LLC., a wholly owned subsidiary of Honeywell International, Inc., for the US Department of Energy's National Nuclear Security Administration under contract DE-NA0003525.

W. Larsen (✉) · R. Schultz · B. Zwink
Sandia National Laboratories, Albuquerque, NM, USA
e-mail: wlarse@sandia.gov

C. Walber et al. (eds.), *Sensors and Instrumentation, Aircraft/Aerospace and Dynamic Environments Testing, Volume 7*,
Conference Proceedings of the Society for Experimental Mechanics Series, https://doi.org/10.1007/978-3-031-05415-0_11

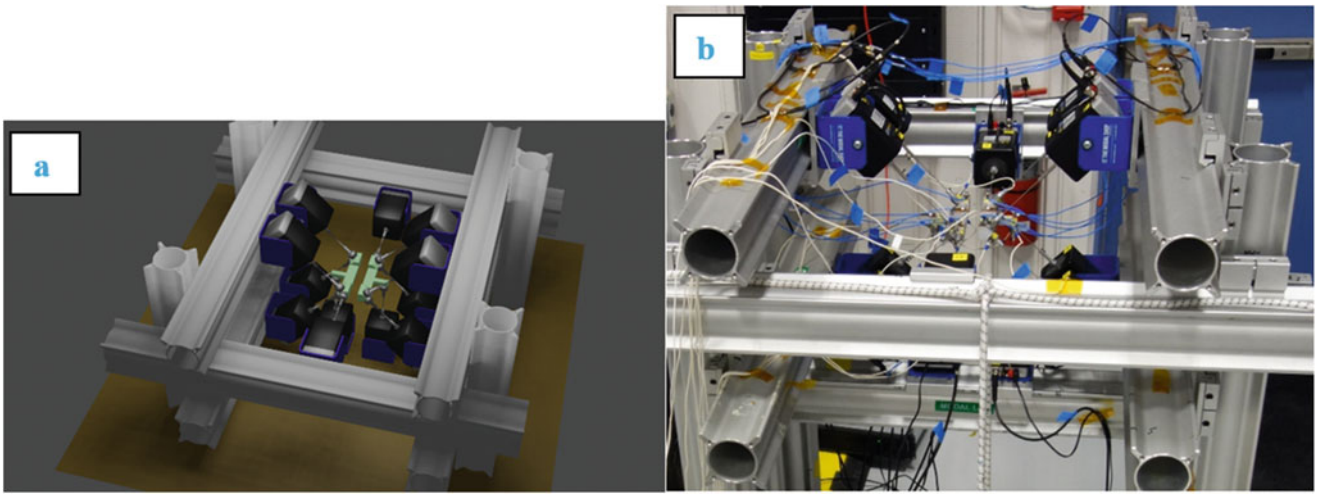

Fig. 11.1 (**a**) ICE model without test unit and (**b**) ICE test setup

Fig. 11.2 (**a**) ICE fixtures and (**b**) instrumented ICE fixtures in test setup

A test was designed including 12 shakers in an attempt to control connection degrees of freedom between the test unit and fixture within the test frequency band. A secondary objective was to obtain an accurate test with a low amount of force as small shakers were used to excite the system. An aluminum frame supports the shakers, and the steel stingers are the only support for the fixture. The unit (which is removed in these photos) then mounts to the two independent fixtures, as seen in Fig. 11.1.

This setup included two custom lightweight fixtures that were designed with the intention of controlling all connection forces to the test unit as directly as possible. The use of multiple independent fixtures allows more modes of the system to be controlled when compared to a rigid single-piece fixture, even modes with relative motion between mounts. This design may be relatively universal for other mounting locations and units. These fixtures could then potentially be scaled up or down to accommodate other units in future iterations of this technique (Fig. 11.2).

Though not strictly necessary, for demonstration purposes, this test article and the fixtures were heavily instrumented. Eight triaxial accelerometers were attached to the unit, four at the base and four on the exterior of the unit. Ten triaxial accelerometers were attached to the fixtures, four near the base of unit and six near the extremities of the fixtures. Twelve force transducers were used between each stinger and its attachment location on the fixtures. Less instrumentation would likely be required routinely for this type of testing, but the additional instrumentation provided increased insight into the dynamics of the test and facilitated experimental trials utilizing different control methods.

11.2 Field and Laboratory Configurations

A reference field environment was created experimentally on a cylinder "system" with three shaker inputs because data from a representative field test was not available. An attempt was made to match overall frequency bandwidth and approximate acceleration levels of previous single degree of freedom specifications. The unit was attached to a modified cylinder, and uniform, uncorrelated inputs were provided to the three shakers. The response of the eight accelerometers on the unit provides a "system" test, and the response power spectral densities for these accelerometers act as the multi-degree of freedom (MDOF) specification for subsequent multi-input/multi-output (MIMO) testing.

The eight accelerometers on the test unit were never removed to reduce sources of error due to instrumentation differences in field and laboratory test configurations. The previously discussed ICE configuration and a standard single degree of freedom (SDOF) configuration are used to compare the two methods.

These tests were performed and compared to assess accuracy and to determine what is feasible for laboratory recreation and specification from field data.

11.3 System Tests

The system tests were conducted at five input levels for 10–4000 Hz of the three shakers seen in Fig. 11.3. The test itself was designed to be narrowband and lightly damped to simulate the intended challenge and produce a system "field" specification.

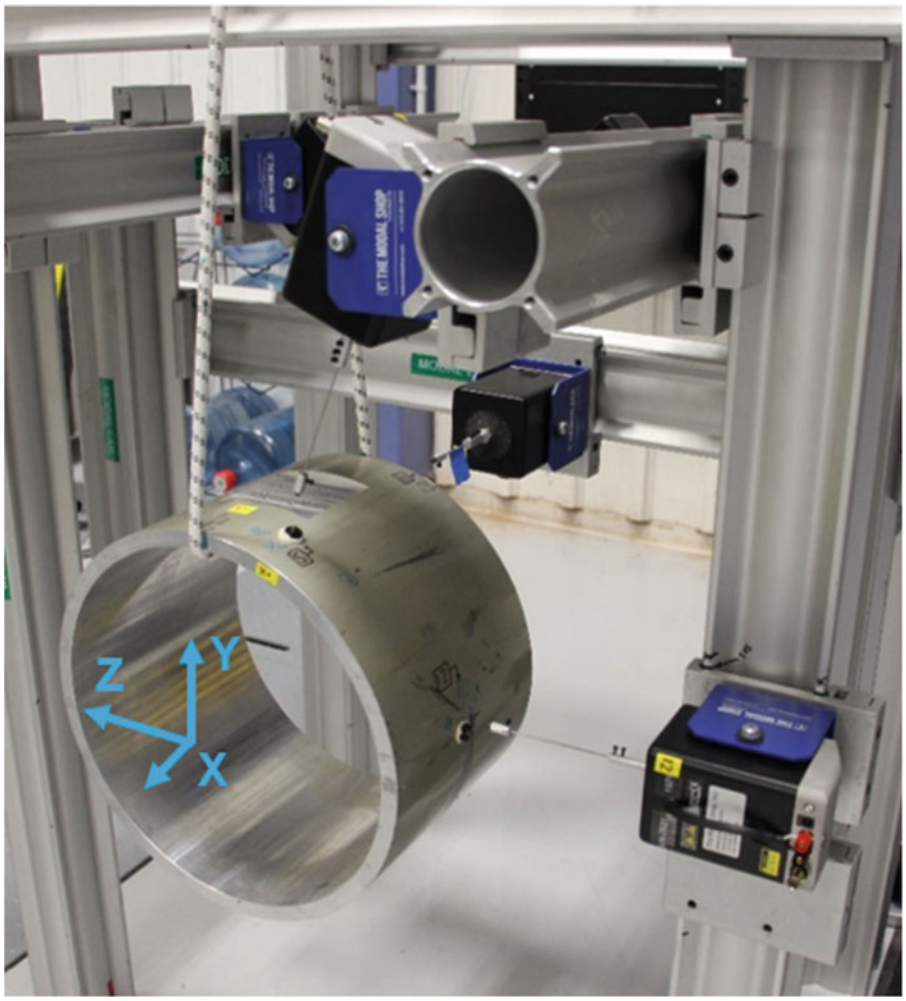

Fig. 11.3 "System" configuration

Three shakers were used to appropriately excite all modes of the system. The overall sum of the 24 acceleration response channels and the root mean square (RMS) of each individual channel was monitored and is included to summarize the responses of the test configuration.

The data quality was deemed acceptable and the system behaved linearly within this amplitude region. The response was rich, with complex dynamics within the test bandwidth of 100–3000 Hz. This simulated field test has similar frequency range, frequency content, and overall response levels as expected of the component mounted in a real system and service environment. One hundred to three thousand Hz is selected as the frequency bandwidth of interest for a specification for the remaining tests. The 24 channels of acceleration responses on the unit from this system test (the blue curve "TEST0118" in Fig. 11.5) will be considered the primary specification.

11.4 ICE Tests

After the system tests, the ICE configuration shown in Fig. 11.4 was set up. To keep the shaker force levels low, shape constraint input estimation was used as the control method in a custom in-house control system used throughout this testing [7]. A match trace technique was also used in an attempt to simultaneously match the sum of the control degrees of freedom and remove any global bias errors. The in-house control system utilizes National Instruments hardware and a custom Python-based control software called Rattlesnake, which is now available open source.

To assess overall success of the test to match the specification, a global error metric from MIL 810 was used [8]. This metric aggregates over degrees of freedom to produce a single curve as a function of frequency to compare two tests and has been proven to be a realistic assessment metric compared to the stress present in a part, as described by Beale et al. [9].

The remainder of this section presents ICE test results where various control methods were utilized for the ICE configuration.

Linearity

The linearity of the ICE setup was assessed by controlling to the specifications created from all five of the amplitude levels displayed in Fig. 11.5. This was done to determine whether this unit and the test method in question is linearly scalable to higher amplitudes. If it is not, this testing method wouldn't be useful. The specification description format in the legend shown here is "SPEC: Number of controls (24), acceleration channels used as control (A), from test setup (SYS), test number (TEST0118), and description (0.01 Vrms) (Fig. 11.6)."

These ICE tests result in excellent recreation of the system tests. Full level response was achieved within the limits of the shakers, meaning higher level testing may be possible. The MIL 810 Global Error Metric also reveals a reasonable recreation of the tests. The lowest amplitude test was consistently used as the reference test in the MIL 810 Global Error Metric calculation, so the linearity of the system tests can be monitored as well (Fig. 11.7).

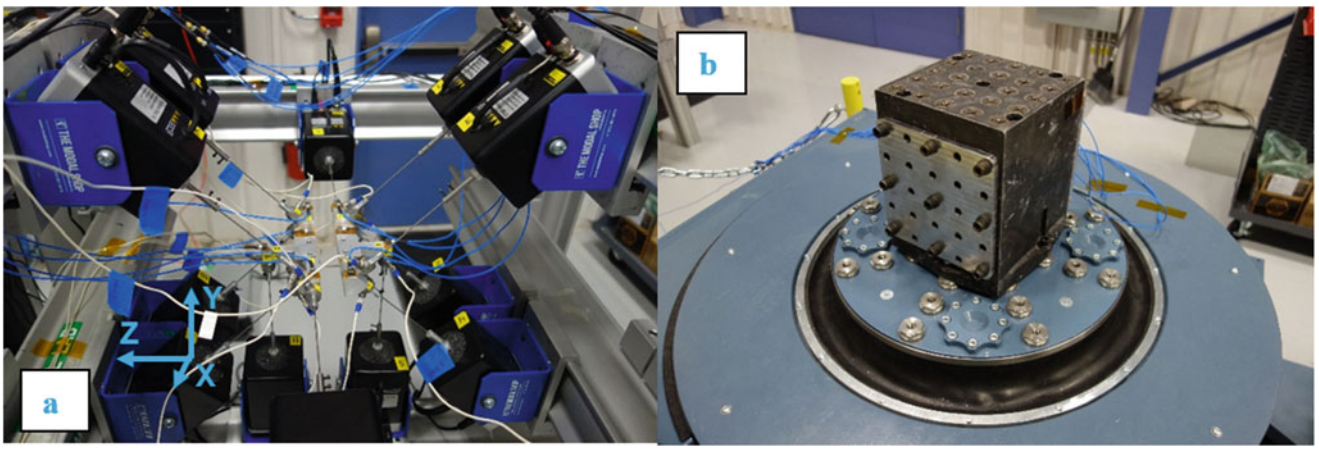

Fig. 11.4 (**a**) ICE configuration and (**b**) SDOF configuration

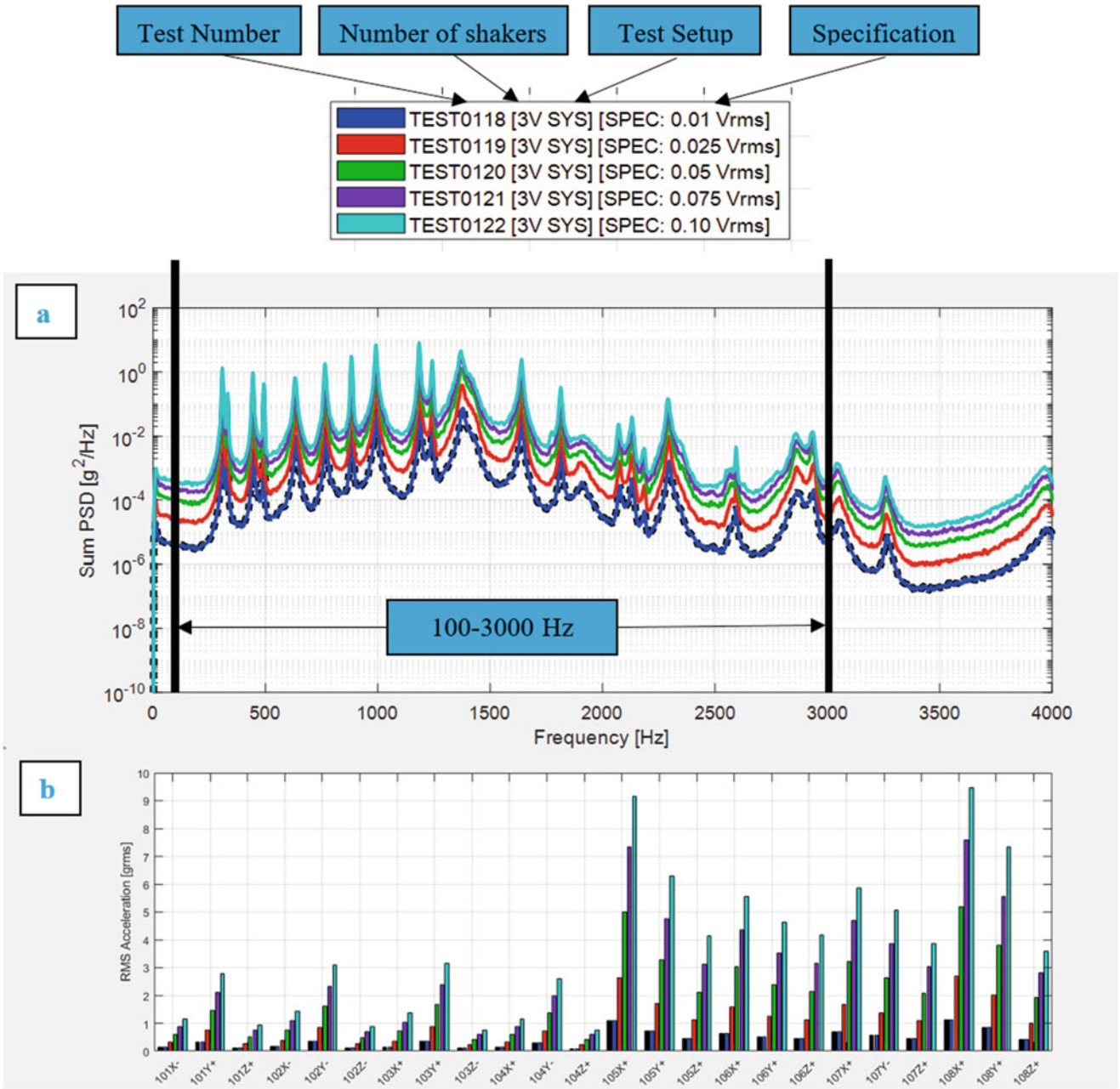

Fig. 11.5 System results: (**a**) sum of 24 acceleration response channels on unit and (**b**) RMS of each individual channel

These results prove this test method is linear within this region and is an accurate, viable test method. There is deviation in the Global Error Metric at approximately 500 Hz, which is a mode mismatch between the boundary conditions of the two tests methods, making it difficult to control in the ICE configuration.

Fixture Control

The previous results indicated that accurate control can be achieved when controlling to accelerometers on the unit. However, it may be desirable to control only to gauges on the fixtures as that would speed up test setup and make changing the test unit simpler. Specifications could also be developed at this level to provide appropriate consistency to this test method. Here, fixture control using different sets of accelerometers is demonstrated. An explanation of three fixture-controlled tests can be seen in Fig. 11.8. Green boxes show the overall fixture control test, purple boxes show the base of the component fixture control test, and blue show the extremity of the fixture control test. These correspond with colors in the legend. This was done to assess how sensitive and controllable the fixture and unit is while also determining how much of the fixture is required to

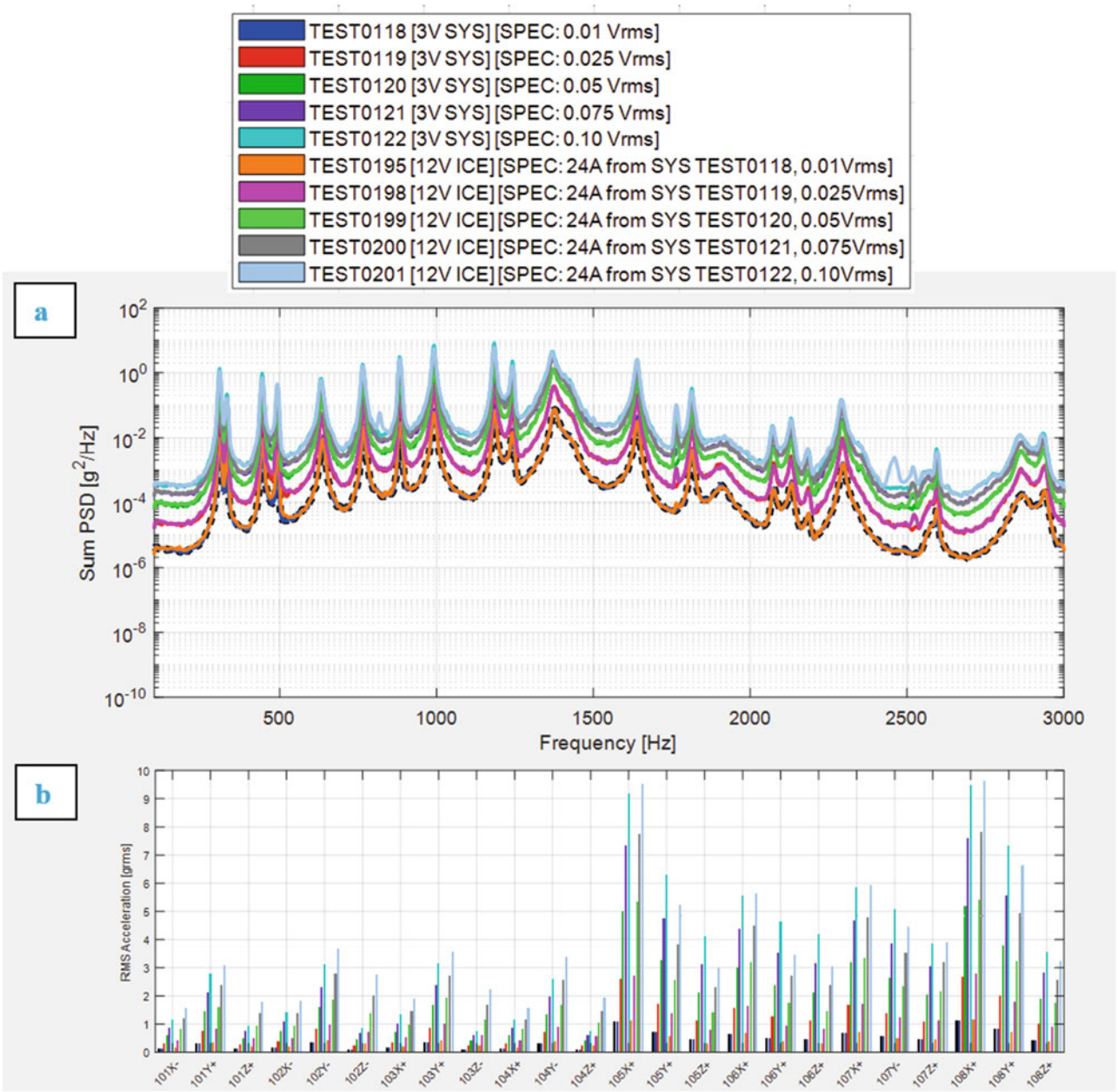

Fig. 11.6 System and ICE results: (**a**) sum of 24 acceleration response channels on unit and (**b**) RMS of each individual channel

be controlled and how close to the unit is required to get the same response. The red curve in Fig. 11.9 is controlling in the ICE configuration using the 24 acceleration channels from the system test, which is what all of these fixture-controlled tests were derived from (Fig. 11.10).

It is notable that there is a slight improvement in matching the specification as the control location becomes closer to the unit, but these overall results and the MIL 810 Global Error revealed reasonable consistency. This allows more possibilities for developing specifications in the future. Potentially a pristine unit could be used to run the first test in the ICE configuration and a specification could then be developed from that for actual subsequent tests of unknown caliber units.

Test Accuracy and Voltage or Force Control

To assess accuracy of this test method at uncontrolled locations, two accelerometers (six acceleration channels) were not included in the control, which is the green curve in Fig. 11.11.

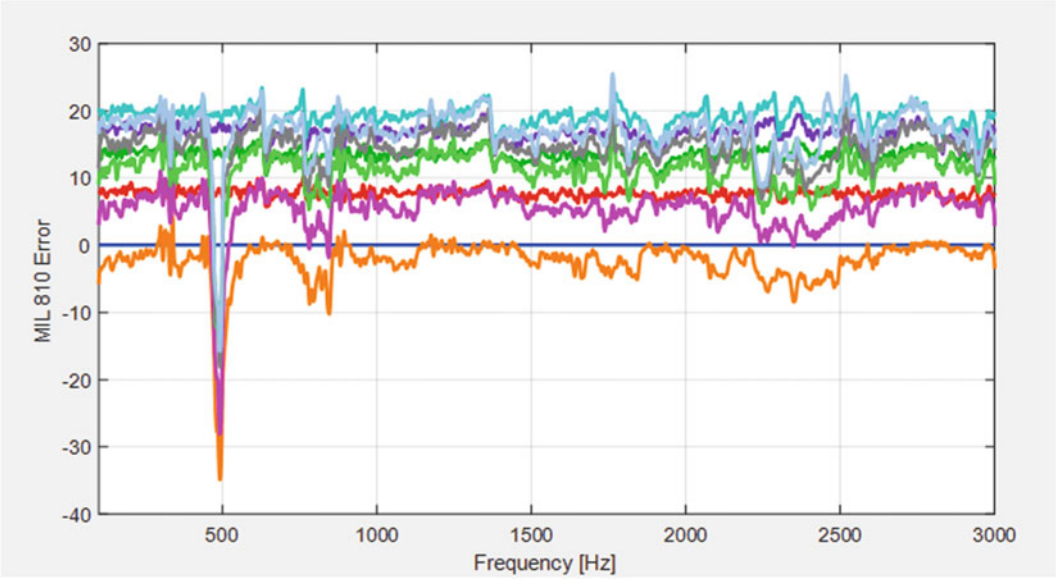

Fig. 11.7 System and ICE MIL 810 Global Error Metric

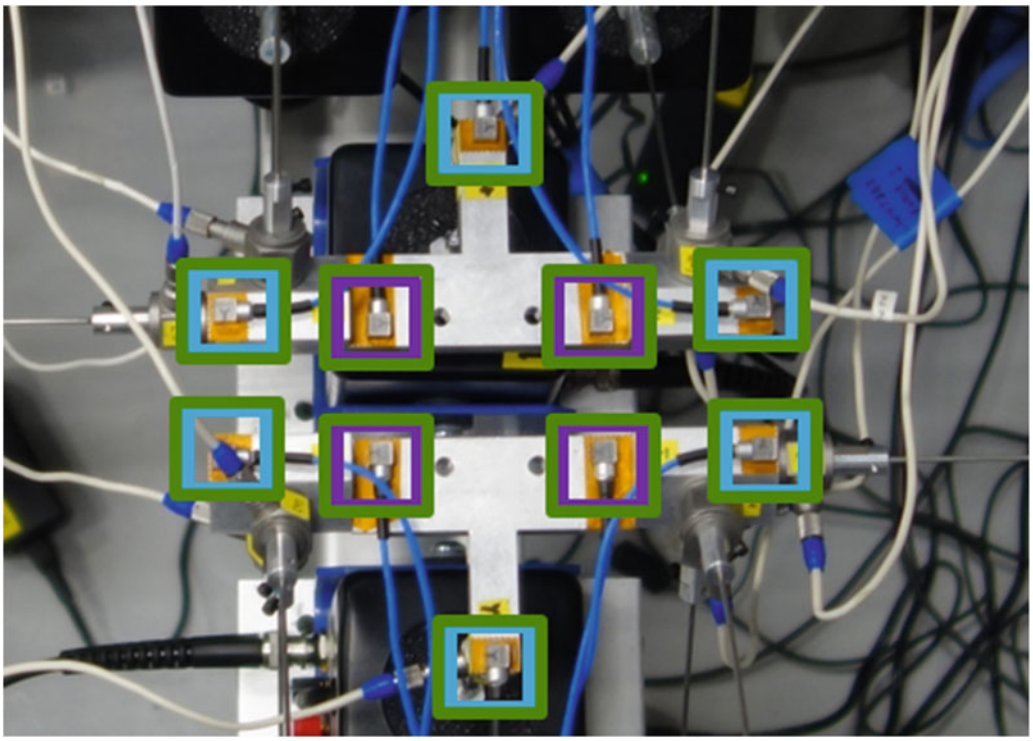

Fig. 11.8 Depiction of control location of fixture control tests

In a similar sense of fixture control, taking a step further back and controlling to the measured voltage of the shakers and measured forces of the force transducers from a previous ICE test, the accuracy and viability of this method are assessed. Purple is voltage control and teal is force control in Figs. 11.11 and 11.12.

The overall results and MIL 810 Global Error revealed consistency of all these techniques. The test that did not control to all 24 acceleration channels, but rather controlled to 18 acceleration channels, produced similar responses to the test that controlled to 24 acceleration channels. This suggests that all (even uncontrolled and unmeasured) locations are being recreated accurately, even if they are not controlled. This gives confidence that this test method is accurately recreating the

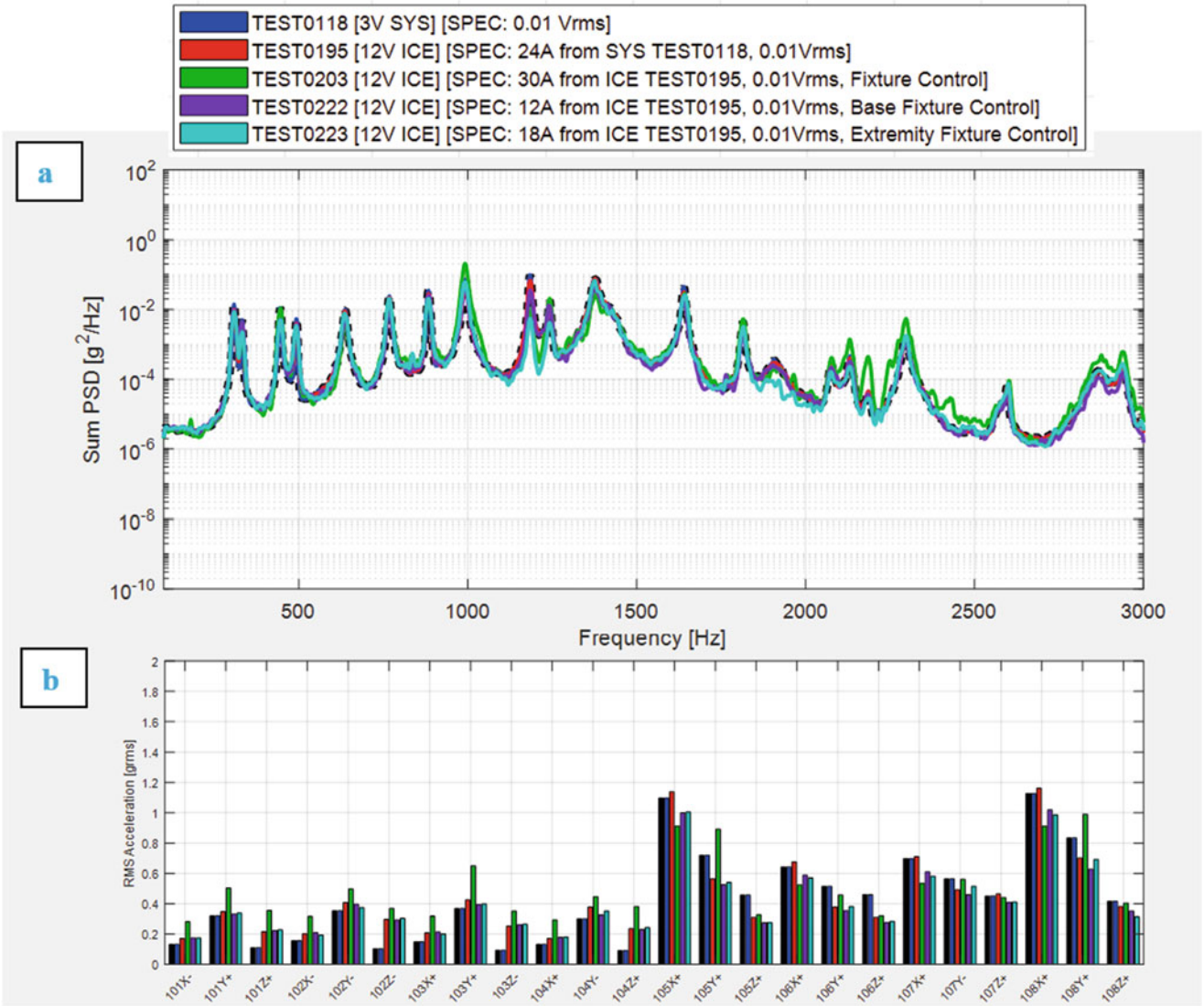

Fig. 11.9 System and ICE fixture control results: (**a**) sum of 24 acceleration response channels on unit and (**b**) RMS of each individual channel

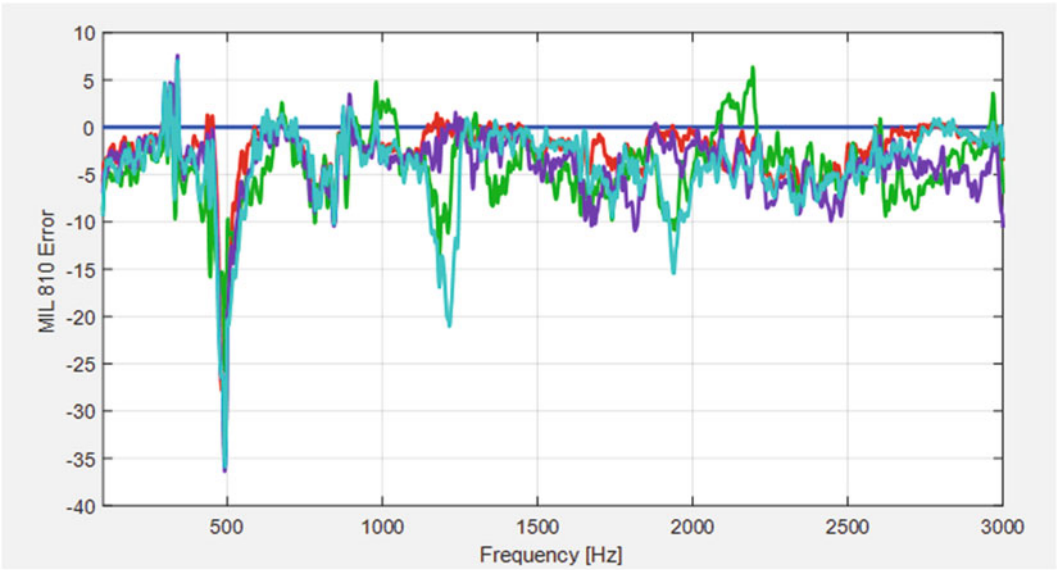

Fig. 11.10 ICE fixture control MIL 810 Global Error Metric

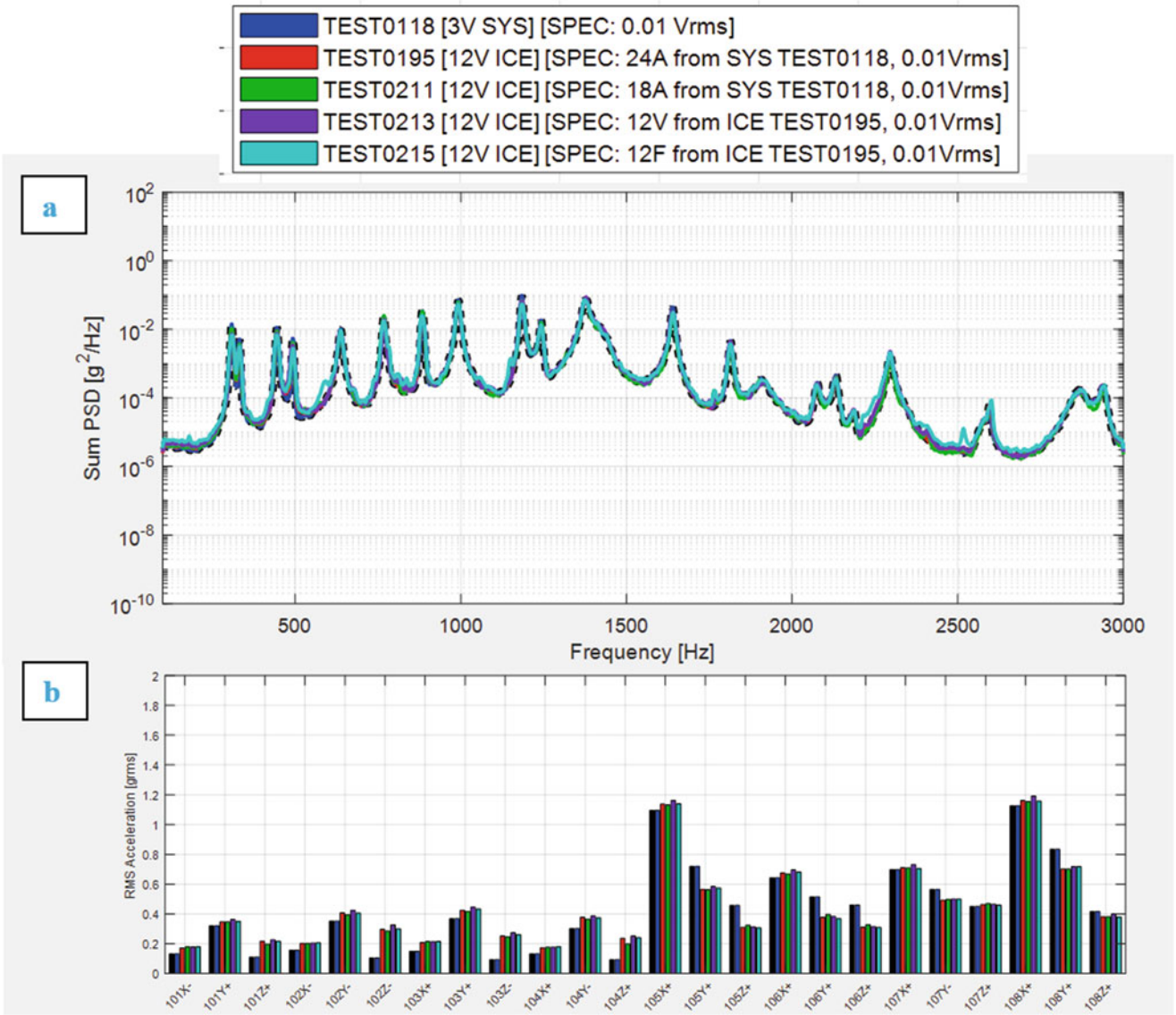

Fig. 11.11 System and ICE limited control channels, force or voltage control results: (**a**) sum of 24 acceleration response channels on unit and (**b**) RMS of each individual channel

full-field environment. The forces required for these tests were all similar as well. This really opens the discussion for how far back in the system you could assign specifications (while also balancing setup differences).

Test Repeatability

To assess repeatability, the unit was removed and replaced (retorqued) on the fixtures in the ICE configuration 4 separate times and controlled with the methods described previously as "24 acceleration control," "12 voltage control," and "12 force control" tests. The most varied of all those methods (force control) are shown here. Other techniques had less variability in their response (Figs. 11.13 and 11.14).

The repeatability appears within nominal test to test differences, and this metric supports the claim that this test setup and method is not sensitive to slight mounting differences, encouraging its reliability. This was also performed at higher amplitude with similar success.

Overall, ICE tests result in good recreation of the system field environments. This technique should be scalable to higher amplitudes. Fixture control allows more possibilities for developing specifications. Nearly identical response (even for six uncontrolled degrees of freedom) indicates that the dynamics match at every point of the component. Force and

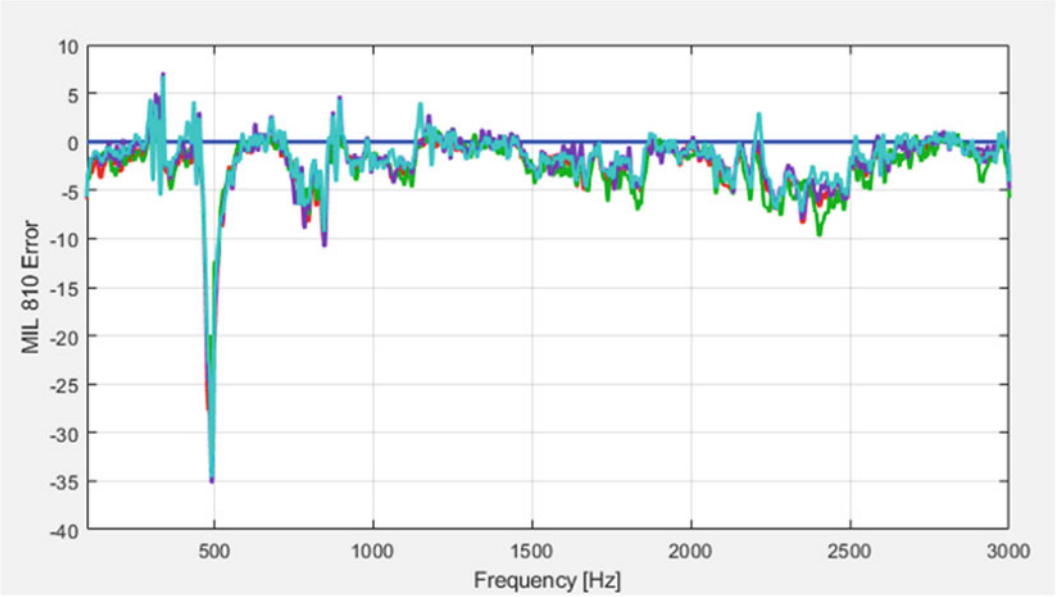

Fig. 11.12 ICE limited control channels, force or voltage control MIL 810 Global Error Metric

voltage control allow more possibilities for developing specifications as well. Repeatability of these tests show variability of removing and reattaching the component is low.

11.5 SDOF Tests

Although these results appear promising, to truly understand the improvement of this testing method over single-axis testing, the system test data was processed in a way that is consistent with standard single degree of freedom methods to develop a single control specification for a location at the base of the unit, shown as the red curve in Fig. 11.15. This was then attached to an Unholtz-Dickie T2000 shaker in the configuration shown in Fig. 11.4. This examines the differences in specification, control, and boundary condition. Also included is simply controlling to the narrowband response at a single location at the base of the unit using a response from the system test to examine the differences in simply the boundary condition mismatch, which is the green curve in Fig. 11.15. Only example data from a single axis (Y-axis) is shown here.

The single degree of freedom test in red is developed using all four accelerometer responses on the base of the unit and enveloping the responses to create one control location at a single base location. This appears to be radically over-testing. The green curve represents controlling to just a single narrowband response from the system test (to determine the amount that the difference in boundary conditions would have), which also does not accurately match the sum of the 24 responses from the system test. The following is an example of the control location for both these SDOF tests (Fig. 11.16).

While the controller is doing an excellent job, even the boundary condition mismatch between the system and SDOF test is apparent in the overall test performance and does not truly represent the field environment.

11.6 Overall System, ICE, and SDOF Comparison

Reviewing the system test (which created the specification), the ICE test, and the SDOF tests in X, Y, and Z, it is apparent which is a better representation of the service environment (Fig. 11.17).

The ICE and system tests are nearly indiscernible, while the single-axis tests are nearly an order of magnitude higher in RMS and more in some frequency bands of the overall sum of the 24 acceleration response channels on the unit (Fig. 11.18).

Perhaps a better representation of the accuracy is the control and response at each individual channel, of which an example is shown in Fig. 11.19.

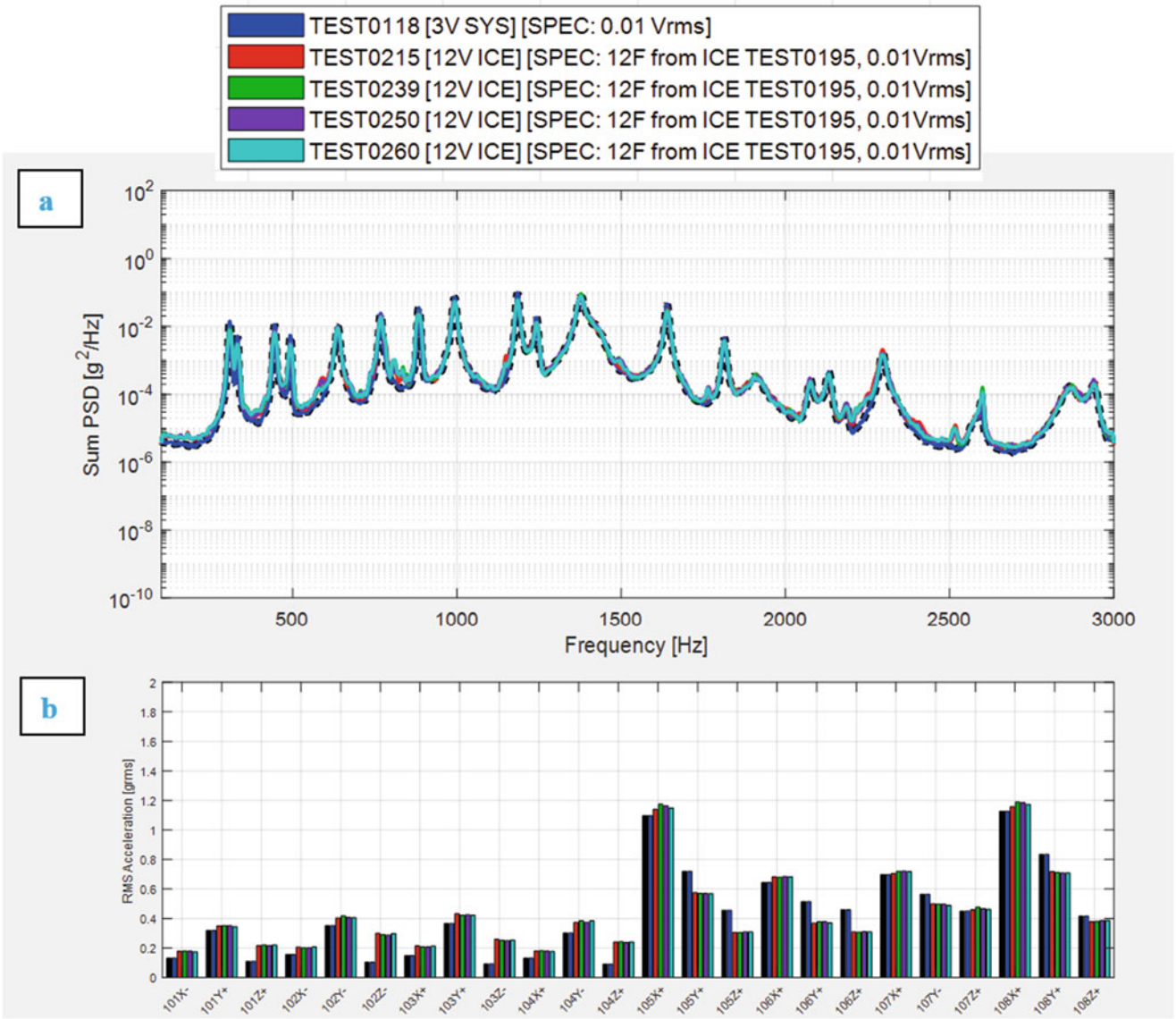

Fig. 11.13 ICE force control results: (**a**) sum of 24 acceleration response channels on unit and (**b**) RMS of each individual channel

These single-axis tests are severely over-testing at the base of the unit over most of the frequency range, but what's most intriguing is that at approximately 1200 Hz, the response of all of the single-axis tests is nearly an order of magnitude lower than the mode present in the system and the ICE tests. This reveals a breakdown in historically accepted logic for this style of testing. It is not guaranteed that simply enveloping response data at the base results in an over-conservative single-axis test.

A couple additional considerations are the setup time and cost from this ICE testing compared to traditional single-axis testing. Single-axis testing required 5–8 minutes from attachment and removal of the unit per axis, while this ICE testing required 4–5 minutes to attach and remove the unit for a single test. This is 1–1.5 times faster, which ultimately results in 3–4.5 times faster for setup alone (accounting for all three axes in single-axis testing). To note, this time assessment excludes actual test time, which would make this margin even higher. The cost of ICE testing is also significantly less, while single degree of freedom testing requires a large shaker, amplifiers, fixtures, facility infrastructure, etc. A general assessment was done and revealed ICE testing is approximately 1/20th of the cost, which allows more facilities and institutions to do this type of testing and should also lower the cost of entry to do MIMO research.

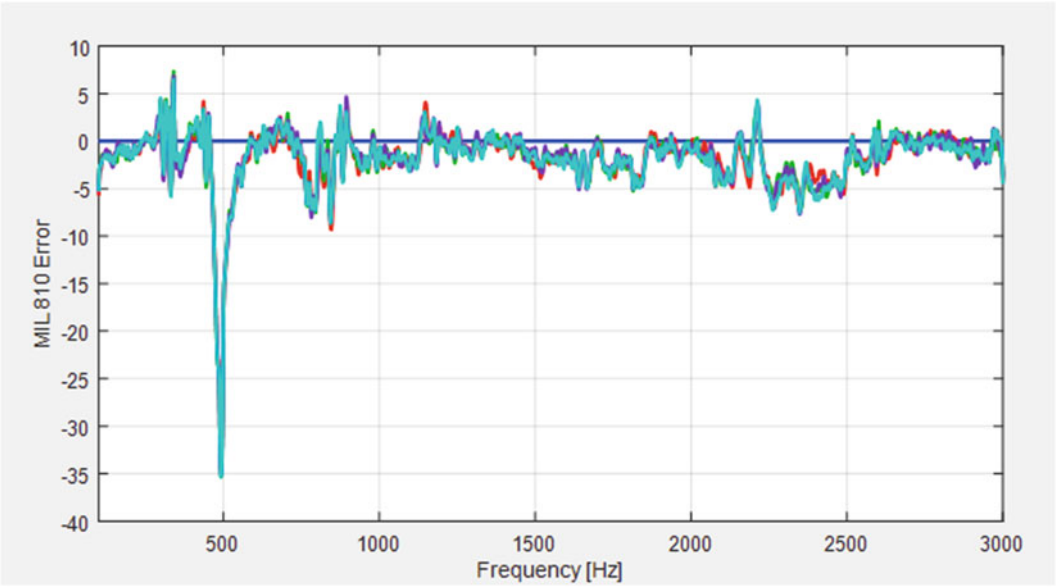

Fig. 11.14 ICE limited control channels, force or voltage control MIL 810 Global Error Metric

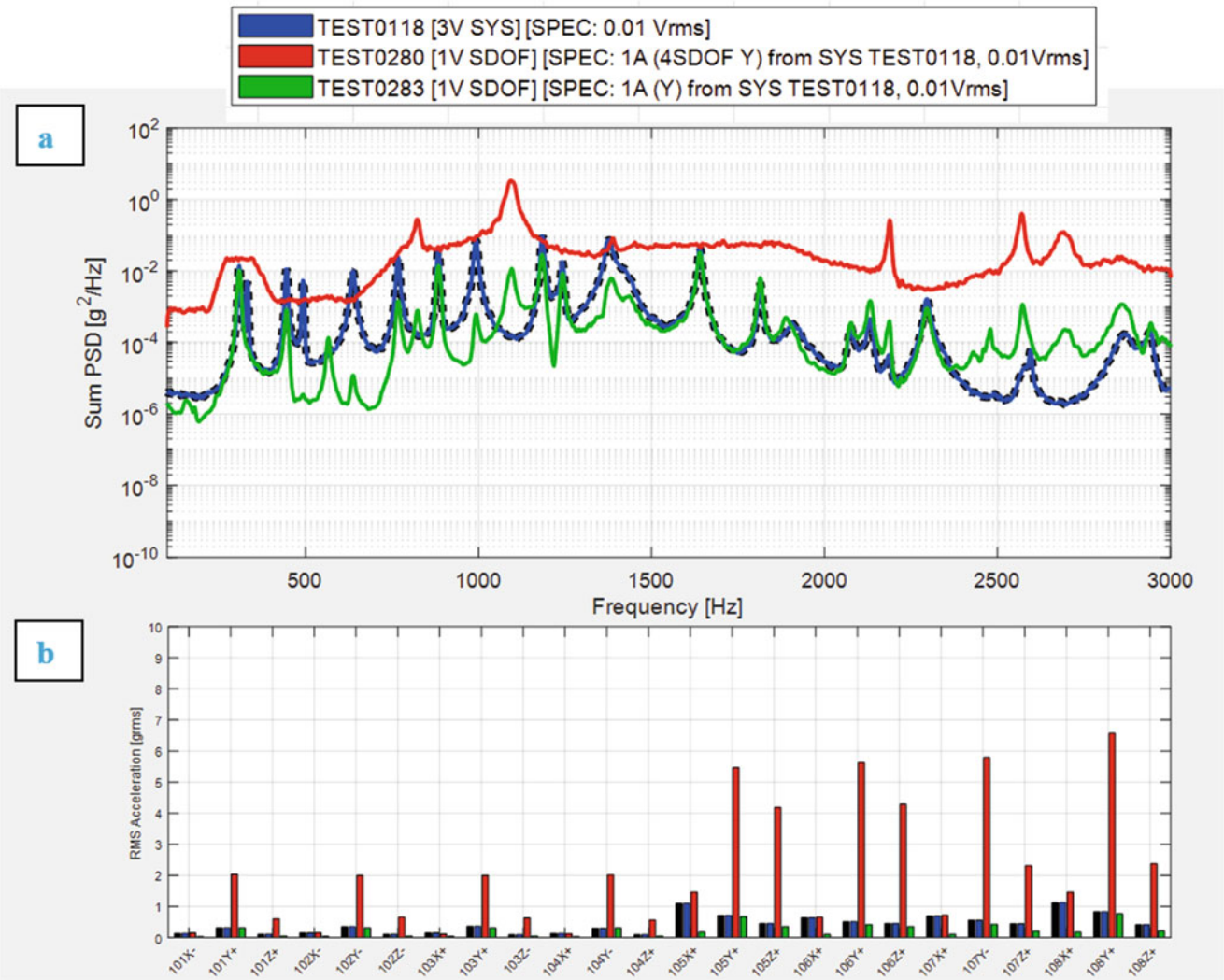

Fig. 11.15 SDOF results in Y-axis: (**a**) sum of 24 acceleration response channels on unit and (**b**) RMS of each individual channel

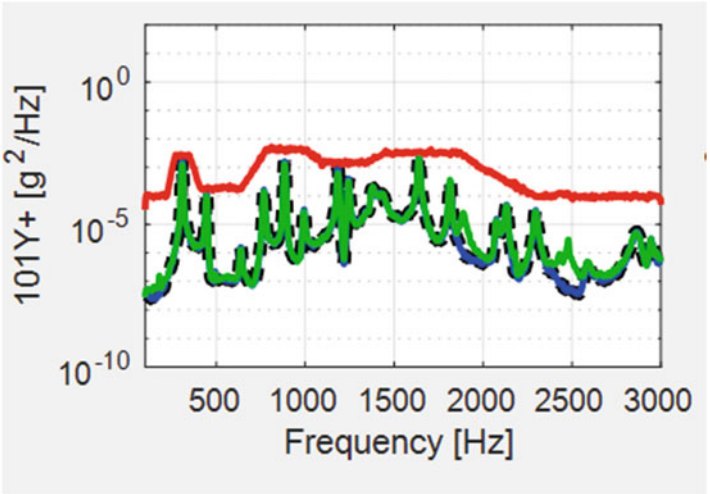

Fig. 11.16 Control location at base of unit

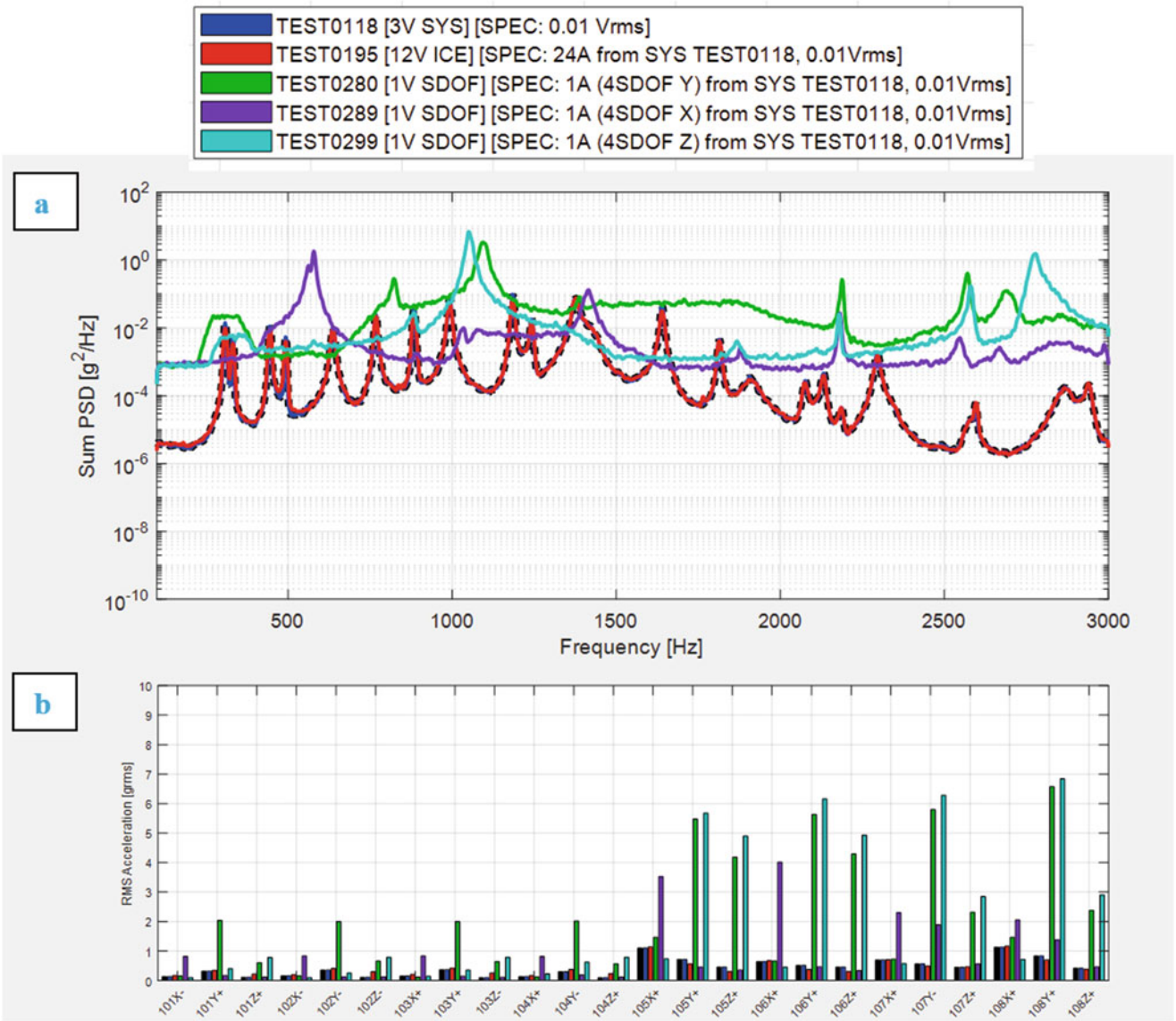

Fig. 11.17 System, ICE, and SDOF results: (**a**) sum of 24 acceleration response channels on unit and (**b**) RMS of each individual channel

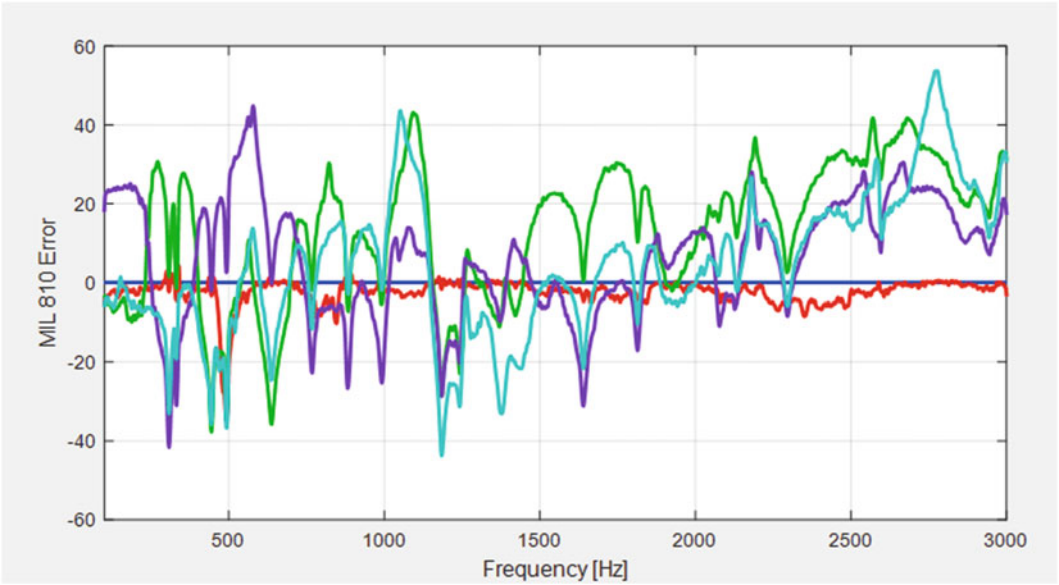

Fig. 11.18 System, ICE, and SDOF tests MIL 810 Global Error Metric

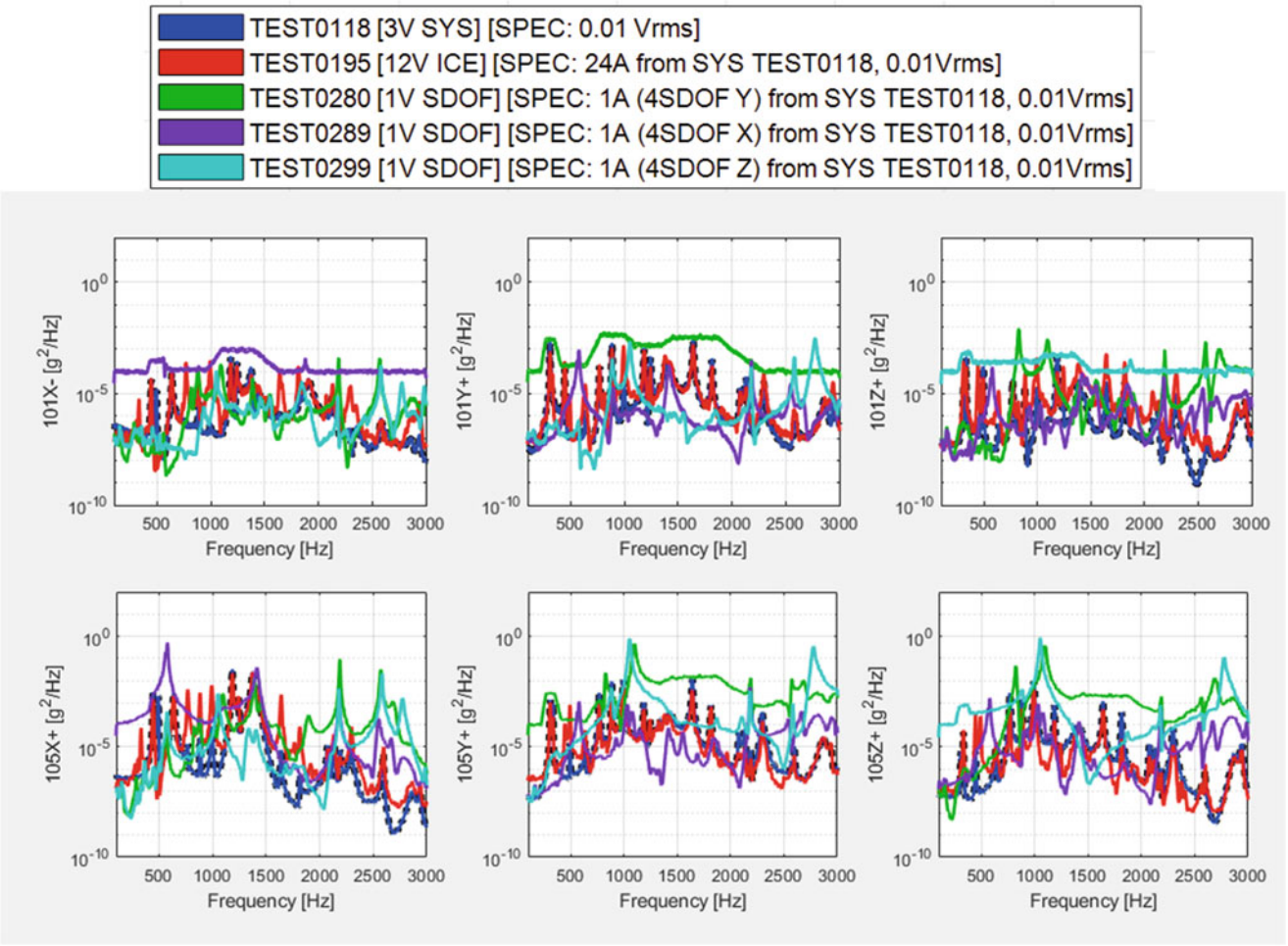

Fig. 11.19 Example individual control and response channels of system, ICE, and SDOF tests

11.7 Conclusion

A successful demonstration of a next-generation component-level multi-axis vibration method was completed on a mass mock aerospace component. Leveraging an intelligently designed fixture, newly developed control methods, the versatility of Rattlesnake (an in-house controller), and a test setup including 12 shakers, an experimentally simulated flight environment was accurately recreated in a test configuration termed ICE (or intrinsic connection excitation). This same experimentally simulated flight environment was also generated and performed using single-axis standard processes, which truly highlighted the dramatic difference of current practices. This ICE proof of concept was very promising and, with increased scale, should prove extremely useful as a testing/development technique moving forward.

A multitude of tests gave insight into many aspects of this new test method. The ICE test method's setup appeared extremely linear in the test bandwidth of interest. Acceleration fixture control demonstrated an alternative to potential for specification creation. Degrees of freedom measured in both the system and ICE test proved that even uncontrolled responses in the ICE configuration were accurately controlled, giving confidence of the dynamics of the system being appropriately excited. Voltage control and force control took a step even further toward possibilities of potential specifications. Setup repeatability of removing and reinstalling the unit revealed nominal test to test discrepancies with little sensitivity to mounting, proving this method to be robust. Single degree of freedom tests was compared using common practice techniques with enveloped system data, revealing a significant over-test for most of the frequency bandwidth, but not all. Some modes in all three single-axis tests were significantly under-tested, highlighting the importance of developing new testing methods such as this. Narrowband single-axis control also showed simply the boundary condition mismatch of traditional methods is something that cannot be overcome without an improved fixturing technique such as ICE.

References

1. Daborn, P.M., Roberts, C., Ewins, D.J., Ind, P.R.: Next-generation random vibration tests. In: IMAC XXXII, the 32nd International Modal Analysis Conference, Orlando, FL (2014)
2. Roberts, C., Ewins, D.J.: Multi-axis vibration testing of an aerodynamically excited structure. J. Vib. Control. **24**(2), 427–437 (2018)
3. Larsen, W., Blough, J., DeClerck, J., VanKarsen, C.: Sensitivity study of BARC assembly. In: Proceedings of IMAC XXXVII, the 37th International Modal Analysis Conference (2019)
4. Zwink, B.: Dynamic Response Matching from Field to Laboratory Replication Methodology. University of Massachusetts Lowell (2020)
5. Soine, D.E., Jones, R.J., Harvie, J.M., Skousen, T.J., Schoenherr, T.F.: Designing hardware for the boundary condition round robin challenge. In: Topics in Modal Analysis & Testing, vol. 9, pp. 119–126. Springer International Publishing, Cham (2019)
6. Larsen, W., Blough, J., DeClerck, J., VanKarsen, C.: Understanding multi-Axis SRS testing results. In: Proceedings of IMAC XXXVI, the 36th International Modal Analysis Conference (2018)
7. Schultz, R., Avitabile, P.: Shape-constrained input estimation for multi-shaker vibration testing. In: Proceedings of IMAC XXXVIII, the 38th International Modal Analysis Conference (2020)
8. DOD: MIL-STD-810G Method 527 Annex C. Department of Defense, New York (2008)
9. Beale, D., Larsen, W., Coffin, P.: Assessment of metrics between acceleration power spectral density metrics and failure criteria. In: Proceedings of IMAC XXXIX, the 39th International Modal Analysis Conference (2021)

Chapter 12
Balancing Impedance and Controllability in Response Reconstruction

Matthew J. Tuman, Matthew S. Allen, Washington J. DeLima, Eric Dodgen, and Jonathan Hower

Abstract One concept in smart dynamic testing is to match the impedance that a component experiences between test and the environment of interest, but this begs the question: how much of an impedance match is needed, and could there be too much? In a prior work, the authors performed MIMO testing with a small component connected to various assemblies, each of which had a differing degree of similarity to the actual flight boundary conditions. The results showed that the fidelity of the response at locations away from the control accelerometers was highly sensitive to the impedance. This work presents further case studies to explore these ideas. Subsequent tests are presented for an assembly that presumably matched the impedance even better, and which was also much more flexible, and the results obtained are even worse than when no attention was given to the impedance. Hence, the work presented here suggests that one should seek a balance between (1) matching the impedance and (2) improving the controllability of the component of interest. The concepts are explored using both test data of a benchmark component, for which the environment of interest was recorded as the component flew on a sounding rocket.

Keywords Shaker test · Operational vibration environment · Substructuring · Force reconstruction

12.1 Introduction

Response reconstruction tests aim to determine whether newly designed parts can survive their intended operational environment. Typically, this test is performed using a single-axis shaker controlling to one accelerometer on the part of interest in a closed loop [1]. Although this methodology has been standard for many years, there are a few challenges that require solutions. First, each axis is excited individually. This requires extra time and expense to perform the test and increased handling of the hardware, which can increase the probability of damage occurring. However, an even more significant concern is that these tests ignore any off-axis motion, while the test may be successfully controlling the accelerometer in the axis of excitation, the part may be subjected to motion in the other directions that is much more severe than the operational environment. Another issue in any kind of shaker testing is that the dynamics of the part change when the shaker is attached (i.e., there is an impedance mismatch at the interface), and often this causes the part to respond at its resonances at much higher amplitudes than would be observed in the operational environment. This over-testing causes many failures to occur during shaker testing that would not occur during operation, and huge expense can be incurred either to redesign the parts or to retest the parts using more conservative environments.

Engineers have known since the 1970s that the impedance mismatch between the shaker test and the operational environment can cause severe over-testing [2], and although some methods exist for addressing this, they all have significant limitations, and none have been universally embraced. Many of the available methods are summarized in Fig. 12.1.

M. J. Tuman
UW-Madison – Department of Engineering Physics, Madison, WI, USA
e-mail: tuman@wisc.edu

M. S. Allen (✉)
Brigham Young University – Mechanical Engineering Department, Provo, UT, USA
e-mail: matt.allen@byu.edu

W. J. DeLima · E. Dodgen · J. Hower
Honeywell Federal Manufacturing & Technologies, Kansas City, MO, USA
e-mail: wdelima@kcnsc.doe.gov; edodgen@kcnsc.doe.gov; jhower@kcnsc.doe.gov

C. Walber et al. (eds.), *Sensors and Instrumentation, Aircraft/Aerospace and Dynamic Environments Testing, Volume 7*,
Conference Proceedings of the Society for Experimental Mechanics Series, https://doi.org/10.1007/978-3-031-05415-0_12

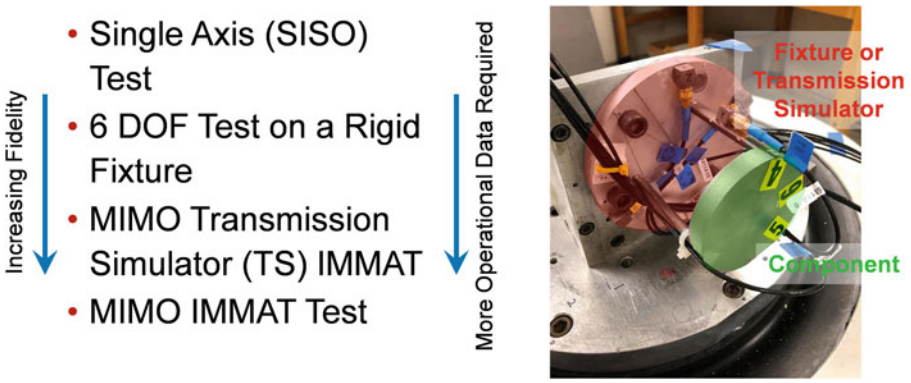

Fig. 12.1 Various methods have been proposed for dynamic environment testing, each of which has differing fidelity and knowledge of the operational environment

Six degree of freedom (6DOF) shaker tables using multi-input-multi-output (MIMO) control have been built [3]. These impressive shakers are able to control multiple degrees of freedom in multiple directions simultaneously, addressing some of the issues outlined above with SISO testing. However, the component under test is still required to be bolted to a massive shaker table, so it is typically difficult to match the impedance. Furthermore, the method loses fidelity if the flexible modes of the table are in the frequency range of interest. At the other end of the spectrum, in terms of fidelity, is the Impedance-Matched Multi-Axis Testing (IMMAT) methodology [4]. This technique also excites the component in all directions using MIMO control, and yet rather than using one massive shaker table, it advocates for using fixturing that mimics the boundary conditions that the part experiences in operation. In the trials to date, this method has recreated dynamic environments far more accurately than single-axis testing [4, 5], yet it presumes that one has enough measurements from the component of interest in the operational environment to determine its modal motion. Specifically, to perform IMMAT on the component shown in Fig. 12.1, one would need to have operational measurements on the fixturing (highlighted red) as well as the component (highlighted green).

In order to obtain a compromise between these approaches, in terms of the fidelity and the data that is required, the authors proposed the transmission simulator IMMAT approach (TS-IMMAT) [6], in which control is only applied to the fixture or transmission simulator (i.e., the part highlighted red in Fig. 12.1), and one then relies on a good impedance match between the operation and test environments to achieve an accurate reconstruction of the response on the component of interest. This work presents a few improvements to this method and studies the method using representative hardware and environment data to understand its advantages and limitations.

Before proceeding, it is worth mentioning two other approaches that are frequently used to address the impedance mismatch. When data on the component (green in Fig. 12.1) is available, one can set response limits, in essence telling the shaker system to reproduce the environment as closely as it can without exceeding those limits. The idea is similar in force limiting [2, 7], although in that case load cells are used between the part and the shaker and the reaction forces are limited. There are some advantages, as the reaction force limits can be estimated using effective mass principles, although several practitioners have found that having load cells connected between the part can be problematic; it introduces additional joints whose preloads are limited by the strength of the force gauges, and hence the joints may slip and change the dynamics during the test. (For a comprehensive reference, see [8] and [9] for a case study showing the behavior of industrial joints at typical preloads.) Recently, Van Fossen and Napolitano [10] presented an alternative in which the connection forces are estimated from accelerometer measurements, in essence presenting a hybrid between force and response limiting methods. Any of these methods could prove very effective as long as (1) reasonable limits are known and (2) using those limits does not degrade the accuracy of the environment too much.

Returning to the TS-IMMAT approach, prior work has suggested that improving the impedance of the transmission simulator (TS) will lead to a more accurate reconstruction of the operational environment for the uncontrolled component [11]. Additionally, this previous investigation found that MIMO simulations based on frequency response functions (FRFs) from a modal pretest can do a reasonable job of predicting response reconstruction accuracy for physical MIMO test. To investigate this further, this work presents tests and simulations showing the accuracy with which the response is reconstructed when more of the operational structure is included (i.e., a next-level assembly is used as the TS). Furthermore, to better predict the accuracy of a MIMO test, a condition number threshold is implemented in the simulations to mimic the physical controller that is used in test. This is a continuation of [6, 11, 12].

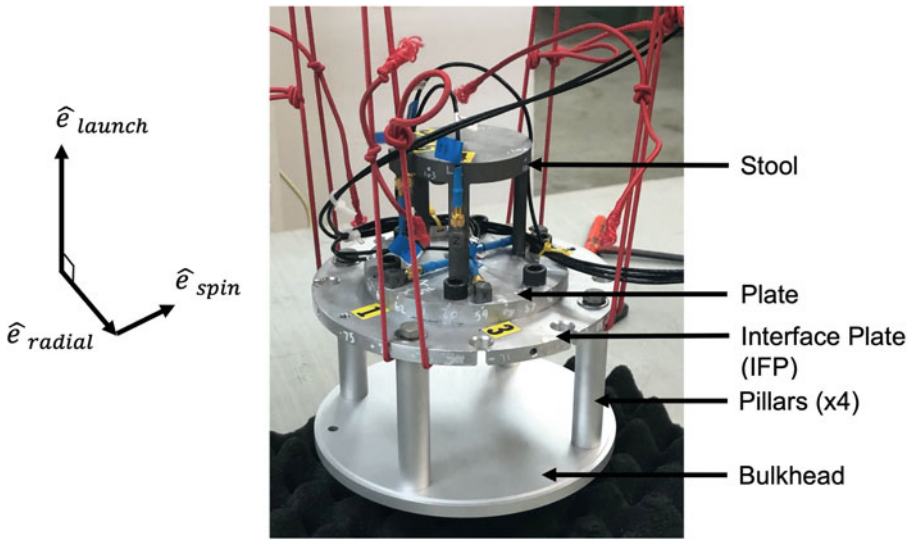

Fig. 12.2 The instrumented next-level assembly

12.2 Assembly and Environment Definitions

The next-level assembly under test is shown in Fig. 12.2. Previous work performed reconstruction tests using assemblies with the same plate (TS) and stool (subcomponent); however, these assemblies did not include the pillars or the bottom bulkhead [11]. The accelerometers are positioned in a cylindrical coordinate system, and the directions referenced throughout the rest of this analysis are specified in Fig. 12.2.

This assembly flew inside a sounding rocket flown for Kansas City National Security Campus in July 2019. The assembly was instrumented with three triaxial on the plate and three triaxial accelerometers on the stool. During flight, the rocket experienced four main phases: boost, coast, deployment of the drogue parachute, and deployment of the main parachute. The operational environment power spectral density (PSD) profiles are constructed from acceleration time data from 0.5 to 20 seconds after launch. This time frame captures the boost and coast phase while excluding any shock event at ignition along with the deployment of the parachutes.

The frequency spacing of the PSD profiles generated is 0.8206 Hz, and the testing bandwidth of interest is 100 to 5000 Hz. Unfortunately, the data from the first accelerometer in the radial direction (channel 1) only recorded noise during flight. Thus, there are eight channels on the plate and nine channels on the stool that recorded useful data.

Three assemblies will be considered in the following analysis and are illustrated in Fig. 12.3.

For each configuration, the goal is to reconstruct the environment on the plate using six small shakers using MIMO control. To assess the success of a TS-IMMAT test for each configuration, the accuracy of the controlled reconstructed plate response and the accuracy of the uncontrolled stool response will be compared. Our prior work [11] presented TS-IMMAT reconstruction tests on Configurations A and B; this work will focus on comparing those with Configuration C.

12.3 MIMO Simulations

The accuracy of MIMO reconstruction tests using the TS approach was found to be sensitive to the forcing input location of the shakers. Because each experimental setup requires a significant amount of time, a process was devised to determine optimal forcing input locations by running multiple MIMO tests in simulation. This procedure required frequency response functions (FRFs) between all the possible shaker input locations and the accelerometers on the component under test.

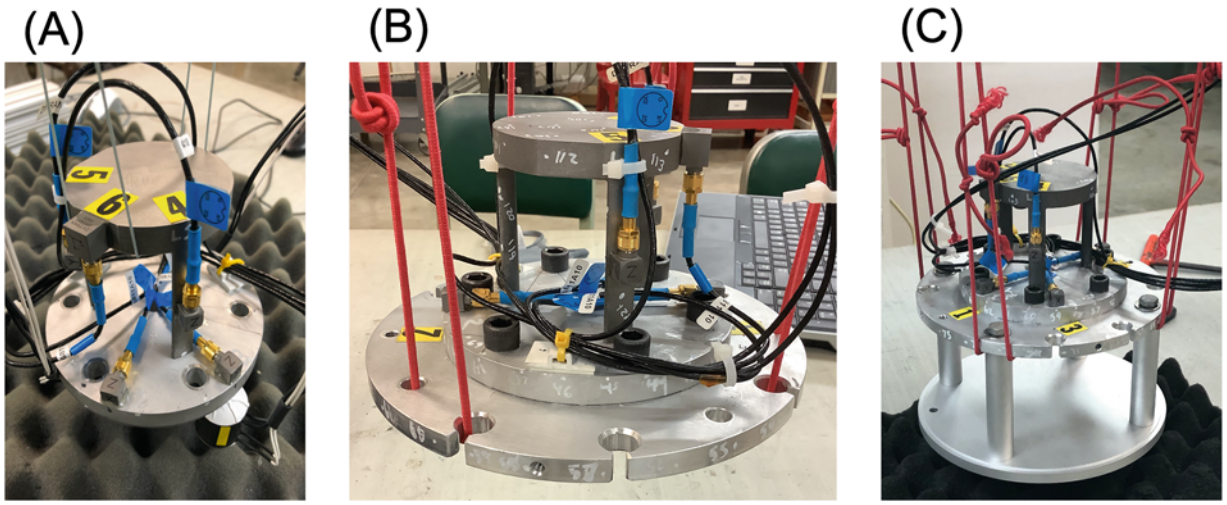

Fig. 12.3 The three assemblies tested are Configuration A with the stool and plate; Configuration B with the stool, plate, and IFP; and Configuration C with the stool, plate, IFP, pillars, and bulkhead

12.3.1 Roving Hammer FRFs

A modal roving hammer test was performed on Configuration C. This physical test constructed a comprehensive FRF matrix relating 82 forcing inputs to the 18 accelerometer channels on the assembly. Data Physics Abacus hardware and SignalCalc 730 software recorded the FRFs in the bandwidth of 0–5250 Hz with a frequency resolution of 0.82 Hz to match the environmental acceleration profiles. Forty-one forcing inputs were recorded on the interface plate with 30 in the launch direction and 11 in the radial direction. Each pillar was characterized using three inputs in the spin direction and two in the radial direction. Finally, 15 inputs were applied on the bottom bulkhead in the launch direction, and 6 inputs were recorded in the radial direction. These FRFs could be used to simulate 82 potential shaker locations.

12.3.2 Mathematical Model

The spectral density of the response $\boldsymbol{S}_{XX}(\omega)$ of an n degree of freedom (DOF) system in the frequency domain at a specific frequency, ω can be computed from a forcing input PSD matrix of d inputs, $\boldsymbol{S}_{FF}(\omega)$, the FRF matrix relating inputs to an outputs, $\boldsymbol{H}_{XF}(\omega)$, and the Hermitian of the FRF, $\boldsymbol{H}^{*}_{XF}(\omega)$, as presented in Eq. (12.1).

$$\boldsymbol{S}_{XX}(\omega) = \boldsymbol{H}_{XF}(\omega) \cdot \boldsymbol{S}_{FF}(\omega) \cdot \boldsymbol{H}^{*}_{XF}(\omega) \tag{12.1}$$

The dimension of $\boldsymbol{S}_{XX}(\omega)$ is $(n \times n)$, $\boldsymbol{S}_{FF}(\omega)$ is $(d \times d)$, and $\boldsymbol{H}_{XF}(\omega)$ is $(n \times d)$. If the operational environment, or PSD matrix ($\boldsymbol{S}_{XX}(\omega)$), is known, Eq. (12.1) can be inverted to solve for the forcing input PSD matrix, $\boldsymbol{S}_{FF,\,est}(\omega)$, using Eq. (12.2). If an overdetermined system is present, where there are more DOF than forcing inputs ($n > d$), the pseudoinverse of the FRF, denoted by $\boldsymbol{H}^{+}_{XF}(\omega)$, can be used to find the forcing input that minimizes least squares error.

$$\boldsymbol{S}_{FF,est}(\omega) = \boldsymbol{H}^{+}_{XF}(\omega) \cdot \boldsymbol{S}_{xx}(\omega) \cdot \left(\boldsymbol{H}^{*}_{XF}(\omega)\right)^{+} \tag{12.2}$$

Using this least squares solution for the estimated forcing input, one can then solve for the estimated response, $\boldsymbol{S}_{XX,\,est}(\omega)$, using Eq. (12.3).

$$\boldsymbol{S}_{XX,est}(\omega) = \boldsymbol{H}_{XF}(\omega) \cdot \boldsymbol{S}_{FF,est}(\omega) \cdot \boldsymbol{H}^{*}_{XF}(\omega) \tag{12.3}$$

Because FRFs are recorded from the modal hammer test and the operational acceleration PSD profiles are known, Eqs. (12.2) and (12.3) can be used to simulate a MIMO test. To simulate various forcing inputs, the columns of $\boldsymbol{H}^{+}_{XF}(\omega)$ are

trimmed to only correspond to the inputs of interest (no more than six in this work). Also, $\boldsymbol{S}_{xx}(\omega)$ is trimmed to include only the eight control accelerometers on the plate. This response PSD matrix contains diagonal and off-diagonal measurements.

12.3.3 Shaker Selection Algorithm

To determine a near-optimal set of shaker locations for the best reconstruction accuracy, the shaker placement algorithm from [13] was adapted. Additionally, to evaluate the success of a MIMO simulation, an error metric from [13] was also used. First, the average dB difference of two ASDs for all relevant accelerometer channels at a frequency line is computed using Eq. (12.4).

$$e_{\mathrm{ASD}}\left(f_i\right) = \sqrt{\frac{1}{n_{\mathrm{accels}}} \sum_{k=1}^{n_{\mathrm{accels}}} \left[\mathrm{dB}\left[\boldsymbol{S}_{X_k X_k}\left(f_i\right)\right] - \mathrm{dB}\left[\boldsymbol{S}_{X_k X_k,\mathrm{lab}}\left(f_i\right)\right]\right]^2} \tag{12.4}$$

For this work, $\boldsymbol{S}_{X_k X_k,\mathrm{lab}}$ is the simulated or experimental acceleration ASD for the kth accelerometer DOF, and $\boldsymbol{S}_{X_k X_k}$ is the operational ASD for the same DOF. After computing an error value for each frequency line, a final metric is computed using Eq. (12.5).

$$e_{\mathrm{ASD}} = \sqrt{\frac{1}{n_{\mathrm{freq}}} \sum_{i=1}^{n_{\mathrm{freq}}} e_{\mathrm{ASD}}(f_i)^2} \tag{12.5}$$

This final error number represents the average dB error across all accelerometers and frequency line. A low error metric communicates a successful reconstruction test and will be used moving forward to compare various tests. With the error metric defined, the shaker location algorithm is as follows:

1. Start with a pool of all possible forcing input locations from the roving hammer test of Configuration C.
2. Simulate the MIMO response for each forcing input location in the remaining pool (controlling to the eight plate accelerometers).
3. Keep the forcing input location that produces the lowest error on the controlled DOF (plate accelerometers), and remove it from the pool of possible locations.
4. Add this kept forcing input location to the set of forcing locations.
5. Repeat steps 2–4 with the kept forcing input location/s from the previous iterations plus each candidate location, and again keep the best candidate location until the number of desired shakers is reached.

To remain consistent with the prior work [11], the optimization stopped once it determined the six best shaker locations for Configuration C.

12.4 Methodology

The workflow for performing the TS-IMMAT reconstruction test was as follows. As mentioned previously, a modal roving hammer test was performed on the next-level assembly (Configuration C) with 82 forcing inputs recorded. Then, using MIMO simulations and the shaker selection algorithm, optimal shaker input locations were determined. Shakers were then attached at these locations. Three SIEMENS Q-MSH electromagnetic (EM) inertial shakers were used to excite the assembly under test in the launch direction. These three shakers were attached directly to the structure using super glue. In the off-launch directions, two APS 300 EM shakers and one LDS 203 EM were connected to the assembly via stingers made of piano wire which were also attached with super glue. The experimental setup with optimal shaker inputs is presented in Fig. 12.4.

To perform the MIMO test, Data Physics Abacus hardware and Data Physics SignalStar Matrix controller software were used. Per requirements of the TS-IMMAT approach, the closed-loop MIMO software only controlled to the accelerometers on the plate. Because one accelerometer channel recorded noisy data during flight and another channel started to record poor measurements in the laboratory, only seven accelerometer channels were controlled to. The control profiles were the PSD

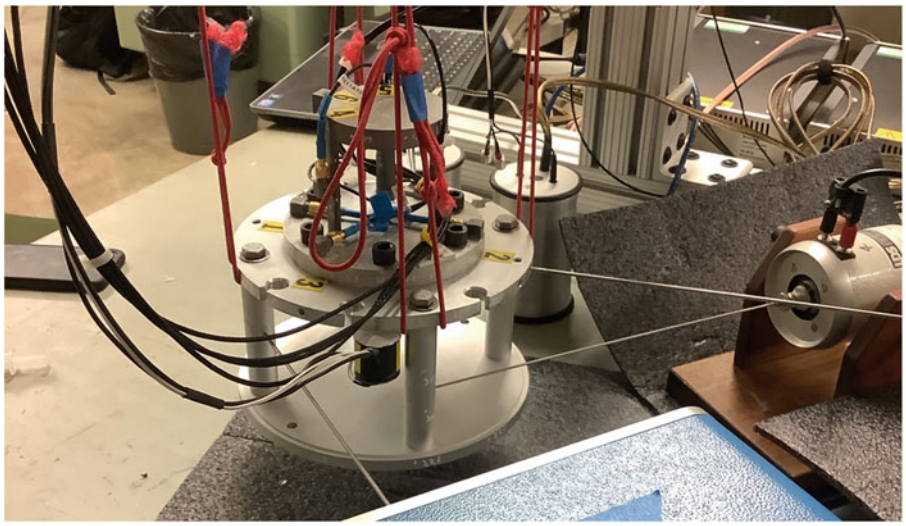

Fig. 12.4 Experimental setup for MIMO reconstruction test of next-level assembly (Configuration C)

matrices constructed from the flight data as described in Sect. 12.2. The remaining nine accelerometer channels on the stool were not controlled to, but they were measured.

12.5 MIMO Reconstruction

Following the methodology provided, a TS-IMMAT response reconstruction test was performed. To visualize the accuracy of this test, Fig. 12.5 presents the auto-spectral densities (ASDs) for the accelerometer channels on the controlled plate. The black line is the operational environment profile that is being controlled to, the blue line is the response recorded during the reconstruction test, and the red lines are a plus or minus 6 dB error envelope of the operational profile. Additionally, for each channel, the dB error is provided in each subplot's title.

The reconstruction in the launch direction (channels 3, 6, and 9) was very accurate in the full testing bandwidth with error values hovering around 6 dB. On the other hand, reconstruction accuracy in the off-launch directions is poor with significant undertesting occurring in the spin direction on channels 2 and 8. This inability to generate the desired response in the off-launch directions leads to a relatively higher error for the plate of 11.4 dB.

In practice we presume that one would not have measurements on the component of interest, but in these tests, we did have accelerometers on the stool so we could evaluate the performance of the proposed TS-IMMAT approach. Turning our attention now to the uncontrolled stool, Fig. 12.6 illustrates the measured ASDs of the accelerometer channels on the stool (blue) with the environment profiles generated from the flight data (black).

Once again, the measured responses in the launch direction (channels 10, 13, and 16) are the most accurate, presumably because the response on the TS was best controlled in this axis of excitation. As might have been expected, because control was significantly worse on the plate in the off-axis directions, the measured responses of the stool in these directions are also worse on average, although not significantly worse than the launch direction. In fact, there are three channels in the off-launch directions (11, 12, and 14) that have a lower error metric than channel 13 in the launch direction. Nonetheless, reconstruction accuracy of this uncontrolled subcomponent was still unsatisfactory with an overall error of 14.7 dB.

Next, with TS-IMMAT reconstruction tests performed on Configuration A, Configuration B, and now Configuration C, the accuracy for each assembly can be assessed quantitatively using the dB error metric. Table 12.1 presents the error metric from 100 to 2000 Hz and 100 to 5000 Hz for the three assemblies tested.

The previous testing of Configuration A and Configuration B suggested that using more of the original operational structure improves the response accuracy for the controlled transmission simulator (plate) and for the uncontrolled subcomponent (stool). Because Configuration B is more similar to the operational structure than Configuration A, Configuration B was presumed to have a better impedance match. However, Configuration C includes even more of the operational structure than the other two assemblies and therefore should best match the impedance.

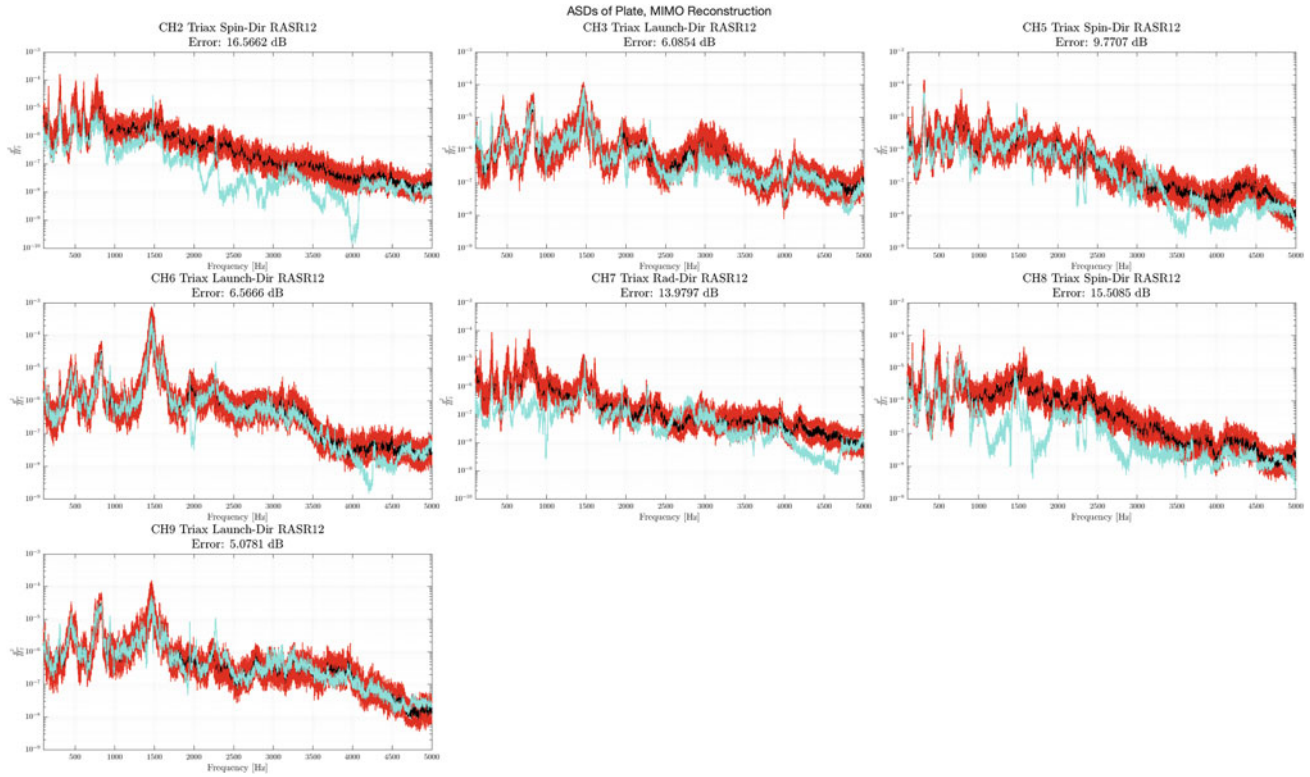

Fig. 12.5 Reconstruction ASDs of the controlled accelerometers on the plate (blue) along with the control ASDs (black) and a ± 6 dB control error envelope (red)

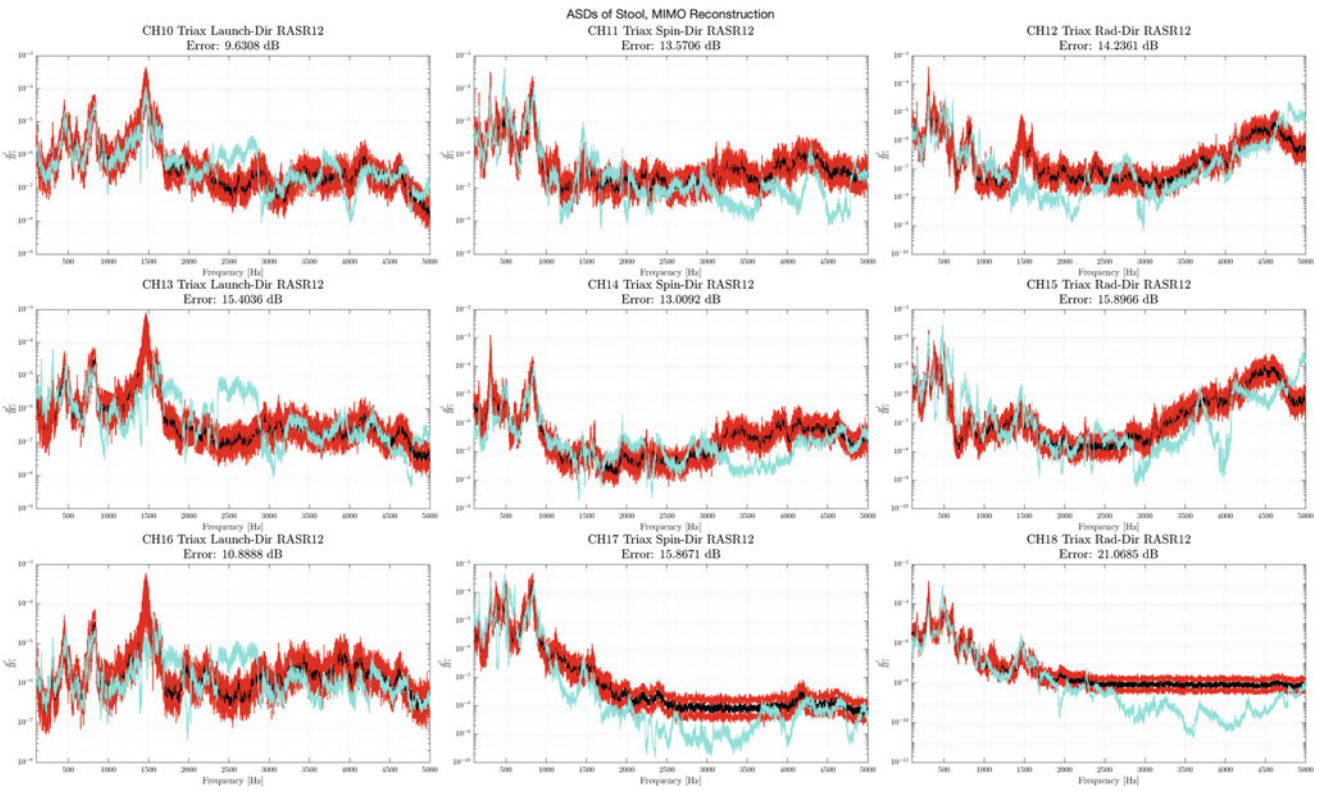

Fig. 12.6 Measured ASDs of the uncontrolled accelerometers on the stool (blue) along with the environment ASDs (black) and a $\pm$ 6 dB environment error envelope (red)

Table 12.1 Error in experimental reconstruction for three assemblies tested

	Error from 100 to 2000 Hz (dB)		Error from 100 to 5000 Hz (dB)	
Assembly	Plate	Stool	Plate	Stool
Configuration A (6 modes)	9.2	12.3	8.9	15.7
Configuration B (9 modes)	7.5	11.4	7.7	12.8
Configuration C (21 modes)	11.7	12.4	11.4	14.7

Table 12.2 Number of flexible modes below 5000 Hz for each configuration

Assembly	Modes
Configuration A	6
Configuration B	9
Configuration C	21

The discovery that Configuration C does not have improved reconstruction accuracy presents some interesting implications that must be explored moving forward. One theory was that the transmission simulator is far more flexible in Configuration C and that this may contribute to the difficulty. Because the stool remained the same in each test, the flexibility of the various transmission simulators can be compared by comparing the number of modes of the assembly that are within the bandwidth of interest for each configuration. This is summarized in Table 12.2.

Because the number of forcing inputs was the same between tests, one would expect that the system with fewer modes will be more controllable, and this could explain why the results degraded for Configuration C. The authors are exploring metrics or concepts that can be used to quantify the difficulty of controlling a particular assembly, and this may help in quantifying these effects. In any event, this study has shown that the ideal test may not simply involve the best possible impedance match but may also need to consider controllability.

With regard to the impedance match, more objective metrics are needed to quantify impedance so one can specify what level of matching is needed. The term impedance matching has been loosely used in this work as an evaluation of how similar the dynamics are between the assembly under test and the assembly during operation. However, there has been no quantitative formulation for this metric, and it has been assumed that more of the original structure guarantees a better match. Configuration C introduces numerous flexible modes of the pillars and the bottom bulkhead, but during operation, there was a casing around the assembly which may drastically change the contribution of these modes to the operational response. Thus, the impedance match of Configuration C may actually be worse than that in Configuration B. Until a more rigorous metric can be developed, caution must be used when assuming that a next-level assembly ensures better an impedance match and thus more accurate reconstruction results.

12.6 Simulation with Condition Number Threshold

As mentioned previously, MIMO simulations are very important in the workflow and have been used to reliably determine forcing inputs for the three assemblies tested. While the MIMO simulations have been useful for finding optimal input locations and can predict which configuration of next-level assembly will have better accuracy for the uncontrolled subcomponent [11], in most cases to date, they have predicted that reconstruction accuracy on the controlled TS (plate) should be much better than what is achieved in experiment. For instance, in simulation we are consistently able to achieve an error of 3 dB on the plate accelerometers for Configurations A and B, but during actual experiments, this control error is typically between 7 and 10 dB. Although the Data Physics control software is proprietary, it is known that a condition number threshold is utilized to limit force input magnitudes that may exceed shaker capabilities. Thus, this section will explore how to implement a condition number in simulation and compare simulated results with and without a condition number threshold used.

12.6.1 Condition Number Threshold Implementation

A condition number threshold is traditionally used when inverting ill-conditioned matrices to limit the magnitude of elements in the inverse. In the MIMO simulation theory, an inversion only takes place in Eq. (12.2) when solving for $\boldsymbol{S}_{FF,\,est}(\omega)$. The following procedure is used to compute the pseudoinverse of the FRF, $\boldsymbol{H}_{XF}^{+}(\omega)$. First, the FRF, $\boldsymbol{H}_{XF}(\omega)$, is decomposed

using the singular value decomposition (SVD). In this derivation, it is assumed there are n outputs and d inputs where d is less than n.

$$\boldsymbol{H}_{XF}(\omega) = \boldsymbol{U}\boldsymbol{\Sigma}\boldsymbol{V}^{\boldsymbol{T}} \tag{12.6}$$

Here, $\boldsymbol{\Sigma}$ is a matrix containing the singular values of the decomposition as shown in Eq. (12.7).

$$\boldsymbol{\Sigma} = \begin{bmatrix} \sigma_1^2 & 0 & 0 \\ 0 & . & 0 \\ 0 & 0 & \sigma_d^2 \end{bmatrix} \tag{12.7}$$

As a property of the SVD, the singular values are ordered by magnitude with the largest singular value being σ_1. Next, we define our condition number, c_i, for each singular value using Eq. (12.8).

$$c_i = \frac{\sigma_i^2}{\sigma_1^2} \tag{12.8}$$

With a threshold value defined, $c_{\text{threshold}}$, the index k is found by satisfying the condition in Eq. (12.9).

$$c_k > c_{\text{threshold}} > c_{k+1} \tag{12.9}$$

Then, a truncated k rank approximation of the pseudoinverse FRF is computed using Eq. (12.10).

$$\boldsymbol{H}_{XF}^{+}(\omega) = \sum_{i=1}^{k} \frac{1}{\sigma_i^2} \boldsymbol{V}_i \boldsymbol{U}_i^{\boldsymbol{T}} \tag{12.10}$$

12.6.2 Simulation Results with Condition Number Threshold

To evaluate the effect of the condition number threshold on MIMO control, each physical experiment presented in Table 12.1 was repeated in simulation with the threshold and without the threshold. The threshold in simulation matches that which was used in experiment; these values ranged from 0.02 to 0.05. Table 12.3 presents the errors for each configuration in the format of *Simulation without Threshold/Simulation with Threshold/Physical Experiment*.

For all three configurations, the errors on the plate are more similar between physical test and simulation when the condition number threshold is used. This is also the case for Configuration A and Configuration B on the stool. Therefore, these results suggest that a condition number threshold improves the ability of a simulation to predict what will occur during a physical test.

The question that now arises is why this threshold makes the simulation more realistic. Looking at Eq. (12.10), small values of σ_i^2 can dramatically increase the magnitude of $\boldsymbol{H}_{XF}^{+}(\omega)$. If a large magnitude $\boldsymbol{H}_{XF}^{+}(\omega)$ is then used in Eq. (12.2), the magnitude of the forcing input, $\boldsymbol{S}_{FF,\,est}(\omega)$, will also increase. This is visualized in Fig. (12.7) showing the simulated forcing input ASDs for Configuration B with a threshold (blue) and without a threshold (purple). Additionally, the rank of $\boldsymbol{H}_{XF}^{+}(\omega)$ is plotted (orange) on the right axis.

As predicted, the forcing input ASDs computed with the threshold are lower in magnitude when $\boldsymbol{H}_{XF}^{+}(\omega)$ is truncated to be of rank less than full. Interestingly, the condition number threshold only affects the forces in a relatively small fraction of the frequency band. This effect is largest in the bandwidth from 2500 to 3000 Hz. Looking at the modal data for Configuration B, it is observed that there are axisymmetric (chip) plate modes at 2600 Hz and 2700 Hz along with a symmetric (bubble)

Table 12.3 Reconstruction accuracy error for the three configurations tested (Simulation without Threshold/Simulation with Threshold/Physical Experiment)

Assembly	Plate error 100–5000 Hz (dB)	Stool error 100–5000 Hz (dB)
Configuration A	3.4/5.2/8.9	11.6/14.9/15.7
Configuration B	2.3/5.0/7.7	16.1/12.0/12.8
Configuration C	5.6/7.01/11.4	12.1/11.4/14.7

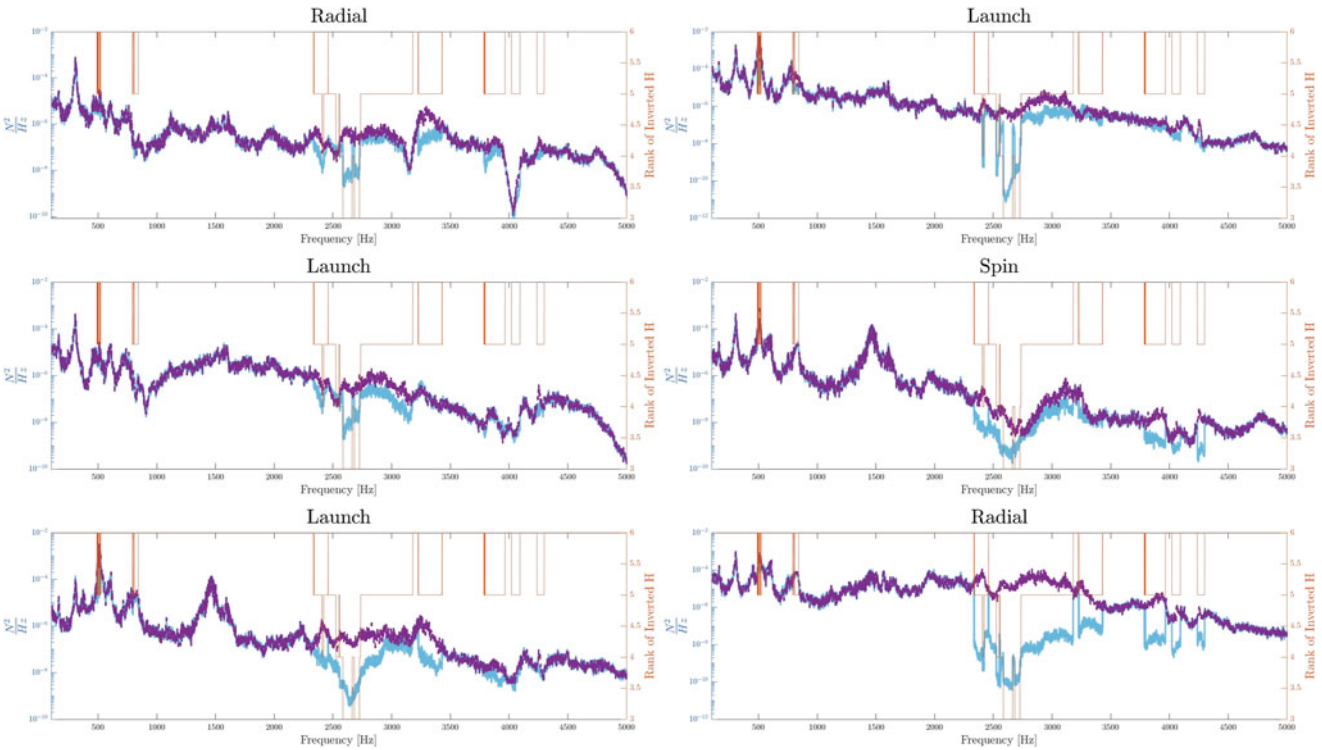

Fig. 12.7 Simulated forcing input ASDs for Configuration B with a threshold (blue) and without a threshold (purple)

plate mode at 3000 Hz. In fact, at the frequency lines where the rank of $\boldsymbol{H}_{XF}^{+}(\omega)$ is less than full, there is always a mode of the assembly nearby. Therefore, the implementation of a condition number threshold in simulation effectively limits the forcing input magnitude near modes of the assembly under test. Similarly, because resonant frequencies of the assembly shift between operation and test, the physical closed-loop control also drives down the input magnitude near the system's resonances. This case study shows that the use of condition number thresholds does have a relatively important effect on the MIMO test and should be used in any simulations.

12.7 Conclusion

This chapter further investigated the influence of impedance on the ability to reconstruct a random vibration environment for a component by controlling to accelerometers only on a transmission simulator that the component is attached to. Prior work [11] suggested that an improved impedance match leads to a more accurate reconstruction response of the uncontrolled subcomponent. This research further examined the impact of impedance by analyzing a next-level assembly, Configuration C.

Configuration C included more of the operational structure than the previous two assemblies that had been studied. The results showed that the test was fairly accurate in reconstructing the environment on the TS in the launch direction, but there was significant deviation from the control in the off-launch directions. As a result, this translated to poor reconstruction accuracy on the uncontrolled stool. Comparing this configuration to the previous two assemblies, it was noted that although Configuration C included more of the operational structure and was presumed to have an improved impedance match, there was a degradation in accuracy on both the TS and the subcomponent of interest. This contradicted the assumptions from the previous work that suggested using more of the operational structure leads to a more successful response reconstruction test.

As a result of this finding, there are a few considerations to address moving forward. First, with increasingly complex assemblies under test, there is a need to explore metrics or concepts that can be used to quantify the difficulty of controlling a particular assembly. In this work we computed the number of flexible modes of the assembly and presented that as one possible metric. It appears that this consideration must be balanced with the impedance match when defining a TS for a particular application, as there are certainly cases where the TS can be too rigid to provide accurate results. The TS and

fixture should be selected to capture only the modes that contribute most to the operational response, instead of simply choosing a fixture that contains the most operational modes.

Finally, to improve upon the ability of MIMO simulations to predict physical MIMO tests, a condition number threshold was implemented. This approach decreased the magnitude of the inverted FRF thereby also limiting the amplitude of the forcing input, similar to what is done in real MIMO tests. Because the FRFs are ill-conditioned near the natural frequencies of the system under test, this approach drives down the input magnitudes at these frequencies. Comparing the error metrics between simulation and physical test, the simulations with the threshold implementation were consistently more predictive of the physical test.

Future work will investigate methods to quantify controllability and impedance while also exploring protocols for determining the dominant modes a TS and testing fixture should capture.

Acknowledgments The authors gratefully acknowledge the Department of Energy's Kansas City National Security Campus, operated by Honeywell Federal Manufacturing & Technologies LLC, for funding this work under contract number DE-NA0002839.

References

1. Piersol, A.: The development of vibration test specifications for flight vehicle components. J. Sound Vib. **4**, 88–115 (1965)
2. National Aeronautics and Space Administration, Force Limited Vibration Testing, NASA-HDBK-7004B. [Online]. Available: http://standards.nasa.gov (2003)
3. Paripovic, J., Mayes, R.L.: Reproducing a component field environment on a six degree-of-freedom shaker. Presented at the the 38th International Modal Analysis Conference (IMAC XXXVIII), Houston, TX (2020)
4. Daborn, P.M., Roberts, C., Ewins, D.J., Ind, P.R.: Next-generation random vibration tests. In: Topics in Modal Analysis II, vol. 8, pp. 397–410. Springer, Cham (2014). https://doi.org/10.1007/978-3-319-04774-4_37
5. Mayes, R.L., Rohe, D.P.: Physical vibration simulation of an acoustic environment with six shakers on an industrial structure. In: Shock & Vibration, Aircraft/Aerospace, Energy Harvesting, Acoustics & Optics, vol. 9, pp. 29–41. Springer, Cham (2016)
6. Schumann, C., Allen, M.S., Tuman, M., DeLima, W., Dodgen, E.: Transmission simulator based MIMO response reconstruction. Exp. Tech. (2021). https://doi.org/10.1007/s40799-021-00454-4
7. Scharton, T.D.: Force limited vibration testing monograph, NASA, RP-1403 (1997)
8. Segalman, D.J., et al.: Handbook on Dynamics of Jointed Structures, vol. 87185. Sandia National Laboratories, Albuquerque (2009)
9. Roettgen, D.R., Allen, M.S.: Nonlinear characterization of a bolted, industrial structure using a modal framework. Mech. Syst. Signal Process. **84**, 152–170 (2017). https://doi.org/10.1016/j.ymssp.2015.11.010
10. Van Fossen, T., Napolitano, K.: An acceleration-based approach to force limiting a random vibration test. In: Special Topics in Structural Dynamics & Experimental Techniques, vol. 5, pp. 315–325. Springer, Cham (2021)
11. Tuman, M.J., Schumann, C.A., Allen, M.S., DeLima, W., Dodgen, E.: Investigation of transmission simulator based response reconstruction accuracy. Presented at the IMAC XXXIX, Virtual (2021)
12. Schumann, C.A., Allen, M.S., DeLima, W., Dodgen, E.: Transmission simulator based MIMO response reconstruction for vehicle subcomponents. Presented at the IMAC XXXVIII, Houston, TX (2020)
13. Nelson, G.D., Rohe, D.P., Schultz, R.A.: Strategies for shaker placement for impedance-matched multi-axis testing. Presented at the IMAC XXXVII, Orlando, FL (2019)

Chapter 13
Challenges and Considerations When Using Hydraulic Modal Shaking in Large-Scale Modal Testing

James C. Akers, Michael T. Hale, and Joel W. Sills Jr.

Abstract As test articles become dimensionally larger, more complex, and massive in weight, combined with the need to excite them to higher than traditional levels in order to identify their nonlinear characteristics, modal shakers that can generate significantly higher force levels, have longer stroke lengths, and possess higher velocity limits are required. While large-scale modal tests may be performed with electrodynamic modal shakers, hydraulic modal shakers become attractive since they can generate higher force levels at lower unit cost with a smaller spatial footprint. While test engineers familiar with electrodynamic modal shakers are familiar with the challenges of displacement and velocity limits and the relatively mild shaker nonlinear distortion due to amplifier gains and shaker flexure structural geometric nonlinearities, they probably are not as familiar with the unique set of challenges hydraulic modal shakers present. These unique challenges include significant nonlinear distortion in the shaker force, issues with the setup of the hydraulic power supply and the associated hydraulic hosing, velocity limits as they relate to potentially damaging the hydraulic actuator piston, and safety issues with operating high-pressure hydraulic systems. This chapter addresses these unique challenges to help the test engineer to better utilize hydraulic modal shakers on large-scale modal tests.

Keywords Electrodynamic modal shakers · Hydraulic modal shakers · Hydraulic power supplies · Large-scale modal test · Nonlinear distortion

13.1 Background

Traditionally electrodynamic modal shakers have been used for modal testing due to their versatility, linearity, and relative ease of setup. For modal tests of small to medium size test articles, they have sufficient stroke length and can provide a sufficient range of force levels to indicate, if not fully identify, nonlinear characteristics. With modal test articles becoming dimensionally larger, more complex (e.g., possessing a significant number of nonlinear mechanisms), and massive in weight, combined with the need to excite them to higher than traditional levels in order to identify their nonlinear characteristics, modal shakers that can generate significantly higher force levels, have longer stroke lengths, and possess higher velocity limits are required. While large-scale modal tests may be performed with electrodynamic modal shakers, hydraulic modal shakers become attractive since they can generate higher force levels at lower unit cost with a smaller spatial footprint. Four hydraulic modal shakers were used in modal testing the National Aeronautics and Space Administration's (NASA's) Ares I-X Flight Test Vehicle (FTV) inside the Vehicle Assembly Building (VAB) in 2009 [1–5]. The Ares I-X FTV was 327 feet tall and weighed 1.8 million pounds. Figure 13.1 shows the Ares I-X FTV inside the VAB. More recently five inertial hydraulic modal shakers were used in modal testing the Space Launch System (SLS) [6, 7] Mobile Launcher (ML) [8, 9] inside the VAB in 2019 [10, 11]. The ML weighs over 10 million pounds and is over 360 feet tall. The ML Deck supports the SLS at eight attachment points located at the bottom of its two boosters, which connect to the ML Vehicle Support Posts (VSP). The ML Tower provides lateral support to the integrated SLS launch vehicle via the Vehicle Stabilization System (VSS) and

J. C. Akers (✉)
Glenn Research Center, National Aeronautics and Space Administration, Cleveland, OH, USA
e-mail: james.c.akers-1@nasa.gov

M. T. Hale
Principal Research Engineer, Trideum Corporation/RTC, Redstone Arsenal, AL, USA

J. W. Sills Jr.
Johnson Space Center, National Aeronautics and Space Administration, Houston, TX, USA

C. Walber et al. (eds.), *Sensors and Instrumentation, Aircraft/Aerospace and Dynamic Environments Testing, Volume 7*,
Conference Proceedings of the Society for Experimental Mechanics Series, https://doi.org/10.1007/978-3-031-05415-0_13

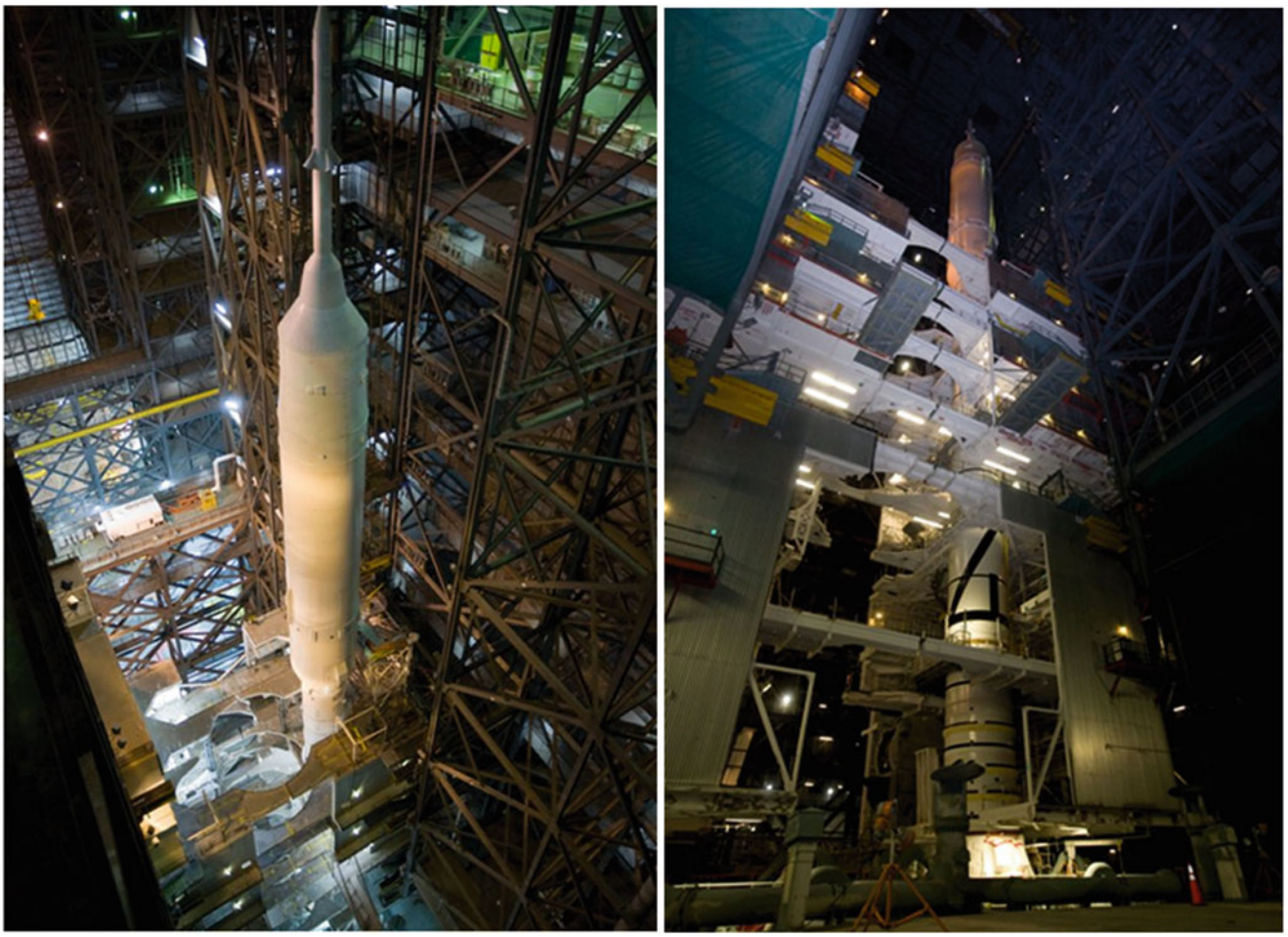

Fig. 13.1 Ares I-X FTV inside VAB

Fig. 13.2 SLS Mobile Launcher rolling out to Launch Pad 39B, September 2018

supports the fuel, power, and data umbilicals running to SLS and MPCV. The ML Tower also provides crew access to the MPCV Crew Module (CM). The ML will serve as the modal test fixture supporting the Artemis 1 integrated vehicle during its ground vibration tests referred to as the integrated vehicle modal test (IMT). Figure 13.2 shows the ML rolling out from the VAB to Launch Pad 39B in September 2018.

Figure 13.3 shows the two types of hydraulic modal shakers, an inertial horizontal and an inertial vertical, used during the ML modal test in 2019. Both hydraulic modal shakers have drip pans to capture any leaking hydraulic fluid, and their

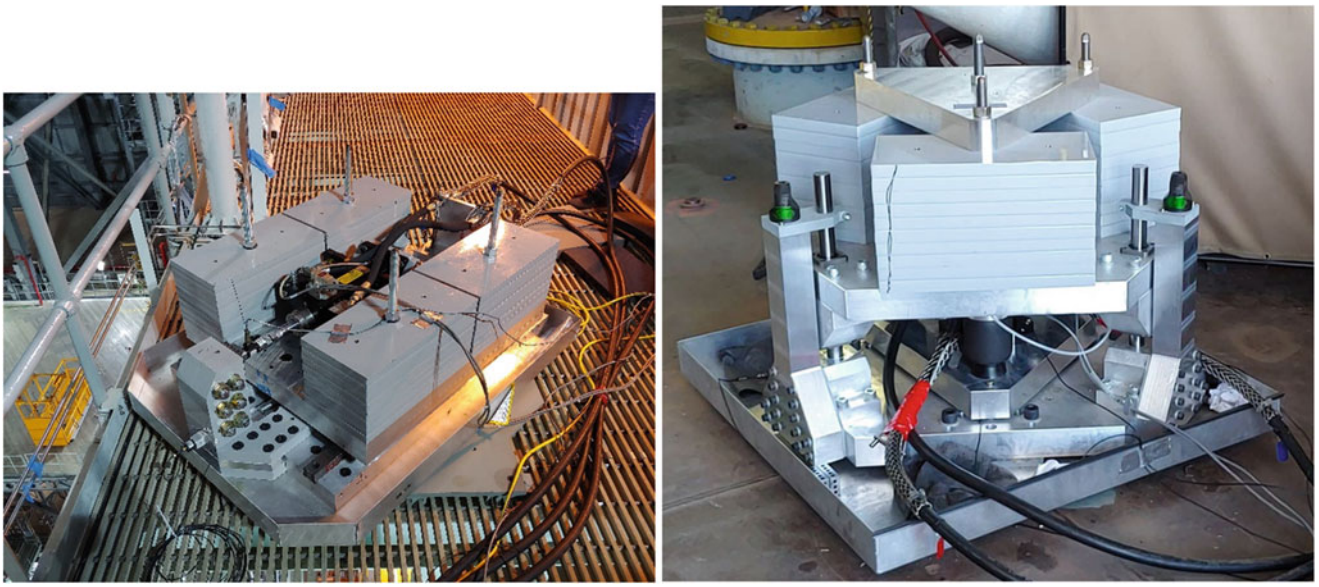

Fig. 13.3 SLS ML modal test modal hydraulic shakers: inertial horizontal shaker (left) and inertial vertical shaker (right)

hydraulic power supplies were not located on the ML to prevent them from adding to the ambient background vibration environment.

While test engineers familiar with electrodynamic modal shakers are familiar with the challenges of displacement and velocity limits and the relatively mild shaker nonlinear distortion due to amplifier gains and shaker flexure structural geometric nonlinearities, they probably are not as familiar with the unique set of challenges hydraulic modal shakers present. The unique challenges associated with hydraulic modal shakers include significant nonlinear distortion in the shaker force, issues with the setup of the hydraulic power supply and the associated hydraulic hosing, velocity limits as they relate to potentially damaging the hydraulic actuator piston, and safety issues with operating high-pressure hydraulic systems. This chapter addresses these unique challenges to help the test engineer to better utilize hydraulic modal shakers on large-scale modal tests.

13.2 Hydraulic Actuator Basics

Hydraulic actuators are comprised of a piston in a housing with pressurized hydraulic fluid used to exert a pressure to the face of the piston to generate a force on the piston, which is transmitted through the piston shaft to what it is attached to with an equal and opposite force exerted on what the hydraulic actuator housing is attached to. Hydraulic actuators can be a single-acting or plunger configuration, double-acting configuration, or a double-acting double-ended (i.e., double rod) configuration as shown in Fig. 13.4. The single-acting or plunger configuration relies on what the hydraulic actuator is pushing against or an internal spring to retract the piston when the hydraulic fluid pressure is decreased (e.g., hydraulic floor jack). The double-acting and double-acting double-ended configurations exert push/pull forces and are extended/retracted by changing the pressure differential across the piston. The double-acting double-ended (double rod) configuration by virtue of the piston being supported in the off-axis directions on both ends provides potentially greater lateral support that can withstand higher off-axis loads than a similar double-acting hydraulic actuator.

Hydraulic actuators used for vibration and shock testing are comprised of a stiff double-acting double-ended hydraulic actuator and a high-frequency response electrohydraulic servo valve [12]. A servo controller sends an electrical command signal to the electrohydraulic servo valve that positions the servo valve in a single-stage servo valve or the pilot valve in a multi-stage servo valve [13]. The servo controller uses position feedback of the hydraulic actuator piston and the position of the multi-stage valves, usually measured with a linear variable displacement transducer (LVDT) [14], to allow the piston to be placed in the desired starting position (usually mid-stroke). The phase lag associated with electrohydraulic servo valve influences the various feedback gains. Hydraulic actuators are inherently unstable, and the servo controller is required to set the desired piston position. In most cases one would set the piston to the center position just prior to initiating the desired

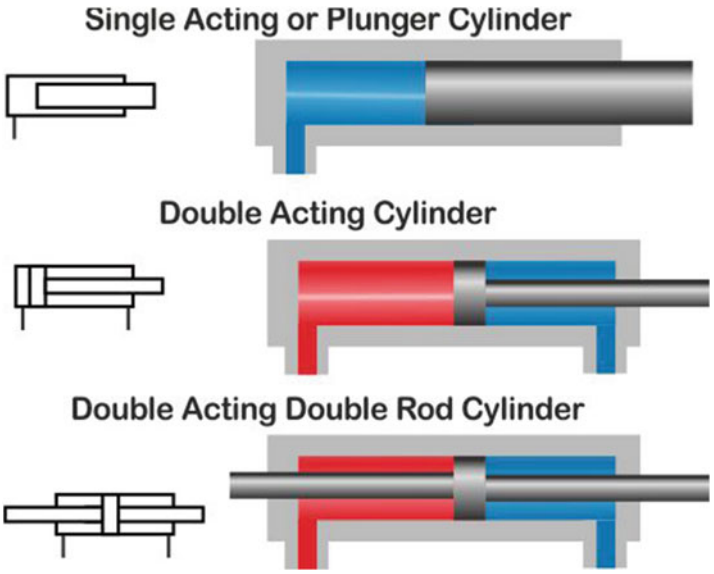

Fig. 13.4 Hydraulic actuator configurations

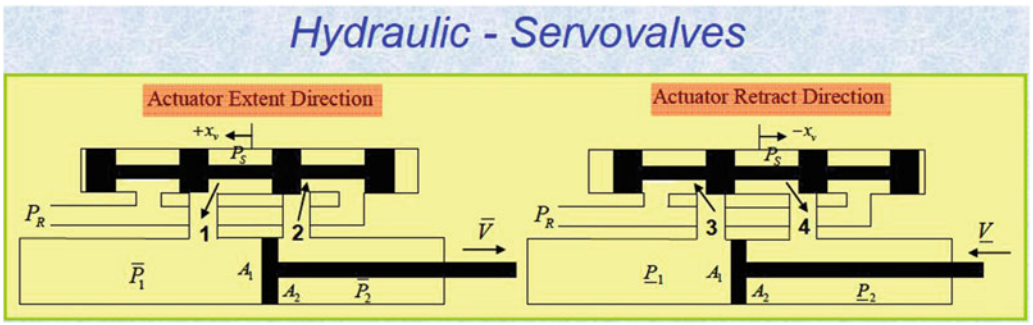

Fig. 13.5 Servo valve extending and retracting hydraulic actuator [2]

motion. In the case of vertically positioned actuators, one would retract all actuators prior to pressuring the system down. The servo controller, its electrical command signal to the electrohydraulic servo valve, and the actuator position and valve position signal feedback is often referred to as the "inner loop." The outer loop control is generally based on force or acceleration feedback and may be open- or closed-loop in nature.

The electrohydraulic servo valve is comprised of a spool or spools, if multi-stage, with lands sliding in a sleeve, which has porting grooves matched to the lands. The openings between the lands and grooves form four flow control orifices that simultaneously direct pressurized hydraulic fluid produced from the hydraulic power supply to one side of the hydraulic actuator and direct the exhausted oil from the other side back to the hydraulic power supply reservoir [15]. Higher flow rate requirements of the hydraulic actuator require multi-stage electrohydraulic servo valves, where each stage is hydraulically, not mechanically, linked to its successor. For the double-acting and double-acting double-ended hydraulic actuator configurations, two hydraulic fluid hoses run between the hydraulic power supply and the hydraulic actuator with the feed line supplying the higher pressure hydraulic fluid and the lower pressure return line bringing back hydraulic fluid from the hydraulic actuator to the hydraulic power supply reservoir. Figure 13.5 shows how the motion of the servo valve sends high-pressure source hydraulic fluid (Ps) to and pulls the lower pressure return hydraulic fluid (Pr) from a double-acting hydraulic actuator in order to make it extend and retract. Figure 13.6 shows a four-stage electrohydraulic servo valve [15].

The servo controller in addition to generating the electrical command signal for the servo valve to move the hydraulic piston, based upon the shaker controller drive signal, also generates a high-frequency dither signal, whose frequency should be well above the modal test frequency range of interest. The purpose of the dither signal is to cause the servo valve to undergo very small-amplitude oscillations (i.e., dither) to prevent sticking from occurring. The dither signal is generally set to a frequency an octave or more above the resonant frequency of the pilot valve where the system transfer function has minimal gain. While this dither signal should be high enough to be outside the modal test frequency range of interest, it

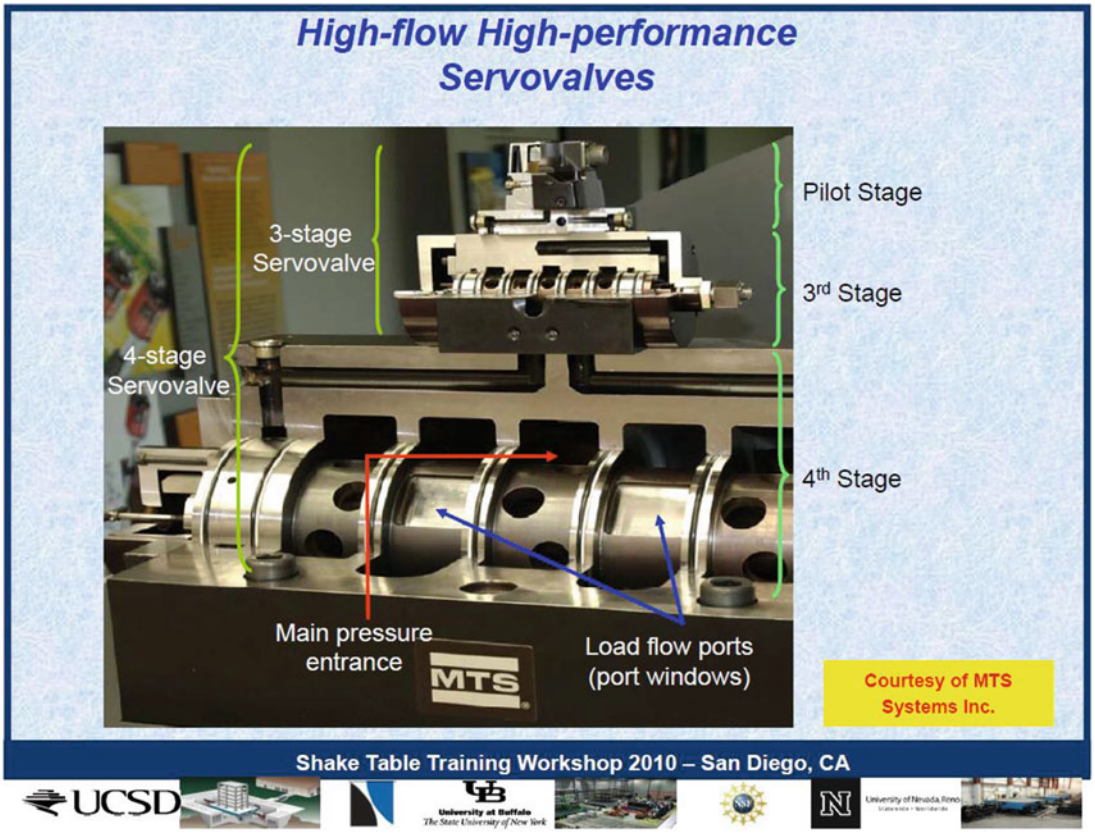

Fig. 13.6 Four-stage electrohydraulic servo valve [15]

may produce local responses in the test article, particularly close to drive point locations, and therefore can affect the data acquisition system (DAQ) full-scale settings, particularly for these channels. Even if the dither frequency is well outside the modal test frequency range of interest, it is recommended that at least one set of data be acquired at an appropriately high sampling frequency to capture the dither signal and the test article's response to it while the shaker drive signal to the servo controller is off. In the unlikely event that the test payload of interest has a localized resonance associated with the dither frequency, the dither may be shifted (typically higher) in frequency to minimize the unwanted effects.

Hydraulic actuators have a dynamic stroke limit and a mechanical stroke limit. When the hydraulic actuator reaches its dynamic stroke limit, the piston starts to engage its dashpots that begin to bleed off the hydraulic fluid that is applying the force on the piston in order to try and reduce the piston's velocity prior to reaching its mechanical stroke limit where it impacts the housing's mechanical stops. The test engineer is cautioned not to operate the hydraulic actuators to exceed their dynamic stroke limits for two reasons. First, if the dashpots are engaged, the hydraulic actuator force has significantly more nonlinear distortion due to the dashpots bleeding off the hydraulic fluid. Therefore, to minimize the hydraulic actuator's nonlinear distortion, the dynamic stroke limits should not be exceeded. Second, typically the distance between the dynamic and mechanical stroke limits is relatively small, so there is a good chance that if the hydraulic actuator exceeds its dynamic stroke limit, it will reach its mechanical stroke limit. Repeated contract with the mechanical stops, particularly at high velocity, can permanently damage the hydraulic actuator piston and its housing.

The hydraulic power supply consists of a hydraulic fluid reservoir tank, hydraulic pump, heat exchanger to maintain the hydraulic fluid temperature, and filtration to maintain the cleanliness of the hydraulic fluid. It is estimated that at least 75% of hydraulic system failures and maintenance activities are the result of contaminated hydraulic fluid. Fluid conditioning plays a critical role in maintaining the performance of all hydraulics equipment. This is especially true in the case of servo-hydraulic equipment where the precision clearances and high relative velocities between the moving parts place extreme demands on the hydraulic fluid [16]. Oil cleanliness should be tested on a regular basis based on system usage, and any time there is a major component failure such as a damaged bearing or valve. When the system is idle, it is highly recommended that oil be continually circulated through the filtration system and that a near operational temperature be maintained. If the modal test is to be performed in either very cold or hot environments, care needs to be taken that the hydraulic power supply heat

exchanger is capable of properly maintaining the temperature of the hydraulic fluid. In addition, if the hydraulic equipment will be exposed to high humidity, oil contamination due to the introduction of water must be prevented [16]. Proper filtration and temperature control are essential for maintaining the quality of the hydraulic oil and the health of the hydraulic actuator. From a modal testing perspective, the hydraulic power supply with its hydraulic pump represents a vibration exciter that needs to be located so that it is vibrationally, and possibly acoustically, isolated from the test article. Of course, the vibration and acoustic isolation of the hydraulic power supply needs to be balanced against the available length of the hydraulic fluid hoses and their isolations from the test article as well. Therefore, vibration and acoustic isolation of the hydraulic power supplies and their hoses needs to be taken into consideration when selecting the layout of the modal hydraulic shakers.

13.3 Hydraulic Actuator Nonlinear Distortion

The source of the hydraulic actuator force nonlinear distortion is due to the servo valve not being a linear flow controller that has a nonlinear flow response, which is a function of the pressure across the valve. The oil flow through the control orifices is a function of both the area of the orifice and the square root of the pressure drop across the orifice. It is this relation of flow to the square root of the pressure drop that is a major source of the hydraulic actuator force nonlinear distortion [12, 15]. A detailed discussion of the nonlinearities of the servo controller can be found in [12, 15]. If the shaker drive signal is a fixed frequency sine wave, the nonlinear flow characteristics of the servo valve produce a hydraulic actuator force that contains predominantly odd superharmonics of the fundamental drive frequency. Compounding this nonlinear effect is the hydraulic actuator acts as a lightly damped single-degree-of-freedom (SDOF) oscillator that amplifies pressure oscillation close to its oil column resonance frequency. The oil column resonance frequency is a function of the hydraulic fluid column height and cross-sectional area, the effective bulk modulus of the hydraulic fluid, and the total mass the hydraulic actuator is supporting, including the mass of the piston itself. Figure 13.7 shows the equation for the oil column resonance frequency [15]. The effective bulk modulus of the hydraulic fluid is a function of pressure and the amount of entrained air in the hydraulic fluid. The more entrained air, the lower the effective bulk modulus (i.e., this is why we bleed our car's brake lines after working on the brake system). In addition to entrained air in the hydraulic fluid lowering its effective bulk modulus and decreasing the hydraulic actuator peak force capability, formation of air bubbles in the hydraulic fluid can lead to cavitation in the hydraulic pumps, which can cause them to fail.

Any superharmonic that is close to the oil column resonance frequency will be amplified by the oil column resonance and lead to further increased nonlinear distortion in the hydraulic actuator force. Figure 13.8 shows examples of the nonlinear distortion that were observed in a hydraulic modal shaker force time history during a linear sine sweep. During higher frequencies in the sine sweep, the fundamental harmonic of the modal shaker force has a higher amplitude than the unfiltered modal shaker force, while at lower frequencies, the opposite is true with the unfiltered modal shaker force having a significant impulsive spike occurring at the positive and negative peaks of the unfiltered modal shaker force. Figure 13.9 shows the corresponding PSD water fall plot clearly showing the dominance of the odd superharmonics.

Figure 13.10 shows the normal probability plot of a hydraulic modal shaker force time history where the shaker drive signal was a bandwidth-limited Gaussian signal [11]. The hydraulic modal shaker force exhibits significant non-Gaussian behavior because the empirical cumulative distribution function (ECD) does not lie on a straight line when plotted in a normal probability plot and has a kurtosis value of 1.5. Both the normal probability plot and the kurtosis value being less than 3 show the positive and negative excursions are not as large as that of a Gaussian distribution. The test engineer is encouraged to look at the ECD in addition to the traditional histogram (i.e., empirical probability density function (EPDF)) because the deviations from a Gaussian distribution in the tail areas (i.e., where the excursions are occurring) can be sometimes hard to see when looking at the EPDF.

Depending upon the relative phasing between the fundamental and superharmonic force components, the peak amplitude of the unfiltered shaker force time history may be greater than or less than that of its fundamental harmonic. Total harmonic distortion (THD) is a measurement of the amount of harmonic distortion present and is the ratio of the sum of the power of all superharmonics to the power of the fundamental harmonic [17]. A THD of 0% indicates no superharmonics present and thus no nonlinear distortion. For reference a square wave has a THD of 48.3%, a sawtooth wave has a THD of 80.3%, and a symmetric triangle wave has a THD of 12.1%. THD however does not contain information about the relative phasing of the harmonics and therefore does not provide insight into the waveform of the shaker force time history. Figure 13.11 shows how the relative phasing between the fundamental and superharmonic force components affects the peak amplitude of the shaker force time history. These three shaker force time histories have the same superharmonic amplitudes and therefore the same THD, where the only difference is the relative phasing of the third superharmonic.

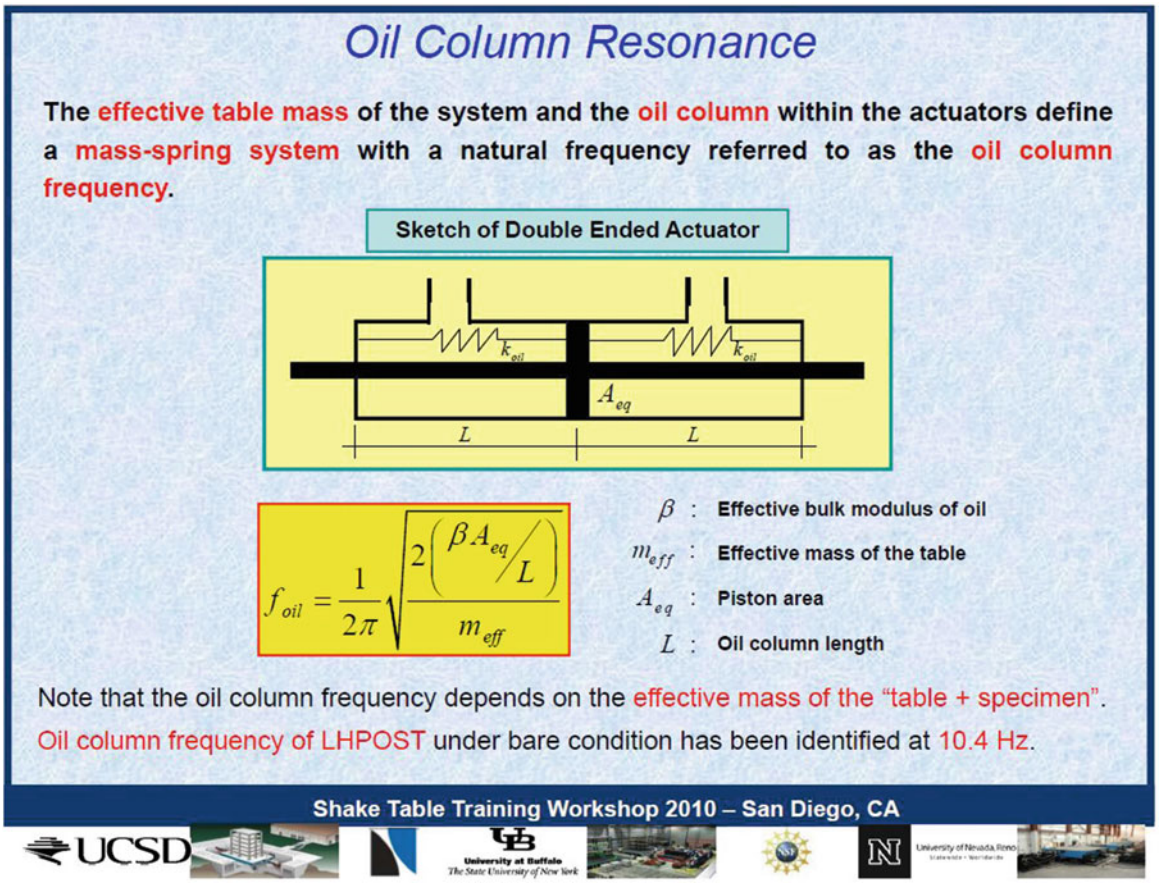

Fig. 13.7 Oil column resonance frequency

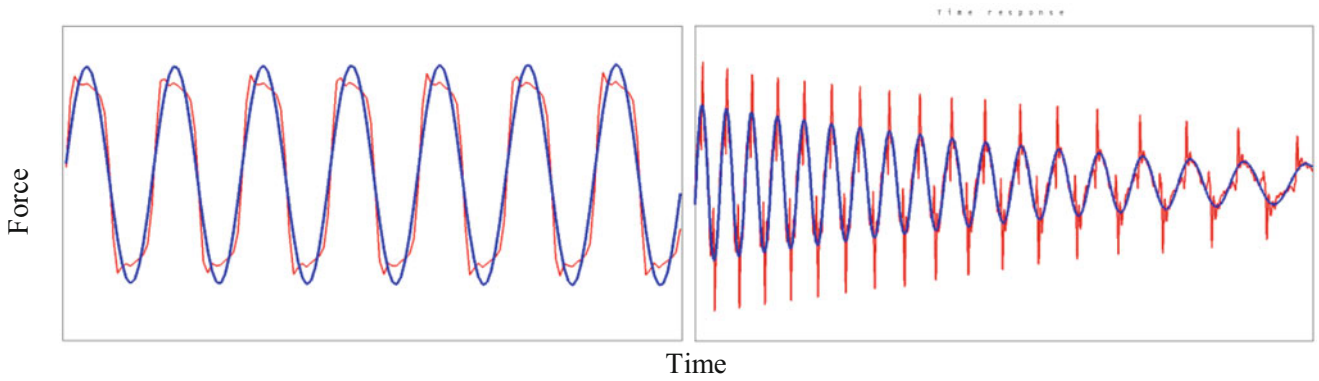

Fig. 13.8 Hydraulic modal shaker force during a linear sine sweep. High frequency (left) and low frequency (right). Unfiltered (red), fundamental harmonic (blue)

If the modal hydraulic shakers are being driven with continuous or burst random signals, the nonlinear distortion of the hydraulic actuator force may require nonlinear filtering to achieve a desired spectral content (e.g., need to adjust the shaker drive signal around 5 Hz to adjust the hydraulic modal shaker force around 15 Hz due to a dominant third superharmonic).

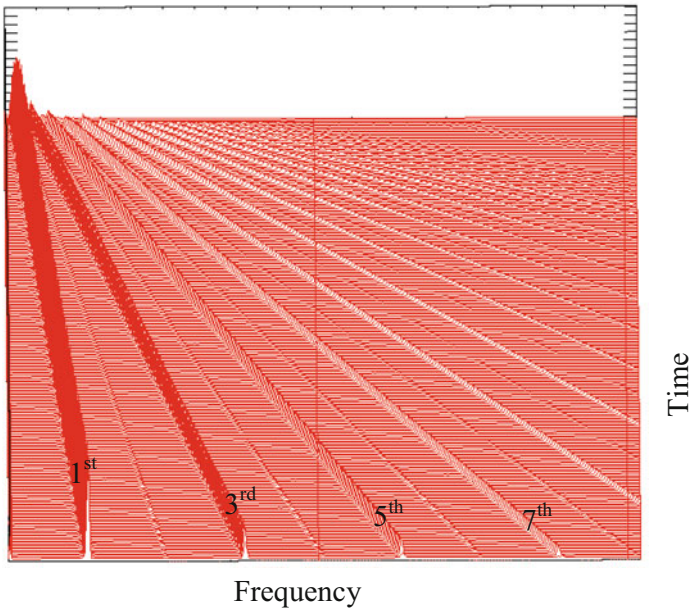

Fig. 13.9 PSD waterfall plot of the hydraulic modal shaker force during a linear sine sweep

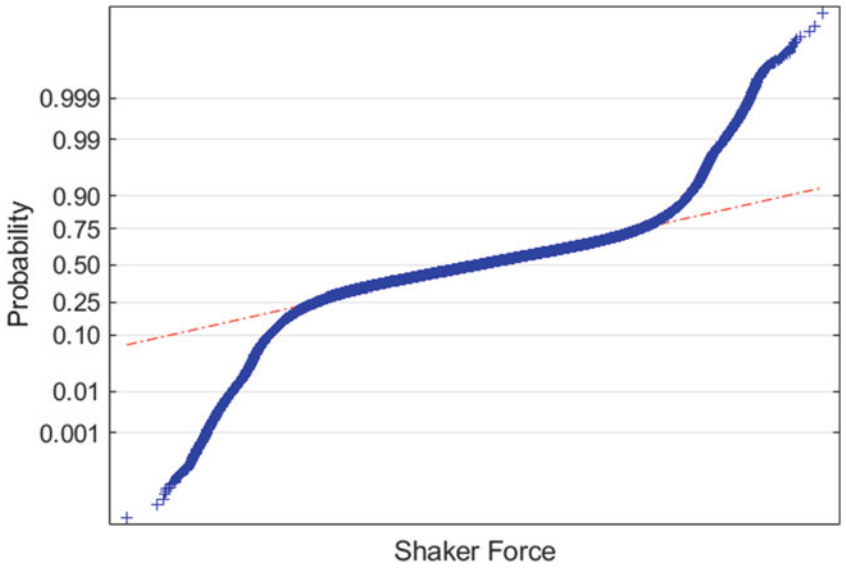

Fig. 13.10 Normal probability plot of a hydraulic modal shaker force time history with Gaussian random drive signal

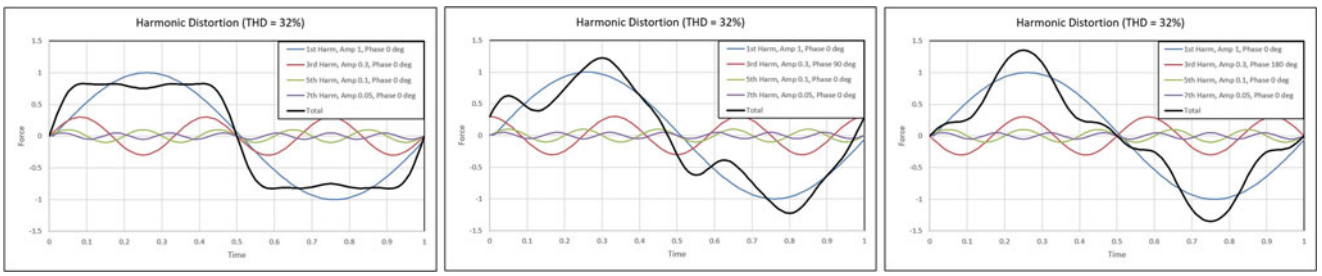

Fig. 13.11 Harmonic distortion, third harmonic phase angle 0° (left), 90° (center), 180° (right)

13.4 Shaker Performance Limits

Electrodynamic modal shakers have performance limits defined by its peak displacement, peak velocity, and peak force. These three parameters in turn specify a low-frequency displacement limit curve, possibly a mid-frequency velocity limit curve, and a high-frequency acceleration limit curve, which form straight line segments on a log frequency vs log acceleration plot. The low-frequency displacement limit is a function of the peak displacement limit, which for an electrodynamic model shaker is a function of the armature flexure design and has a slope proportional to frequency squared (i.e., 40 dB/dec or 12 dB/oct). The mid-frequency velocity limit is a function of the maximum current the shaker amplifier can produce and has a slope proportional to frequency (i.e., 20 dB/dec or 6 dB/oct). If the shaker amplifier is sized large enough, it does not impose a velocity limit, and the electrodynamic modal shaker only has a low-frequency displacement limit and a high-frequency acceleration limit. The high-frequency acceleration limit is simply the peak force divided by the total mass the shaker is moving (i.e., the sum of the armature mass and the mass the shaker is driving on). Figure 13.12 shows an example of a theoretical electrodynamic modal shaker performance limit curves, where the solid black line represents the performance curve when the shaker is pushing on 50 lbm. Note that when this shaker is pushing on 100 lbm, the acceleration limit curve is lowered sufficiently that the performance curve only consists of the displacement limit and acceleration limit curves.

Hydraulic modal shakers have their performance limits defined by its displacement limit, peak velocity, peak dynamic force, oil column resonance frequency, and servo valve corner frequency [18]. The hydraulic modal shaker's oil column acts as a second-order mechanical system that above the oil column resonance frequency has a slope proportional to the inverse of the frequency squared (i.e., −40 dB/dec or −12 dB/oct). The servo valve acts as a first-order mechanical system that above its corner frequency has a slope proportional to the inverse of the frequency (i.e., −20 dB/dec or −6 dB/oct). Hydraulic modal shaker displacement limits are typically set to be equal to or slightly less than their dynamic stroke limit in order to avoid engaging the dashpots or accidentally reaching their mechanical stroke limit. Hydraulic power supplies are designed to produce a specified flow rate of hydraulic fluid. The pressurization that results is due to the resistance to that flow. Therefore, as the hydraulic modal shaker actuator piston velocity increases, the hydraulic pressure decreases. Hence the hydraulic modal shaker mid-frequency velocity limit is a function of both the hydraulic power supply maximum flow rate and the minimum pressure needed to adequately "float" the hydraulic actuator piston in order to prevent it from rubbing up against the housing and undergoing scoring. The plateau in the high-frequency acceleration limit is a function of the peak dynamic force the

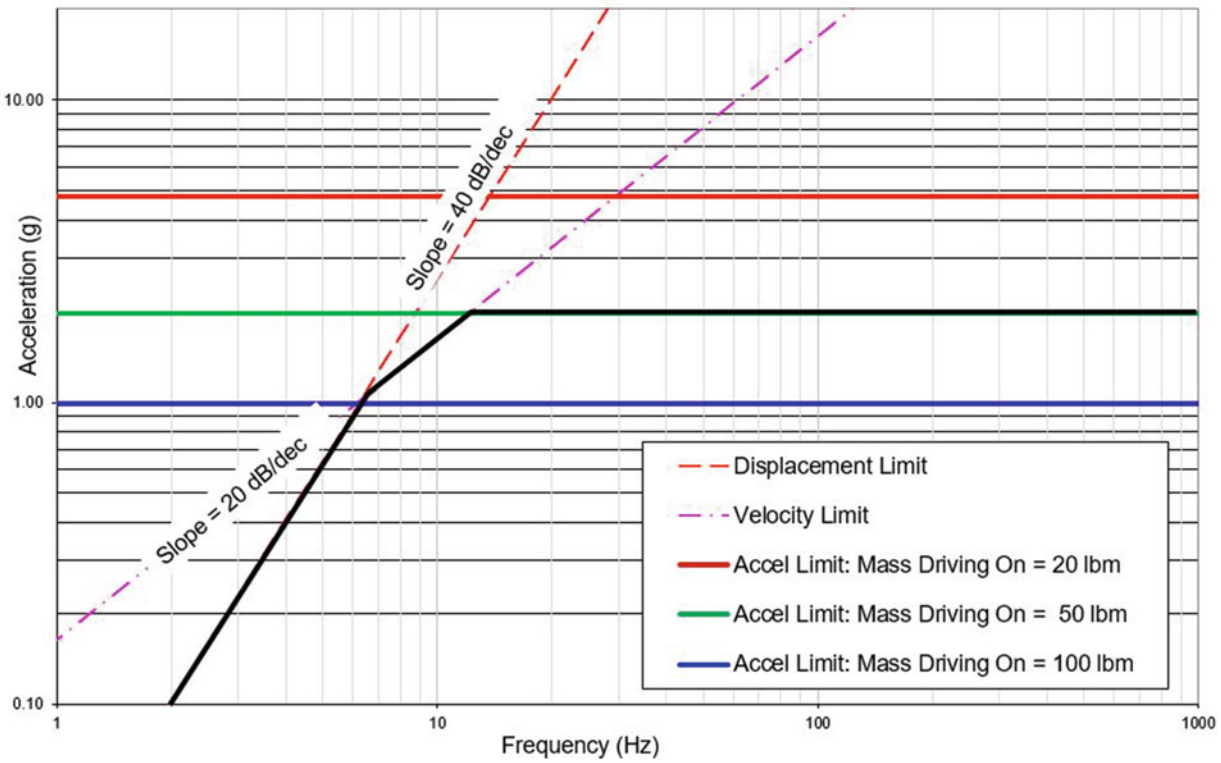

Fig. 13.12 Electrodynamic modal shaker performance limit curve

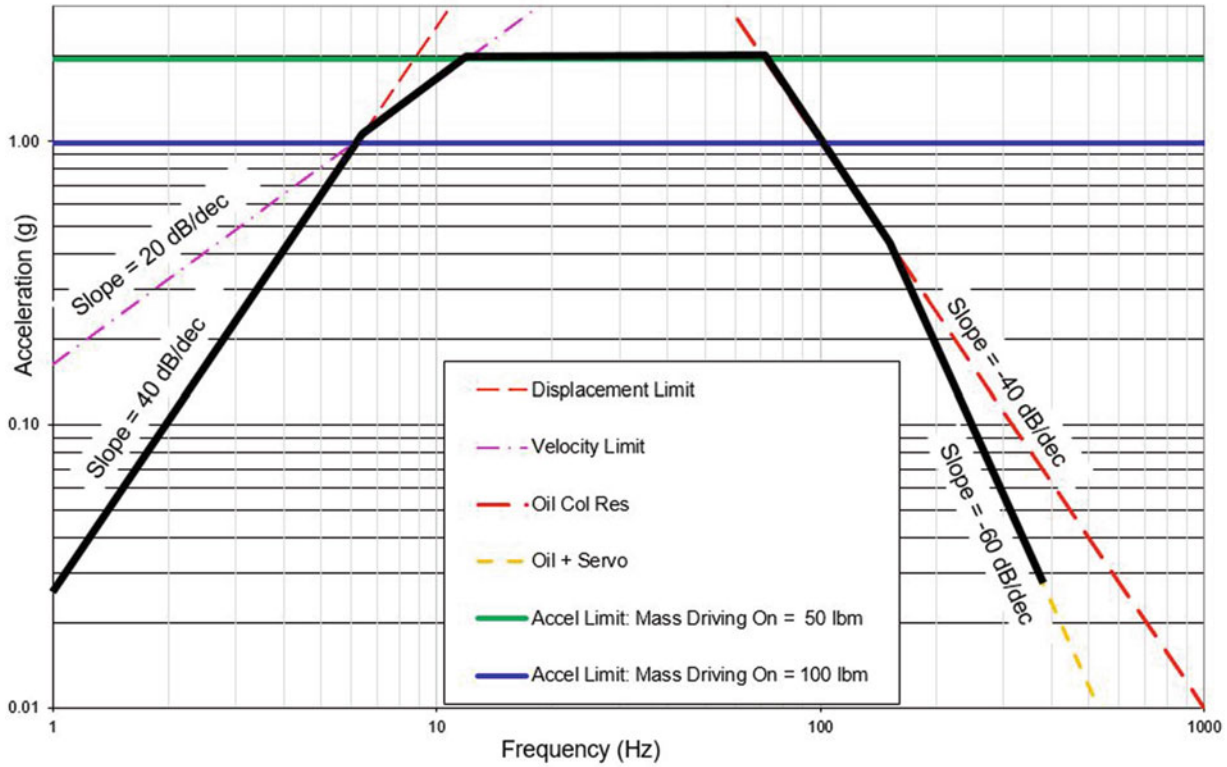

Fig. 13.13 Hydraulic modal shaker performance limit curve

hydraulic modal shaker can produce and the total amount of mass it is driving, which includes the actuator piston mass. At frequencies above the oil column resonance frequency and servo valve corner frequency, the high-frequency acceleration limit curve has a slope proportional to the inverse of the frequency cubed (i.e., −60 dB/dec or −18 dB/oct). Figure 13.13 shows an example of a theoretical hydraulic modal shaker performance limit curves, which assumes no nonlinear distortion in the shaker force, where the solid black line represents the performance curve when the shaker is pushing on 50 lbm, the oil column resonance frequency is 70 Hz, and the servo valve corner frequency is 150 Hz. Note that when this shaker is pushing on a 100 lbm, the acceleration limit is lowered sufficiently that the hydraulic modal shaker is not velocity limited.

The electrohydraulic servo controller does not limit the hydraulic actuator displacement and therefore does not prevent the hydraulic actuator from exceeding its dynamic stroke limits, reaching its mechanical stroke limit, or exceeding its velocity limit. However, the LVDT displacement signal of the hydraulic piston is available for recording and monitoring during testing to help with this. In order to get an accurate measurement of the hydraulic actuator displacement, it is recommended that an in situ calibration be performed where the hydraulic actuator piston is fully extended and fully retracted with the LVDT signal recorded at both locations to obtain an accurate LVDT displacement sensitivity.

There are two options for limiting the displacement of a hydraulic actuator. One option is to incorporate an outer nonlinear closed-loop controller. The other option is to perform a series of open-loop pretest runs to develop a combination of drive signals and servo controller gains that prevent the hydraulic actuator from exceeding its dynamic stroke and velocity limits. In either case it is recommended that test engineers monitor the hydraulic actuator displacements, hydraulic pressure, and hydraulic actuator force and be able to make manual adjustments to the servo controller gains as needed. A computerized monitoring system with video surveillance to provide real-time views of the modal shakers is very helpful in protecting the health of the modal shakers and test article [10].

As already pointed out, the relative phasing between the fundamental and superharmonics force components can lead the peak amplitude of the shaker force time history at a particular frequency to be greater than or less than that of its fundamental harmonic. Therefore, the theoretical shaker performance limit curve of a hydraulic modal shaker may not be a conservative upper bound of the actual shaker performance limit curve. To generate an actual hydraulic modal shaker performance limit curve in its test setup, the test engineer can drive the hydraulic modal shaker with a sine sweep with the test engineer closely monitoring it and operating it as close as possible to its displacement, velocity, and acceleration limits. This shaker force time history can then be sine post processed using a band-pass tracking filter to generate the spectrum of the fundamental harmonic

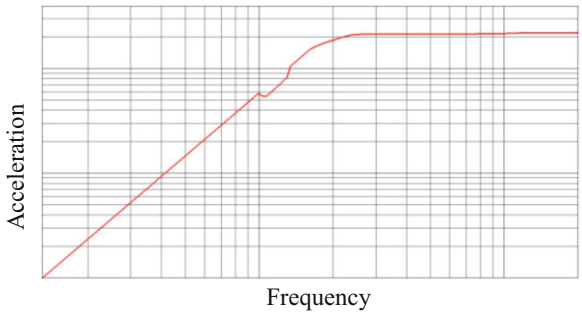

Fig. 13.14 Actual hydraulic modal shaker performance limit curve

of the shaker force, which can then be further adjusted to come up with the actual hydraulic modal shaker performance limit curve. Figure 13.14 shows an actual hydraulic modal shaker performance limit curve. At low frequencies it is defined by a peak displacement that was set to be 75% of the dynamic stroke limit. The bucket in the knee and the knee itself in Fig. 13.14 are a result of the velocity limit (i.e., maintaining a minimum hydraulic pressure). At high frequencies it is defined by the peak dynamic force and the amount of mass it is driving on. The oil column resonance frequency and servo controller corner frequency lie above the frequency range of interest resulting in no high-frequency roll-off in this plot. Accurate actual hydraulic modal shaker performance limit curves are a key part in end-to-end force response simulations that are discussed below.

13.5 Operational and Safety Concerns

If for some reason, there is a major failure in the servo controller or with the feedback signals to it (e.g., a broken feedback cable, LVDT goes bad), the hydraulic actuator has the potential to move to full stroke at full force. This failure mode is very similar to the failure mode produced by a major failure in the electrodynamic modal shaker amplifier (e.g., op amp fails). This is why personnel should not be touching or near a hydraulic modal shaker when the servo controller is on regardless of whether the hydraulic power supply is on because there can be significant stored energy in the hydraulic system. Dashpots help in such cases, but there will still be a significant transient event. This potential transient event needs to be taken into account when sizing the hydraulic modal shakers, in the selection of the shaker attachment hardware, and in selecting the drive points.

Uninterruptible power supply (UPS) backups to the servo controllers are highly recommended to ensure the servo controllers remain under power in the event of a power outage to minimize any transient forces into the test article. This is necessary since there is still a significant amount of potential energy remaining in the hydraulic system because the pressure in the hydraulic fluid supply line does not instantaneously drop to zero when the hydraulic power supply is turned off or loses power. To ensure the UPS system is functioning as intended in the event of a power outage, an instrumented bare head test should be conducted. Simply disconnect line power and ensure that the UPS engages and that there is no transient behavior of the excitation system.

Hydraulic modal shakers are stiff compared to electrodynamic modal shakers. If a hydraulic actuator loses the command signal to its servo controller, the servo controller (inner loop) will use all available force to keep the piston stationary at the user-defined neutral position (typically center stroke), unlike an electrodynamic modal shaker whose resistance is only a function of the inertia of its armature and the stiffness of the armature flexures, which are relatively small. Hence if the hydraulic modal shaker is fixed and loses it command signal, its drive point becomes fixed and can develop significantly high loads. This is especially concerning in the case of over-actuated test configurations, where two or more hydraulic modal shakers are driving very close to each other on the test article. This could be the result of wanting to get more force into a particular location on the test article to better excite a particular mode. One solution to this issue is to integrate either active or passive delta-P circuitry into the system design. The delta-P circuitry, either electrical or hydraulic in nature, will sense pressure differences between hydraulic actuators with a common line of action and will cross port the hydraulic fluid in such a manner as to make the hydraulic actuators softer (passive), similar to the way electrodynamic exciters would behave. The effectiveness of delta-P configurations is a design parameter that should be analyzed on a case-by-case basis, and while it will typically not be effective over the maximum operating pressure range, implementation is highly recommended for over-actuated systems. The integration of passive delta-P consists of cross porting internal to the slave valve(s), and while flow requirements to the valve increases, there is a secondary advantage in that THD may be significantly reduced. Again,

this potential failure mode needs to be taken into consideration when sizing and choosing the layout of the hydraulic modal shakers.

When using hydraulic modal shakers and their associated hydraulic power supplies and hydraulic hosing, safety procedures should be followed to protect personnel, test article, and facility. Of fundamental importance is that the pressure rating of the actuators, bearings, and supply lines is documented and that the hydraulic power supply is not allowed to exceed these maximum pressure limits. Safety issues related to spillage and leakage need to be taken into account in the test planning, preparation, and execution. A drip pan to collect dripping/leaking hydraulic fluid from the hydraulic actuator and its hydraulic fittings may be needed. Some amount of residual leakage is to be expected, and keeping the work area associated with any servo-hydraulic system clean should be considered mandatory continual maintenance. Safety procedures for inspection and detection of leaking/cracked hydraulic hoses should be implemented to prevent potential contamination of the test article with hydraulic fluid. Personnel safety procedures should also be followed to prevent personnel from being exposed to the hazards from operating hydraulic systems. Personnel safety procedures should cover hazards such as being sprayed by the hot hydraulic fluid, being hit by flailing hydraulic hoses, and when handling hoses the potential of having hydraulic fluid injected under the skin, which can have grave medical complications [19].

When using an electrodynamic modal shaker or a hydraulic shaker modal shaker as an inertial shaker (i.e., pushing against an inertial mass instead of a support stand in order to generate a force against the test article, sometimes referred to as proof mass actuators), the amount of force the shaker can generate at low frequency is a function of both its stroke limit and the total inertial mass. For an electrodynamic modal shaker, this total inertial mass includes the mass of its housing and field coils. For a hydraulic modal shaker, this total inertial mass includes the mass of the hydraulic actuator housing. If high-force levels are needed at very low frequency, the total inertial mass could be well over several hundred pounds.

Two inertial shaker options to consider are suspending the shaker or mounting the shaker on a slide system that is fixed to the test article. Suspending the shaker potentially provides the greatest amount of vibration isolation but also incurs the additional safety constraints due to having a potentially very heavy suspended weight. In addition, for a hydraulic modal shaker, care needs to be exercised to ensure the hydraulic hoses do not structurally short the shaker (i.e., transmit shaker vibrations back into the test article). If mounting the shaker on a slide system mounted to the test article, two options to consider are roller or ball bearing rails and hydrostatic bearings. While hydrostatic bearings provide the lowest friction and smoothest support, care needs to be taken that they are energized prior to energizing the electrodynamic or hydraulic modal shaker. For hydraulic modal shakers, this typically means the hydrostatic bearing hydraulic power supplies are independent of those for the hydraulic actuators. Also, there should be a mechanical locking device to lock the hydraulic modal shaker when not being used to prevent rubbing occurring in the hydrostatic bearing when it is not energized. It is recommended that a minimal set of accelerometers be mounted on an inertial shaker to monitor its dynamics and motion during testing. For inertial shakers supported on a slide system mounted to the test article, it is recommended that sufficient in-line accelerometers be mounted to the shaker's inertial mass and an in situ calibration using the acceleration of the inertial mass be used to verify the force being measured by the load cell used to measure the shaker force into the test article. Differences between the load cell force and the acceleration of the inertial mass can indicate stick/slip or significant friction is occurring in the slide system and the load cell force is inaccurate and leading to incorrect modal parameters, in particular mass scaling of the test mode shapes. For inertial shakers supported on a slide system mounted to the test article and pushing on a vertical post that is part of the shaker fixture, the compliance of this vertical post may need to be modeled if it is not sufficiently stiff. To verify the stiffness properties of the vertical post, strain gauges near the line of rotation and in-line accelerometers at the top and bottom of the vertical post could be installed and monitored during testing.

If piezoelectric load cells or load washers are used to attach the inertial shaker to the test article that incorporate a preload bolt in series with the load cell, it is recommended that long time constant signal conditioners be used to measure the bolt preload during installation instead of using the bolt torque. Having the correct preload is important because piezoelectric load cells or load washers need to have the proper amount of compression to work properly. The static compression provided by the preload bolt needs to be high enough that the maximum dynamic tensile loading does not cause the load cell to see less than a minimum amount of dynamic compression loading in order to remain a linear sensor. The static compression provided by the preload bolt also must not be too great so the maximum dynamic compressive loading does not exceed the structural limits of the load cell or load washer (i.e., exceed its crush limit load). In addition because the preload bolt load is in series with the load cell or load washer load, the load being measured by the load cell or load washer can be up to 20% below the true loading (i.e., up to 20% of the load is being taken up by the preload bolt). Therefore, an in situ calibration should be performed to obtain an accurate load cell or load washer sensitivity.

The best practice is to disconnect the unused shaker from the test article so that it has no effect. For inertial shakers supported by a hydrostatic bearing, this also means the hydrostatic bearings should be energized. However, disconnecting shakers may not always be possible due to access issues. In that case it is recommended a sensitivity analysis be performed with the test article pretest FEM to determine the effect of having unused shakers attached to the test article on the test article

FEM modes. This will determine if the test article FEM needs to be test configuration specific, which can potentially make the bookkeeping of the test article FEM correlation more cumbersome.

13.6 Pretest Analysis: End-to-End Force Response Simulation

It is recommended for large-scale modal tests that in addition to the standard pretest analysis, which verifies the layout of the modal shakers and sensors (e.g., accelerometers) is sufficient to identify all target modes, an end-to-end force response simulation should be performed to verify the modal shakers have sufficient force capability and the types of modal accelerometers have sufficiently low noise floors and dynamic ranges. This end-to-end simulation should include the sensor, ambient environment (i.e., vibration and electronic noise), and data acquisition noise levels. This end-to-end simulation should also include an accurate presentation of the shaker performance (i.e., shaker forces not exceeding its displacement, velocity, acceleration (peak force) limits, etc.). This will help to inform what excitation types to use: single-point, multi-point, continuous random, burst random, sine sweep, and normal mode tuning. Continuous random and burst random have the simplest setup and tend to linearize the response of the test article. For simulations using either continuous random or burst random, a single recorded continuous random shaker force time history of sufficient duration can be manipulated to generate multiple uncorrelated random shaker force time histories using a "slinky approach" [11]. The "slinky approach" takes the recorded random shaker force time history and removes the first time interval, having a duration greater than or equal to the maximum frame length that will be used when processing the time histories into FRF, and appends it to the end, to generate the second modal shaker uncorrelated random shaker force time history. Then this process is repeated, but now operating on the second modal shaker uncorrelated random force time history to generate the third modal shaker uncorrelated random shaker force time history. This process is repeated as needed to generate uncorrelated random shaker force time histories for all modal shakers. Figure 13.15 shows the "slinky approach" for creating three modal shaker uncorrelated random force time histories, where T_i represents the ith time interval of the original modal shaker random force time history.

If the time interval chosen has a duration shorter than the data processing frame length, these random time histories will not be uncorrelated because from the data processing perspective, the time histories in each data block appear to be predominantly time shifted random signals, which have a significantly nonzero coherence and are thus not uncorrelated [20].

If measured modal shaker random force time histories are not available, but the modal shaker force PSD is available, uncorrelated Gaussian random signals can be filtered with a band-pass filter approximating the modal shaker force PSD to generate modal shaker uncorrelated random force time histories. Depending upon the desired crest factor, say 5, one can then set the 5σ level to be equal to the maximum modal shaker force. Then these modal shaker uncorrelated random shaker forces can be used in an end-to-end force response simulation, discussed below, and compute the peak velocities and displacements, and check them against the modal shaker displacement and velocity limits, respectively, and make adjustments as necessary to ensure modal shaker limits are not exceeded. This open-loop approach eliminates the need for designing a complicated mathematical model of the modal shaker and the long run times of the associated force response analysis simulations.

Sine dwell and sine sweeps have the advantage of putting more energy into the test article at a particular frequency, which can be helpful if the noise levels are high and can better identify the nonlinearities of the test article, but are also prone to excite unwanted rattling in the test article. Two approaches to multi-point sine dwell testing are optimal phasing [21] and frequency wrapping [22]. The optimal phasing approach has all shakers driving at the same frequency, but with different phasing. The optimal phasing approach has the advantage of putting the most energy into the test article of these two approaches, but has the disadvantage that closed-loop control of the modal shakers is needed in order to maintain their relative phasing, especially in frequency bands around the test article resonance frequencies. If the modal shakers were operated open-loop, at frequencies close to the test article resonance frequencies, the modal shakers would lose their relative phasing producing corrupted FRF from which accurate modal parameters could not be extracted. The optimal phasing approach has another disadvantage in that it requires at least as many phasing combinations as shakers, so that a modal test

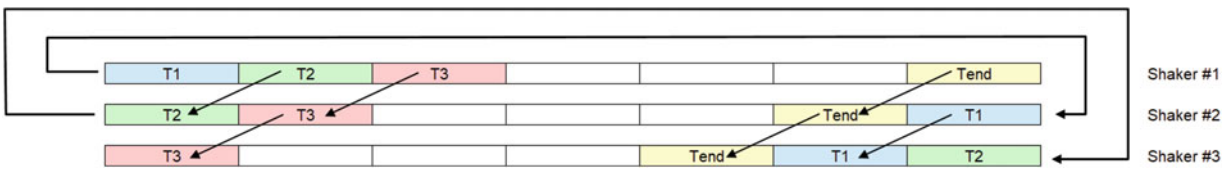

Fig. 13.15 Generating uncorrelated random force time histories

using three modal shakers would require three sine sweeps. The frequency wrapping approach has each modal shaker driving at a different frequency at any time and thus has the advantage of not requiring close-loop control to maintain the relative phasing between the modal shakers, but has the disadvantage that it does not as strongly excite the test article as the optimal phasing approach. Normal mode tuning, which excites the test article at a single frequency, requires closed-loop control of the modal shakers for proper scaling of the force magnitudes and phasing. Typically, modal tests use slow sweep rates (e.g., 0.5 oct/min) to give the test article time to reach close to its steady-state resonance response at each mode. For a sweep frequency range (i.e., in excess of an octave), a logarithmic sweep rate is preferred instead of a linear sweep rate in order to get the same number of cycles of excitation into both the lowest frequency and highest frequency modes. However, depending on the frequency range of interest, a faster sine sweep rate may be required due to the test schedule or the modal shaker thermal cooling issues. The effect of the sine sweep rate on the response of a SDOF oscillator is discussed in [23, 24].

For both large electrodynamic and hydraulic modal shakers, it is recommended a few accelerometers be mounted on them and/or their support structure to capture their dynamic motion during testing. This can help to identify unexpected vibration levels in them and their support structure that can potentially lead to off-axis misalignment issues, which in turn produce unmeasured forces into the test article that will corrupt the test data (i.e., incorrect FRF). It is recommended a mini-modal hammer tap test be performed on the modal shaker setups themselves to provide insights into whether modifications to the modal shaker setups are needed prior to when the modal test begins (e.g., better securing the modal shakers to their support stands, adding a thin foam pad between the shaker and its support stand to increase damping, etc.). Also, for large electrodynamic and hydraulic modal shakers, the shaker attachment hardware needs to be strong enough to withstand the shaker forces while at the same time minimizing off-axis excitation into the test article. The design of the hardware connecting the actuator to the test article can be challenging and requires significant design consideration. Commensurate with this, the test article needs hardpoints at which these high forces can be applied. This may require analyzing the test article to ensure it can either withstand the maximum force the modal shakers can produce or determine the force limits to be set for the modal shakers.

13.7 Hydraulic Multi-Axis Shaker Vibration Test Facilities and Beyond

Civil engineers have used single-axis and multi-axis shaker vibration test facilities utilizing hydraulic shakers to seismically test civil engineering structures for many decades because of the high displacement, velocity, and force requirements [15, 25–28]. Both the European Space Agency (ESA) and NASA have built their own multi-axis shaker vibration test facilities utilizing hydraulic shakers to test large-scale aerospace flight hardware. The European Space Agency (ESA) European Space Research and Technology Center (ESTEC) HYDRA 6-DOF multi-axis hydraulic shaker vibration test facility has eight hydraulic actuators and a custom-built nonlinear shaker controller to significantly reduce the nonlinear distortion [29–36]. The NASA Mechanical Vibration Facility (MVF), which has 16 vertical and 4 horizontal hydraulic actuators, was designed to test NASA Multi-Purpose Crew Vehicle (MPCV) Orion class spacecraft having a total mass of 75,000 lb, center of gravity (cg) height above the MVF Table of 284 in, and a diameter of 18 feet [37–41]. However, as structures become increasingly larger, it simply may not be practical to use either electrodynamic or hydraulic modal shakers due to the high level of the ambient vibration environment and/or due to operational constraints. Civil engineers have turned to using Operational Modal Analysis (OMA), which uses the ambient vibration environment to identify the modal parameters of civil structures [42–54]. Similarly, aerospace engineers have also used OMA to identify the modal parameters of large-scale ground-based structures [55] and of launch vehicles during flight from their flight data [56–58]. For aircraft and spacecraft, their modal parameters have been identified from the analysis of their response to attitude control inputs [59] and for the Hubble Space Telescope from its response to attitude control inputs and jitter [60, 61].

Even if the test engineer will be using electrodynamic or hydraulic modal shakers to excite the test article (i.e., traditional Experimental Modal Analysis), they are encouraged to expand the standard data quality checks performed on recorded ambient data to include OMA techniques. This can provide a quick look at the test article modes and in particular which modes are well excited by the ambient environment and help to determine the minimum modal shaker forces needed to obtain an adequate signal-to-noise ratio.

13.8 Conclusion

Hydraulic modal shakers become more attractive as test articles become dimensionally larger, more complex, and massive in weight, combined with the need to excite them to higher than traditional levels to identify their nonlinear characteristics. Hydraulic modal shakers can generate higher force levels, have longer stroke lengths, and possess higher velocity limits, at lower unit cost with a smaller spatial footprint compared to electrodynamic modal shakers. However, they present some unique challenges, which the test engineer needs to be aware of to successfully utilize them in a modal test. This chapter has covered the basics of electrohydraulic servo valves and hydraulic actuators, what causes the nonlinear distortion in the hydraulic modal shaker force and how it manifests itself in the response of the test article, operational limits that need to be respected, and safety issues and best practices that need to be followed when operating and maintaining a high-pressure hydraulic system. Keeping these things in mind, the test engineer can find hydraulic modal shakers to be a valuable tool in performing high-force large-scale modal tests. However, the test engineer may find that even with hydraulic modal shakers, the test article cannot be sufficiently excited or for large-scale test articles that they "naturally ring" due to the ambient environment. If so, they are encouraged to consider adding Operational Modal Analysis techniques to their tool set.

Acknowledgments The authors would like to thank the NASA Engineering and Safety Center (NESC), NASA Glenn Research Center, and Redstone Test Center for funding this work.

References

1. Ares I-X Press Kit, October 2009. https://www.nasa.gov/pdf/396682main_Ares_I-X-pk.pdf
2. Ares I-X Test Flight, Rock-a-bye Rocket. https://blogs.nasa.gov/Ares_I-X/tag/modal-test/
3. Buehrle, R., Templeton, J., Reaves, M., Horta, L., Gaspar, J., Barolotta, P., Parks, R., Lazor, D.: Ares I-X Flight Test vehicle modal test. NASA/TM-2010-216182, January 2010. https://ntrs.nasa.gov/archive/nasa/ casi.ntrs.nasa.gov/20100003382.pdf
4. Buehrle, R., Templeton, J., Reaves, M., Horta, L., Gaspar, J., Barolotta, P., Parks, R., Lazor, D.: Ares I-X Launch vehicle modal test measurements and data quality assessments. In: Proceedings of the 27th International Modal Analysis Conference (2010)
5. Buehrle, R., Templeton, J., Reaves, M., Horta, L., Gaspar, J., Barolotta, P., Parks, R., Lazor, D.: Ares I-X Launch vehicle modal test measurements and data quality assessments. https://ntrs.nasa.gov/api/citations/20100005180/downloads/ 20100005180.pdf (2010)
6. SLS Fact Sheet. https://www.nasa.gov/exploration/systems/sls/factsheets.html
7. NASA Facts: Space Launch System. https://www.nasa.gov/sites/default/ files/files/SLS-Fact-Sheet_aug2014-finalv3.pdf
8. Mobile Launcher: NASA Fact Sheet. https://www.nasa.gov/sites/default/files/ atoms/files/mobilelauncher_ factsheet_v2.pdf
9. Mobile Launcher Umbilicals and Support: NASA Facts. https://www.nasa.gov/sites/default/files/atoms/files/ml_umbilicals20160523.pdf
10. Stasiunias, E., Parks, R., Brendan, D., Chandler, D.: Modal test of the NASA mobile launcher at Kennedy Space Center. In: Proceedings of the 38th International Modal Analysis Conference (2020)
11. Akers, J., Sills, J.: Space launch system mobile launcher modal pretest analysis. In: Proceedings of the 38th International Modal Analysis Conference (2020)
12. TEAM Corporation: Hydraulic test systems outperform with waveform replication control. http://www.teamcorporation.com/images/curts_papers/38Waveform%20Replication%20for%20Accurate%20Replication.pdf
13. Electrohydraulic Servo Valve: Wikipedia. https://en.wikipedia.org/wiki/Electrohydraulic_servo_valve
14. Linear Variable Differential Transformer: Wikipedia. https://en.wikipedia.org/wiki/Linear_variable_differential_transformer
15. Conte, J. Luco, J.: Shake table control fidelity in signal reproduction & sources of signal distortion. In: Shake Table Training Workshop, San Diego, CA (2010)
16. Team Corporation Fluid Requirements for Team Hydraulic Systems. https://teamcorporation.com/maintenance-and-operational-notes/Hydraulic_Fluid_Requirements_Team_Corporation.pdf
17. Total Harmonic Distortion: Wikipedia. https://en.wikipedia.org/wiki/Total_harmonic_distortion
18. Fitz-Coy, N., Nagabhushan, V., Hale, M.: Benefits and challenges of over-actuated excitation systems. J. Shock Vib. **17**(3), 285–303 (2010)
19. Ayers, P.: NASD Hydraulic Systems Safety, Colorado State University Cooperative Extension, June 27, 2021. https://nasdonline.org/1100/d000891/hydraulic-systems-safety.html
20. Wirsching, P., Paez, T., Ortiz, K.: Random Vibrations: Theory and Practice, pp. 104–141. Dover Publications, New York (1995)
21. Napolitano, K., Yoder, C.: Optimal phasing combinations for multiple input source excitation. In: Proceedings of the 32nd International Modal Analysis Conference (2014)
22. Napolitano, K., Linehan, D.: Multiple sine sweep excitation for ground vibration tests. In: Proceedings of the 27th International Modal Analysis Conference (2009)
23. Lollock, J.: The effect of swept sinusoidal excitation on the response of a single-degree-of-freedom oscillator. In: Proceedings of the 43rd AIAA/ASME/ASCE/AHS/ASC Structures, Structural Dynamics, and Materials Conference (2002)
24. Kabe, A., Sako, B.: Structural Dynamics: Fundamentals and Advanced Applications, vol. I, Section 5.7. Academic Press an imprint of Elsevier (2002)
25. Motamedi, M., Ventura, C.: System identification of a full scale wood frame building specimen subjected to shake table tests. In: Proceedings of the 37th International Modal Analysis Conference (2019)

26. Pacific Earthquake Engineering Research Center, Earthquake Simulator Laboratory, UC Berkley. https://peer.berkeley.edu/uc-berkeley-simulator-laboratory
27. Pacific Earthquake Engineering Research Center, Charles Lee Powell Laboratories, University of California San Diego (UCSD). https://structures.ucsd.edu/facilities/laboratories
28. Rodrigo, A., Hernandez, F., Diaz, P., Gutierrez, G.: System identification of a five-story building using seismic strong-motion data. In: Proceedings of the 37th International Modal Analysis Conference (2019)
29. Valentin, C., Rixed, D., Woerkom, P.: The HYDRA Control Study. http://www.em.tue.nl/pdfs/Valentin_2007.pdf
30. Bruyne, S., Vdn der Auweraer, H., Peeters, B., Anthonis, J., Appolloni, M., Cozzani, A.: Model based control of a multi-axis hydraulic shaker using experimental modal analysis. In: Proceedings of the 16th IFAC Symposium on System Identification, July 2012. https://www.sciencedirect.com/science/article/pii/S1474667015380046
31. ESTEC Test Centre Infrastructure Facility Description. https://emits.sso.esa.int/emits-doc/ESTEC/AO7020_RD2_Infrastructure-315.pdf
32. Brinkmann, P.: HYDRA, a new tool for mechanical testing. https://ntrs.nasa.gov/api/citations/19950007673/downloads/19950007673.pdf (1995)
33. Remedia, M., Aglietti, G., Appolloni, M., Cozzani, A., Kiley, A.: Multi-DOF transient testing validation by means of virtual testing. In: Proceedings of AIAA Sci Tech Forum, January 2018. https://arc.aiaa.org/doi/10.2514/6.2018-1947
34. Aglietti, G., Remedia, M., Apolloni, M., Kiley, A.: Spacecraft structure model validation and test philosophy. AIAA J. **57**(F) (2019) https://arc.aiaa.org/doi/10.2514/1.J057757
35. HYDRA Mulit-axis Shaker. https://www.european-test-services.net/services-mechanical-Hydra-Vibration.html
36. European Space Research and Technology Centre: Wikipedia. https://en.wikipedia.org/wiki/European_Space_Research_and_Technology_Centre
37. Winkel, J., Akers, J., Suarez, V., Staab, L., Napolitano, K.: Modal survey of the MPCV Orion European Service module structural test article using a multi-Axis shake table. In: Proceedings of the 36th International Modal Analysis Conference (2018)
38. Staab, L., Winkel, J., Suárez, J., Jones, T., Napolitano, K.: Fixed base modal testing using the mechanical vibration facility 3-axis base shake system. In: Proceedings of the 34th International Modal Analysis Conference (2016)
39. Space Environments Complex. https://www1.grc.nasa.gov/facilities/sec/
40. Orion Vibe Test at NASA Glenn's Plum Brook Station. https://www.youtube.com/watch?v=SX3P-foK_mw
41. Podcast Episode 39: Plum Brook Station. https://www.youtube.com/watch?v=bw3FXMXgkaI
42. Avci, O., Alkhamis, K., Abdeljaber, O., Hussein, M.: Operational modal analysis and finite element model updating of a 53 story building. In: Proceedings of the 39th International Modal Analysis Conference (2021)
43. Motamedi, M., Ventura, C., Consultores, O.: Ambient vibration tests and modal response analysis of Guayaquil Metropolitan Cathedral in Guayaquil, Ecuador. In: Proceedings of the 38th International Modal Analysis Conference (2020)
44. Daems, P., Peeters, C., Guillaume, P., Helsen, J.: Operational modal analysis of wind turbine drivetrain with focus on damping extraction. In: Proceedings of the 38th International Modal Analysis Conference (2020)
45. Motamedi, M., Ventura, C., Adebar, P., Murugavel, A.: Ambient vibration tests and modal response analysis of an old age high-rise building in downtown Vancouver, Canada. In: Proceedings of the 37th International Modal Analysis Conference (2019)
46. Chauhan, S.: Fundamentals of operational modal analysis. In: Proceedings of the 35th International Modal Analysis Conference (2017)
47. Li, X., Ventura, C., Feng, Y., Pan, Y., Kaya, Y., Xiong, H., Zhang, F., Cao, J., Zhou, M.: Ambient vibration testing of two highly irregular tall buildings in Shanghai. In: Proceedings of the 34th International Modal Analysis Conference (2016)
48. Batel, M.: Operational modal analysis – another way of doing modal testing. Sound and Vibration Magazine, August 2002. http://sandv.com/downloads/0208batl.pdf
49. Sarlo, R., Tarazaga, P.: Modal parameter uncertainty estimates as a tool for automated operational modal analysis: applications to a smart building. In: Proceedings of the 36th International Modal Analysis Conference (2018)
50. Christensen, S., Andersen, M., Brandt, A.: Dynamic characterization of the little belt suspension bridge by operational modal analysis. In: Proceedings of the 36th International Modal Analysis Conference (2018)
51. Niu, Y., Kraemer, P., Fritzen, C.: Operational modal analysis for the Guangzhou New TV Tower. In: Proceedings of the 29th International Modal Analysis Conference (2011)
52. Chauhan, S., Tcherniak, D., Basurko, J., Salgado, O., Urresti, I., Cargangiu, C., Rossetti, M.: Operational modal analysis of operating wind turbines: application to measured data. In: Proceedings of the 29th International Modal Analysis Conference (2011)
53. Ozbek, M., Rixed, D.: Optical measurements and operational modal analysis on a large wind turbine: lessons learned. In: Proceedings of the 29th International Modal Analysis Conference (2011)
54. Brinker, R., Ventura, C.: Introduction to Operational Modal Analysis. Wiley, New York (2015)
55. Akers, J., Sills, J.: Operational modal analysis of the space launch system mobile launcher on the Crawler Transporter ISVV-010 rollout. In: Proceedings of the 39th International Modal Analysis Conference (2021)
56. James, G., Kaouk, M., Cao, T.: Progress in operational analysis of launch vehicles in nonstationary flight. In: Proceedings of the 31st International Modal Analysis Conference (2013)
57. James, G., Kaouk, M., Cao, T., Fogt, V., Rocha, R., Schultz, K., Tucker, J., Rayos, E., Bell, J., Alldredge, D., Howsman, T.: Operational analysis in the launch environment. In: Proceedings of the 30th International Modal Analysis Conference (2012)
58. Bartkowicz, T., George, J.: Ares I-X In-Flight Modal Identification. In: Proceedings of the 52nd AIAA/ASME/ASCE/AHS/ASC Structures, Structural Dynamics, and Materials Conference (2010)
59. Pickrel, C., White, P.: Flight flutter testing of transport aircraft: in-flight modal analysis. In: Proceedings of the 21st International Modal Analysis Conference (2003)
60. Sills, J.: Spacecraft system identification using science instrument optical jitter measurements. In: Proceedings of the 13th International Modal Analysis Conference (1995)
61. Blair, M., Sills, J.: Hubble space telescope on-orbit system identification. In: Proceedings of the 12th International Modal Analysis Conference (1994)

Chapter 14
Damage and Loose Rivet Detection on an Airbus A320 Panel Using Non-contact Measurement Techniques

André Tavares, Davide Mastrodicasa, Giancarlo Kosova, Emilio Di Lorenzo, and Bart Peeters

Abstract Efficient and reliable detection of damages is of critical importance in the aerospace industry. Within the context of non-destructive testing (NDT), advanced non-contact measurement techniques can be leveraged to obtain full-field responses of a target structure, facilitating the development of structural health monitoring (SHM) methodologies. The motivation of this chapter is to compare several types of measurement techniques, excitation signals, and post-processing methods applied to an Airbus airplane panel with sections of damaged and loose rivets. Its response is obtained using both digital image correlation (DIC) and laser Doppler vibrometry (LDV) techniques. The panel is excited with modal shakers or PZT patches using chirp or pseudorandom signals, for different frequency ranges. Full-field measurements were obtained, along with other more localized measurements on the area containing defects. On a later stage, methodologies inspired on nonlinear analysis and machine learning (ML) techniques were applied for damage detection. A description of the obtained results from these different experimental settings is shown in this chapter, together with a successful structural characterization and detection of damages on the airplane panel.

Keywords Digital image correlation (DIC) · Laser doppler vibrometry (LDV) · Non-destructive testing (NDT) · Nonlinear analysis · Machine learning (ML)

14.1 Introduction

The aeronautical industry grows early with the increase of global population able to afford travelling by air. In 2019, the world fleet was estimated to be consistent of 28 thousand aircraft, and this number is expected to rise up to 40 thousand by 2029 [1]. With the expansion of business in commercial aviation, there is an expansion of the maintenance, repair, and overhaul (MRO) market, which represented ten percent of the total airline operational costs in 2019, in an estimated overall of $82 billion [2]. With this increase, derive new challenges and research for innovative techniques to perform maintenance and damage detection.

A. Tavares (✉)
Siemens Industry Software NV, Leuven, Belgium

KU Leuven, Department of Mechanical Engineering, Leuven, Belgium
e-mail: tavares.andre@siemens.com

D. Mastrodicasa
Siemens Industry Software NV, Leuven, Belgium

Department of Mechanical Engineering, Vrije Universiteit Brussel, Brussels, Belgium
e-mail: davide.mastrodicasa@siemens.com

G. Kosova
Siemens Industry Software NV, Leuven, Belgium

Aerospace and Mechanical Engineering Department, University of Liège, Liège, Belgium
e-mail: giancarlo.kosova@siemens.com

E. Di Lorenzo · B. Peeters
Siemens Industry Software NV, Leuven, Belgium
e-mail: emilio.dilorenzo@siemens.com; bart.peeters@siemens.com

C. Walber et al. (eds.), *Sensors and Instrumentation, Aircraft/Aerospace and Dynamic Environments Testing, Volume 7*,
Conference Proceedings of the Society for Experimental Mechanics Series, https://doi.org/10.1007/978-3-031-05415-0_14

In this context, innovative non-destructive testing (NDT) techniques are paving the way for the creation of such innovative methodologies, with advanced measurement techniques such as digital image correlation (DIC) and laser Doppler vibrometry (LDV). DIC is a non-contact full-field image analysis technique that allows to retrieve strains and displacements in three dimensions at the surface of any type of material and under arbitrary loading. It has received special attention in the structural dynamics field since it can obtain full-field measurements with dense grids of points [3]. For similar reasons, LDV has gained popularity as a non-contact full-field technique relying on the Doppler shift effect of the laser beam, to obtain vibration measurements.

Structural damage induces nonlinear behavior, which can be effectively captured with methods of nonlinear system identification and machine learning (ML), therefore making them suitable techniques for a monitoring context. Assuming that a damage could be a source of nonlinear behavior [4], methods for nonlinearity detection and location identification could be applied for damage detection. In particular, exciting a structure with a pseudorandom excitation with several periods and realizations, the uncorrelated nonlinear response and the uncorrelated noise can be estimated [5]. Two approaches can be used. One is based on the study of the harmonics in the uncorrelated nonlinear response. The other uses the frequency-averaged ratio between nonlinear and total responses, which means one value for each analyzed point. The second approach is better suited for an analysis with a large number of measurement points and high-frequency ratio, so it is the one used in this chapter. ML in its turn makes use of advanced computational algorithms to capture nonlinear behavior. These can be combined with feature engineering techniques or used in end-to-end approaches (more commonly within a deep learning (DL) context), to build automated damage detection methodologies [6].

In this chapter, both DIC and LDV full-field measurements were performed to a fuselage panel of an A320 Airbus aircraft. These measurements focused both on the study of the full panel's structural characterization with modal analysis and on the study of a localized area containing rivets, with the purpose of detecting loose and damaged ones. Both nonlinear analysis and ML techniques were employed for this purpose.

14.2 Experimental Setup

This chapter focuses on studying a fuselage panel from an Airbus A320, made from aluminum (AL 2024-T3) and coated with a primer aircraft paint. As shown in Fig. 14.1a, this panel contains a service door mounted that gives access to an underlying pressure release valve, used during daily maintenance of the aircraft. This door has a supporting frame fixed with countersunk rivets to the panel. Some of these rivets were manually damaged to simulate a possible damage scenario on such an aircraft panel, as can be seen in Fig. 14.1b, which shows the corresponding back section of the panel. One of the center rivets of this section was damaged to a point of not being fully elastically connected to the structure, in order to simulate a loose rivet scenario.

Fig. 14.1 Test specimen. (**a**) Fuselage panel from Airbus A320 aircraft. The section of damaged rivets is highlighted in a red rectangle. (**b**) Section of rivets as seen from the back of the panel

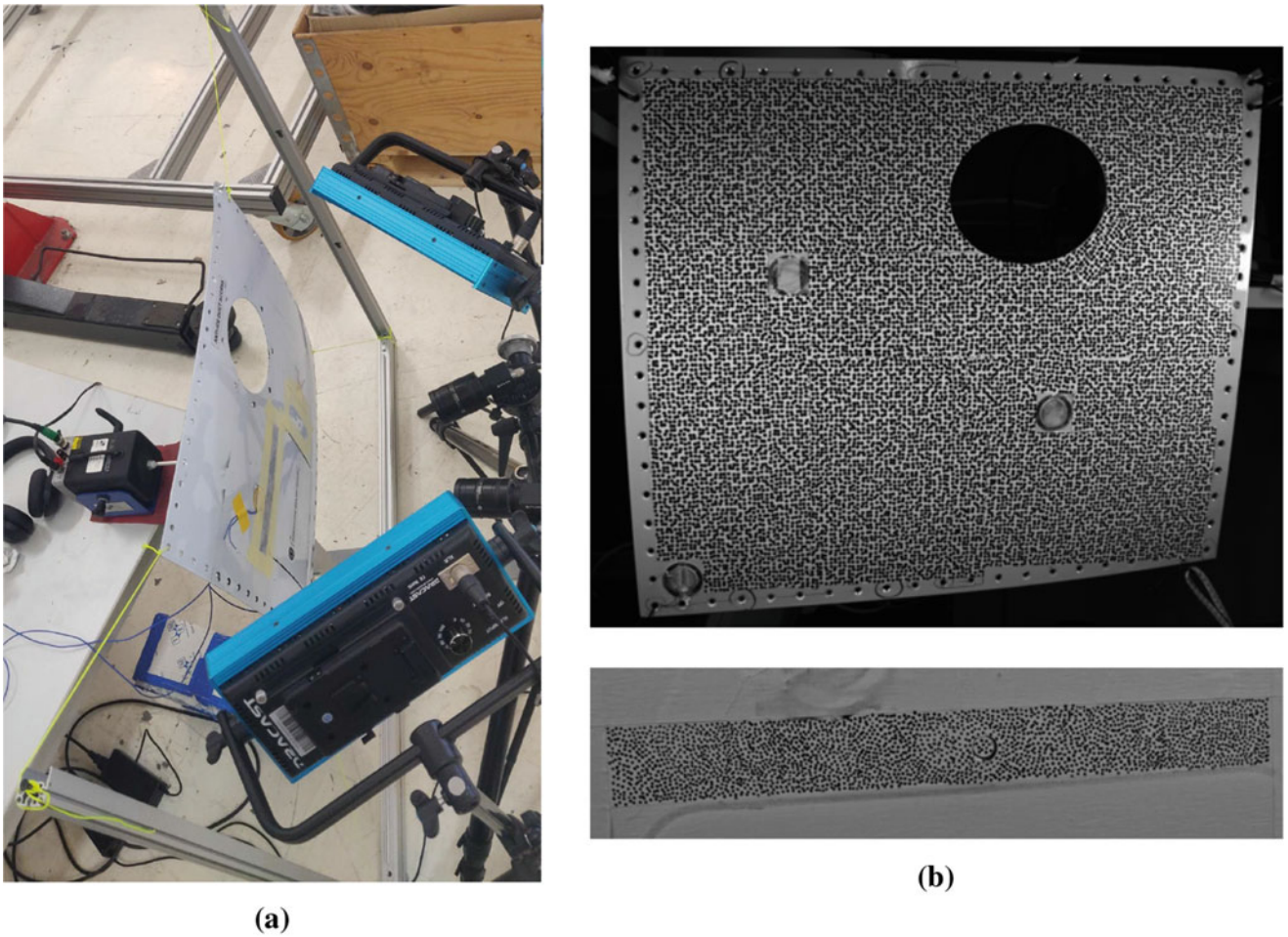

Fig. 14.2 DIC experimental setup and speckle pattern. (**a**) DIC experimental setup. (**b**) Speckled structure

14.2.1 Digital Image Correlation (DIC) Setup

The idea behind this measurement campaign is to investigate the capability of using DIC for a full-field modal parameter estimation and damage detection by using a smart aliasing technique that allows to use low-speed camera for characterizing structural high-frequency behavior. The experimental setup, before the application of the speckle pattern, is shown in Fig. 14.2. The fuselage panel was suspended on a frame by using soft bungees in order to simulate free–free boundary conditions, and a modal shaker placed on the back of the structure was used for inducing the excitation. The first measurement campaign was conducted for estimating the whole structural behavior by exciting the test bed with a pseudorandom, in the bandwidth 10–400 Hz. Using a reconstruction method, it was possible to use cameras at slow speed, 50 Hz, to reconstruct a high sampled signal, 800 Hz. This was possible by sending to the structure a periodic excitation signal, a pseudorandom in this case, and acquiring pictures at different timesteps during the different periods. In this way, it is possible to reconstruct the excitation signal using a camera sampling frequency minor with respect to the maximum excitation frequency. This method was used for reconstructing 2 periods of 2.56 s for a total amount of 4096 pictures.

The second measurement campaign was conducted for investigating the capabilities of using DIC for damage detection. Therefore, a smaller field of view (FOV), focusing on the loose rivets area, was studied. In order to excite the local defect resonances, a higher excitation bandwidth was used by sending to the shaker a pseudorandom signal in the range 800–1600 Hz. In the same way, the smart aliasing method was used. 5 periods of 1.28 s were reconstructed for a total amount of 20,480 pictures.

Fig. 14.3 LDV experimental setup

14.2.2 Laser Doppler Vibrometer (LDV) Setup

The second experimental setup used in this chapter involved using an Optomet SWIR Laser Doppler Vibrometer (LDV), as shown in Fig. 14.3. It is a contactless measurement technique based on the Doppler effect associated with the scattering of a laser beam after reflecting on a vibrating surface. Compared to more traditional measurement instruments, such as strain gauges and accelerometers, the LDV provides a fast and straightforward solution to measure velocity (or displacement and acceleration), without the need to mass load the test specimen. The panel was excited with a piezoelectric (PZT) patch, which was attached on the top surface (as seen in Fig. 14.1a). Two ways of providing the excitation were tried, one through a Siemens SCADAS system, and the other through the signal generator within the Optomet LDV. The signal itself was amplified 50 times using the amplifier Falco Systems WMA-300. Two different excitation signals were tried, pseudorandom up to 20 kHz and chirp signal up to 80 kHz (measurements with the pseudorandom signal were not made up to higher frequencies, due to practical issues related with the test setup). The purpose of measuring high frequencies lies in capturing localized resonant damage behavior, as stated by the local defect resonance concept [4].

14.3 Results

14.3.1 DIC Full-Field Modal Analysis and Damage Detection

The specifications of the cameras and the DIC processing parameters are shown in Table 14.1 together with the geometry, Fig. 14.4, extracted directly from the camera pictures. One accelerometer in the driving point location was also used to obtain a reference result to compare with the DIC estimated modal parameters. The estimated modal parameters, together with some of the DIC mode shapes, are shown in Table 14.2 and Fig. 14.5.

15 natural frequencies and mode shapes were identified in the bandwidth of interest. It was possible to find a good correlation between the accelerometer and DIC results both in terms of natural frequencies and modal damping. Only the 7th mode was not identified by using the accelerometer. This is probably due to the sensor being placed on a nodal point for that mode shape.

Table 14.1 DIC parameters

Parameters	Value
Focal length	12.5 mm
Max fps full resolution	75 fps
Resolution	2448(H) × 2048(V) px
Subset	29
Step	22
Interpolation	Bicubic splines
Shape function	Quadratic

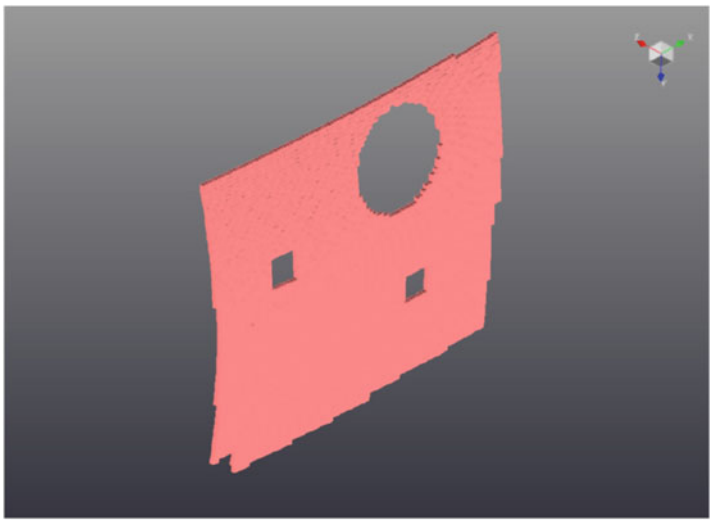

Fig. 14.4 Fuselage panel geometry

Table 14.2 Modal parameters' comparison

	DIC		Accelerometers	
Mode	f_n (Hz)	ζ_n (%)	f_n (Hz)	ζ_n (%)
1	22.80	2.95	22.71	2.50
2	29.51	5.32	29.50	3.59
3	36.78	1.19	36.84	1.11
4	61.08	1.58	60.83	3.40
5	72.22	2.41	72.21	2.16
6	82.54	0.68	81.43	1.46
7	86.37	1.17	–	–
8	117.58	0.98	117.27	1.15
9	126.05	1.86	126.05	1.82
10	183.48	0.88	182.83	1.10
11	246.62	0.81	246.29	1.08
12	274.52	0.74	274.21	0.73
13	288.77	0.63	291.76	0.72
14	331.01	0.36	331.09	0.90
15	392.43	0.18	392.26	0.43

As expected, due to the huge FOV and therefore the high DIC noise floor, it was not possible to identify any loose rivet on the structure working directly on the whole structure's mode shapes. Therefore, as already mentioned in Sect. 14.2.1, the FOV was reduced by just taking into consideration the damaged rivet's area. This gave us the possibility to reduce the DIC noise floor and therefore to go higher in the frequency domain in order to excite some local defect resonances.

Figure 14.6 shows an example of such a mode shape where it is clearly distinguishable localized high vibration amplitude of the damaged loose rivet.

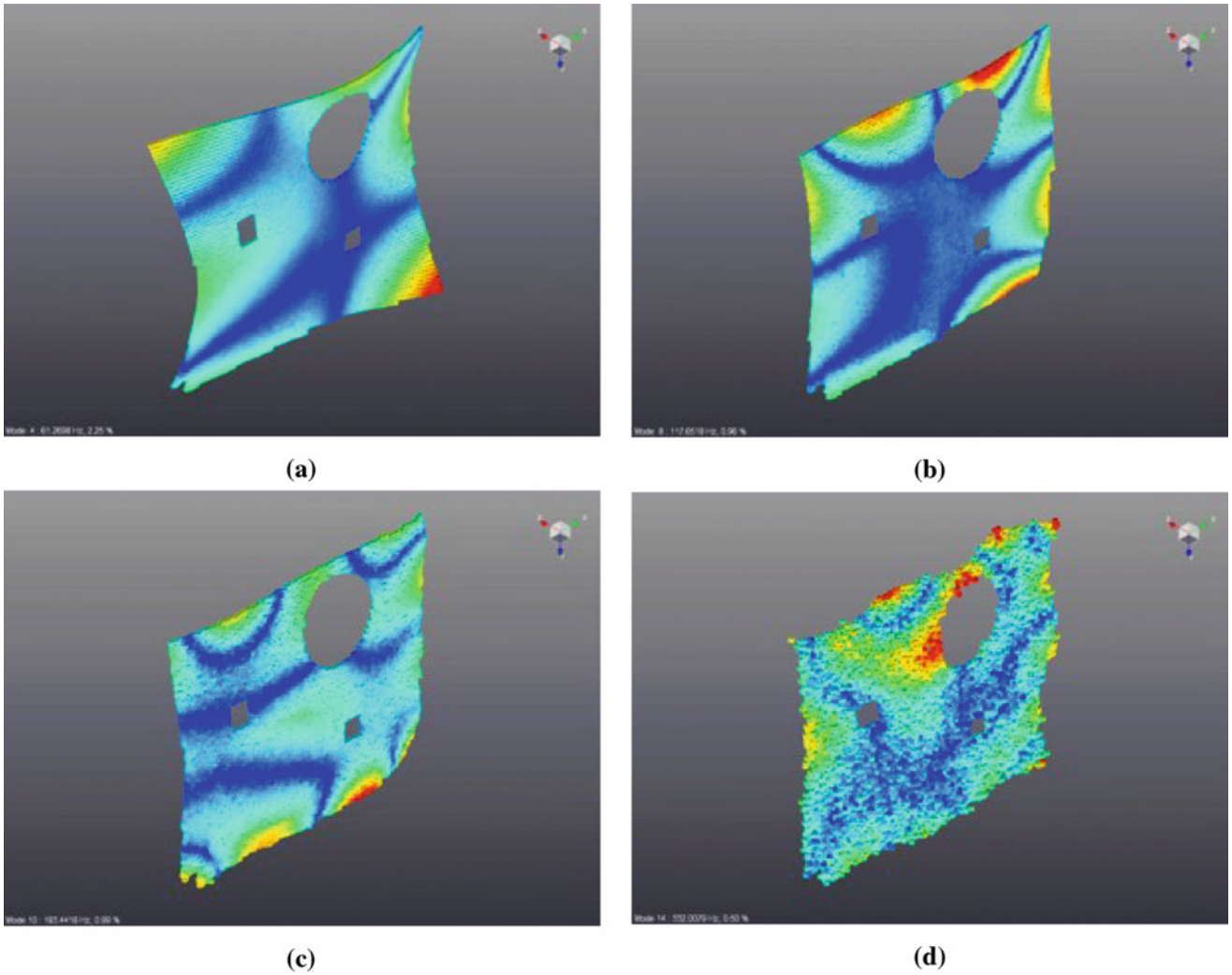

Fig. 14.5 DIC mode shapes. (**a**) 4th DIC mode shape. (**b**) 8th DIC mode shape. (**c**) 10th DIC mode shape. (**d**) 14th DIC mode shape

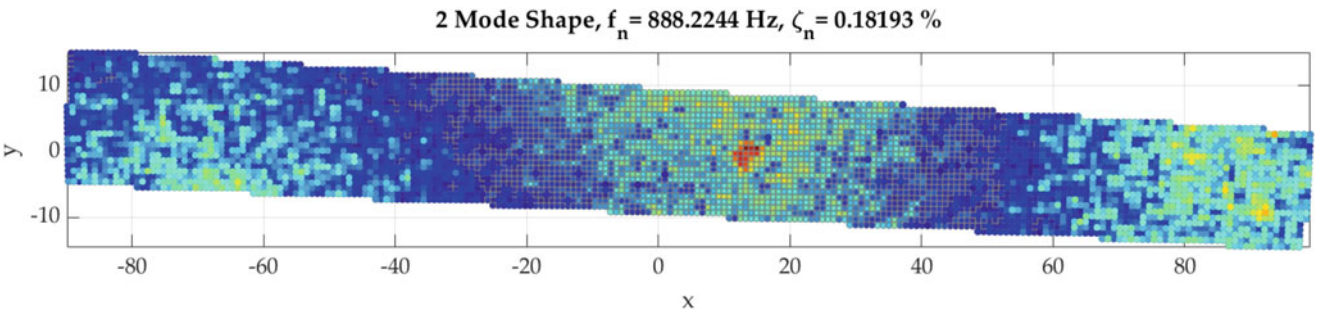

Fig. 14.6 Mode shape with highlighted defect

14.3.2 Damage Detection with Nonlinear Analysis

The panel is excited with a pseudorandom excitation with 3 periods and 5 realizations up to a frequency of about 20 kHz that is 40% of the sampling frequency. It is assumed that this frequency is high enough to detect nonlinear phenomena due to damages or loose rivets. The uncorrelated nonlinear response is estimated. Then, the mean value over the frequency band of excitation of the relative autopower spectrum (RAS) is calculated as

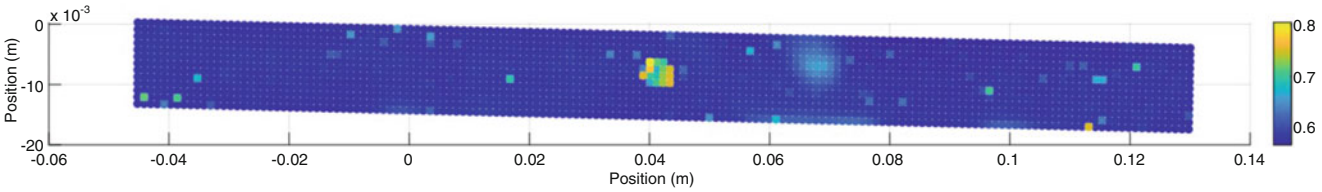

Fig. 14.7 $\overline{RAS}$ of the riveted area

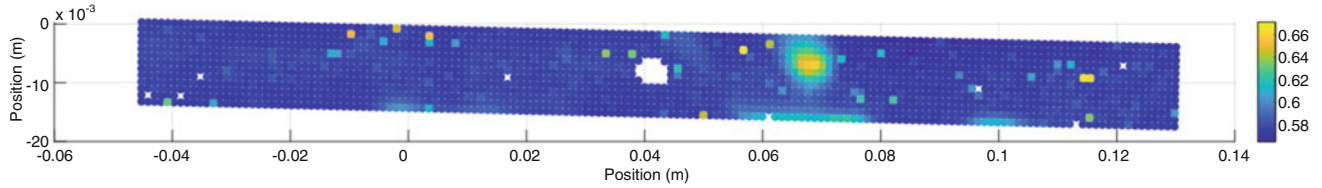

Fig. 14.8 $\overline{RAS}$ of the riveted area, removing central rivet and outlier points

$$\overline{RAS}_i = \frac{\overline{X}_{u_i}}{\overline{X}_i} \quad \in [0, 1], \tag{14.1}$$

where the symbol $\overline{}$ stands for the mean of the spectrum over the excitation bandwidth, X_u is the uncorrelated nonlinear response, X is the total response, and the subscript i stands for the i-th point of measurement. $\overline{RAS}_i$ has a value closer to 1 when the nonlinear contribution is stronger. A damaged location is identified if this quantity is higher for a certain location with respect to the surrounding area.

The results of the calculation of the $\overline{RAS}$ for the riveted area in the back of the panel (Fig. 14.1) are shown in Fig. 14.7. The central loose rivet, at the position of 0.04 m, is clearly detected. Removing the central loose rivet points from the graph in Fig. 14.7, together with the so-called outlier points, the graph in Fig. 14.8 is obtained, where the colorscale is consequentially updated. The outliers are points where the measurement has high noise level due to light reflections. An option to reduce this undesired phenomenon is present in the Optomet software but not activated here due to setup incompatibilities. In Fig. 14.8, the area at around 0.07 m is more clearly detected. It is most likely an area of debonding between the external panel and the internal fitting of the pressure relief door (Fig. 14.1a). Finally, a couple of points at around 0.18 m are detected, probably in correspondence of another loose rivet. It should be specified that the loose rivets are detected as noise-dominated points, while the area of debonding is detected as a nonlinearity dominated.

14.3.3 Damage Detection with ML Techniques

The use of ML techniques was also leveraged to perform damage detection on the aircraft panel. Among the different techniques presented in [6], the Gaussian Anomaly Detection Automated by Clustering (GADAC) technique was selected for this analysis since it was shown to provide good results and be of easy application, being an unsupervised learning technique. GADAC is a combination of the K-means clustering algorithm with the Anomaly Detection algorithm based on the Multivariate Gaussian Distribution. It focuses on clustering the highest amplitudes in mode shapes and detecting points whose amplitudes fall of a Multivariate Gaussian Distribution, labeling them as defects. The more interested reader is referenced to find a more detailed description in [6].

GADAC can be applied both to the mode shapes and the second derivatives of the mode shapes from the structure. The mode shapes themselves were obtained through modal analysis performed with the PolyMAX modal parameter estimator [7]. The selection of modes was done automatically with the DBSCAN automated modal parameter selection technique presented in [8]. The fact that the measurement is done until high frequencies helps to get mode shapes dominated by localized resonant defect vibration. In its turn, the second derivative helps to highlight the presence of a defect in a mode shape. Figure 14.9 shows the difference between a mode shape and its second derivative, and as can be seen, whereas the former contains generalized panel displacement motion, the latter contains higher amplitudes located in the area of a defected rivet.

Fig. 14.9 Absolute magnitude of (**a**) high-frequency mode shape and (**b**) the corresponding second derivative

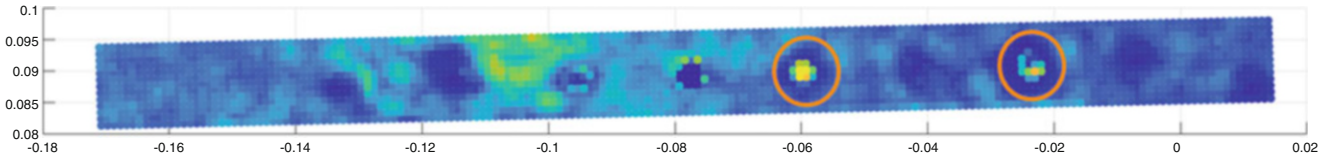

Fig. 14.10 Results obtained with the GADAC technique for the mode shapes (detected damaged rivets localized with orange circles)

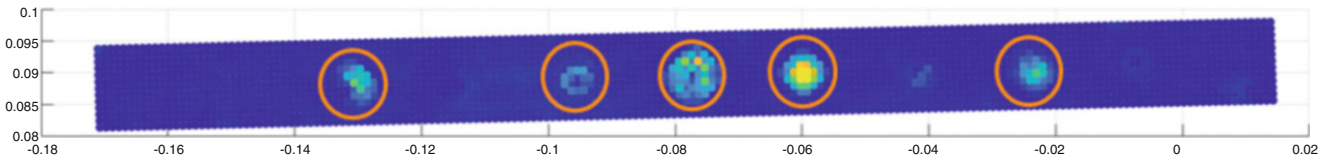

Fig. 14.11 Results obtained with the GADAC technique for the mode shapes (detected damaged rivets localized with orange circles)

Figures 14.10 and 14.11 show the results obtained with this technique both for the analysis of the mode shapes and their second derivatives. The ones for the second derivatives look somewhat more clear and achieve the detection of more damaged rivets than the results for the mode shapes, which follows on the premise that second derivatives highlight the presence of a defect in a mode shape. The regions of high detectability are highlighted in an orange circle, which correspond to the locations of the identified damaged rivets on the panel. In the results for the mode shapes, the loose rivet area achieved little detectability since this rivet is not moving fully elastically connected to the structure, meaning that no displacement was registered for that area in a major part of the mode shapes. For the second derivatives instead, the algorithm managed to obtain some detectability for the loose rivet.

14.4 Conclusions

Both DIC and LDV measurements allowed to study the aircraft fuselage panel's structural behavior. The first DIC measurement campaign allowed to obtain a high correlation between DIC and accelerometers' estimated modal parameters. The second one gave us a first indication of the capabilities of DIC for damage detection. High-potential raw results are shown directly on the mode shapes. However, more advanced damage detection techniques will be investigated in the next future to improve the obtained results.

Considering the LDV measurements, the damage detection with nonlinear and ML techniques shows qualitatively similar results. The ML is, however, more sensible to detect most of the areas of damage. On the other hand, different settings were used for the two approaches. In particular, for the ML-based detection, a higher-frequency range was excited and observed. Moreover, the option for limiting the number of outlier points was also used. Finally, it must be said that the measurement for nonlinear detection was about 3 times longer than the ML one, due to the need to measure different periods and realizations of a pseudorandom excitation. Future works aim at making a one-to-one comparison for evaluating the sensibility of the two methods.

Acknowledgments The authors gratefully acknowledge SIM (Strategic Initiative Materials in Flanders) and VLAIO (Flemish Government Agency Flanders Innovation & Entrepreneurship) for their support of the ICON project DETECT-ION, which is part of the research program MacroModelMat (M3), coordinated by Siemens (Siemens Digital Industries Software, Belgium). André Tavares is supported by a VLAIO Baekeland PhD mandate [nr. HBC.2020.2300]. Davide Mastrodicasa is supported by a VLAIO Baekeland PhD mandate [nr. HBC.2019.2595]. Giancarlo Kosova is a fellow of the DyVirt project (Marie Skłodowska-Curie grant agreement No 764547) funded by European Union's Horizon 2020 research and innovation program. Brussels Airlines is also acknowledged for providing the specimen under test.

References

1. Cooper, T., Smiley, J., Porter, C., Precourt, C.: Global fleet & MRO market forecast commentary. Oliver Wyman (2018).
2. IATA: Airline maintenance cost executive commentary. An Exclusive Benchmark Analysis (FY2019 Data) by IATA's Maintenance Cost Technical Group (2019)
3. Di Lorenzo, E., Mastrodicasa, D., Wittevrongel, L., Lava, P., Peeters, B.: Full-field modal analysis by using digital image correlation technique. In: Rotating Machinery, Optical Methods & Scanning LDV Methods, vol. 6, pp. 119–130. Springer, Berlin (2020)
4. Solodov, I.: Local defect resonance (LDR): A route to highly efficient thermosonic and nonlinear ultrasonic NDT. In: AIP Conference Proceedings, vol. 1581, pp. 1663–1670. American Institute of Physics, College Park (2014)
5. Kosova, G., Lorenzo, E.D., Peeters, B., Kerschen, G.: Nonparametric localization of structural nonlinearities from input-output data. In: Proceedings of the 38th International Modal Analysis Conference (IMAC), Houston, TX (2020)
6. Tavares, A., Di Lorenzo, E., Peeters, B., Coppotelli, G., Silvestre, N.: Damage detection in lightweight structures using artificial intelligence techniques. Exper. Techniq. **45**(3), 389–410 (2021)
7. Peeters, B., Van der Auweraer, H., Guillaume, P., Leuridan, J.: The PolyMAX frequency-domain method: a new standard for modal parameter estimation? Shock Vibr. **11**(3), 4, 395–409 (2004)
8. Tavares, A., Di Lorenzo, E., Cornelis, B., Peeters, B., Gryllias, K., Desmet, W.: Automated damage localization for lightweight plates. In: Accepted for the Structure Health Monitoring of Intelligent Infrastructure 10th Conference (SHMII-10), Porto, Portugal (2021)

Chapter 15
Localisation of Sonic Sources on a Contemporary Violin Made on a Guarneri del Gesù Model

Elvio Bonisoli, Marco Casazza, Domenico Lisitano, Stefano Averame, Marco Carlo Masoero, and Louena Shtrepi

Abstract Violins are probably known among the most technically complex musical instruments. Their dynamics is usually studied through structural vibration methods. However, these methods present a few limitations. Therefore, this chapter focuses on the qualitative identification of violin sonic areas generating different musical notes. For such a purpose, a recently introduced tool by Siemens, the Simcenter Sound Camera, which is an array-based sound source localisation technique, was implemented. A contemporary violin, based on a Guarneri del Gesù model, was used as a test instrument. Stationary excitation was induced by an expert violin player to generate different notes. The locations of the sound sources were identified for several configurations and frequency bandwidths, inside an anechoic chamber, i.e. open-field conditions. The identified areas were qualitatively compared with the analysis of vibrations in global and local modes. The comparison confirmed the strong importance of "f" holes and lungs of the instrument, which were clearly identified as the main sound sources and signature vibration modes of the violin.

Keywords Simcenter Sound Camera · Global-local modes · f-holes · Vibro-acoustics · Modal analysis

15.1 Introduction

Violins are fascinating musical instruments, with a very complex and historically based building method. The building process has been optimised along nearly four centuries by experience, handed down by violin-makers from generation to generation. This learning-by-doing process supported violin-makers in gaining the practical expertise to optimise the perceived quality of generated sound and to identify the most relevant constructive variables on sound quality.

In [1], a previous study performed a complete experimental modal analysis (EMA) on a contemporary violin, made in 2011 by the Italian violin-maker Enzo Cena on the basis of a Guarnieri del Gesù model, to study the influence of the soundpost position on the structural behaviour, natural frequencies, mode shapes and damping ratio. The violin showed local modes of localised portion of the violin structure and global mode of the top or bottom plates and f-holes which are responsible for sound emission characteristics. The soundpost position, on the basis of the violin model and sound quality perception, is defined, having a variability range of a few centimetres, to subjectively optimise the violin sound. However, previous tests and EMA assessed that the subjectively selected optimal soundpost position is the position which minimises the damping ratio of the global modes, meaning that, under such configuration, the energy loss by the structure is minimised.

The classical EMA requires the use of accelerometers to measure the system responses. Ideally, the accelerometers should be located in the points with higher response amplitude. However, the violin is a light system, about 330 g, while six (mono- and tri-axial) accelerometers were used in [1], weighing in total about 380 g. The added mass is not negligible and, being placed in the location with higher motion, substantially modifies the violin dynamics, even if changes are not easy to quantify experimentally. Thus, alternative methods should be found to assess violin vibration modes in a non-contact manner.

E. Bonisoli (✉) · D. Lisitano · S. Averame
Politecnico di Torino, Department of Mechanical and Aerospace Engineering, Torino, Italy
e-mail: elvio.bonisoli@polito.it

M. Casazza
University of Salerno, Department of Medicine, Surgery and Dentistry "Scuola Medica Salernitana", Baronissi, Italy

M. C. Masoero · L. Shtrepi
Politecnico di Torino, Department of Energy "Galileo Ferraris", Torino, Italy

C. Walber et al. (eds.), *Sensors and Instrumentation, Aircraft/Aerospace and Dynamic Environments Testing, Volume 7*,
Conference Proceedings of the Society for Experimental Mechanics Series, https://doi.org/10.1007/978-3-031-05415-0_15

For this reason, the study evaluates an alternative method with respect to laser vibrometry [2]. In particular, since the sound emission is related to the global motion of the violin, the idea behind this work is to study the structural dynamics of the violin based on the emitted sound. This work initially proves that sound emissions of different fundamental frequencies are concentrated in different locations of the violin. Then, the study proves that strict correlation exists between the experimental mode shapes, identified from both modal analysis and the sound source localisation methods.

This chapter is structured as follows: the sound source localisation methodologies are briefly summarised in Sect. 15.2, and the experimental setup and performed acquisition are described in Sect. 15.3. Results of the sound source localisation and acoustically identified modes shapes are presented in Sect. 15.4.

15.2 Sound Source Localisation Methods

In literature different techniques involving microphones are described. In particular, nearfield acoustic holography is one of the oldest known microphone-array-based methods for sound source localisation. It can still be considered as the reference for an industrialised case, being available now for more than 30 years [3]. This approach requires a rectangular microphone array where all microphones are equally spaced. It still has the best spatial resolution known today, which is the ability to separate two closely spaced sound sources. The frequency range of this technique is bounded on the lower end by the size of the array and on the upper end again by the spacing between the microphones.

Simcenter Sound Camera involves Bayesian focusing as an innovative microphone array method for sound source localisation. It outperforms traditional methods both in sound source localisation and quantification. It covers the full frequency range and allows a wider distance to the source compared to traditional methods. It works both for correlated and uncorrelated sources, contrary to other wide-band methods. A complete review of acoustic beamforming that is focused on the interesting performance for noise source localisation is presented in [4]. This technology is implemented with the aim of measuring the qualitative violin sonic areas generating different musical notes.

15.3 Experimental Setup

The experimental acquisition is performed in the Anechoic Chamber of the Department of Energy “Galileo Ferraris” of Politecnico di Torino. The anechoic chamber has a size of $8.0 \times 6.4 \times 5.2$ m. The A-weighted equivalent background noise level is about 24.5 dB, and the mid-frequency reverberation time (from 0.5 to 2 kHz) is 0.11 s.

The test setup is shown in Fig. 15.1. One of the authors, being an expert violinist, was involved in playing the violin during the acquisition. The violin behaviour was acquired using the Simcenter Sound Camera. The system consists of an array of microphones, in the configuration adopted for this chapter, shown in Fig. 15.1. In particular, 81 digital microphones are distributed over 9 arms, with a total diameter of 60 cm. This configuration is optimal for all-around, near field and far field application, with a distance between the instrument and the measured object being less than 1 m.

The acquisitions were performed playing the violin in front of the Simcenter Sound Camera. A single note was excited with the bow in as much as possible stationary matter. Four different notes are played: G, D, A and E, having their fundamental frequencies at 196 Hz, 298 Hz, 440 Hz and 660 Hz, respectively. The frequencies are related to the strings’ vibration frequency, which excites the violin structure. The acquisitions were performed twice, showing both the front and the back table of the violin to the Simcenter Sound Camera.

The acquisitions were processed with the Simcenter Sound Camera software, which automatically uses the best sound localisation methodology based on the distance measured in real time by its IR sensors.

15.4 Sound Source Localisation

This work focuses on understanding which are the sources of sound on the violin and to verify the assumption that structural vibrational mode shapes are the sonic modes.

Exciting the violin by bowing a string in stationary condition means to excite the structure with a specific frequency, i.e. the characteristic natural frequency of the excited cord. In a perfectly stationary condition, the violin will respond at the same frequency of the excitation.

Fig. 15.1 Experimental setup (left) and acquisition system (right)

However, since the strings possess several harmonics of different fundamental excitation frequencies, the violin will respond with all the string harmonics. Among the frequencies of response, there will be a frequency close to the violin structural natural frequencies. Hence, the violin will vibrate with the corresponding mode shape. Consequently, in our hypotheses, it should be possible to catch the vibration mode shape based on the sound localisation holograms.

15.4.1 Localisation of Sound Sources

The first aim of this work is the localisation of sound sources of the violin. The results for each response peak of the spectrogram at each excitation are shown in Figs. 15.2, 15.3, 15.4, and 15.5. The results of the back plate are not reported, because the sound source localisation method did not prove to be effective enough, due to the reflection of the major contribution of the front plate sound wave in the violinist body, which makes the localisation difficult.

The sound localisation was not too much precise at lower frequencies, because a larger acquisition diameter would be required for a more accurate localisation. However, the resolution in the sound source localisation was quite accurate for frequencies higher than 500 Hz.

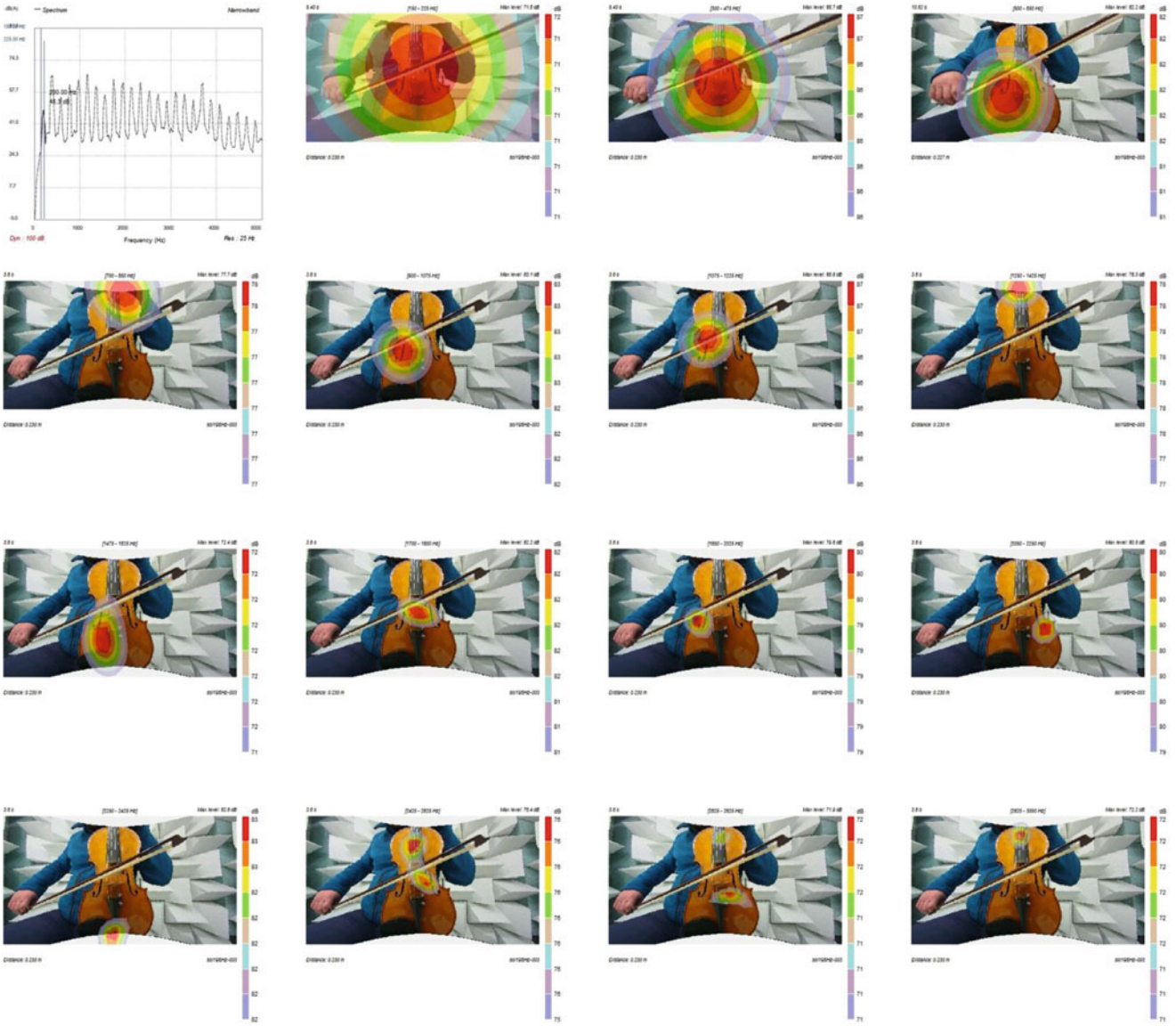

Fig. 15.2 Excitation with G, 196 Hz, response spectrogram and sound source localisation in the frequency range 0÷3000 Hz

Analysing all the acoustic spectrum peaks for the different excitation frequencies, some common sound sources were identified, in correspondence to the two f-holes located in the upper plate, to the two top plate lungs and the bridge.

15.4.2 Structural Mode Shape Qualitative Analysis

In this section, the sound source localisation tools were tested to identify qualitatively the structural mode shapes. The processing was performed with a higher dynamic range, which implies a less accurate localisation, but a larger sound emission. This setting corresponds to a more extended sound localisation map.

The global modes experimentally identified in [1] were all above ~600 Hz. Unfortunately, the sound source localisation is not good at such a low frequency, as shown before. Therefore, the multiple harmonics of the global mode were identified through the Simcenter Sound Camera results.

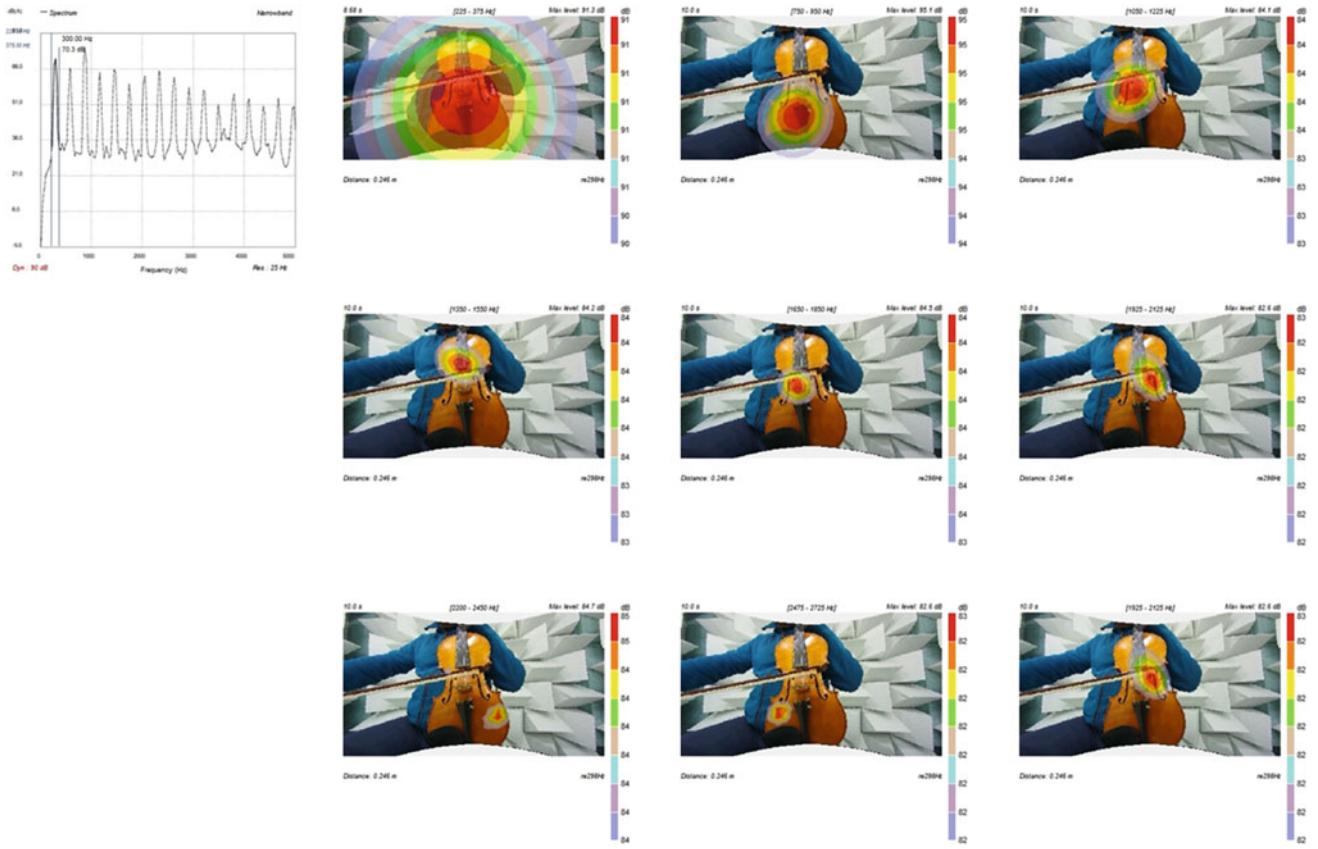

Fig. 15.3 Excitation with D, 298 Hz, response spectrogram and sound source localisation in the frequency range 0÷3000 Hz

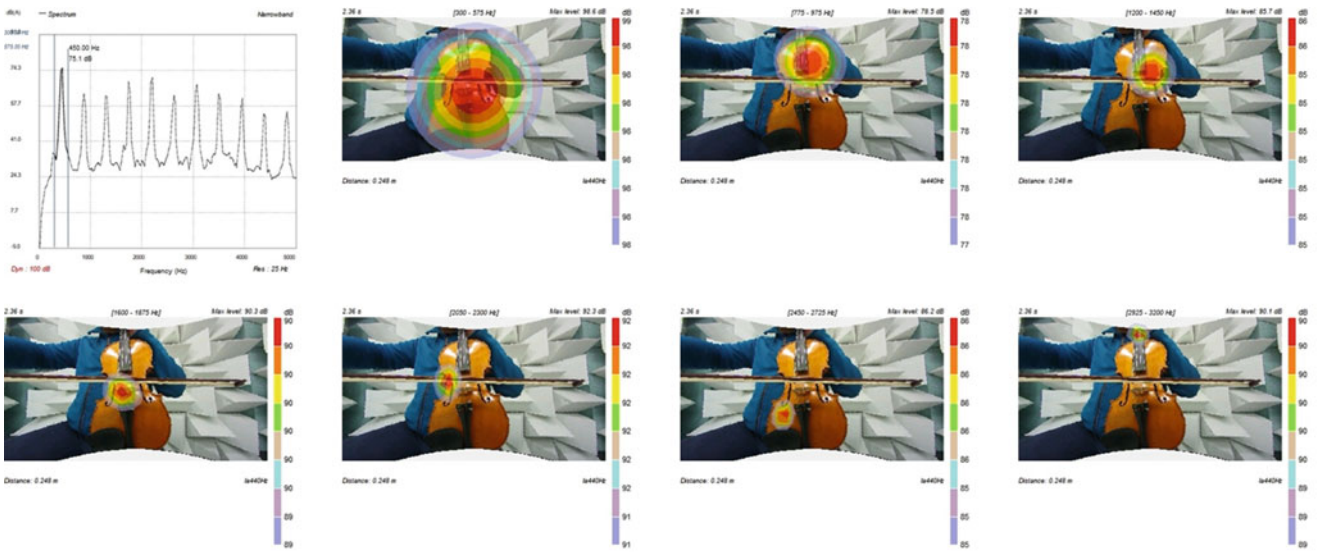

Fig. 15.4 Excitation with A, 440 Hz, response spectrogram and sound source localisation in the frequency range 0÷3500 Hz

The mode shapes numerically computed from a solid model of the tested violin, tuned on the experimental results of [1], were compared to the Sound Camera sound source localisation maps. The natural frequency values are to be considered with a reasonable updating, in particular due to the partially unknown orthotropic properties of the woods.

In Fig. 15.6, the mode related to the right f-hole top part is shown. The sound source localisation at that frequency, corresponding to the E note at 660 Hz, is qualitatively close to the numerical mode shapes. In this case, the second harmonics

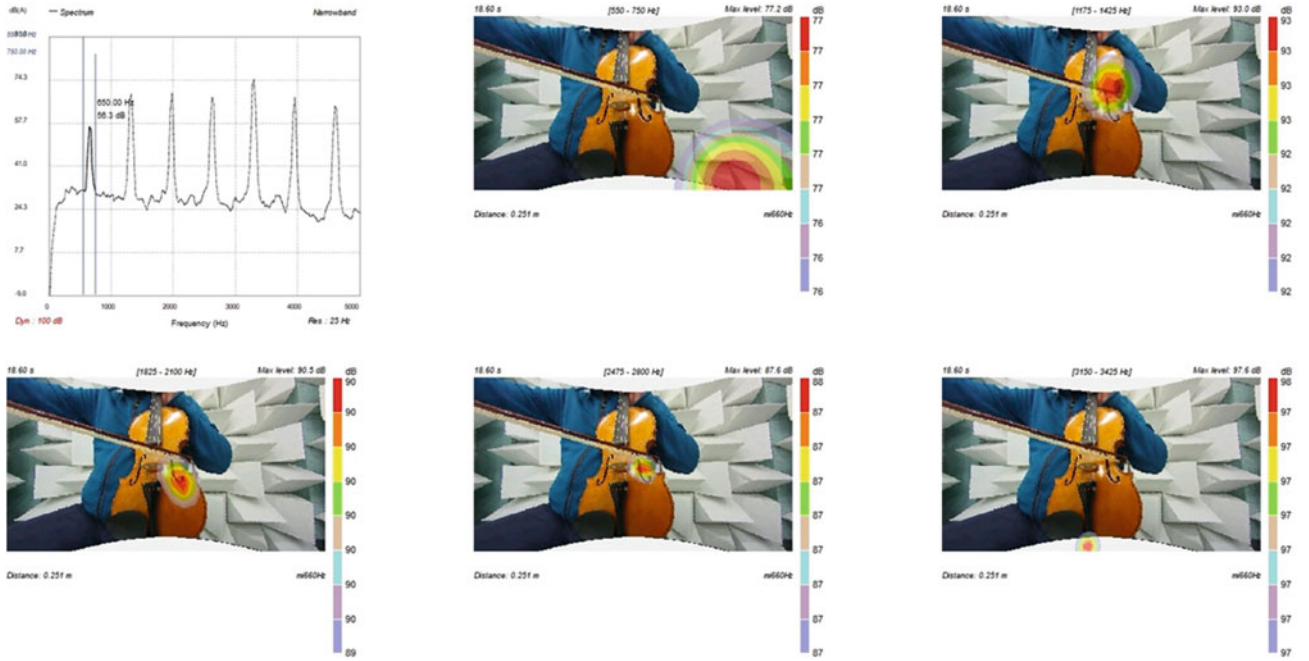

Fig. 15.5 Excitation with E, 660 Hz, response spectrogram and sound source localisation in the frequency range 0÷3500 Hz

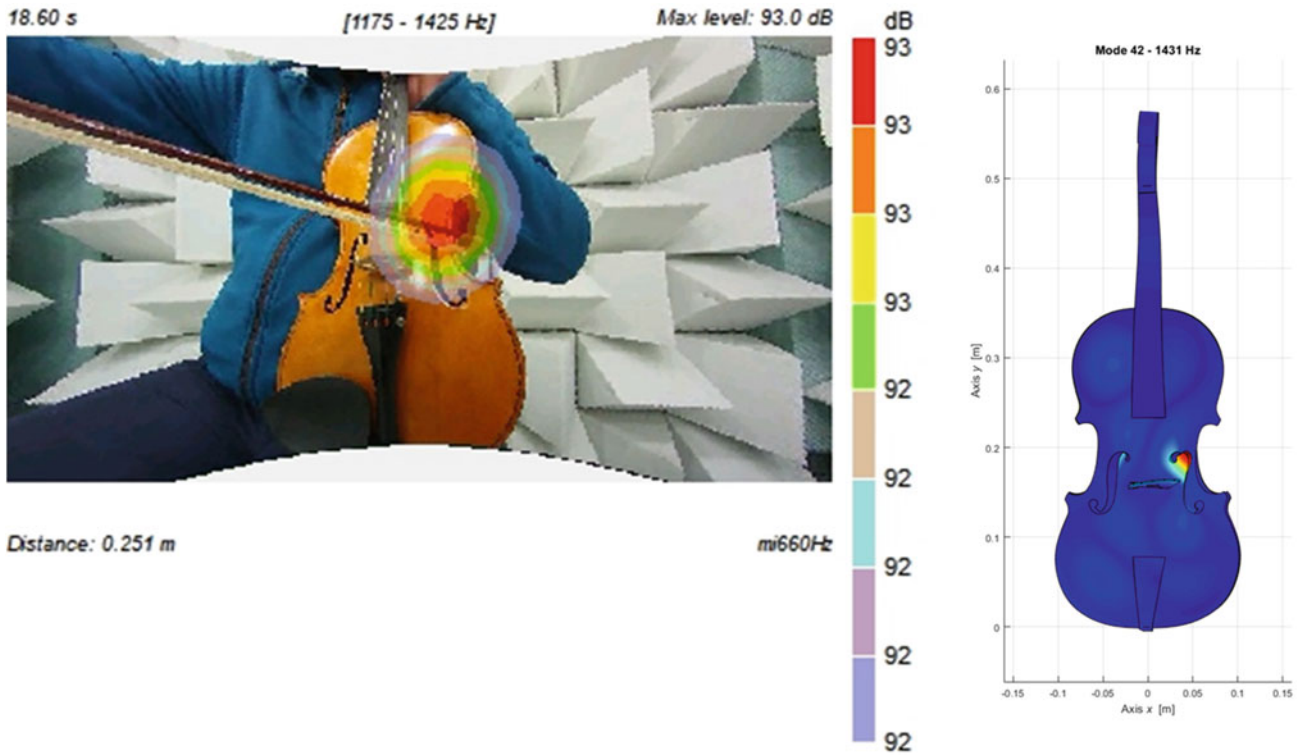

Fig. 15.6 f-hole mode shape

of the excitation frequency was really close to the detected mode. Hence, the response at that frequency was mostly related to the f-hole vibration.

A global mode shape of the top plate, related to the top and bottom left lungs, is shown in Fig. 15.7. The experimental sound source was generated by an excitation, corresponding to the G note at ~196 Hz. The mode shapes were identified at

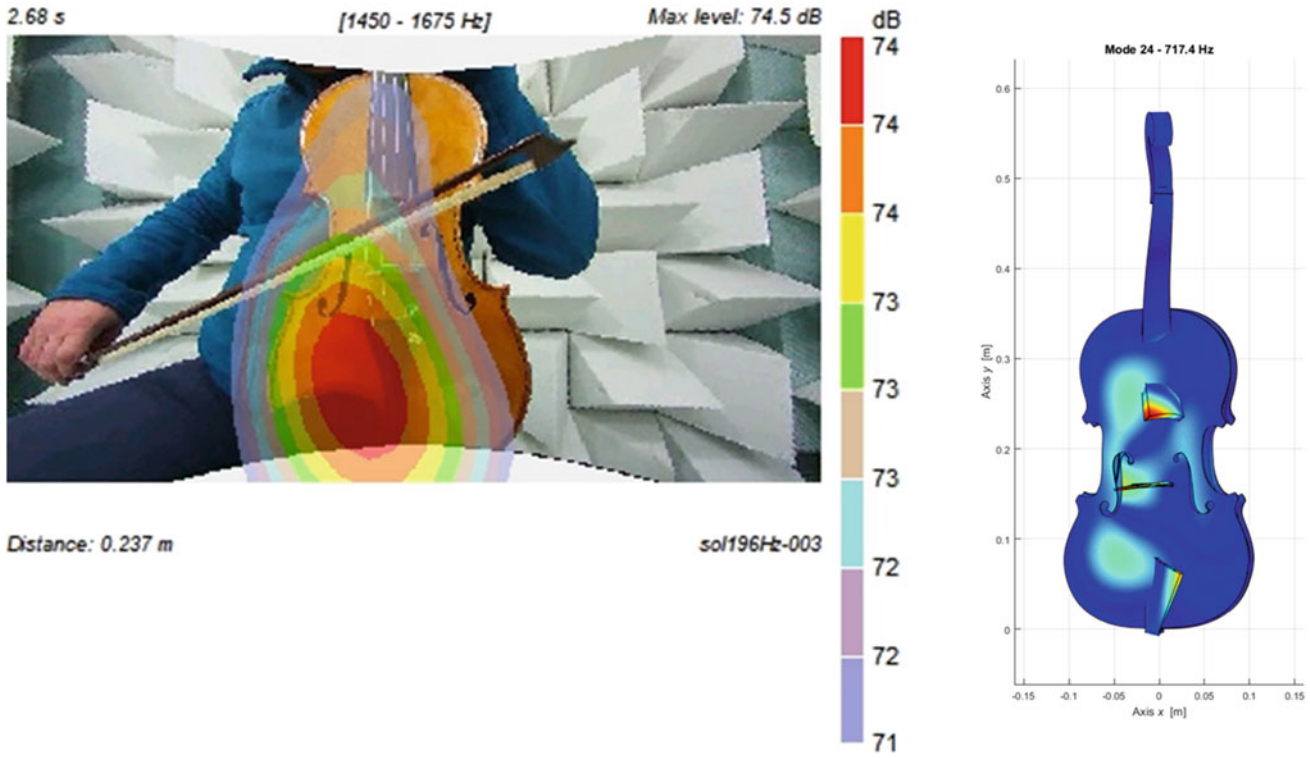

Fig. 15.7 Left lung mode shape

almost double frequency with respect to the numerical mode shapes, because of the intrinsic nonlinearity of the excitation and of the system.

As in the previous case, also the bridge mode, shown in Fig. 15.8, was identified at a double frequency with respect to the numerical forecast.

A more complete mode shape of the top plate, involving the right bottom lung, the left f-hole and the central part of the top front plate, was numerically and experimentally identified in Fig. 15.9. As for the previous case, the mode shapes were qualitatively quite close. However, the natural frequency was again double, due to the inherent structure nonlinearity.

A neck sonic mode shape was also identified in Fig. 15.10. In this case, the ratio between the experimental natural frequency is almost 6. This can be a sixth harmonics of the real mode or an higher-order bending of the neck. This is quite difficult to be understood, and it represents a limitation of the sound source localisation method applied to the multi-degrees-of-freedom shape identification.

15.5 Conclusion

An experimental campaign was performed to test the feasibility of an alternative experimental method to identify the structural sonic mode shapes of a violin using commercial sound source localisation hardware and the related methodologies. The selected Simcenter Sound Camera configuration was quite accurate in the localisation of the sound sources for frequencies higher than approximately 500 Hz. All the most important sectors of the violin, identified in the literature as responsible for the sound emission, were correctly identified. Due to the frequency limits, it was not possible to identify the lower-frequency structural mode shapes. However, those mode shapes can be qualitatively identified at frequencies multiple of their natural frequencies. Finally, the explored experimental method currently does not allow to identify the structural mode shapes, if there is not a preliminary estimation of the natural frequencies.

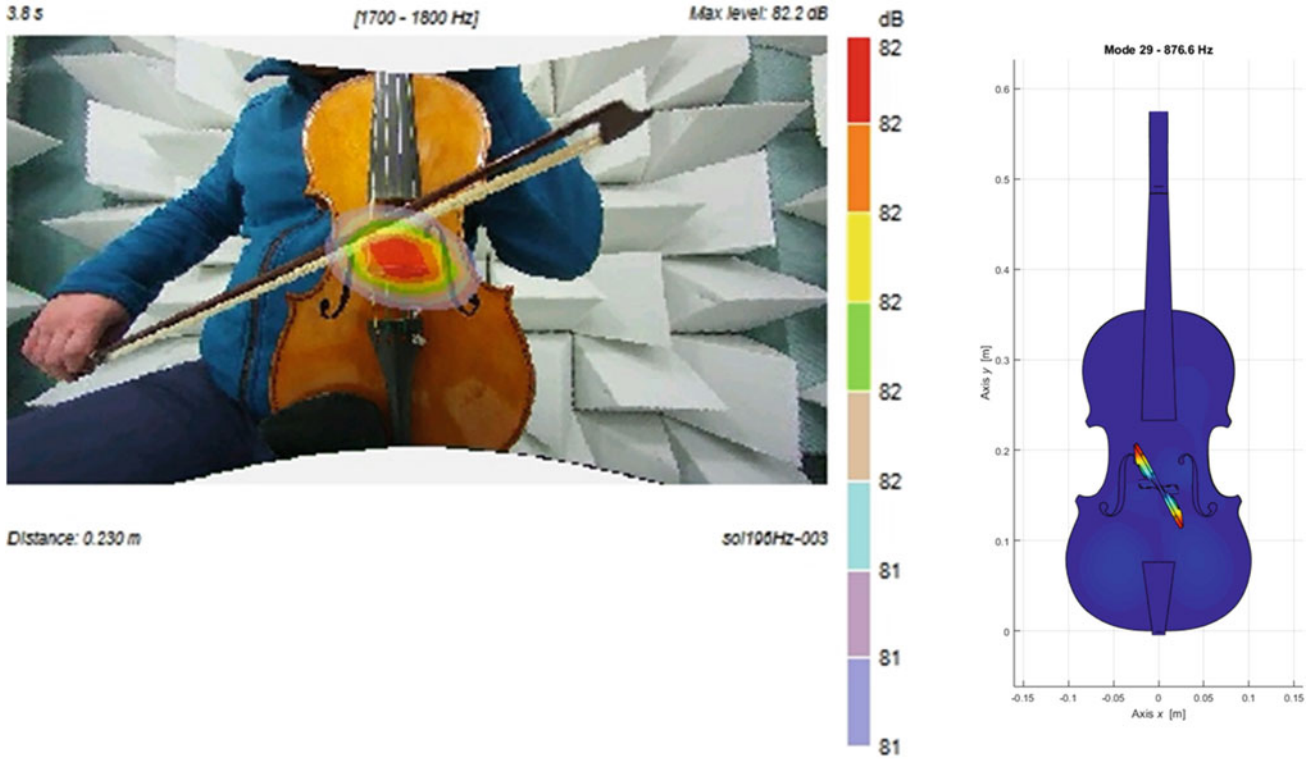

Fig. 15.8 Bridge mode shape

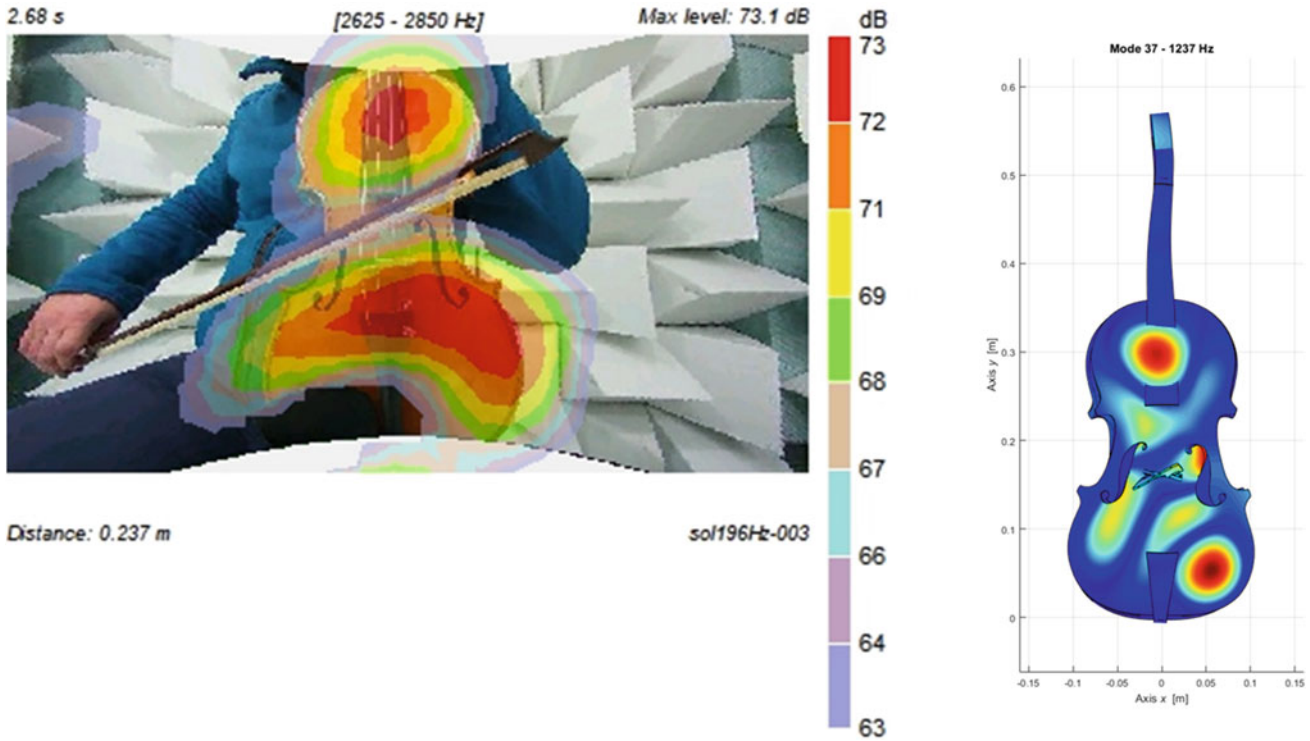

Fig. 15.9 Lungs higher frequency mode shape

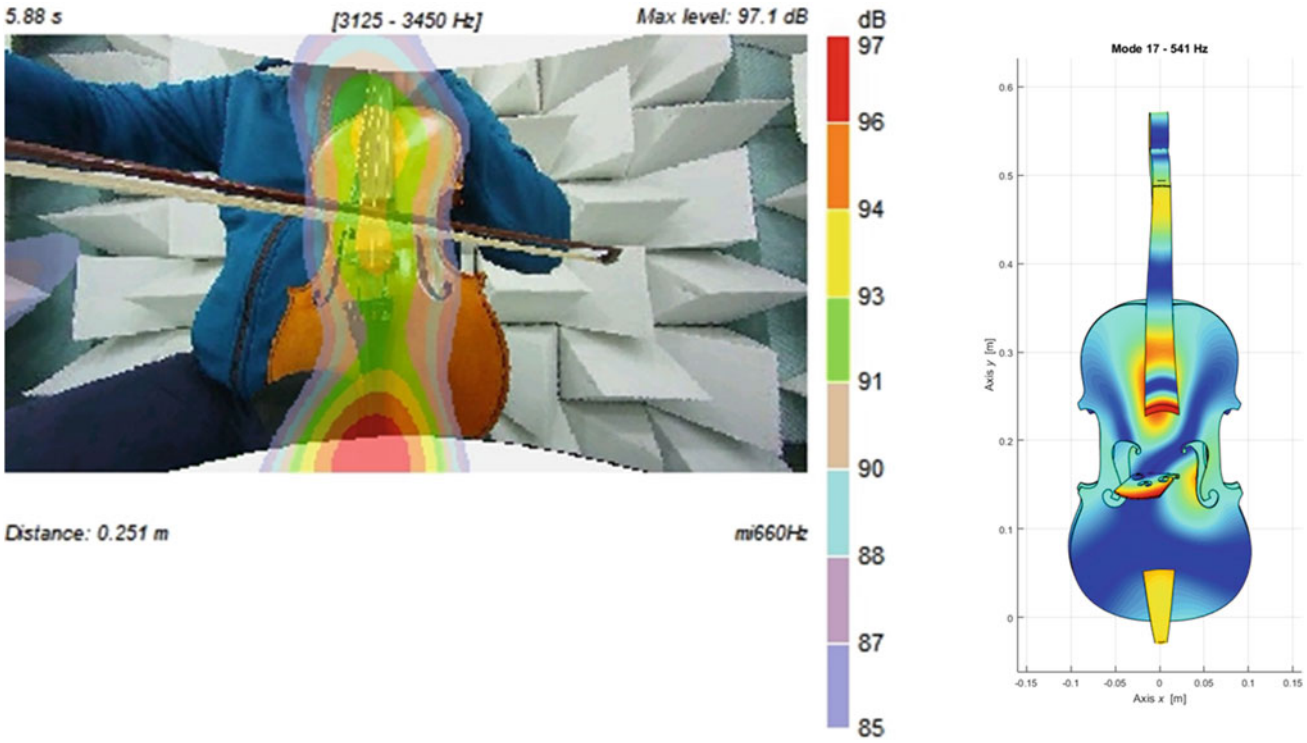

Fig. 15.10 Neck mode shape

Acknowledgements The authors wish to acknowledge Dr. Simone Geroso, PFD Simulation & Test Solutions of Siemens PLM Software, and Dr. Marco Brunelli, CEO of BSim Group, for the important technical support. Finally, the authors wish to thank the Accademia Liuteria Piemontese "S. Filippo" (Torino, Italy) and the violin-maker Enzo Cena for the suggestions and technical support in relation to violin-making know-how.

References

1. Bonisoli E., Casazza M., Lisitano D., Dimauro L.: Parametric experimental modal analysis of a modern violin based on a Guarneri del Gesù model. In: Rotating Machinery, Vibro-Acoustics & Laser Vibrometry. Proceedings of the 36th IMAC, Ch. 21, vol. 7, pp. 219–230. Springer (2018). https://doi.org/10.1007/978-3-319-74693-7_21
2. Gren, P., Tatar, K., Granström, J., Molin, N.E., Jansson, E.V.: Laser vibrometry measurements of vibration and sound fields of a bowed violin. Meas. Sci. Technol. **17**(4), 635–644 (2006). https://doi.org/10.1088/0957-0233/17/4/005
3. https://blogs.sw.siemens.com/simcenter/bayesian-focusing-allrounder-for-localization-and-quantification-of-sound-sources/available in 1 Oct 2021
4. Chiariotti, P., Martarelli, M., Castellini, P.: Acoustic beamforming for noise source localization – reviews, methodology and applications. Mech. Syst. Signal Process. **120**, 422–448 (2019). https://doi.org/10.1016/j.ymssp.2018.09.019